

NAT'L INST. OF STAND & TECH

A11106 121422

NIST
PUBLICATIONS



Nanotechnology

Compiled and Edited by:

Michael T. Postek,
Assistant to the Director for Nanotechnology

Joseph Kopanski,
Program Office

David Wollman,
Electronics and Electrical Engineering Laboratory

August 2006

NIST Special Publication: 1052

NIST

National Institute of Standards and Technology
Technology Administration, U.S. Department of Commerce

QC
100
U57
#1052
2006
C.2



U.S. Department of Commerce

Carlos M. Gutierrez, Secretary

Technology Administration

Robert Cresanti, Under Secretary of Commerce for Technology

National Institute of Standards and Technology

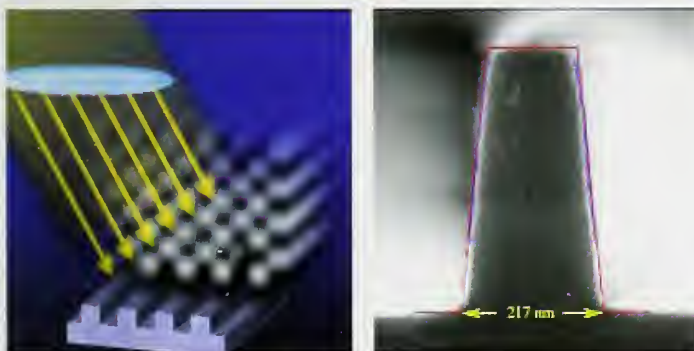
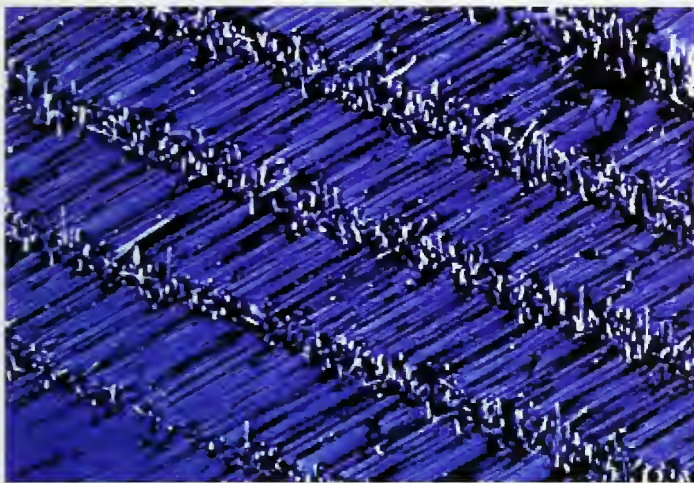
William Jeffrey, Director

Certain commercial entities, equipment, or materials may be identified in this document in order to describe an experimental procedure or concept adequately. Such identification does not imply recommendation or endorsement by the National Institute of Standards and Technology, nor does it imply that the materials or equipment used are necessarily the best available for the purpose.

National Institute of Standards and Technology Special Publication 1052

Natl. Inst. Stand. Technol. Spec. Publ. 1052, 186 pages (August 2006)

CODEN: NSPUE2



NIST Special Publication 1052

Accomplishments in Nanotechnology

Compiled and Edited by:

**Michael T. Postek,
Assistant to the Director
for Nanotechnology,
Manufacturing Engineering
Laboratory**

**Joseph Kopanski,
Program Office**

and

**David Wollman,
Electronics and Electrical
Engineering Laboratory**

U. S. Department of Commerce
Technology Administration
National Institute of Standards and
Technology
Gaithersburg, MD 20899

August 2006



National Institute of Standards and Technology • Technology Administration • U.S. Department of Commerce

Acknowledgments

Thanks go to the NIST technical staff for providing the information outlined on this report. Each of the investigators is identified with their contribution. Contact information can be obtained by going to:

<http://www.nist.gov>

Acknowledged as well, is the invaluable assistance and support provided by Mark Bello of the NIST Public and Business Affairs Office, Thelma Allen, Douglas Smith and Anne Chaka of the NIST Program Office. Bessmarie (Beamie) Young is also thanked for her contribution to the design of the cover for this document. Mylene Ouimette and Ilse Putman of the NIST Information Services Division are thanked for their assistance in getting the document prepared for publishing and Geoff Holdridge of the National Nanotechnology Coordination Office and WTEC is thanked for his invaluable assistance in document formatting and preparation.

Table of Contents

Table of Contents

Introduction.....	1
 1 - Fundamental Nanoscale Phenomena and Processes	
Nanoscale Science, Joseph A. Stroscio and Daniel T. Pierce (PL).....	5
Nanotechnology with atom optics, Jabez J. McClelland PL).....	7
Nanoscale Characterization of Polymeric Materials Degradation, Tinh Nguyen, Xiaohong Gu, and Jon Martin (BFRL).....	9
Nanomechanical Characterization of Nanoparticle-filled Polymeric Coatings and Composites, Stephanie Scierka and Peter Votruba-Drzal (BFRL).....	11
Creating Visual Models of Nanoworlds, Judith Devaney (ITL).....	13
Brillouin Light Scattering, Ward Johnson, Sudook Kim, Colm Flannery, and Pavel Kabos (MSEL).....	15
Nanolithography: Next-Generation Polymer Photoresists, Vivek M. Prabhu (MSEL).....	16
Modeling for Organic Conduction, Carlos A. Gonzalez (CSTL).....	17
Spin Electronics, William H. Rippard and Matthew R. Pufall (EEEL).....	19
Nanomagnetodynamics, Robert D. McMichael (MSEL).....	21
Nanomagnetism, John Unguris and Mark Stiles (PL).....	22
Synthesis, Characterization, and Manipulation of Magnetic Nanoparticles, Guangjun Cheng and Angela R. Hight Walker (PL).....	24
Nanomagnetodynamics: Fundamental Properties, Thomas J. Silva, (EEEL).....	25
Bioelectronics Michael Gaitan, Darwin Reyes-Hernandez, and Brian Polk, EEEL, Laurie Locascio, and Sam Forry CSTL	27
Single Molecule Nanovials, Michael Gaitan EEEL, and Laurie Locascio and Wyatt Vreeland, CSTL.....	29
Optical Manipulation of Nanocontainers and Nanotubes, William D. Phillips, Kristian Helmerson (PL).....	31

Table of Contents

Fundamental Properties of Quantum Dots, Kevin Silverman (EEEL).....	33
Multiscale Modeling of Nanostructures, Vinod Tewary and David Read (MSEL).....	35
Designing the Nanoworld: Nanosystems and Nano optics, Garnett W. Bryant (PL).....	36
Precision Metrology for Nanoscale Quantum Technologies, John Lawall and Garnett W. Bryant (PL).....	38
Control of Cold Quantum Gases for Atomic Clocks and Quantum Information Processing, Paul S. Julienne and Eite Tiesinga (PL).....	40
Quantum Computing with Trapped Ions, David Wineland and Tom O'Brian (PL).....	42
Neutral Atom Quantum Computation, William D. Phillips, James Porto (PL).....	44

2 - Nanomaterials

Polymer Miscibility of Imidazolium Compatibilized Nanotubes, Jeffrey Gilman (BFRL).....	45
New Materials to Protect Firefighters from Burn Injuries, Jeffrey Gilman and Kuldeep Prasad (BFRL).....	46
Characterization and Photoreactivity of Titanium Dioxide Nanostructures, Stephanie Scierka and Joannie Chin (BFRL).....	47
Optical Properties of Carbon Nanotubes, John Lehman (EEEL).....	49
Characterization of Single Walled Carbon Nanotubes, Angela R. Hight Walker (PL).....	50
Stability of Nanowires, Geoffrey B. McFadden (ITL).....	51
Semiconductor Quantum Dot Structure Metrology, Alexana Roshko (EEEL).....	53
Chemistry and Structure of Nanomaterials, Daniel A. Fischer (MSEL).....	55
Mechanical Metrology for Small-Scale Structures, Edwin R. Fuller, Jr. and George D. Quinn (MSEL).....	56
Highly Charged Ion Modified Materials, Joshua M. Pomeroy and John D. Gillaspy (PL).....	57
Nanoscale Metrology of III-Nitride Semiconductor Films and Nanowires, Norman Sanford and John Schlager (EEEL).....	58
Mathematical Modeling of Nanomagnetism, Michael J. Donahue and Donald G. Porter (ITL).....	60
Magnetic Materials For Nanoscale Sensors and Ultra-High Density Data Storage, William F. Egelhoff, Jr. (MSEL).....	62

Table of Contents

3 - Nanoscale Devices and Systems

Evanescence Microwave Probing and High-resolution Microwave Power Imaging, Michael Janezic, James Baker-Jarvis, and Pavel Kabos (EEEL).....	63
Chemical Sensing with Nanowires & Nanotubes, Richard E. Cavicchi (CSTL).....	64
III-Nitride Semiconductor Nanowires: Growth and Characterization, Kris Bertness and Norman Sanford (EEEL).....	65
Measuring & Understanding Charge Transport in Molecules, Roger van Zee, (CSTL).....	66
MOS Device Characterization and Reliability Project, John S. Suehle and Eric M. Vogel (EEEL).....	68
Nanoelectronic Device Metrology Project, Curt A. Richter and Eric M. Vogel (EEEL).....	70
Nanomagnetodynamics: Devices, Stephen E. Russek, (EEEL).....	72
Nanoscale Engineered Magnetic Sensors, David P. Pappas, (EEEL).....	74
Single Photon Sources and Detectors, Richard Mirin (EEEL).....	76
Terahertz Technology, Erich Grossman and Robert Schwall (EEEL).....	78
Nanoscale Fabrication, James Beall (EEEL).....	80
Johnson Noise Thermometry, Wes Tew, Sam Benz, Sae Woo Nam (EEEL).....	82
Quantum Communications, Sae Woo Nam (EEEL).....	84
Quantum Computing Using Superconducting Phase Qubits, Ray Simmonds (EEEL).....	86
Quantum Sensors, Kent Irwin (EEEL).....	88
Single Electronics for Standards and Metrology, Mark Keller and Neil Zimmerman (EEEL).....	90
Quantum Voltage Metrology, Samuel Benz and Yi-hua Tang (EEEL).....	92
Architectures for Fault-tolerant Quantum Computing, Emanuel Knill (ITL).....	94
Synthesis of Quantum Logic Circuits, Stephen S. Bullock (ITL).....	96
Quantitative single-molecular pair fluorescence resonance, Lori S. Goldner (PL).....	98
Bacteriophage/Quantum-dot nanocomplex to detect biological target in clinical or environmental isolates, Jeeseong Hwang (PL).....	100

Table of Contents

4- Instrumentation Research, Metrology and Standards for Nanotechnology

Chemical Sensor Microscopy for Nanotechnology, Tinh Nguyen and Xiaohong Gu (BFRL).....	101
Nanomechanical Properties of Polymer Thin Films, Christopher M. Stafford (MSEL).....	103
Nanomechanical Metrology, Douglas T. Smith and Lyle E. Levine (MSEL).....	104
Improving Image Resolution in Nanotechnology, Alfred Carasso (ITL).....	105
Optical Metrology for Nanolithography, John H. Burnett, Simon G. Kaplan, and Eric L. Shirley (PL).....	107
True Three-Dimensional Tomography Utilizing Bayesian Statistical Inference, Donald Malec and Juan Soto (ITL).....	109
Structure and Dispersion Measurements of Polymeric Building Materials, Li-Piin Sung (BFRL).....	111
Synthetic X-ray Spectrum Images for 3D Chemical Imaging at the Nanoscale, John Henry J. Scott and Nicholas Ritchie (CSTL).....	113
Carbon Nanotube Metrology, Paul Rice and Tammy Oreskovic (MSEL).....	115
Nanotribology and Surface Properties, Stephen Hsu (MSEL).....	116
Neutron Reflectometry for Highly Accurate Nanometer Metrology, Joseph A. Dura (MSEL).....	117
Gradient Reference Specimens for Advanced Scanned Probe Microscopy, Michael J. Fasolka and Duangrut Julthongpiput (MSEL).....	118
Quantitative Nanomechanical Properties, Donna C. Hurley (MSEL).....	119
Highly Charged Ions in EUV Lithography, John D. Gillaspay and Joshua M. Pomeroy (PL).....	120
Electrical Test Structure Metrology, Michael Cresswell and Richard Allen (EEEL).....	122
Molecular Nanomagnets, Brant Cage and Stephen E. Russek, (EEEL).....	124
Nanomagnetic Measurements, John Moreland, (EEEL).....	126
Nanoparticle Measurements for Biological Applications, John Moreland, (EEEL).....	128
Imaging Methods for Nanoparticle and Cell Systems to Investigate Toxicity, Cynthia J. Zeissler and Peter E. Barker (CSTL).....	130

Table of Contents

5 - Nanomanufacturing

Development of High-resolution Variable Pressure Reference Scanning Electron Microscope, Andras E. Vladar, Michael T. Postek and John S. Villarrubia (MEL).....	133
Scanning Probe Microscopy for Nanoscale Measurements, Ronald Dixson, Joseph Fu, George Orji, and Theodore Vorburger (MEL).....	135
Scanning Probe Microscopy for Nanoscale Measurements: Atom-Based Height Standards, Joseph Fu, Ronald Dixson, George Orji, and Theodore Vorburger (MEL).....	137
Atom-Based Dimensional Metrology, Rick Silver (MEL).....	139
Critical Dimension Metrology using Scanning Electron Microscopy and a Model-Based Library, John S. Villarrubia and András E. Vladár (MEL).....	141
SI traceable force for scanning probe microscopy and instrumented indentation, Jon R. Pratt (MEL).....	143
Phase-sensitive Scatterfield Optical Imaging for sub-10 nm Dimensional Metrology, Rick Silver (MEL).....	145
Advanced Control Systems and Positioning for Nanoscale Measurements and Standards, Nicholas G. Dagalakis (MEL).....	147
Molecular Measuring Machine, John A. Kramar (MEL).....	149
Agile Nanoassembly to Prototype, Test, and Manufacture Functional Nanodevices, Thomas W. LeBrun (MEL).....	151
Development of Nano-tip Electron Guns for the Scanning Electron Microscope, Andras E. Vladar and Michael T. Postek (MEL).....	153
Measurement Strategy for Line Edge and Linewidth Roughness Metrology, John S. Villarrubia and András E. Vladár (MEL).....	155
Combinatorial Metal Selection for Catalytic Growth of ZnO Semiconductor Nanowires, Albert V. Davydov (MSEL).....	157
Electrical Properties of On-Chip Interconnections, Daniel Josell and T.P. Moffat (MSEL).....	158
Horizontal Growth and In Situ Assembly of Oriented Semiconductor Nanowires, Babak Nikoobakht and Stephan J. Stranick (CSTL).....	159
Organic Electronics, Eric K. Lin (MSEL).....	161

Table of Contents

6 - Major Research Facilities and Instrumentation Acquisition

The NIST Advanced Measurement Laboratory Nanofab, Robert Celotta (CNST), Russ Hajdaj (CNST) and Eric M. Vogel (EEEL).....	163
Probing Nanoscale Disorder with Neutron Tunneling Spectroscopy, Robert M. Dimeo and Dan A. Neumann (MSEL).....	164
Probing the Nanostructure of Lipid Membranes with the AND/R (Advanced Neutron Diffractometer/Reflectometer), M. Mihailescu and David Worcester (MSEL).....	165

Appendix 1

Cross Reference to NIST Nanotechnology Focus Areas.....	167
---	-----

Appendix 2

Key Words.....	173
----------------	-----

Introduction

The National Institute of Standards and Technology (NIST) is the Nation's measurement and standards laboratory, established by the U.S. Congress in 1901. Today, NIST's mission is to promote U.S. innovation and industrial competitiveness by advancing measurement science, standards, and technology in ways that enhance economic security and improve our quality of life. To enable accurate and precise measurements at the nanoscale, NIST is conducting scientific research into fundamental nanoscale properties, developing appropriate standards, and is providing calibrations and traceability to basic standard international (SI) units. NIST seeks to fulfill its mission by working closely with industry, academia, and other government agencies. NIST's work in nanotechnology is in coordination with the National Nanotechnology Initiative (NNI), which is administrated by the Subcommittee on Nanoscale Science, Engineering, and Technology (NSET) of the National Science and Technology Council. (See the NNI web site at www.nano.gov.) Under the NNI, NIST is developing a broad range of nanometrology (measurements) and nanomanufacturing techniques necessary for the successful commercialization of nanotechnology. In recent testimony before Congress, Dr. Tom Cellucci, president of Zyvex Corporation stated: *"Much of our leadership position and the jobs generated for Americans can be directly attributable to NIST. NIST fulfills a vital role in bringing the promise of nanotechnology to the American people. NIST is responsible for developing the measurements, standards, and data critical to private industry's development of products for a potential market that is estimated to exceed a trillion dollars in the next decade."*

NIST, as an agency of the U.S. Department of Commerce, also works to help facilitate international trade by working with international standards organizations and other national metrology institutes. Key issues in the future for U. S. success in international trade, with respect to nanotechnology, will be traceability of measurements and "harmonization" of international measurements and standards.

This document includes a list of selected NIST accomplishments in nanotechnology for the period of fiscal years 2004 and 2005. These accomplishments are grouped into the NNI's Program Component Areas (PCAs), which are defined below. The NNI has established the PCAs as the major subject areas for research and development vital to the successful commercialization of Nanotechnology. A bibliography of NIST publications in nanotechnology from the years 2000 to 2005 is also included on the accompanying compact disk.

NNI Program Component Areas

The NNI sets out four goals detailing the overarching strategy and plans of the initiative. Program Component Areas (PCAs) are the major subject areas under which related NNI projects and activities are grouped. The PCAs relate to areas of investment that are critical to accomplishing the NNI goals. These areas cut across the interests and needs of the participating agencies, and by grouping together work that is taking place within multiple agencies, advancement may be further expedited. The PCAs are intended to provide a means by which the NSET Subcommittee, the Office of Management and Budget (OMB), Congress, and others may be informed of the relative investment in these key areas, and by which the agencies funding R&D can better direct and coordinate their activities. Detailed investments and agency plans for each PCA will be included in the annual NNI supplement to the President's budget. The PCAs are relatively broad and are expected to continue to adequately describe the activities within the NNI for the next several years. The PCAs are defined as follows:

- **Fundamental nanoscale phenomena and processes**

Research leading to the discovery and development of fundamental knowledge pertaining to new phenomena in the physical, biological, and engineering sciences that occur at the nanoscale.

Introduction

Elucidation of scientific and engineering principles related to nanoscale structures, processes, and mechanisms.

- **Nanomaterials**

Research aimed at discovery of novel nanoscale and nanostructured materials and at a comprehensive understanding of the properties of nanomaterials (ranging across length scales, and including interface interactions). Also, R&D leading to the ability to design and synthesize, in a controlled manner, nanostructured materials with targeted properties.

- **Nanoscale devices and systems**

R&D that applies the principles of nanoscale science and engineering to create novel, or to improve existing, devices and systems. This PCA includes the incorporation of nanoscale or nanostructured materials to achieve improved performance or new functionality, and possibly greater levels of miniaturization. The systems and devices themselves may, but need not necessarily, be less than 100 nanometers in size to meet this definition.

- **Instrumentation research, metrology, and standards for nanotechnology**

R&D pertaining to the tools needed to advance nanotechnology research and commercialization, including next-generation instrumentation for characterization, measurement, synthesis, and design of materials, structures, devices, and systems. This PCA also includes R&D and other activities related to development of standards, including standards for nomenclature, materials, characterization and testing, and manufacture.

- **Nanomanufacturing**

R&D aimed at enabling scaled-up, reliable, cost effective manufacturing of nanoscale materials, structures, devices, and systems. Includes R&D and integration of ultra-miniaturized top-down processes and increasingly complex bottom-up or self-assembly processes.

- **Major research facilities and instrumentation acquisition**

Establishment of user facilities, acquisition of major instrumentation, and other activities that develop, support, or enhance the Nation's scientific infrastructure for the conduct of nanoscale science, engineering, and technology research and development. Includes ongoing operation of user facilities and networks.

- **Societal Dimensions**

Various research and other activities that address the broad implications to society, including benefits and risks, such as:

- Research directed at environmental, health, and safety impacts of nanotechnology development and risk assessment of such impacts
- Education-related activities, such as development of materials for schools, undergraduate programs, technical training, and public outreach
- Research directed at identifying and quantifying the broad implications of nanotechnology for society, including social, economic, workforce, educational, ethical, and legal implications

Individual PCAs may encompass basic research through application-oriented efforts, including experimental, theoretical, modeling, and simulation approaches. There is a gradation within the PCAs in the scale or level of organization, ranging from fundamental nanostructure phenomena through nanomaterials, devices and systems, tools and instrumentation, and manufacturing. The last two PCAs listed above are different in nature, in that they provide for state-of-the-art research facilities and for addressing societal implications. The basic nature of the infrastructural research at NIST supports all of the PCAs including Societal Dimensions.

Introduction

Instrumentation, Metrology, and Standards/Nanomanufacturing

The NNI gives NIST a leadership role in the *Instrumentation Research, Metrology, and Standards for Nanotechnology* PCA. The nanometrology PCA is pervasive, crosscutting, and unifying to all the NNI PCAs. Instrumentation provides the necessary data upon which scientific conclusions can be based, and correct metrology provides the ability to properly and accurately interpret these data. Researchers in NIST's seven laboratories are also developing the traceable measurements, standards, data, and models that will provide the enabling infrastructure to facilitate the commercialization of nanotechnology. NIST's nanotechnology work is also making possible new, quantum-based realizations of the fundamental units in support of international metrology and, ultimately, international trade. NIST works with all the other federal agencies in exploiting nanotechnology in areas such as homeland security and environmental protection to the benefit of the missions of all the partnering agencies. NIST also shares the responsibility for the *Nanomanufacturing* PCA with the National Science Foundation and functions to provide the needed metrology necessary to exploit the research and discoveries in nanotechnology providing a bridge between discovery and products for the Nation.

Unique NIST Resources

NIST measurements and standards capabilities are critical to maintaining US industry's technological leadership. Four key resources are available for nanotechnology and nanometrology research: the Advanced Measurement Laboratory, the Center for Nanoscale Science and Technology, the Center for Neutron Research, and the Advanced Chemical Sciences Laboratory. These resources are strongly augmented by nanometrology research in all of the technical laboratories across the entire NIST campus.

- **Advanced Measurement Laboratory (AML).** The AML is a 49,843 m² (536,500 SF) state-of-the-art laboratory complex opened in FY 2004. This laboratory provides NIST with an ultra controlled metrology environment (temperature, vibration, air quality, humidity, and power) for nanomanufacturing and nanometrology. The AML is the most environmentally stable laboratory of its kind in the world and houses NIST's most advanced metrology tools. The complex of five buildings includes a state-of-the-art nanofabrication facility. This entire laboratory complex will enable NIST and its partners to produce and disseminate world-class measurement standards enabled by next-generation metrology capabilities beyond currently obtainable levels.
- **NIST Center for Nanoscale Science and Technology (CNST).** The Center enables science and industry by providing essential measurement methods, instrumentation, and standards to support all phases of nanotechnology development, from discovery to production.
- **NIST Center for Neutron Research (NCNR).** A national user facility that serves more than 2,000 scientists annually, the NCNR is the only cold (i.e. low energy) neutron facility with comprehensive capability in the United States - providing tools essential to study the complex biological, polymeric and composite materials that are at the forefront of nano-materials research.
- **Advanced Chemical Sciences Laboratory (ACSL).** The ACSL was built to house programs in biotechnology, analytical, environmental, clinical, and other related chemical measurements and standards. The state-of-the-art ACSL features advanced designs that will help NIST meet the 21st-century needs for accurate chemical measurements, standards, and methods used for pharmaceutical manufacturing, medical diagnosis, pollution monitoring and clean up, and other research in nanotechnology.

Michael T. Postek

Assistant to the Director for Nanotechnology

Introduction

Common NIST Abbreviations Used in this Document

- BFRL..... Building and Fire Research Laboratory
- CSTL..... Chemical Science and Technology Laboratory
- EEEL Electronics and Electrical Engineering Laboratory
- ITL..... Information Technology Laboratory
- MEL..... Manufacturing Engineering Laboratory
- MSEL..... Materials Science and Engineering Laboratory
- PL..... Physics Laboratory
- TS..... Technology Services
- CNST..... Center for Nano Science and Technology
- NCNR..... NIST Center for Neutron Research

Please note that in the author line for each project, the numbers in parentheses refers to the NIST Division within the Laboratory.

Further information about these and other topics can be found at:

http://www.nist.gov/public_affairs/guide/index.htm

Nanoscale Science

Development and application of new, nanometer scale measurement and fabrication tools to explore the quantum properties of nanostructures, atoms, and electron systems and their interactions. The quantum properties of nanostructures, confined electron systems and their interactions with atoms, the effects of reduced size and dimensionality, the effects of electron spin, and the fundamentals of nanoscale magnetism are probed using advanced scanning tunneling microscopy and spectroscopy. Bottom up fabrication of atomic scale structures, atom by atom, using novel techniques developed at NIST are combined with traditional MBE fabrication technologies.

Joseph A. Stroscio and Daniel T. Pierce, PL (841)

In this program we are investigating systems and fabrication technology at the forefront of nanoscale science and technology using scanning tunneling microscopy (STM) and spectroscopy techniques. In addition to using the STM probe tip to measure physical properties, we are also using it to manipulate atoms to form new quantum structures. Nanofabrication technologies are being combined with traditional fabrication methods using molecular beam epitaxy to create future atomic scale devices. In this report we highlight two recent achievements, involving the novel dynamics of atoms observed in atom manipulation [1], and the electronic structure of 1-dimensional single atom chain systems [2].

Atom Dynamics during Atom Manipulation

Manipulation of single atoms with the scanning tunneling microscope is made possible through the controlled and tunable interaction between the atoms at the end of the STM probe tip and the single atom that is being manipulated. In the STM tunneling junction used for atom manipulation, a host of interactions that depend on the electric potentials, the tunneling current, and tip-adatom proximity effects that come into play in the atom manipulation process. Understanding these interactions and their optimization is central to understanding the atom manipulation process and is required for the efficient and reliable atom manipulation needed for large-scale construction of atomic scale devices.

Imaging with the STM places the probe tip sufficiently far from the sample so that tip-sample interactions do not initiate atom movement, and hence one can

image a stationary single atom. In order to move a single atom, we turn on the tip-adatom interaction by bringing the tip closer to the adatom by means of adjusting the tunneling junction resistance (the junction resistance is set by the ratio of the tunneling voltage to the tunneling current). It is useful to view the interaction as creating a highly localized potential well that traps the adatom under the tip. A great deal of information about the adatom motion can be learned from recording the tip height trace during the manipulation process. A new type of image, we call a “manipulated atom image” is obtained by repeating this tip height trace measurement by rastering the tip over the surface, as in the normal STM topographic mode, except now with the adatom trapped in the moving tip-induced potential well. Details on the scale of a small fraction of a lattice constant are observed in the manipulated atom image, as shown in Fig. 1.

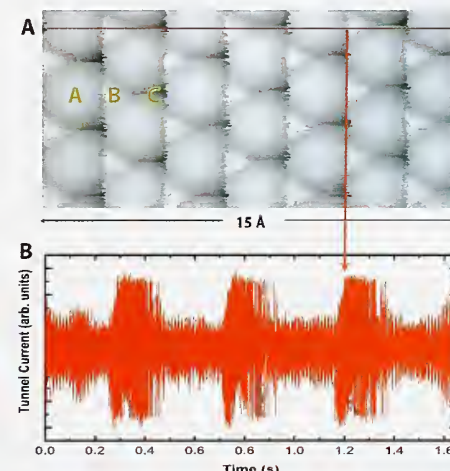


Figure 1. (A) Manipulated atom image of Co over Cu(111) surface. Tunnel current, 50 nA; sample bias, -5 mV ; $T = 4.3\text{ K}$. The labels A, B, and C denote fcc, hcp, and top sites, respectively. (B) Tunnel current recorded during manipulated atom image going through the hcp and fcc sites as indicated by the horizontal line in (A). The arrow shows the increased noise in the tunnel current corresponding to the position of the hcp site.

Our understanding of the manipulated atom image follows from the dynamics of the adatom motion hopping between fcc and hcp sites on the Cu(111) surface. The manipulated atom image for Co on Cu(111) can be thought of as a binding site image for the Co atoms, with the additional contrast changes between the fcc and hcp sites yielding information concerning the difference in the surface potential energy for these two sites. Using the motion of the Co atom to image the local binding sites and give information on the local surface potential is an example of a new class of measurements based on single atom transducers sensing local environments,

which we refer to as an “atom based metrology”.

Audio frequency components of the tunnel current can be used as a real-time diagnostic of the atom manipulation process. For Co on Cu(111), a periodic rasping sound is heard during the acquisition of a manipulated atom image, see video on website <http://realex.nist.gov:8080/ramgen/hiphopatoms.rm>. An examination of the tunneling current signal shows that this occurs when the Co atom is placed over the hcp site (see Fig. 1). It is this increase in noise density that gives rise to the “rasping” sound. An examination of the tunneling current noise properties shows that the Co atom is switching between the favored fcc site and the metastable hcp site, and it is this switching phenomena that is responsible for the periodic rasping sound.

Insight into the switching dynamics is obtained from analyzing the two-state random telegraph noise (RTN) measured in the tunneling current signal. From an analysis of the residence time distributions in the RTN we arrive at a switching rate for the Co atom to go from the fcc to hcp site, and vice-versa, as shown in Fig. 2. The transfer rates show two distinct regimes; a transfer rate independent of tunneling current, voltage and temperature that is ascribed to quantum tunneling between the two wells, followed by a transfer rate with a strong power law dependence on current or voltage, indicative of vibrational heating by inelastic electron scattering.

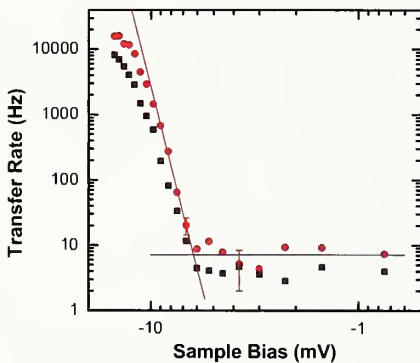


Figure 2. Transfer rate versus sample bias at constant tip height, obtained by measuring the distribution of residence time in the hcp and fcc states from two-state random telegraph noise in the tunnel current. Junction resistance 150 kilohms; $T = 2.3$ K. R_{hcp} , red circles; R_{fcc} , black squares. Solid red line shows a power-law fit to the initial threshold region; blue horizontal line shows the average transfer rate for the low-bias region for the hcp transfer rate.

End States in One-Dimensional Chains

The ability to fabricate structures on the nanoscale and measure their electronic properties presents the opportunity to discover new phenomena. We have ob-

served a new kind of electronic state at the ends of a one-dimensional nanostructure. This “end state” is a direct consequence of the lower dimensionality of the structure. Such end states can be thought of as zero-dimensional analogs to two-dimensional states that occur at the surface of a crystal. To study electronic states in one-dimension, we fabricate atomic chains by depositing gold on stepped silicon surfaces (Fig. 3). The energetics of the stepped surfaces drives the formation of atomic chains that cover the entire surface. Perfect chains can be up to 70 atoms in length, limited only by atomic defects.

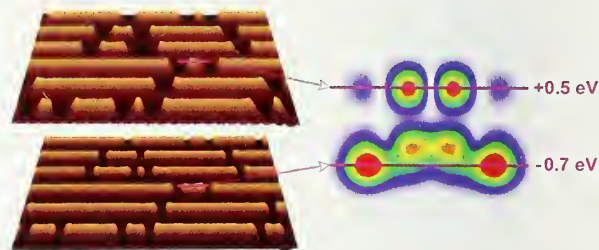


Figure 3. $8\text{ nm} \times 19\text{ nm}$ STM topography images of the same sample area at positive (top left) and negative (bottom left) biases reveal a contrast reversal over the end atoms. A tight binding model shows the density of states along a four-atom chain (right) with atomic position along the horizontal direction and energy along the vertical direction. Red shows regions of high density of states. At $+0.5\text{ eV}$ the density of states is localized over the center two atoms while at -0.7 eV localized states are found over the end atoms.

To characterize this new kind of electronic state, we made spatially resolved scanning tunneling spectroscopy measurements along finite chains to map the density of states. These measurements reveal quantized states that form in isolated chain segments. Furthermore, a transfer of spectral weight from the filled to the empty states over the atoms at the ends of the chains is directly attributable to the formation of end states. A comparison to a tight-binding model demonstrates how the formation of end electronic states transforms the density of states and the quantized levels within the chains. The end states effectively lower the energy levels of the filled states within the chains, suggesting a possible driving force for their formation.

Selected Publications

1. J. A. Stroscio and R. J. Celotta, Science **306**, 242 (2004).
2. J. N. Crain and D. T. Pierce, Science **307**, 703 (2005).

Nanotechnology with atom optics

The ultimate goal of nanotechnology is the absolute control over matter on an atom-by-atom basis. Only with this level of control can a wide range of new quantum electronic and photonic devices be fabricated with the necessary accuracy and high yield to make the next generation of electronic and information processing architectures possible. Conventional nanofabrication techniques, such as optical and electron beam lithography, and focused ion beam milling, have made great progress in recent years, but it is clear that they will not serve at the single-atom level. We are developing new, radical approaches to atom-by-atom nanofabrication that make use of the exquisite control afforded by atom optics – the use of laser beams, electric fields and magnetic fields to cool, trap, ionize, accelerate, implant, and otherwise manipulate single atoms.

Jabez J. McClelland, PL (841)

In order to controllably fabricate material at the single-atom level, it is necessary to have some way to reliably access a single atom whenever it is needed. In essence, we need a source of “atoms on demand.” One way to achieve this is by freezing atoms on a surface and collecting them when needed, as is done with low-temperature scanning-tunneling-microscopy-based atom manipulation. As an alternative, we are exploring the use of laser cooling and trapping of neutral atoms to realize a completely deterministic source of atoms. Such a source, we have discovered, has unique properties that make it ideally suited for deterministically implanting single ions in host materials with nanometer-scale resolution.

Our most significant recent accomplishment has been the demonstration in the laboratory of a deterministic source of single Cr atoms with 99% fidelity – that is, if an atom is “requested” from the source at any random time, it will produce one atom (rather than zero or more than one atom) with a probability of 99%.

The source is based on a magneto-optical trap (MOT), which uses six mutually orthogonal laser beams and a set of magnetic field coils that produce a field minimum at a central point in space. Atoms from an evaporation source are cooled by the laser beams and captured by the light force, which is made spatially dependent by the magnetic field gradient. The result is a population of very cold atoms trapped in the center of the MOT.

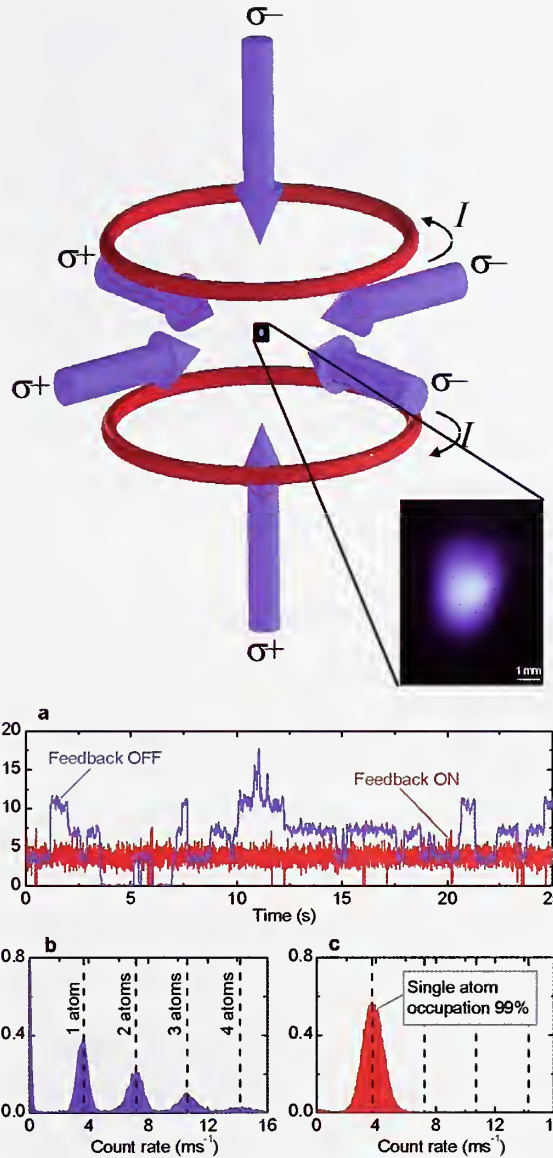


Figure 1. A magneto-optical trap with feedback-controlled loading maintains a population of exactly one atom with 99% probability.

A key ingredient in making the MOT into a deterministic source of atoms is very high efficiency fluorescence detection. This allows us to observe the arrival and departure of individual atoms in the trap with good signal-to-noise. With this high detection efficiency, we are able to implement a fast feedback control loop, which essentially turns on loading only when the trap is empty and dumps the trap contents if it by chance contains more than one atom. With a moderate amount of optimization of the feedback loop parameters, we have demonstrated 99% single-atom fidelity for random sam-

pling of trap contents, and also forced periodic ejection at rates up 10 Hz with fidelity over 90%. These results have been published in recent journal articles [1-2].

The next phase of our project involves extraction and focusing of the single atoms with nanometer resolution. In order to accomplish this, we will take advantage of the extremely low temperatures ($\sim 120 \mu\text{K}$) achievable in a MOT. These cold temperatures result in a very compact phase space volume for the atoms in the source, which allows very tight focusing of extracted atoms if a suitable set of optics is implemented. When an atom is called for, we will photoionize the atom in the trap with a fast laser pulse and extract it with a moderate electric field. Ion ray tracing calculations, which take into account the temperature and spatial extent of the source, show that with relatively simple electrostatic lenses, we will be able to focus the extracted ions to spot sizes that approach 1 nanometer.

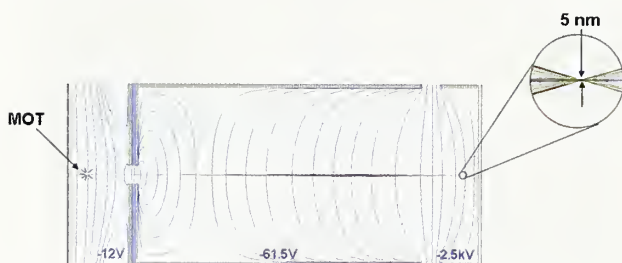


Figure 2. Ion ray tracing calculations show that single atoms from an ionized magneto-optical trap (MOT) can be focused to the nanometer-scale.

In a parallel development, we have also been investigating the implementation of our deterministic source with other atoms that might enable new technologies if they can be implanted singly with good fidelity. We have identified erbium as such an atom because as a rare earth it has technologically important optical properties when implanted in a host material. For example, erbium dopants provide the optical gain in fiber lasers used extensively in the telecommunications industry. An experimental program has begun to demonstrate laser cooling and trapping of erbium for the first time, and recently the first fluorescence measurements have been made in preparation for this.

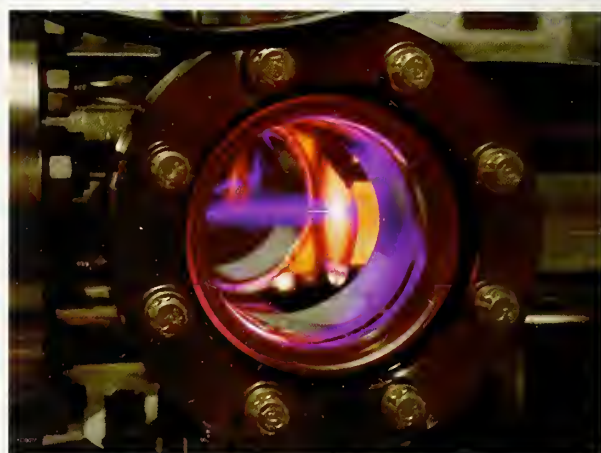


Figure 3. An atomic beam of erbium atoms is illuminated by a laser beam in the first step toward realizing a deterministic source of single erbium atoms.

Selected Publications

1. S. B. Hill and J. J. McClelland, *Appl. Phys. Lett.* **82**, 3128 (2003).
2. S. B. Hill and J. J. McClelland, *J. Opt. Soc. Am. B*, **21**, 473 (2004).

Nanoscale Characterization of Polymeric Materials Degradation

Development of reliable methodologies to predict long-term performance has been the ultimate goal of both users and producers of polymeric materials used in various industries including building and automotive. This project aims to provide nanoscale physical degradation of polymeric coatings exposed to the environments. This information is essential for understanding the degradation mechanism and developing accurate prediction models for polymeric coatings. This work is part of the NIST/Industry Consortium on Service Life Prediction of Coatings, which has been going on for ten years.

Tinh Nguyen, Xiaohong Gu, and Jon Martin,
BFRL (861)

Polymeric coatings are used extensively in outdoor structures, both for aesthetic and functional purposes. However, these materials undergo degradation during service. In this research, polymer-coated samples are exposed to outdoor environments and NIST-developed accelerating devices that can precisely vary UV light intensity and wavelengths, temperatures, and relative humidities. In addition to traditional techniques that provide data for kinetics and mechanistic studies, and for verifying service life prediction models, atomic and nanoscale techniques such as positron annihilation spectroscopy (PAS) and atomic force microscopy (AFM) are also employed to provide early physical changes of coatings. This highlight presents some examples on the use of AFM for studies of nanoscale physical degradation of polymeric coatings exposed to the environments. One example to demonstrate the utility of AFM for studies of automotive coatings photodegradation is illustrated in Figure 1. These are AFM height images of a commercial polyurethane coating on a car bumper before (top) and after exposure (bottom) to ultraviolet (UV) radiation in an artificial weathering device. The line profile and RMS roughness data (right, top) indicate that the coating surface before exposure is very smooth, with no evidence of pinholes or pits. After exposure, pits ranging from 150 nm to 400 nm in diameter and 2 nm to 5 nm in depth have developed on this sample surface.

One particularly useful application of AFM for quantitative studies of early degradation of coatings is its ability to measure the enlargement and deepening of pit formation with exposure at the nanoscale level.

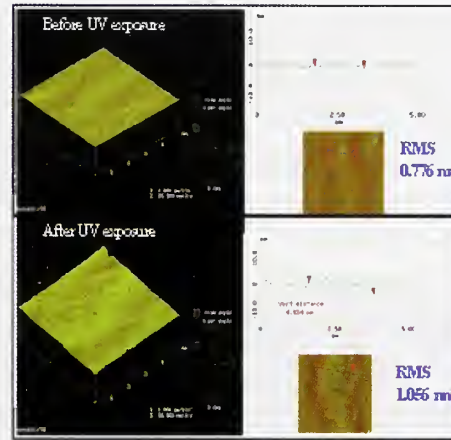


Figure 1. $5 \mu\text{m} \times 5 \mu\text{m}$, 3-D AFM height images (left) and 2-D images and line profiles (right) of a commercial automobile polyurethane-coated bumper before and after exposure to UV radiation.

This is demonstrated in Figure 2 for a urethane coating exposed for 6160 h in an artificial UV device at 70 % RH and 50 °C. For this measurement, the AFM images were taken at the same location after each exposure time. The pit depth is observed to increase nearly linearly with time, but its diameter enlarges rapidly at first then slows down. This quantitative data is useful for kinetics studies of the degradation and allows us to assess the effects of surface morphological changes on coatings appearance.

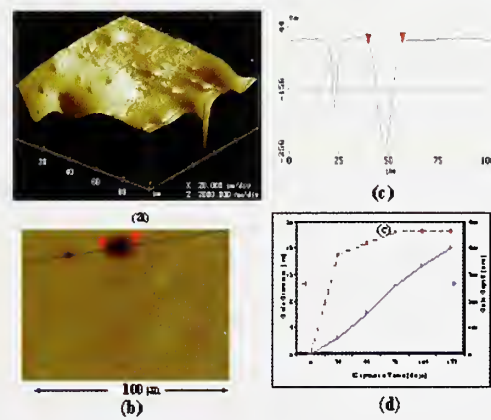


Figure 2. Imaging and measurement of pit enlargement and deepening by AFM for a coating exposed to the environment; a) 3-D image, b) 2-D image with a line crossing two pits, c) corresponding line profile showing pit width and depth, and d) depth and diameter of the large pit as function of exposure time.

These results and extensive nanoscale evidence clearly indicate that photodegradation of a polymeric coating is not a uniform thickness loss (ablation) process but is a heterogeneous phenomenon with localized pit-

ting, which grows with time. This information is essential for developing accurate models to predict long-term performance of coatings.

AFM can also provide valuable information on surface microstructure changes caused by weathering, one example is shown in Figure 3. These are height and phase images of a 70 % (mass fraction) poly(vinylidene fluoride) (PVDF) and 30 % copolymer of PMMA and poly(ethyl acrylate) (PMMA-co-PEA) before and after exposure to an UV source.



Figure 3. $1 \mu\text{m} \times 1 \mu\text{m}$ AFM height and phase images of surface of a film containing 70% PVDF and 30% PMMA-co-PEA before and after exposure to UV.

Before exposure the surface is covered with an amorphous material. However, the amorphous material is removed after UV exposure, revealing the fine lamellae structure. From AFM results, contact angle, and spectroscopic data, it has been determined that the enrichment of crystalline PVDF material on the surface is responsible for the excellent UV resistance of these coatings.

AFM is useful for detection of nanoscale pits formed in protective coatings, as shown in Figure 4. These height images and line profile show that nanopits have developed in this polyurethane coating after 30 d exposure to a corrosive environment. This result is the first evidence to verify NIST conceptual and mathematical models proposed several years ago that corrosive elements from the environments migrate to the metal surface underneath an intact film is through pathways developed during exposure, and that the pit formation occurs at the “hydrophilic” domains in the films.

The postulation that pitting occurs in the hydrophilic regions of a polymer film is verified by Figure 5, which shows AFM images and IR changes of a blend film of an inert PS and a hydrolysable polyethyl acrylate (PEA) after exposing to HCl vapor. The PEA matrix is hydrolyzed and removed, which is seen as pits in the film.

In Corrosion Environment; 120 μm Thick PU Coating on Steel, 30 d at 24 °C

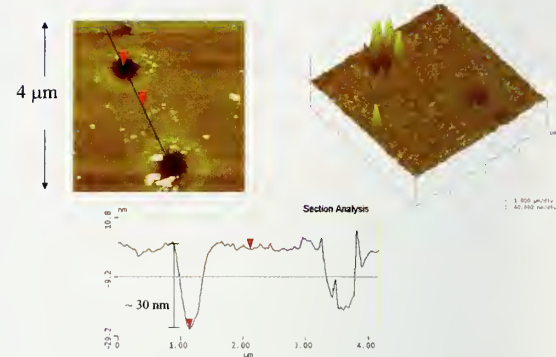


Figure 4. AFM height images of polymer-coated steel in NaCl , showing nanoscale pit formation.

Preferential Degradation of Hydrophilic Regions

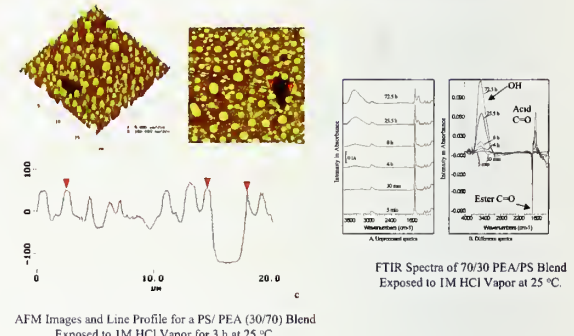


Figure 5. AFM image of a PS/PEA blend exposed to hydrolysis environment showing the removal of hydrolysable PEA matrix, which is seen as pits.

Although both photo and hydrolytic degradation is believed to occur in the degradation-susceptible regions in a film, information about the location and nature of these nanometer regions is unknown. Work is on-going to answer these questions.

Nanomechanical Characterization of Nanoparticle-filled Polymeric Coatings and Composites

The polymeric coatings industries seek experimental protocols to access the formulation, casting, resulting optical and nanomechanical properties, and measure the subsequent photodegradation effects of polymeric nanocomposites. Project objectives are to develop experimental protocols for measuring the nanomechanical properties of nanoparticle filled polymers through establishing relationships between the extent of dispersion, photodegradation effects, and changes in nanomechanical properties of polymeric materials.

Stephanie Scierka and Peter Votruba-Drzal,
BFRL (861)

Inorganic fillers, such as Titanium Dioxide (TiO_2) and Zinc Oxide (ZnO), have historically been added to polymeric building materials to enhance both the appearance properties and the mechanical durability. A common misconception is that these fillers are considered to be inert despite their semi-conductor electronic structure. Little regard has been given to understanding potentially important effects related to their quantum mechanical properties. For example, recent research has revealed TiO_2 films exhibit measurable photocatalytic activity when exposed to ultraviolet (UV) irradiation. This property may be used to engineer polymer nanocomposite coatings that self-sterilize by degrading chemical and bacterial contaminants by demineralization. The challenge of this project is to establish experimental protocols to access the formulation, casting, resulting optical and nanomechanical properties, and measure the subsequent photodegradation effects of polymeric nanocomposites. Successful development of experimental protocols may lead to the novel engineering of polymeric nanocomposite coatings such as those that maximize the beneficial photocatalytic activity for sterilization but minimize the negative effects of photodegradation, and enhance fire resistance, and mechanical strength.

Recent accomplishments include the presentation of our research results at the 2004 Fall Materials Research Society Meeting and the 2005 Adhesion Society Meeting. At those meetings we reported the results from model epoxy nanocomposite thin films containing one of three types of titanium dioxide (TiO_2) particles that were degraded using an integrating sphere-based ultraviolet weathering chamber. Instrumental Indentation Testing (IIT) was used to measure nanomechanical changes in the surface region (top 1000 nm) of thin films resulting from UV exposure. Attenuated Total Reflectance- Fourier Transform Infrared Spectroscopy (ATR-FTIR) and

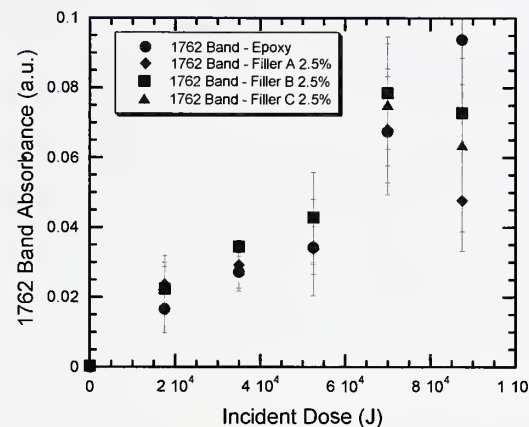


Figure 1. Extent of UV degradation in the epoxy system as monitored by ATR-FTIR. An increase in the oxidation products is shown by the $C=O$ stretch at 1762 cm^{-1} . Error bars represent the estimated uncertainty of 95 % confidence intervals.

Differential Scanning Calorimetry (DSC) were used to support the mechanical results with chemical and thermal data. The addition of nanoparticles increased the elastic modulus of the thin films. Exposure to UV radiation increased the elastic modulus of the nanocomposite thin films. The unfilled epoxy was the most photosensitive sample tested, exhibiting the highest rates of chemical oxidation (Figure 1), the largest decrease in the glass transition (T_g), and the greatest increase in elastic modulus with increased exposure (Figure 2).

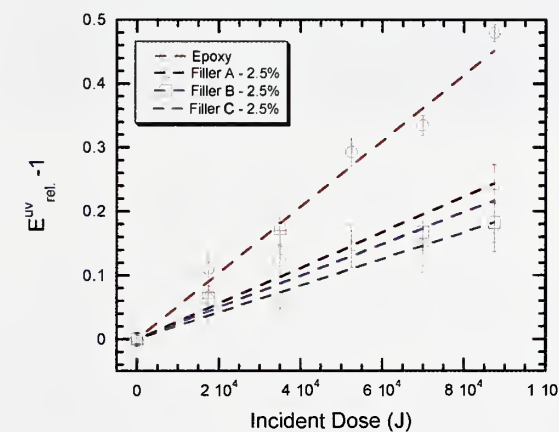


Figure 2. Relative increase in the elastic modulus of the first 1000 nm of the polymeric nanocomposites due to UV exposure. Error bars represent the estimated uncertainty of 95 % confidence intervals. Lines are added as a visual guide.

The rate of increase in the elastic modulus was reduced with increasing volume fraction of nanoparticles. Similar trends were observed in the nanocomposite films, but the rates of change were much lower than the unfilled epoxy and decreased with increasing volume

fraction of nanoparticles. The addition of particles resulted in an increase in surface roughness with additional exposure and increased the uncertainty in measurements for the filled samples, making it difficult to quantify differences in the rate of change due to photoreactivity.

These results were received with considerable interest from industrial representatives at the meetings. Future studies will use a more photostable matrix where accelerated rates of degradation can be linked to particle reactivity and will include characterization of particle dispersion. These methods of characterization may be included in Phase IV of the Service Life Prediction of Polymeric Coatings Industrial Consortium within the Building and Fire Research Laboratory.

Selected Publications

1. Scierka, S., Drzal, P.L., Forster, A.L., Svetlik, S., "Nanomechanical Properties of UV Degraded TiO₂/Epoxy Nanocomposites, Materials Research Society Proceedings Volume 841, 2004.
 2. Drzal, P.L., Scierka, S., Forster, A.L., Svetlik, S., "Instrumented Indentation of Model Photodegraded TiO₂/Epoxy Nanocomposites", Proceedings of the 28th Annual Adhesion Society Meeting, 2005.
-

Creating Visual Models of Nanoworlds

The place where quantum and macro effects meet, the nanoworld is full of the unexpected. In such an environment, visual models of laboratory and computational experiments can be critical to comprehension. We are developing an immersive visual modeling system that enables scientists to easily view and interact with their data in multiple ways in real time.

Judith Devaney, ITL (891)

Computational and laboratory experiments are generating increasing amounts of scientific data. Often, the complexity of the data makes it difficult to devise *a priori* methods for its analysis, or the data is from new landscapes, such as the nanoworld, where we have little experience. Moreover, there may be ancillary data, from databases for example, that would be helpful to have available. We are developing visual analysis capabilities in an immersive environment that allow scientists to interact with data objects in a three-dimensional landscape rather than simply viewing pictures of them. Fully immersive computer graphics include one or more large rear projection screens to encompass peripheral vision, stereoscopic display for increased depth perception, as well as head tracking for realistic perspective based on the direction the user is viewing. With visual exploration, scientists can easily perceive complex relationships in their data, quickly ascertaining whether the results match expectations. Real time interaction adds to the potential for speeding the process of insight.

In a fast moving field like nanotechnology, it is important to be able to create and interact with new visual models quickly. Our visual environment is built for generality, flexibility and speed. Rather than a single monolithic program, it is a collection of tools designed to work together to create, display, and interact with visual models. We have created three main categories of tools: infrastructure software, representation software, and scene interaction software. We join programs together using Unix pipes and filters for creation and transformation. We construct Dynamically Shared Objects (DSO's) for functionality, and scenegraph objects for ease of placement.

The Program DIVERSE

Our visual environment centers around a core infrastructure program called DIVERSE (Device Independent Visualization Environment-Reconfigurable, Scalable, Extensible). DIVERSE, which was developed by Virginia Tech with support and technical contributions by

NIST, is an interface that facilitates the development of immersive computer graphics programs for use on a wide variety of graphics displays. DIVERSE provides a toolkit to load in previously compiled objects, called DSOs. DSOs can be used to describe the graphics display, input devices, navigation techniques or interaction styles for a given visualization. Using collections of DSOs, applications can be reconfigured without recompiling. The same DSO that defines how a wand controls an object can be used both in an immersive environment and on a laptop computer. With the ability to import the output of conventional visualization programs, and access to the increasing capabilities of commodity graphics cards, we have a very rich environment in which to express and communicate visual models.

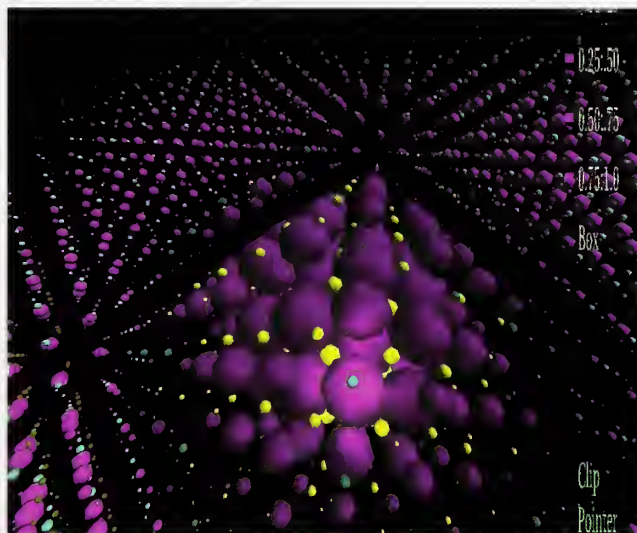


Figure 1. Image of a quantum dot created from the output of a computer simulation of the optical properties of nanostructures. The spheres represent s-orbitals.

Representation

Representation refers to the process of transforming raw data into a visual geometric format that can be viewed and manipulated. The key to quickly and easily visualizing scientific data in an immersive environment is the capability provided by the set of tools used to convert raw data to immersive data. We have created a variety of tools to make glyphs, color them, place them, and render them to a desired level of transparency and other properties. While our system is based on our own internal representation, we take advantage of representations computed by other packages by providing tools to take the output of common packages and convert them into the format that places them in our environment.

Interaction

For efficient scientific exploration, it is important to have user interaction that is both easy to set up and easy to adapt to differing needs. Individual DSOs that add new functionality to our visualization software system are loaded at run-time, and their behavior is cumulative. Together, a set allows for a huge range of combinations data visualization modes. We have developed a wide range of DSOs that allow a user to interact with the objects to be viewed. This includes functionality to move objects around, select individual objects or sets, assign functionality to the selections, interact with outside software, bring data into the system, send data out of the system, and load or unload objects during a visualization. They can also interactively select the level of detail in a scene. Individual DSOs can add simple capability to a scenegraph, such as adding a particular light source or an object to represent a pointer for the user to select objects. DSOs can also add tasks to the objects of a scenegraph. When selected, an object can be assigned the task of turning on or off another object or itself, or executing a command to dynamically interact with another DSO or an external program. Objects can change visibility, initiate new simulations, define clipping planes, and so on. DSOs provide a variety of ways to navigate through the environment, including changing the scale at will. They allow individual scenes as well as time sequences (i.e., movies) to be viewed.

The output of an interaction can be saved as a simple image, as a movie, or the interaction itself can be saved as an experience that can be replayed at a later time.

Applications to the Nanoworld

We have successfully applied our visual analysis techniques and tools to the study of a variety of nanoscale phenomena. Among these are visual analyses of

- s-orbitals for the simulation of electronic and optical properties of complex nanostructures such as semiconductor nanocrystals and quantum dots (see Figure 1),
- electric, magnetic, and energy field vectors from the simulation of optical scattering by metamagnetic materials (see Figure 2),
- intermediate voltage electron microscope measurement approaches to attain three-dimensional chemical images at nanoscale-resolution, and
- dynamics of molecular interactions leading to the formation of smart gels.



Figure 2. Image of the electric, magnetic, and energy field vectors in a single time step in the simulation of resonant optical scattering by metamagnetic materials.

Selected Publications

1. J. E. Devaney, S. G. Satterfield, J. G. Hagedorn, J. T. Kelso, A. P. Peskin, W. L. George, T. J. Griffin, H. K. Hung, R. D. Kriz, Science at the Speed of Thought, in *Ambient Intelligence for Scientific Discovery*, (Y. Cai, ed.), Lecture Notes in Artificial Intelligence 3345, February 2005.
2. J. Sims, G. Bryant, H. Hung, Intrinsic Surface States in Semiconductor Nanocrystals: HgS Quantum Dots, American Physical Society, Los Angeles, CA, March 21-25, 2005.
3. R. D. Kriz, J. Kelso and A. Ray, Visual Interpretation and Analysis of HPC Nanostructure Models using Shared Virtual Environments, *Modeling and Simulation* 1 (4), 2002, pp. 9-10.
4. J. Kelso, L. E. Arsenault, S. G. Satterfield and R. D. Kriz, DIVERSE: A Framework for Building Extensible and Reconfigurable Device Independent Virtual Environments, in *Proceedings of the Virtual Reality 2002 Conference*, Orlando, FL, March 24-27, 2002.

Brillouin Light Scattering

Brillouin light scattering is being developed as a tool for characterizing acoustic and magnetic waves at gigahertz frequencies in nanostructures and thin-film materials. Measurements and modeling in 2004 focused primarily on interactions of spin waves in ferromagnetic films and acoustic wave propagation in nanopatterned polymers.

Ward Johnson, Sudook Kim, Colm Flannery
MSEL (853); and Pavel Kabos, EEEL (818)

Brillouin light scattering (BLS) is an experimental technique that measures the intensity of spectral components of light that is inelastically scattered by vibrational waves (phonons) or spin waves (magnons) in a material. Fabry-Perot interferometric techniques are used to acquire accumulated spectra through repeated mechanical sweeping of the etalon spacing.

BLS is the only laboratory technique that is currently available for directly detecting magnons of finite wave number. Because of this capability and because of innovations in interferometric techniques, BLS has been increasing applied to problems in magnetics over the past couple of decades. It also has been extensively used for characterizing phonons and determining elastic constants of thin films. In recent years, BLS has begun to be employed on other systems with nanoscale dimensions, including patterned thin-film structures on substrates. The power of BLS for characterization of magnetic and elastic properties at the nanoscale arises from the gigahertz operating frequency range (which includes modes localized in nanostructures), noncontacting detection, selectivity with respect to wave vector and frequency, and ability to detect modes at the thermal level of excitation.

In this work, BLS measurements and modeling of magnetic and vibrational modes are being pursued on several material systems, including ferromagnetic films, nanopatterned polymeric films, nanoporous low-dielectric-constant (low- κ) dielectrics, spin-momentum-transfer devices, molecular rotors, and carbon nanotubes.

Over the past year, we developed and applied methods for measuring magnons that arise directly or indirectly from microwave pumping of metallic ferromagnetic films in a static magnetic field (Figure 1). BLS spectra were studied as a function of scattering angle, microwave power, and laser power to provide information on magnon-magnon interactions in Ni₈₁Fe₁₉

(Permalloy). The results demonstrate, for the first time, detection of nonzero-wave-number magnons arising from the decay of pumped uniform-precession magnons in metallic thin films. The metrology that we have developed will serve as a powerful new tool for characterizing interactions of magnons that limit the speed of magnetic-storage devices, spin-valve sensors, and other thin-film magnetic devices.

BLS measurements and modeling of vibrational modes in nanoimprinted polymeric lines were performed in collaboration with Colorado State University, University of Akron, and NIST Polymers Division. In addition to bulk and surface modes, the spectra revealed flexural and Sezawa modes that are localized in the imprinted lines. These results suggest the possibility of characterizing anisotropic elastic constants on a scale of tens of nanometers in these structures and other nanoscale lines on substrates. Especially since elastic constants in nanostructures are expected to deviate from bulk values, such information is important for modeling mechanical integrity and elastic interactions, which will play a critical role in the fabrication and performance of a variety of next-generation electronic devices.

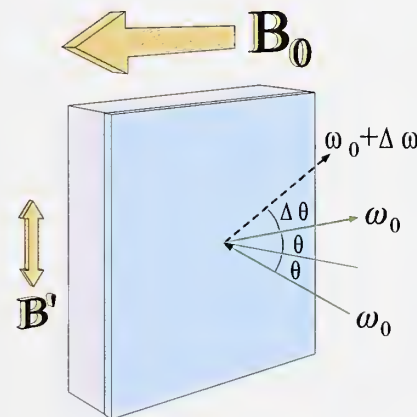


Figure 1. Scattering of light off spin waves in a ferromagnetic thin film with microwave excitation.

Nanolithography: Next-Generation Polymer Photoresists

Photolithography, the process used to fabricate integrated circuits, is the key enabler and driver for the microelectronics industry and the workhorse technology for nanoscale fabrication. Lithographic feature sizes have reached sub 100 nm length scales, but significant challenges have arisen for future size decreases because both the image resolution and the thickness of the imaging layer are approaching the macromolecular dimensions characteristic of the polymers used in the photoresist film. Unique high-spatial resolution measurements are developed to identify the limits on materials and processes that challenge the development of photoresists for next-generation lithography.

Vivek M. Prabhu, MSEL (854)

Photolithography is the driving technology used by the microelectronics industry to fabricate integrated circuits with ever decreasing sizes. In addition, this fabrication technology is rapidly being adopted in emerging areas in optoelectronics and biotechnology requiring the rapid creation of nanoscale structures. In photolithography, a designed pattern is transferred to the silicon substrate by altering the solubility of areas of a polymer-based photoresist thin film through an acid catalyzed deprotection reaction after exposure to radiation through a mask. To fabricate ever smaller features, next generation photolithography will be processed with shorter wavelengths of light requiring photoresist films less than 100 nm thick and dimensional control to within 2 nm.

To advance this key fabrication technology, we work closely with industrial collaborators to develop and apply high-spatial resolution and chemically specific measurements to identify the ultimate materials limits for advanced photoresists. We seek to also identify and to understand changes in material properties, interfacial behavior, and process kinetics at nanometer scales that can significantly affect the patterning process.

We apply and advance unique measurement methods to provide structural measurement of fabricated nanoscale structures and new insight and detail into the complex physico-chemical processes used in advanced chemically amplified photoresists. These methods include x-ray and neutron reflectivity (XR, NR), small angle x-ray and neutron scattering (SAXS, SANS), near-microscopy (AFM).

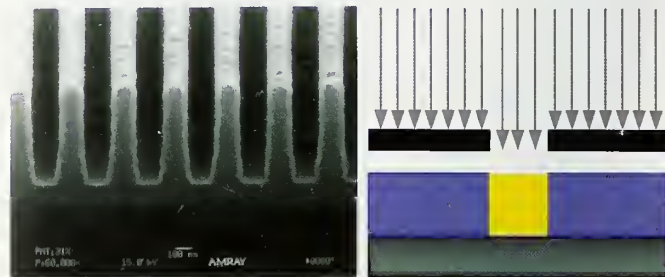


Figure 1. Left: Nanoscale structures fabricated with photolithography. The nominal line width is 180 nm. Right: Schematic of the photolithographic process to create nanoscale structures.

edge x-ray absorption fine structure spectroscopy (NEXAFS), solid state nuclear magnetic resonance (NMR), quartz crystal microbalance (QCM), fluorescence correlation spectroscopy (FCS), and atomic force

Recent accomplishments include: profiling the distribution of water at photoresist–liquid interfaces for immersion lithography and the developer counterion distribution in ultrathin films immersed in a developer solution; photoresist component segregation with NEXAFS spectroscopy; quantification of the post-exposure bake time on the reaction–diffusion of photoacid 3D deprotection volume; and quantified the effects of developer and additives on the final resolution of lithographic features using a model reaction–front bilayer geometry. Each of these factors greatly influences the resolution of the final nanoscale structure.

This past year, SEMATECH selected NIST to apply these fundamental measurements to identify materials sources of the fabrication limits of advanced 193 nm photoresists. This knowledge is needed for the evaluation of future nanofabrication technologies based on photolithography. In addition, Intel has assigned a scientific staff member to work with the Polymers Division/MSEL to identify materials issues in the resolution of EUV photoresist materials.

Modeling for Organic Conduction

Recently, there has been increased interest in molecular electronics due to the prospect of designing efficient electronic nano-scale components that could exhibit functionalities not achievable with silicon devices (e.g. optical emitters). Despite the significant progress made in the development of techniques to fabricate and characterize molecular conductors, the fact remains that molecular electronics is currently more of an art than a science characterized by a significant lack of reproducibility. The scientific and technological objective of this project is to evaluate/develop theoretical and computational tools that model the electrical activity and transport properties of organic molecules used in nanoelectronic devices.

Carlos A. Gonzalez, CSTL (838)

The decrease in the size of transistors by a factor of two every eighteen months, the trend known as Moore's law, has led to the fabrication of microelectronic devices that are increasingly faster, more powerful, and ubiquitous. However, it is projected that the physical limits of even the most advanced lithographic techniques under development will be reached in the foreseeable future. Beyond that time, continued increases in circuit density will require a paradigm shift in the design, make-up, fabrication, and operation of electronic components. Molecular electronic is seen by many as a viable alternate component technology. Molecules, either singly or in small ensembles, perform the function of the electronic components. Significant progress has taken place in the field. Molecular field-effect transistors (IBM, Lucent), reversible molecular switches (Hewlett-Packard), molecular negative-differential resistors (MEC, Inc), and molecular rectifying-diode have all been discovered and characterized, and Hewlett-Packard recently announced a prototype molecular-memory device with a density of ~ 10 GBits/cm². Despite this progress, it has become clear that there is a marked need for the development of robust theoretical and experimental tools that could be used on a routine basis in the design of novel materials leading to the development of reliable electronic devices based on molecular electronics. In this project, reliable and efficient theoretical methodologies leading to the understanding of the fundamental mechanisms governing electrical conductance in organic materials at the molecular level are developed and compared to experimental data. Theoretical studies of the electronic transport of molecular wire circuits are conducted using a time-independent Landauer scattering formalism based on a

first-order expansion of the system non-equilibrium Green's function (NEGF). In this model, the molecular bridge is bound to the metallic electrodes by means of thiolate groups at the head and tail of the bridge. Possible effects of the system's chemical stability, conformational changes of the organic conductor, and excited states on the transport properties of the device are also investigated. In addition, methods to predict the effects of electrostatic interactions at the molecule-electrode junction on the Current-Voltage curve are currently being examined. These effects could lead to technologically important phenomena such as molecular rectification and negative differential resistance. In this research, a simple methodology to study trends in conductance of molecule-metal junctions based on Density Functional Theory calculations (DFT) of modified quasi-molecular Green functions in a capacitor-like electric field was developed. This method, called the *Green Function Condensed-to-Fragments* model (GFCF), is based on a series of assumptions about the voltage spatial profile and the molecule-surface chemisorptive coupling in metal-molecule interfaces that seem to be validated for a number of junctions. The method assumes that the voltage drops entirely at the interfaces and that the junction conductance can be approximately factorized as a product of contact and molecular contributions. The main advantage of this approximate methodology rests on the fact that it is very simple to use, computationally efficient, and its results can be analyzed in terms of familiar chemical concepts such as molecular orbitals and dipole moments. The model has been used in the calculation of I-V curves of a series of the π -conjugated oligomers: 4-phenylethynyl-1-[4-thiol)-phenyl-ethynyl] benzene (OPE), 2-amino-5-nitro-4-phenylethynyl-1-[4-thiol)-phenylethynyl] benzene ($\text{NH}_2\text{-OPE-NO}_2$), and 2-fluoro-4-phenylethynyl-1-[4-thiol)phenylethynyl]benzene (F-OPE). The results of these calculations were compared to the corresponding experimental I-V curves. These three oligo(phenylene-ethynylene)s are highly conjugated systems with similar electronic structure, and possible differences in their conductance behavior should be only the result of substitution in the central ring. The results obtained in this work indicate that the I-V curves exhibited by substituted π -conjugated oligomers attached to gold electrodes can be interpreted qualitatively with the help of the quasi-Green function matrix projected onto fragments of the isolated molecule. This conclusion is supported by the reasonable qualitative agreement between the computed and experimental I-V curves in the case of OPE, F-OPE, and $\text{NO}_2\text{-OPE-NH}_2$, especially at voltages lower than 1.3 V (see Fig. 1).

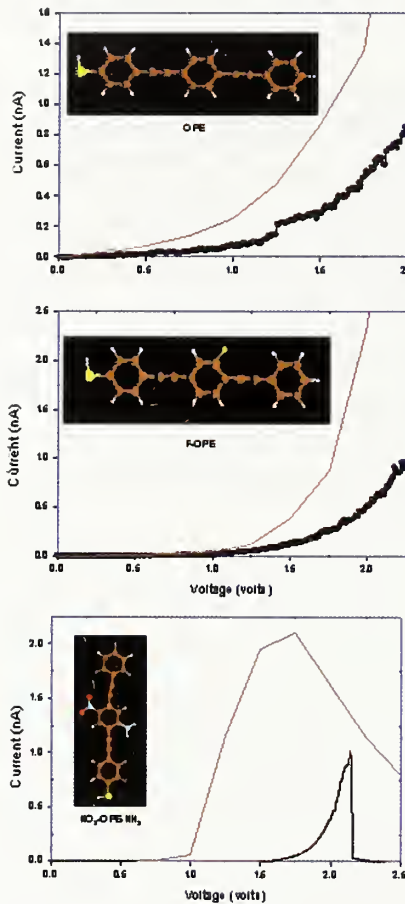


Figure 1. Comparison of theoretical (red line) and experimental (black dots) I-V curves for OPE's.

A similar qualitative agreement in the case of saturated hydrocarbons such as C₁₂H₂₅SH, oligo(phenylene vinylenes) as well as in a series of substituted platinum(II) acetylides indicates that the GFCF method is transferable to different molecular systems and that its reliability just depends on the voltage spatial profile of the system. The discrepancies between the theoretical and experimental I-V curves observed at larger voltages can be attributed to limitations of the method in this voltage regime. However, it is very encouraging to see that even at these voltages the simple theoretical scheme used here predicts the right trends for the three molecules studied. The results of our calculations lead to the conclusion that the I-V switching observed in NO₂-OPE-NH₂ correlates well with significant rearrangements in the electronic structure of the molecule (mainly through the p_z atomic orbitals) reflected in the behavior of the corresponding Green functions with the voltage. In the case of OPE and F-OPE these drastic changes are not observed and the systems behave as simple molecular tunneling wires. The results of this research pose the possibility of using standard quantum-chemical calculations as a “screening tool” to aid in the rational design of

other molecular systems that could exhibit novel and technologically important I-V behavior. We are currently testing the reliability and transferability of the model on a larger variety of molecular systems for which reliable experimental data is available.

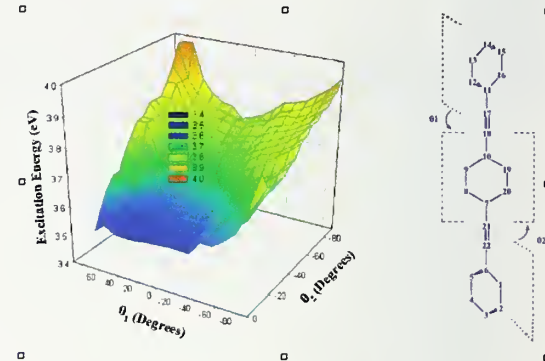


Figure 2. Changes in the excitation energy of OPE as a function of the ring torsion angles.

We are also investigating the nature of the interaction between the molecule and the metal at the interface. In particular, we are applying highly correlated *ab initio* molecular orbital theory in order to determine possible changes in the electronic structure of the molecule due to chemisorption to the metallic surface. Properties such as geometrical parameters, chemical stability, binding energies and UV-vis spectra (see Figure 2) have been computed and the results compared to available experimental data.

This research is conducted within the recently established NIST Center for Theoretical and Computational Nanosciences. Within the context of this center it is envisioned that the theoretical models developed and validated in this work will provide a set of important tools that will complement the experimental studies conducted by researchers in the nascent molecular electronics industry as well as in research centers at NIST, National Labs and Universities.

Spin Electronics

The Spin Electronics program is creating the foundations for the development of new magnetoelectronic technologies that utilize the electron spin instead of its charge. It investigates the transfer of spin angular momentum from electrons to magnetic thin films to induce magnetization dynamics for applications as microwave oscillators in high-speed signal processing and switching of discrete memory elements.

William H. Rippard and Matthew R. Pufall,
EEEL (818)

Wireless communications devices are ubiquitous, ranging from simple radios to complex structures such as cell phones and wireless Internet systems. All these devices are based upon the transmission and reception of electromagnetic signals, with higher frequencies being required for high data-transmission rates. Common oscillators for wireless applications operate in the gigahertz regime but are large (several millimeters on a side) and must be added onto semiconductor chips after their manufacture, increasing component cost. Further, magnetic data storage technologies require novel methods of high-speed operation of nanoscale memory elements. Traditional magnetic recording and magnetic random access memory (MRAM) technologies are encountering problems as they seek to push dimensions below 50 nanometers and speeds above 1 gigahertz.

This project concentrates on spin-momentum transfer (SMT) from electron currents to multilayer, ferromagnetic films. SMT is a newly discovered phenomenon that appears in nanometer-scale magnetic devices. We are studying devices that use SMT to induce coherent magnetic precession. The precession frequency can be tuned from 1 gigahertz to more than 40 gigahertz by changing the current amplitude or magnetic field angle applied to the structures. Spin-polarized currents can also be used to switch small magnetic elements used in nanoscale magnetic recording and MRAM technologies. These new techniques may enable more efficient switching of sub-50-nanometer structures at speeds above 5 gigahertz with considerably less power and better selectivity.

We are using electron-beam-lithographed point contacts and nanopillar structures to achieve the high current densities needed to induce magnetic excitations in multilayer films. For sufficiently high current densities and applied magnetic fields, there is an abrupt increase in the resistance of a point-contact junction. The resistance step is attributed to precessional dynamics induced by the

SMT effect. We have found that SMT is a generic effect occurring for a wide range of experimental conditions: for in-plane fields, out-of-plane fields, and intermediate angles as well as for a number of different device structures. We have also discovered that SMT occurs in a number of different and previously unexplored alloys of Co, Fe and Ni.

The origin of the SMT effect is conservation of angular momentum. When a dc current flows perpendicular to the plane (CPP) of a GMR “spin-valve” device, electrons are spin-polarized by the “reference” magnetic layer. Inelastic electron scattering then leads to the transfer of spin angular momentum to the “sense” magnetic layer. This transfer of angular momentum can result in coherent oscillations in the sense layer ranging from a few gigahertz to more than 40 gigahertz, the same range used for wireless applications. These new devices are only 40 nanometers in diameter and compatible with standard semiconductor processing, making the new technology attractive for applications.

Work is now focusing on developing tunable oscillators and on investigating the fundamental mechanisms that govern the interaction between magnetization and spin current.

Tunable Coherent Spin Waves Generated by Direct Current

We have successfully excited high-frequency magnetic oscillations in a magnetic multilayer structure with a direct current. The oscillations are caused by the torque exerted on the magnetization by the electron spins in the current. The current is injected at high density through a 40 nanometer contact into the magnetic multilayer. At a certain critical value, the current induces precessional oscillations in one of the two magnetic film layers. These oscillations, detected as a voltage change due to the GMR effect, range in frequency from 1 to 40 gigahertz, with spectral widths as small as 2 megahertz. The small widths imply that the oscillations have lower damping and greater coherence than most known magnetic excitations. The frequency of the oscillations increases with an externally applied magnetic field. For in-plane fields, frequencies as high as 40 gigahertz were obtained. An increase in current causes the oscillation frequency to decrease, with a tunable range of 1 to 5 gigahertz.

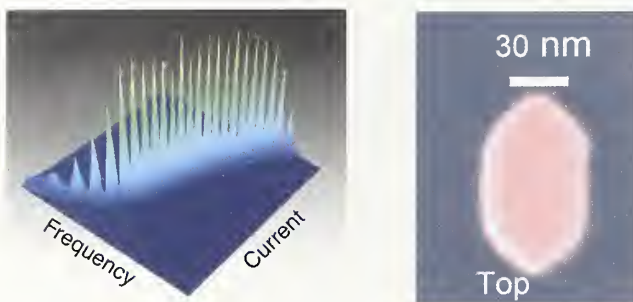


Figure 1. Current controlled high frequency excitations and scanning-electron-microscope image of a nanopillar device.

Spin-Transfer Switching of Magnetic Devices Using Pulsed Currents

We have demonstrated magnetization reversal in 100-nanometer-sized magnetic thin-film devices with ultrashort spin pulses. The devices have two magnetic layers separated by a nonmagnetic spacer layer. The devices have two stable states: parallel and antiparallel alignment of the magnetizations of the free and fixed layers. The state can be read by using the GMR effect. A current pulse is applied to the device, causing reversal of the free-layer magnetization. We studied rapid reversal due to current pulses whose durations ranged between 100 picoseconds and 100 nanoseconds. The pulse duration required for reversal decreases with increasing current amplitude; for the highest currents applied, reversal occurred in less than 300 picoseconds. This is the shortest reversal time reported yet for SMT-based switching. Such a result is promising for applying SMT as a method of writing magnetic data in MRAM and magnetic hard disk drives, which will be required to operate at gigahertz rates in the near future.

Telegraph Switching Induced by Spin-Momentum Transfer

We have also demonstrated that a high density spin-polarized direct current passing through a small patterned magnetic element induces two-state random telegraph switching of the magnetization via the SMT effect. The magnetization undergoes large, 40 to 90 degree angular rotations between two states at rates up to 2 gigahertz for a wide range of currents and applied magnetic fields. The switching involves the collective motion of a large number of spins. Such a collective, dynamic source for random telegraph noise is substantially different from that those found in superconducting devices and semiconductor circuitry, where isolated atomic-level defects are usually responsible for two-state fluctuations.

Frequency Modulation and Phase Locking in Spin-Transfer Microwave Oscillators

Initial work on SMT focused only on the continuous wave output of the new devices. However, such pure tones transmit no information. Instead, the outputs must be modulated, for instance in amplitude (AM) or frequency (FM), in order to transmit data. We are now able to modulate the current passed through the device. As the current is modulated at frequencies much less than the natural oscillation frequency set by the device, sideband lobes appear on both sides of the original carrier frequency. The details of the outputs can be understood in terms of standard communications theory. The devices can also be “injection-locked” to an external drive signal close to their natural oscillation frequencies. In this scenario, the devices are forced to oscillate at the same frequency as the injected signal. Over this locking region the relative phases of the two signals can be controlled by the dc current passed through the device. We are investigating locking and phase-shifting architectures for possible directional micro-wireless communications.

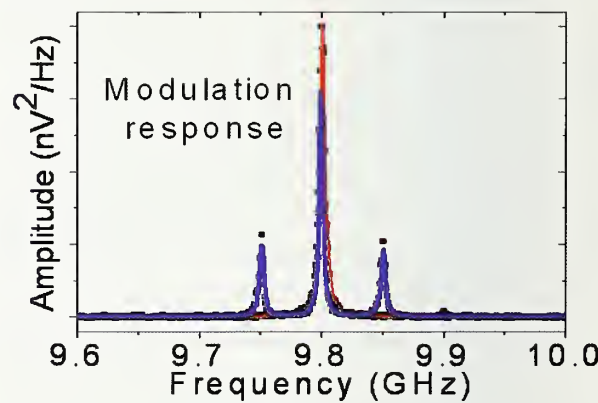


Figure 2. Output of the device with DC current injection only (single peak at 9.8 GHz); device output with additional modulation included at 50 megahertz and amplitude of 400 microamperes (peak at 9.8 GHz with satellites at 9.75 and 9.85 GHz).

Nanomagnetodynamics

In order to pursue the rapid development path set out for hard drives and magnetic memory, industry needs the ability to measure and control magnetization on nanometer length scales and nanosecond time scales. This project focuses on the metrology of dynamics and damping in magnetic thin films, especially on the effects of nano-scale dimensions and defects in ferromagnetic resonance measurements.

Robert D. McMichael, MSEL (855)

We develop ferromagnetic resonance (FMR) techniques to measure the static and dynamic properties of thin films and patterned arrays of technologically important ferromagnetic metals and their interfaces with normal metals. The primary results include measurements of interfacial effects in magnetic damping, which governs behavior on the sub-nanosecond time scale, and assessment of the magnetic homogeneity of thin films or patterned arrays of magnetic bits. These results are communicated to the magnetic data storage industry through conference presentations, journal articles and site visits.

We have initiated a new investigation into the properties of patterned magnetic film edges. The importance of edges in the switching of magnetic thin film devices has been recognized, but no techniques for characterizing magnetic edge properties have yet been developed. Our initial models show that microwave frequency ferromagnetic resonance measurements will be sensitive to the edge properties. These edge properties will be useful in the micromagnetic design of non-volatile magnetic RAM memory.

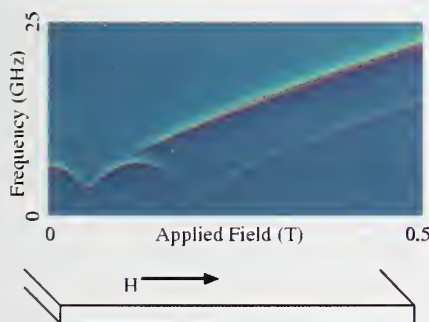


Figure 1. Evolution of the ferromagnetic resonance spectrum as a function of applied field in a 16 nm thick strip of Permalloy. The low frequency trace is due to the edge mode. Other modeling has shown the edge mode to be sensitive to edge conditions.

A continuing thrust of this project has been the development of models that describe broadening of the

FMR linewidth by defects. These models, which are specifically designed for thin films, account for both inhomogeneity and magnetic interactions. Our earlier models were restricted to “local” defects such as anisotropy. One important application of these models provides a method for measurement of anisotropy variations and axis alignment in perpendicular recording media. This year, we have capped off the model development with a model for the nonlocal effects of film roughness.

Testing of the roughness-linewidth model involved making variable roughness substrates, characterizing the roughness by atomic force microscopy (AFM) and measuring nearly conformal Permalloy overlayers in FMR. Using only the AFM microstructural data and the known properties of Permalloy, and assuming conformal roughness, our model predictions agreed extremely well with the measurements. Allowing one free parameter describing thickness variations, the agreement with the experiment is nearly perfect. Validation of this model is the first example of linewidth modeling based entirely on measured microstructure.

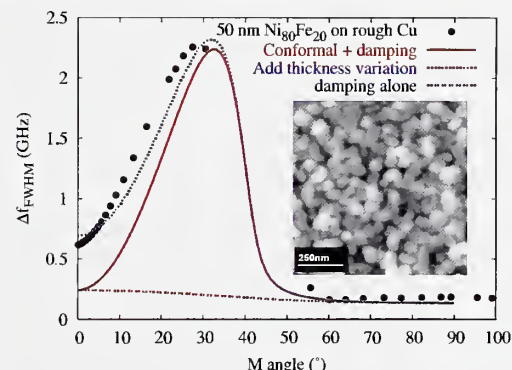


Figure 2. FMR line broadening measured in a Permalloy film and calculated almost entirely from the microstructure of the underlayer shown in the inset.

Nanomagnetism

To make magnetic devices in the nanometer regime, manufacturers need to be able to characterize the structures they build and to accurately model their behavior. We are developing the capability of measuring the magnetic properties of nanostructures in the presence of applied fields and with applied currents. With these capabilities, we are measuring the changing properties of devices as their size is reduced. In parallel, we are developing models that quantitatively describe the physics captured by these devices.

John Unguris and Mark Stiles, PL (841)

Magnetic Nanoconstrictions

Small, patterned magnetic thin film structures play a critical role in emerging magneto-electronic technologies, which range from non-volatile random access memories to magnetic field sensors. One potential advantage of miniaturizing these devices is that the size and geometry of the patterned structure may be used to shape the internal magnetic nanostructure and control the device operation. Imaging this internal nanostructure is a measurement challenge, since the structures consist of only a small amount of magnetic material and can easily be perturbed by conventional magnetic imaging methods such as Magnetic force Microscopy (MFM).

One such structure is the magnetic nanoconstriction. Nanoconstrictions make ideal structures for reproducibly trapping magnetic domain walls, and furthermore, since the local current density in the constriction can be large, the domain walls can be manipulated using current induced spin torques. Magnetic nanoconstrictions therefore provide a means of building magnetic devices that can be switched using current pulses, without applying external magnetic fields.

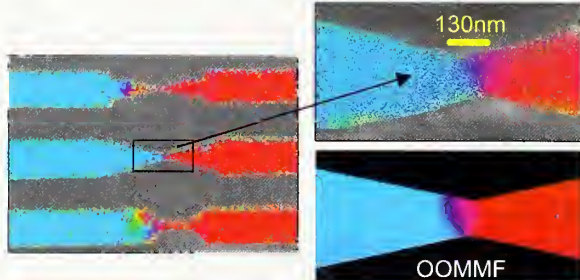


Figure 1. SEMPA images of various magnetic nanoconstrictions. A magnified image of one of the constrictions is shown along with a corresponding OOMMF micromagnetics calculation.

To image the structure of domain walls trapped and manipulated in nanoconstrictions, we have used the NIST Scanning Electron Microscopy with Polarization Analysis (SEMPA) facility. Samples with various geometries and sizes were prepared using electron beam lithography. We have been completely successful non-invasively imaging static domain walls and domain structures after applying current pulses. We have found that the domain wall's shape depends sensitively upon the constriction geometry.

Imaging Magnetic Sensors

Recent advances in thin film and multilayer magnetism offer the exciting possibility of creating a new generation of magnetic sensors that are small, inexpensive and as sensitive as currently used, more cumbersome sensors, such as SQUIDs. Development of this new generation of sensors requires understanding and controlling the magnetic nanostructure in order to enhance sensitivity and eliminate potential sources of magnetic noise.

We are working with other groups at NIST to test and measure possible new materials and devices for use as sensors. One potentially useful device is a zigzag shaped magnetic sensor. The device's magnetic sensitivity is based on anisotropic magnetoresistance (AMR) and therefore requires the magnetization to be tilted with respect to the current passing through the device. In the zigzag sensor the shape anisotropy forces the magnetization to tilt relative to the current. We have used SEMPA to measure how well various zigzag geometries accomplish this angular biasing and to look for potential sources of magnetic noise.

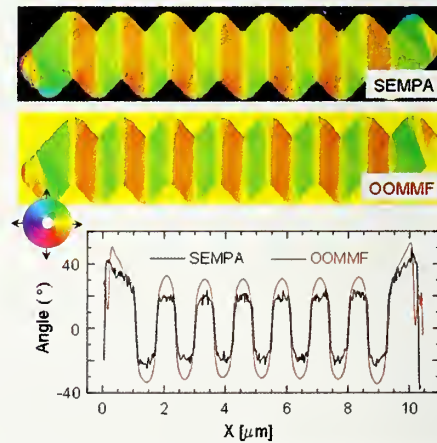


Figure 2. SEMPA image of a zigzag magnetic sensor element compared with the OOMMF micromagnetics simulation. Line scans through the center of the elements show the magnitude of

the magnetic oscillations.

SEMPA imaging is especially useful since it not only images the magnetization directly, but also provides a quantitative measurement of magnetization directions that can be compared directly with the results of micromagnetic calculations. The SEMPAs images also reveal potential magnetic trouble spots such as trapped magnetic singularities which can interfere with reproducible magnetic response, as well as defects that can produce magnetization-related noise. Work is currently underway to allow imaging electrically active magnetic sensors which will allow a better understanding of noise sources and failure modes in real devices.

Current Induced Magnetic Switching

In a magnetic multilayer, changing in the relative orientation of the magnetizations of two layers changes the current flowing through the multilayer. This effect, called giant magnetoresistance, is used in magnetic sensors, magnetic random access memory (MRAM), and read heads in magnetic disk drives. Currently, an inverse effect, where the current changes the magnetic configuration, is being studied for possible applications. In this case, a current passing through a multilayer exerts a torque on the magnetizations of different layers causing the magnetizations to rotate.

Large enough currents passing through such multilayers can switch the magnetizations of the layers between parallel and antiparallel or cause one to rapidly precess around the other layer. If the size of the current necessary to reverse magnetizations can be reduced sufficiently, spin-transfer torques could provide a way to switch bits in magnetic random access memory (MRAM). In other devices, it should be possible to make current-controlled oscillators.

We have developed quantitative models for these spin-transfer torques to help the development of devices based on this effect. In particular, we recently developed an analytic formula for the torque as a function of the device geometry and the magnetic configuration. Such a formula will allow rapid simulation of prototypes for device optimization. To test these results, we have carried out extensive micromagnetic simulations as a function of current and applied magnetic field to compare with existing experimental results. We find that these simulations explain most, but not all of the experimental results quantitatively. The differences between the simulations and the experiments suggest both new measurements and necessary extensions of the model.

This work has been described in four papers over the last year, building on three prior publications. It has

been reported in five invited talks in academia, conferences, and industry, with four more invited talks scheduled in the near future. Presently, we are extending the modeling to describe structures with non-uniform magnetization.

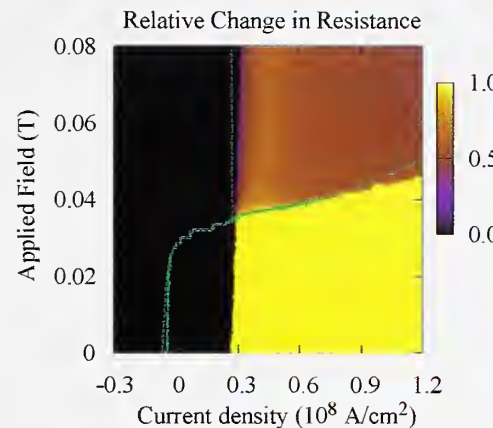


Figure 3. Resistance of a magnetic nanopillar at 300 K as a function of current and applied field. The current is swept from negative to positive values. Green lines indicate configuration changes when the field is swept in the opposite direction.

Selected Publications

1. Zigzag Shaped Magnetic Sensors, F. C. S. da Silva, W. C. Uhlig, A. B. Kos, J. Aumentado, M. J. Donahue, J. Unguris, D. P. Pappas, *J. Appl. Phys.* **85**, 6022 (2004).
2. Current-Driven Switching in a Single Exchange-Biased Ferromagnetic Layer, T. Y. Chen, Y. Ji, C. L. Chien, and M. D. Stiles, *Phys. Rev. Lett.* **93**, 026601 (2004).
3. Boltzmann Test of Slonczewski's Theory of Spin Transfer Torque, J. Xiao, A. Zangwill, and M. D. Stiles, *Phys. Rev. B* **70**, 172405 (2004).
4. Spin Configurations and Classification of Switching Processes in Ferromagnetic rings down to sub-100 nm dimensions, M. Kläui, C.A.F. Vaz, T.L. Monchesky, J. Unguris, E. Bauer, S. Cherifi, S. Heun, A. Locatelli, L.J. Heyderman, Z. Cui and J.A.C. Bland, *J. Magn. Magn. Mater.* **272-276**, 1631 (2004).

Synthesis, Characterization, and Manipulation of Magnetic Nanoparticles

Magnetic nanoparticles have potential applications in catalysis and magnetic recording, as well as in medical sensors and biomedicine. The ability to reproducibly synthesize, characterize, and manipulate these nanoparticles is critical for successfully realizing these applications.

Guangjun Cheng and Angela R. Hight Walker,
PL (844)

The nanoscale synthesis of inorganic materials has advanced significantly in the last few years. Our group uses a refined thermo-decomposition method to synthesize magnetic cobalt nanoparticles with controllable sizes and shapes. We have, for instance, synthesized monodispersed colloidal mixtures of cobalt nanoparticles in the epsilon (hcp) crystalline form, the bulk, room-temperature ferromagnetic phase of Co. X-ray powder diffraction (XRD) and transmission electron microscopy (TEM) have been used to characterize the magnetic nanoparticles.

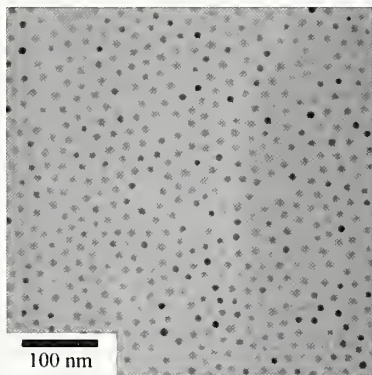


Figure 1. TEM image of monodispersed 15 nm cobalt nanoparticles

We have also produced magnetic-field-induced (MFI) assemblies of Co nanoparticles. Under the influence of a magnetic field, Co nanoparticles dispersed in a colloidal solution assemble into linear chains along the direction of the applied field. After the removal of the magnetic field, the MFI chains fold into a three-dimensional (3D) super-coiled structure. Optical Microscope and TEM have been used to characterize these morphologies. A superconducting quantum interference device (SQUID) magnetometer is used to measure the magnetic properties of MFI assemblies.

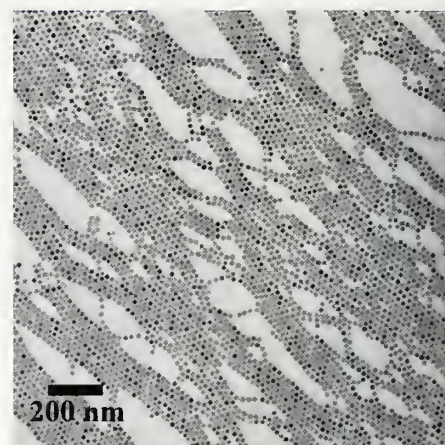


Figure 2. TEM image of MFI chains of cobalt nanoparticles.

We have been able to create MFI chains as long as 1 cm in length, corresponding to approximately one million magnetic dipole nanocrystals stacked head to toe along the magnetic field lines. Moreover, we found that reversal of the direction of the magnetic field leads to a propeller-like rotation of the chains by 180 degrees around their two-fold axis to again align the supra dipole along the magnetic field direction. Surprisingly, the other possibility in which each of the individual magnetic dipoles reorient does not occur, demonstrating that the individual magnetic dipoles are strongly coupled to each other, even more than they are to the external magnetic field. Removal of the magnetic field causes rapid collapse of the linear structures and these floppy chains fold into a three-dimensional, globular, coiled structure. Light agitation leads to fragmentation, yielding predominantly small ring structures.

To fully realize the biological potential of these magnetic nanoparticles, methods are being developed to improve their bio-compatibility by coating them with gold or silver. These bimetallic nanoparticles are expected to maintain the magnetic properties of Co, while the Au or Ag coatings improve their biocompatibility. Co/Au and Co/Ag nanoparticles are prepared by growing Au or Ag on the pre-synthesized Co nanoparticles. Magneto-Raman spectroscopy developed in our laboratory and SQUID magnetometry are used to characterize these bio-inert particles.

Nanomagnetodynamics: Fundamental Properties

This project is developing instruments, techniques, and theory for the understanding of the high-speed response of commercially important magnetic materials. Techniques used include linear and nonlinear magneto-optics and pulsed inductive microwave magnetometry. Emphasis is on high-frequency (above 1 gigahertz), time-resolved measurements for the study of magnetization dynamics under large-field excitation. Research addresses the nature of coherence and damping in ferromagnetic systems and their effects on the fundamental limits of magnetic data storage. The project provides results of interest to the magnetic disk drive industry, developers of magnetic random-access memory, and the growing spin-electronics community.

Thomas J. Silva, EEEL (818)

Advances in magnetic information storage are vital to economic growth and U.S. competitiveness in the world market for computer products and electronic devices. Our primary customers are the magnetoelectronics industries involved in the fabrication of magnetic disk drives, magnetic sensors, and magnetic random-access memory (MRAM).

Data-transfer rates are increasing at 40 percent per year (30 percent from improved linear bit density, and 10 percent from greater disk rotational speed). The maximum data-transfer rate in nanometric devices is currently 200 megabytes per second, with data-channel performance of over 1 gigahertz (in the microwave region), with corresponding magnetic switching times of less than 1 nanosecond. At these rates, a pressing need exists for an understanding of magnetization dynamics, and measurement techniques are needed to quantify the switching speeds of commercial materials.

The current laboratory demonstration record for storage density is over 30 gigabits per square centimeter (200 gigabits per square inch). How much further can longitudinal media (with in-plane magnetization) be pushed? Can perpendicular recording, patterned media with discrete data bits, or heat-assisted magnetic recording extend magnetic recording beyond the superparamagnetic limit at which magnetization becomes thermally unstable? We are developing the necessary metrology to benchmark the temporal performance of new methods of magnetic data storage.

Our technical strategy is to identify future needs in

the data-storage and other magnetoelectronic industries, develop new metrology tools, and do the experiments and modeling to provide data and theoretical underpinnings. We concentrate on two major problems in the magnetic-data-storage industry: (1) data-transfer rate, the problem of gyromagnetic effects, and the need for large damping without resorting to high fields, and (2) storage density and the problem of thermally activated reversal of magnetization. This has led to the development of instrumentation and experiments using magneto-optics and microwave circuits. Microwave coplanar waveguides are used to deliver magnetic-field pulses to materials under test. In response, a specimen's magnetization switches, but not smoothly. Rather, the magnetization vector undergoes precession. Sometimes, the magnetization can precess nonuniformly, resulting in the generation of spin waves or, in the case of small devices, incoherent rotation.



Figure 1. Mike Schneider next to cryogenic and room-temperature pulsed inductive microwave magnetometers.

Metrology

We use several methods to detect the state of magnetization as a function of time.

- ◆ The magneto-optic Kerr effect (MOKE) makes use of the rotation of polarization of light upon reflection from a magnetized film. We have used MOKE with an optical microscope to measure equilibrium and nonequilibrium decay of magnetization in recording media.
- ◆ The second-harmonic magneto-optic Kerr effect (SH-MOKE) is especially sensitive to surface and interface magnetization. We have used SHMOKE for time-resolved vectorial measurements of magnetization dynamics and to demonstrate the coherent control of magnetization precession.
- ◆ In our pulsed inductive microwave magnetometer

(PIMM), the changing magnetic state of a specimen is deduced from the change in inductance of a waveguide. This technique is fast, inexpensive, and easily transferable to industry. It may also be used as a time-domain permeameter to characterize magnetic materials. Since the development of the PIMM at NIST, similar systems have been built at several industrial research laboratories and universities.

While these instruments have immediate use for the characterization of magnetic data-storage materials, they are also powerful tools for the elucidation of magnetodynamic theory. The primary mathematical tools for the analysis of magnetic switching data are essentially phenomenological. As such, they have limited utility in aiding industry in its goal to control the high-speed switching properties of heads and media. We seek to provide firm theoretical foundations for the analysis of time-resolved data, with special emphasis on those theories that provide clear and unambiguous predictions that can be tested with our instruments.

Surface Dependence for Rotatable Anisotropy

We found that there is a surface contribution to the rotatable anisotropy in Permalloy. Contributions to the magnetic anisotropy for which the magnetization direction itself is the source of symmetry breaking are generally categorized as “rotatable anisotropy,” and act to enhance the gyromagnetic frequency. In a comprehensive study intended to determine the physical origins of rotatable anisotropy in single-layer Permalloy films, the pulsed inductive microwave magnetometer was successfully used to measure the anisotropy energy density as a function of magnetization angle. We found that the component of the energy density that is independent of magnetization angle, and therefore results in a rotatable anisotropy, is inversely proportional to film thickness. These results have significant implications for data storage applications, where the thickness of the magnetic sensor layer in a disk drive must be substantially reduced to accommodate higher areal densities of data.

Large-Angle Magnetization Dynamics

We examined the relationship between nonlinear magnetic response and the change in the Gilbert damping parameter α for patterned and unpatterned thin Permalloy ($Ni_{80}Fe_{20}$) films subjected to pulsed magnetic fields. An improved magnetization-vector-resolved technique based on the second-harmonic magneto-optic Kerr effect (SH-MOKE) was used to measure magnetization dynamics after pulse field excitation. The magnetization excitations were achieved with pulsed fields that were aligned parallel to the hard axis of thin Permalloy films while a DC bias field was applied along the easy axis. At low-bias fields, α is inversely related to the bias field, but

there was no significant reduction in the absolute value of the magnetization, as might be expected if there were significant spin-wave generation during the damping process. We discuss the discrepancies between data obtained by ferromagnetic resonance, where spin-wave generation is prevalent, and pulsed field studies, and conclude that fundamental differences between the two techniques for the excitation of the ferromagnetic spin system might explain the different proclivity toward spin-wave generation manifest by these two experimental methods.

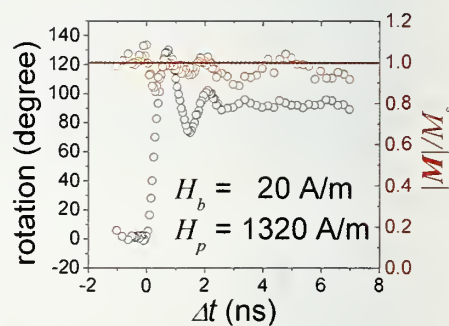


Figure 2. Vector-resolved, time-domain SH-MOKE signal for magnetization dynamics in Permalloy measured at low applied bias field H_b at which the damping is significantly enhanced. The data show no substantial evidence of inhomogeneities during the magnetization switching process, demonstrating that spin-wave generation does not explain the enhancement of damping for this particular experimental geometry.

Selected Publications

1. J. P. Nibarger, R. Ewasko, M. Schneider, and T.J. Silva, “Dynamic and Static Magnetic Anisotropy in Thin-Film Cobalt Zirconium Tantalum,” *J. Magn. Magn. Mater.* **286**, 356-361 (February 2005).
2. M. L. Schneider, A. B. Kos, and T. J. Silva, “Finite Co-planar Waveguide Width Effects in Pulsed Inductive Microwave Magnetometry,” *Appl. Phys. Lett.* **85**, 254-256 (July 2004).
3. M. L. Schneider, A. B. Kos, and T. J. Silva, “Dynamic Anisotropy of Thin Permalloy Films Measured by Use of Angle-Resolved, Pulsed Inductive Microwave Magnetometry,” *Appl. Phys. Lett.*, in press.
4. M.L. Schneider, T. Gerrits, A.B. Kos, and T.J. Silva, “Contributions to the Gyromagnetic Damping in Pulsed Inductive Microwave Magnetometry,” submitted.
5. R. Bonin, M.L. Schneider, and J.P. Nibarger, T.J. Silva, “Dependence of Magnetization Dynamics on Magnetostriiction in NiFe Alloys,” submitted.
6. T. Gerrits, M.L. Schneider, and T.J. Silva, “Observation of Enhanced Damping in $Ni_{80}Fe_{20}/Cu$ Bilayers,” submitted.

Bioelectronics

Experiments in cell biology have been virtually unchanged for many decades, involving manual handling of cell culture flasks, changing the cell media (feeding the cells), exposing the cell culture to a compound of interest, and observing cell response and viability using a microscope. For this reason, cell biology experiments are typically very time consuming and labor intensive. Recently, the trend has been to conduct studies that involve large arrays of small cell cultures by automating these steps as much as possible using robotic instrumentation, but the experiments are still essentially the same. A true paradigm shift is to pattern or isolate single cells, or small cell populations, and to probe their individual response using optical, electronic, and mechanical methods. The technical approach of this research effort is use thin film electrodes to capture single cells from solution by dielectrophoresis, to anchor them patterned self assembled monolayers, and to interface sensitive single molecule optical measurement methods to probe single cell response.

Michael Gaitan, Darwin Reyes-Hernandez, and Brian Polk, EEEL (812), Laurie Locascio, and Sam Forry CSTL (839)

Recent scientific reports describe the ability to stimulate electronically and probe single cell activity and to transport, sort, and position single cells. These capabilities have resulted in significant advances in biological sciences and medicine. An excellent example is patch clamp technology that has revolutionized the field of electrophysiology. Advances in microfabrication methods have recently led to the development of patch clamp arrays and other automated on-chip techniques; however, the widespread adoption of more complex integrated systems for biologically relevant measurements continues to face technological hurdles. These include complicated materials integration issues (maintaining a bio-compatible environment for cells within the *in vitro* measurement systems, developing stable and drift-free electrodes for accurate measurements in varied buffer solutions, etc.), the difficulty of accurately determining the electrical/electromagnetic response of integrated electronic/MEMS/fluidic systems, and issues related to reproducible fabrication of integrated devices. By addressing these critical measurement infrastructure needs, NIST will accelerate the development of powerful new bioelectronic platforms and techniques.

Our technical approach is to integrate microelectronic, MEMS, and microfluidic systems with cells in order to achieve a new level of control over the electronic/biological interfaces under study. We will develop methods to adhere and grow cells in defined patterns in a biological hybrid *in vitro* environment that incorporates microelectronic circuits, both electrochemical and rf, to stimulate and sense cell activity. Microchannel networks will be used to transport the biological specimens to exact locations and to deliver precise amounts of chemicals or drugs to the local cellular environment. These techniques will allow us to apply precise electrical, electromagnetic, and chemical stimulation to the cells and to measure their metabolic, electrical, and physiological responses. We will focus our initial research efforts on the study of retinal (neuronal) cells and will later progress to other cell systems.

Two weeks growth of retinal cells on poly(ethyleneimine). Cells are covering all the polycation area.

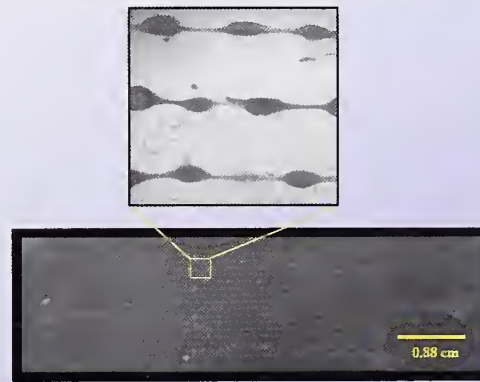


Figure 1. Two weeks growth of retinal cells on poly(ethyleneimine). Cells are covering all the polycation area.

Accomplishments

A method was developed to adhere retinal cells on micropatterned polyelectrolyte multilayer (PEM) lines adsorbed on poly(dimethylsiloxane) (PDMS) surfaces using microfluidic networks. PEMs were patterned on flat, oxidized PDMS surfaces by sequentially flowing polyions through a microchannel network that was placed in contact with the PDMS surface. Polyethyleneimine (PEI) and poly(allylamine hydrochloride) (PAH) were the polyions used as the top layer cellular adhesion material. The microfluidic network was lifted off after the patterning was completed, and retinal cells were seeded on the PEM/PDMS surfaces. The traditional practice of using blocking agents to prevent the adhesion of cells on unpatterned areas was avoided by allowing the PDMS surface to return to its uncharged state after the patterning was completed.

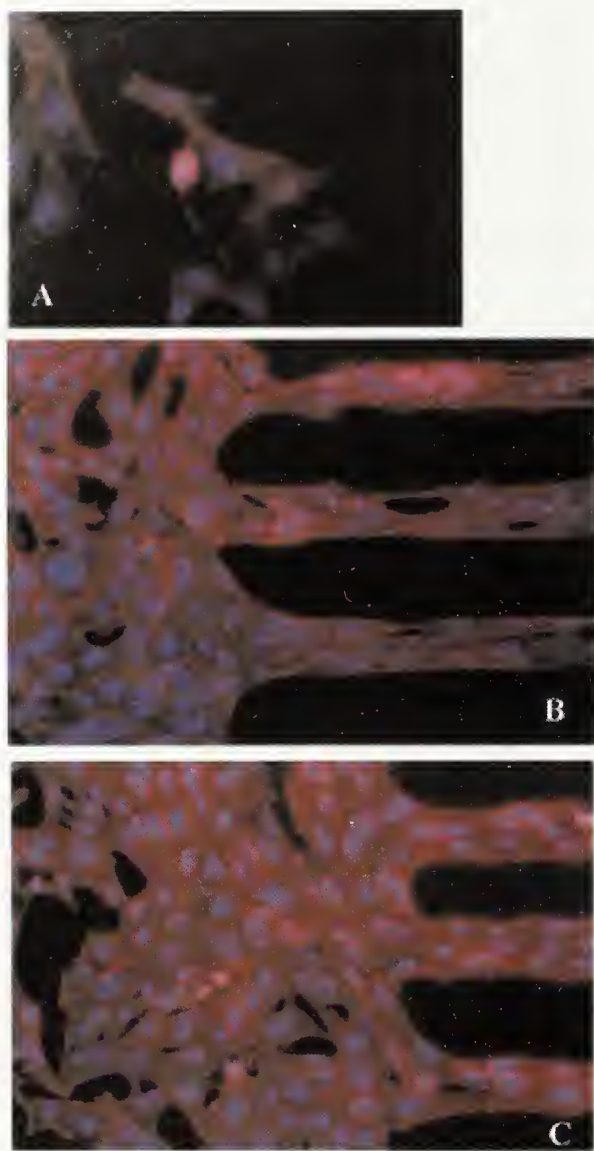


Figure 2. Fluorescent images of the cytoskeleton and nuclei of R28 cells on polystyrene (A), PAH (B), and PEI (C). The cytoskeleton is denoted by the red color, whereas the nuclei are observed in blue color. The morphology on polystyrene and the larger areas of PAH and PEI are similar. Cells are elongated when patterned in smaller areas as observed on the PEM lines (B) and (C)). Two weeks growth of retinal cells on poly(ethyleneimine). Cells are covering all the polycation area.

The adhesion of rat retinal cells on the patterned PEMs was observed 5 h after seeding. Cell viability and morphology on the patterned PEMs were assayed. These materials proved to be nontoxic to the cells used in this study regardless of the number of stacked PEM layers. Phalloidin staining of the cytoskeleton revealed no apparent morphological differences in retinal cells compared with those plated on polystyrene or the larger regions of PEI and PAH; however, cells were relatively more elongated when cultured on the PEM lines. Cell-to-cell

communication on adjacent PEM lines was observed as interconnecting tubes containing actin that were a few hundred nanometers in diameter and up to 55 μm in length. This approach provides a simple, fast, and inexpensive method of patterning cells onto micrometer-scale features.

Selected Publications

1. D. R. Reyes, E. Perruccio, S. P. Becerra, L. E. Locascio, M. Gaitan, "Patterning Retinal Cells on Polyelectrolyte Multilayers," The 7th International Conference on Miniaturized Chemical and BioChemical Analysis Systems (μ TAS 2003), Oct 05-09, 2003, Squaw Valley, California, pp. 713-716 (18-FEB-2004).
2. J. Shah, J. Geist, L. Locascio, M. Gaitan, R. Mulpuri, W. Vreeland, "Surface modification of PMMA for application of wall coating polymers for microchip electrophoresis", Electrophoresis, (Approved by ERB)
3. D. R. Reyes, L. E. Locascio, M. Gaitan, "Polyelectrolyte Multilayers", Encyclopedia of Biomaterials and Bioengineering, Marcel Dekker, New York, pp. 1-15 (2005).

Single Molecule Nanovials

The biotechnology and healthcare industries require measurements of large sample arrays as part of their combinatorial approach to disease recognition and drug development. For example, manufacturers of technologies such as DNA and protein arrays are striving to make larger arrays that can more efficiently support larger combinatorial measurements. As the size of the sensors is decreased, the sample size (and hence the number of molecules in the sample) also decreases. Since biological molecules are expected to have variation in their behavior, a question arises concerning whether the statistical variation of biological molecules will affect the accuracy of those measurements; e.g., is there a minimum sample size that is required to yield a result that is comparable to traditional ensemble measurements. The ability to measure the structure and function of single biomolecules will yield the statistical behavior of their large populations. The primary objective of this work is to develop methods to encapsulate small populations or single DNA, RNA, and protein molecules in 20 – 100 nm vesicles that will enable them to be moved and held in position for optical characterization. This method could not only enable new methods for single molecule measurements and single molecule standard reference material, but also enable direct observation and measurement of nanoparticle formation.

Michael Gaitan, EEEL (812), and Laurie Locascio and Wyatt Vreeland, CSTL (839)

The semiconductor electronics industry has driven the development of fabrication tools that are capable of patterning structures that are smaller than cellular dimensions (i.e., on the order of 100 nm). In combination with micromachining methods developed by MEMS research, it is possible to create three-dimensional structures that are commensurate with the size of biomolecules. We will utilize nanofabrication methods and enhanced surface coatings to develop novel solid-state structures for the control and manipulation of single biomolecules. These methods will be based on electrofluidic, electro-mechanical, optical, and magnetic transport of biomolecules in confined nanometer-scale environments.

We have developed and shown that monodisperse vesicle populations can be formulated with size control over the range of 20 – 100 nm by controlling the flow rates in fluidic networks. The vesicles are formed by

self-assembly of phospholipid molecules that are diluted in a water miscible solvent stream that is hydrodynamically focused into a water stream. Furthermore, other molecules that are diluted in the water stream will become encapsulated in the vesicles as they form. If the concentration of those molecules is sufficiently small, single molecules will be encapsulated. Since the method is in a planar format, one can for the first time directly observe nanoparticle formation. Ongoing work is to accurately characterize this formation process, to incorporate the capability to modulate the type and the number of molecules entrapped in the liposome nanovials, and to interface the stream with optical techniques to study single molecule dynamics downstream.

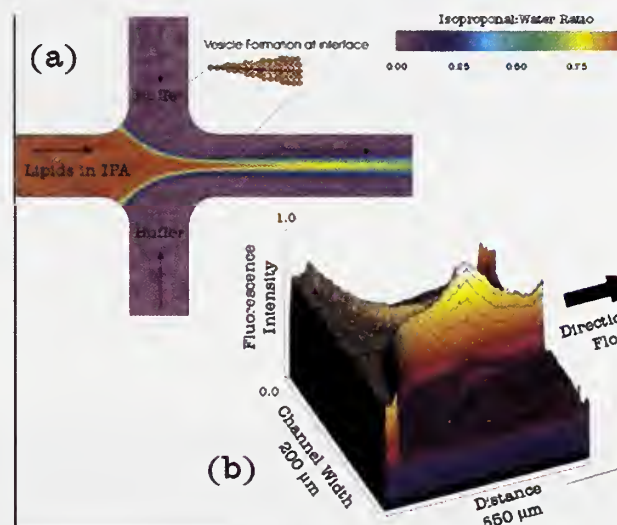


Figure 1. (a) Schematic of liposome nanovial formation process in the microfluidic channel. Color contours represent the concentration ratios of IPA to aqueous buffer. (b) 3-D color contour map of DiIC18 fluorescence intensity at focused region during liposome formation.

Accomplishments

A method has been developed to form liposome nano-vials in a continuous flow system. Microfluidics is used to elicit control over the spontaneous self-assembly of liposomes from a solution of dissolved phospholipids. In this work, we hydrodynamically focus a stream of lipid tincture at a microchannel cross-junction between two aqueous buffer streams. In a typical procedure, isopropyl alcohol (IPA) containing the dissolved lipids plus a fluorescent dye (DiIC18) flows through the center inlet channel, and an aqueous phosphate buffered saline solution flows through the two side inlet channels. DiIC18 is a membrane-intercalating dye that exhibits enhanced ver

fluorescence when trapped in a lipid membrane as compared to the fluorescence of the dissolved dye. The flow rates of the IPA and buffer channels are adjusted to control the degree of hydrodynamic focusing and the width of the center stream, thus controlling the IPA/buffer dilution process.

2. A. Jahn, W. N. Vreeland, M. Gaitan, L. E. Locascio, "Controlled Vesicle Self-Assembly in Microfluidic Channels with Hydrodynamic Focusing," *JACS* 126, 2674-2675, 2004.

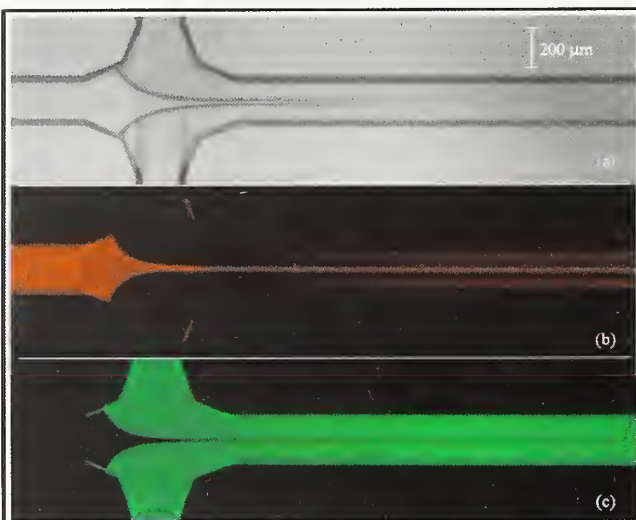


Figure 2. Photomicrograph (a) of the hydrodynamically focused stream of isopropanol injected into a water buffer. The isopropanol rapidly diffuses into the water and the boundary that is observed due to the mismatch of the dielectric constant of the fluids disappears. In (b) a red fluorescent membrane intercalating dye molecule is diluted in the isopropanol that is imbedded in the phospholipid membrane when the liposomes are formed. In panel (c), a green water soluble dye marker is mixed with the water buffer.

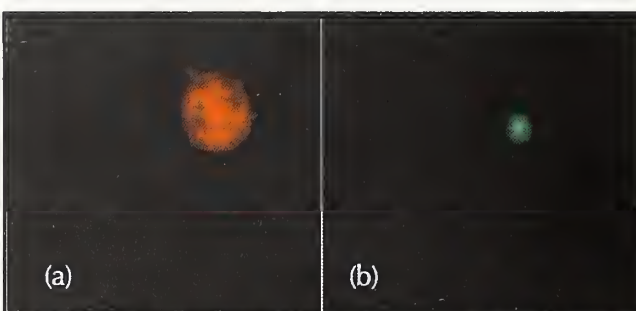


Figure 3. Fluorescent photomicrograph of a single vesicle formed using the technique. In panel (a), the membrane of the liposome is imaged using the red membrane intercalating dye marker. In panel (b) the water aqueous interior of the liposome is imaged using the green fluorescent water soluble dye marker. The number of water soluble molecules that will be captured in the liposome nanovial can be controlled by changing the concentration of those molecules in the water buffer stream.

Selected Publications

1. M. Gaitan, "Nanotechnology in Integrative Systems: Introduction to Integrative Systems," *Nanoscale Science and Technology*, Kluwer Academic Press, pp. 373-388 (17-AUG-2004).

Optical Manipulation of Nanocontainers and Nanotubes

Storage, transport, and manipulation of tiny amounts of material are important for applications that include drug delivery, micro-analysis, and the creation of model analog of biological systems. We are developing techniques for the production and manipulation of nanocontainers, "artificial cells" such as liposomes and polymerosomes as well as nanotubes based on lipid or polymer layers. These cells and tubes can store and transport materials, and be used as nano-scale reactor vessels.

William D. Phillips and Kristian Helmerson, PL
(842)

The cell is, arguably, Nature's factory for the nano-manufacturing of proteins and other macromolecules necessary for sustaining life. Much of this work is carried out by small numbers of molecules in many confined reaction compartments of nanometer dimensions. These nanoscale compartments are integrated into reaction networks, which allow for the transport of information in the form of the chemical compounds. Many groups, including ours at NIST, are working on the development of biomimetic cells and cell networks. The goal is to create reaction networks consisting of well-characterized nano-reaction vessels for directed delivery and controlled reaction of chemical compounds.

The process of self-assembly is used widely by Nature for building complex, functional structures out of nano-scale building blocks. Amphiphilic molecules (molecules with a section that is hydrophilic and a section that is hydrophobic), such as lipids, can self-assemble into bilayer membranes that can then be formed into shapes with sizes ranging from several tens of nanometers to hundreds of microns. When the membranes assemble into liposomes (spherical structures consisting of a lipid bilayer membrane that separates the aqueous interior environment from the aqueous external environment) they are a natural choice as containers for performing biochemical reactions in ultra-small volumes.

Giant liposomes are approximately 10 μm in diameter, enclosing about a pico-liter of volume. The membrane is similar in size and composition to that of a cell and therefore giant liposomes should be a natural container for complex biochemical reactions to occur in. A number of groups are investigating the use of giant liposomes as ultra-small containers for biochemical reactions. The basic idea is to bring two liposomes into con-

tact and then induce the membranes to fuse such that the contents of each liposomes mix. We use optical trapping to bring two giant liposomes into contact and then use an optical scalpel (a focused, pulsed UV laser beam), aimed at the contact point between the lipid membranes, to induce fusion of the two liposomes into one (see Figure 1). With this technique have demonstrated a controlled chemical reaction using liposomes as containers. One or two figures should be included in most cases.

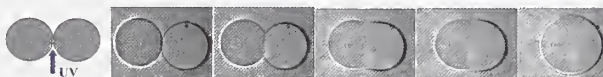


Figure 1. Schematic diagram, and photographic images of two liposomes, brought into contact with optical tweezers and induced to fuse by an optical scalpel.

Polymersomes, which are vesicles similar to liposomes but have a self-assembled membrane composed of amphiphilic polymers, can also be used as biocompatible nano-containers. Similar to liposomes, polymersomes can be trapped and manipulated with optical tweezers. We have also, demonstrated fusion of polymersomes initiated by the pulsed UV laser, but the process is typically much slower than the fusion of liposomes, often requiring several UV pulses. One potentially useful feature of polymersomes, however, is that the polymers can be cross-linked to form even more stable structures.

Lipid nanotubes have recently been observed between live cells and are purported to be conduits for intercellular organelle transport. Lipid nanotubes can also be "pulled" from lipid membranes. Researchers in Sweden are using micropipettes inserted into lipid membranes to stretch nanotubes and connect them to other liposomes, thereby forming complex networks of channels and containers for processing chemical reactions. Recently, we have demonstrated that optical manipulation techniques, such as optical tweezers, could be used to stretch lipid membranes to form nanotubes (see illustrations A-D in figure 2). Although the lipid nanotubes formed are relatively stable, they are manifestations of strongly distorted lipid membranes and hence, they are not extremely robust. If the lipid nanotubes are released or the system perturbed, then the nanotubes would tend to collapse back to a structure that minimizes the energy of the system, which in this case would be the initial liposome.

Similar to liposomes, the membranes of polymersomes can be stretched to form nanotubes. This approach is particularly appealing because the polymersomes are readily cross-linked. We incorporate a surfactant in the polymer membrane, which modifies the visco-elastic

properties of the membrane, such that nanotubes can be readily pulled from the membrane using optical tweezers. We have been able to pull nanotubes up to a ~1 cm in length and were only limited by our sample chamber. We subsequently stabilize our pulled nanotubes by free radical polymerization of polymers. The cross-linked nanotubes are extremely robust. They can be washed and removed from solution, which we did to prepare them for imaging by transmission electron microscopy (TEM). The inset of figure 2 is a TEM image of a cross-linked polymer nanotube. The outer diameter of this cross-linked polymer nanotube is ~80 nm.

The polymer membranes that we pull on with optical tweezers to form nanotubes appear to be as easy to manipulate as lipid membranes, especially with regard to forming network structures such as a Y-junction. Figure 2 contains a composite image of a network composed of polymer nanotubes and polymersomes, imaged via a fluorescent membrane dye. Optical tweezers were used to pull nanotubes from polymersomes and attach them to other polymersomes (see illustration A-F in figure 2). The several Y-junctions apparent in this image were formed by either pulling an additional nanotube from a polymersome that already had a nanotube attached to it and the two nanotubes subsequently merged to form the junction, or by pulling a nanotube from the membrane of an existing nanotube.

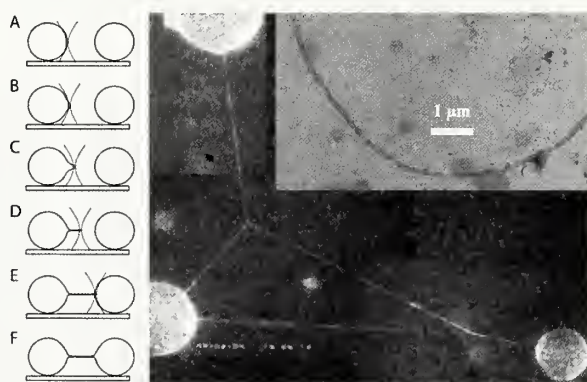


Figure 2. The illustration on the left shows the procedure for creating polymersome-nanotube networks using optical tweezers. The tweezers directly pull on the polymer membrane to stretch out a nanotube, which can then be inserted into the membrane of another vesicle. The fluorescence micrograph is a composite image of a polymersome-nanotube network formed by optical tweezers. The structures can be made highly stable by subsequently cross-linking the polymers. The inset (upper right) is a TEM image of a cross-linked polymer nanotube.

Fundamental Properties of Quantum Dots

Self-assembled semiconductor quantum dots (QDs) are remarkably flexible nanostructures that exhibit unique optical and electronic properties due to their size ($\sim 1000 \text{ nm}^3$) compared to bulk semiconductors and quantum wells. They exhibit atomic-like properties due to their three-dimensional electronic confinement, which offers substantial opportunities for unique and improved devices. Quantum dots have yielded superior performance when incorporated into conventional devices such as semiconductor lasers (low threshold current density and low temperature dependence) and amplifiers (reduced cross-gain modulation and large bandwidth). They are also employed as single photon sources and detectors for such applications as quantum computing and cryptography. However, many of the fundamental optical, electronic, and structural properties of quantum dots have not been measured, yet measurements are sorely needed for the accurate modeling and optimization of QD devices. We have developed and applied tools to measure semiconductor quantum dot properties, including the dipole moment, homogeneous lineshape, and carrier dynamics.

Kevin Silverman, EEEL (815)

Spectral hole burning (SHB) is a powerful tool for measuring the optical properties of semiconductor quantum dots (QDs). We employ two complementary techniques, ultrafast transient SHB and high-resolution CW SHB, to measure the linewidth and relaxation dynamics of these nanostructures from cryogenic to room temperature.

Around room temperature, the homogenous linewidth of the QD transition is long and significant cross-relaxation between QDs at different energies occurs. This affects the threshold current density in QD lasers and limits the isolation between channels in a QD semiconductor optical amplifier. We have developed a two-color, differential transmission (DT) measurement capability to temporally and spectrally resolve the carrier dynamics in QDs resonant and non-resonant with pump excitation. It uses an RF chopping scheme whereby the pump beam is an optically narrowband signal chopped at low frequency and the probe beam is broadband, modulated at a high frequency. Both are coupled to a waveguide sample containing QDs, allowing us to increase the interaction length with the weakly absorbing QDs. After interaction with the sample, the light is sent to a spectrometer, detected with a photodiode, and the

DT signal is demodulated.

From the rise and decay times observed in the DT measurements, we determined conclusively, for the first time, that carrier transfer at room temperature occurs between InGaAs/GaAs QDs resonant with pump excitation and those QDs initially empty. In addition, the width of the initial spectral hole produced an estimate of 12 nm for the homogeneous broadening in the QDs.

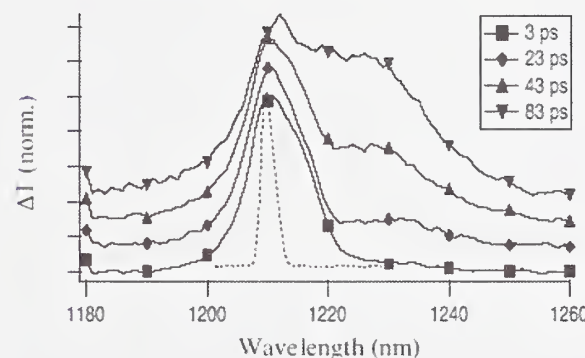


Figure 1. Pump-probe spectroscopy of InGaAs/GaAs quantum dots showing pump (dotted) spectrum and differential transmission of probe (solid line at various delay times).

The temperature dependence of the escape rate was also measured using degenerate DT spectroscopy, with an optical gating technique, in which the probe is separated from the pump by means of a non-linear optical gate. The results indicated that single carriers initially escape to the wetting layer before being recaptured by other dots. The escape rate could be modeled with a 4 LO phonon absorption or a thermal model, yielding a barrier for escape of between 128 and 175 meV for the QDs studied.

At cryogenic temperatures, the interaction between QD excitons and acoustical modes in the host semiconductor is dramatically reduced. Here, semiconductor QDs act as sources of single photons-on-demand, indistinguishable photons and entangled pairs of photons. Of fundamental importance to these applications is the coherence time of the QD exciton and its relationship to the radiative lifetime. Here, narrow linewidth sources are required to resolve the relatively narrow spectral holes. For this we employed two tunable laser diodes as the pump and probe sources. In addition, we added a heterodyne detection scheme, which is necessary when operating at the picowatt power levels required to avoid saturating the transition. Fig. 2 displays the spectral hole burned by a low intensity pump laser at a sample temperature of 10K. From a lorentzian fit to this data, we

determined the linewidth of the transition to be $0.74 \mu\text{eV}$ which corresponds to a dephasing time (T_2) of 1.7 ns . The dephasing time is of critical importance to quantum computing applications since it sets an upper limit on the time that coherent qubit manipulations can occur.

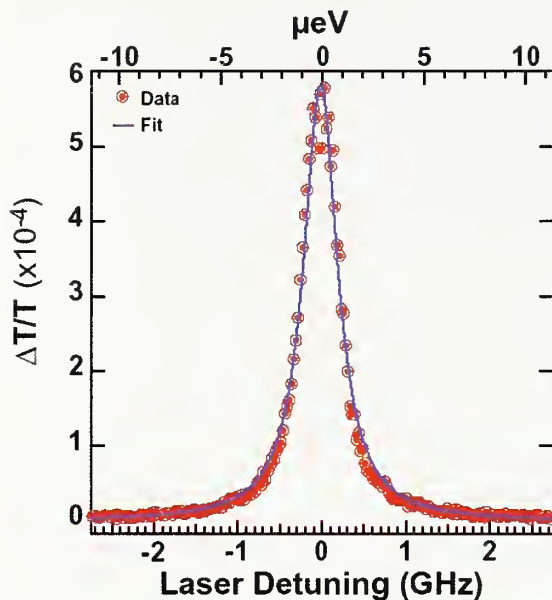


Figure 2. Low-intensity spectral hole at 10K. The linewidth of the transition here is $0.74 \mu\text{eV}$ full-width at half-maximum.

We have also measured the lifetime (T_1) of the QD exciton in this sample with the method of time-resolved single photon counting (fig. 3). An exponential fit to this data yields a radiative lifetime of 900 ps . Comparing this with our previous measurement we find the relation $T_1 = 2*T_2$ holds in this case and the QDs interrogated here are purely radiatively broadened. Being radiatively broadened ensures that the QD is well isolated from the semiconductor matrix that surrounds it and may fairly be dubbed an ‘artificial atom’.

The measurement of fundamental optical and electronic properties of quantum dots places NIST at the forefront of important data generation as input to the design and simulation of QD devices. Future generation communication systems will benefit in a variety of performance measures.

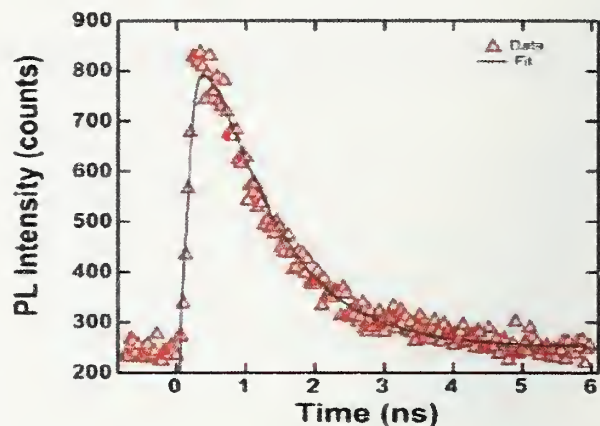


Figure 3. Time-resolved photoluminescence trace of the QD sample at 10K. Solid line is a convolution of the instrument response function and an exponential decay of 900 ps .

The measurement of fundamental optical and electronic properties of quantum dots places NIST at the forefront of important data generation as input to the design and simulation of QD devices. Future generation communication systems will benefit in a variety of performance measures.

Selected Publications

1. K.L. Silverman, R. Mirin, S.T. Cundiff, "Lateral coupling of InGaAs/GaAs quantum dots investigated using differential transmission spectroscopy", Phys. Rev. B **70**, 205310-1 – 5 (2004).
2. J.J. Berry, Martin Stevens, R. P. Mirin and K. L. Silverman, "High-resolution spectral hole burning in InGaAs/GaAs quantum dots.", Applied Physics Letters **88**: 06114 (2006).

Multiscale Modeling of Nanostructures

We have developed a multiscale model for nanostructures in solids. The model relates the physical processes at the interatomic level to measurable lattice distortions at the nanometer level and macroscopic stresses and strains. The model links the subnano (interatomic), nano (nanostructures), and macro length scales by integrating the powerful techniques of molecular dynamics, lattice-statics Green's function, and continuum Green's functions.

Vinod Tewary and David Read, MSEL (853)

Technical description

Mathematical modeling is a very important tool for understanding the mechanical behavior of nanomaterials and for research and design of devices based upon nanostructures. A nanostructure needs to be modeled at the following scales: (i) the core region of the nanostructure (sub-nanometer) where the nonlinear effects may be significant, (ii) the region of the host solid around the nanostructure (nanometer), and (iii) free surfaces and interfaces in the host solid (macro). A nanostructure causes lattice distortion in the host solid that manifests as strain throughout the solid. The strain is essentially a continuum-model parameter whereas the lattice distortions are discrete variables that must be calculated by using a discrete lattice theory. Hence one needs a multiscale model that relates the discrete lattice distortions at the microscopic scale to a measurable macroscopic parameter such as strain.

Conventional models of nanostructures are based upon either the continuum theory, which is not valid close to the defect, or molecular dynamics (MD) that is CPU intensive and usually limited to small crystallites, which may introduce spurious size effects. We need a computationally efficient multiscale model that links the length scales from sub-nano to macro and can be used on an ordinary desktop. Such a model will be a valuable tool for research and engineering designs as well as for teaching as it can provide quick answers to 'what if'-type questions.

Our model is based upon the lattice-statics Green's function (LSGF) G that reduces asymptotically to the continuum Green's function (CGF). The displacement field in this model containing N atoms is given by

$$\mathbf{u}(\mathbf{l}) = (1/N) \sum_{\mathbf{k}} G(\mathbf{k}) \mathbf{F}(\mathbf{k}) \exp(i\mathbf{k} \cdot \mathbf{l})$$

where \mathbf{l} is a lattice site, \mathbf{k} is a reciprocal space vector, and $\mathbf{F}(\mathbf{k})$ is the Kanzaki force which is calculated by

using MD without making the linear approximation. For small \mathbf{k} , $G(\mathbf{k})$ reduces to CGF. Thus, for large \mathbf{l} , the above equation reduces to macroscopic continuum theory while the discrete lattice effects are retained in $\mathbf{F}(\mathbf{k})$. Thus, our model is truly multiscale as it seamlessly links the discrete atomistic effects in $\mathbf{F}(\mathbf{k})$ to macroscopic scales through the GF. Even for a million-atom model, the calculation of GF takes only a few CPU seconds on a standard 3 GHz desktop.

Accomplishments

Initial conference presentations and a journal paper on this new approach have been well received. We are now applying our approach to more challenging systems with potential industrial applications such as Ge quantum dots in Si and InAs quantum dots in GaAs. We are now able to model quantum dots of actual sizes, up to about 8 nanometers, on a desktop computer. To model such a large quantum dot, it is necessary to include at least a million atoms in the host lattice. An attempt to model such a system using MD would need huge computational effort. It is usual to model such quantum dots using the simple continuum theory. Figure 1 shows our calculated displacement field for an 8 nm diameter Ge quantum dot in a million atom model of Si host in [100] and [110] crystallographic directions. For comparison, results predicted by the isotropic continuum model are also shown. The difference is significant near the QD/ host interface which is the region of practical interest.

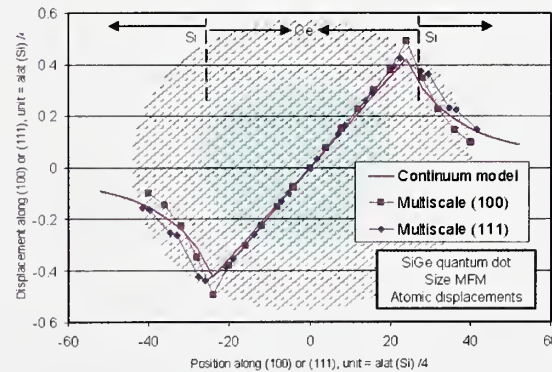


Figure 1. Displacement field through a section of an 8 nm diameter Ge quantum dot in Si.

Designing the Nanoworld: Nanosystems and Nanooptics

Developing and exploiting precision metrology for quantum and nanotechnology requires nanoscale modeling of ultrasmall structures, devices, the optics of these structures, their dynamical operation, and their response to probes. Atomic/nanoscale simulations of the electronic properties and nanooptics of complex nanosystems at the nano/molecular interface, including semiconductor nanocrystals, self-assembled dots, nanodot arrays and solids, metallic nanoparticles, and bio/nanohybrids, are being carried out to provide the foundation needed for the metrology and design of nanolasers, nanodetectors, biomarkers and sensors, quantum devices, and nanomaterials.

Garnett W. Bryant, PL (842)

Theory is used to extend the fundamental understanding of systems at the atomic/nanoscale interface as necessary to interpret experiment, explore new applications in nanoscale and quantum technologies, and motivate new and enhanced precision metrology for these nanotechnologies. We are developing the theoretical understanding needed to create nanooptics structures for applications as, for examples, nanosensors and biolabels, single photon sources and qubits for quantum information processing, and as the nanoscale optical communication structures needed in emerging quantum and nanoscale technologies.

Semiconductor nanocrystals and quantum dots have been intensely studied for their potential as tailorabile, man-made, artificial atoms. Artificial molecules and solids fabricated from nanocrystals and quantum dots offer intriguing new possibilities, not possible in natural molecules and solids, because quantum-dot molecules and solids are not limited by the rules of chemical binding that determine natural molecules and solids. Nanodot nanosystems require nanodots with precisely determined geometry, nanodots tailored with internal structure for enhanced functionality, and arrays of close-packed nanodots (quantum-dot molecules and solids). To provide an understanding of these nanosystems, models of nanodots (such as the atomic model for an InAs self-assembled dot shown in figure 1) must describe variations in composition on the atomic scale, realistic shapes and faceting, coupling between closely spaced nanodots, and nanoarchitectures of dots. Atomic scale theory is needed to describe these nanostructures. We have developed an empirical tight-binding theory of nanodot nanosystems that allows us to study individual nanocrystals and quantum dots, and, importantly, the complex

nano/biohybrids and nanodot nanoarchitectures that are built from nanodots. Ab initio models for small dots are used to validate the calculations for complex structures.

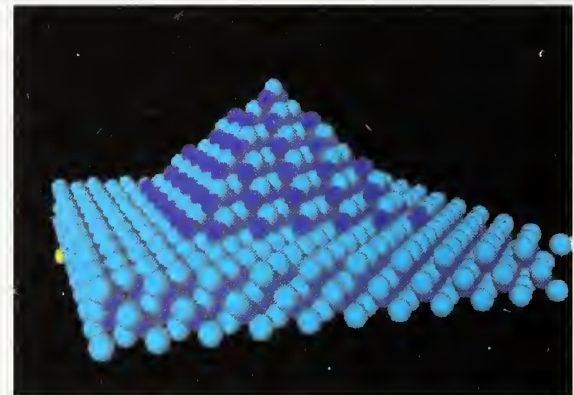


Figure 1. Atomic model for an InAs self-assembled dot.

We have used the theory to model the individual dots that serve as the building blocks for complex structures to determine how the electronic structure of these nanodots can be tailored by shape and internal structure. Surface effects significantly influence the functionality of semiconductor nanocrystals, especially nano/biohybrids being used as nanosensors. Passivation with ligands or high band-gap semiconductor shells is necessary to reduce trap densities, enhance quantum yield and increase photostability. Considering CdS nanocrystals with unrelaxed, unfaceted surfaces, we have shown that passivated dots with saturated dangling bonds have no surface states in the fundamental band gap and all near-band-edge states are quantum-confined internal states. When only the surface cations are passivated, an anion-derived surface state band and a band of back-bonded surface states exists near the valence band edge. When only surface anions are passivated, a broad band of mixed surface/internal states exists between the conduction band edge and the onset of internal states. Because of this strong sensitivity to passivation, explicit models for surface effects are necessary for precise modeling of the electronic states. We also showed that capping the CdS dot with more than two monolayers of ZnS significantly reduces the influence of the surface on the internal electronic structure and optical properties. Such information is critical for designing complex nanostructures with optimal optical response.

Nanoarchitectures of dots could push classical computing almost to the atomic regime and provide coherent quantum structures needed for quantum computing. An understanding of how dots couple in these structures is essential. We have shown that interdot coupling in dot

molecules (the atomic-scale charge density of a typical electronic state in a double-dot molecule is shown in figure 2) and arrays modifies significantly level ordering and state symmetries. For 1D arrays of stacked dots, the dispersion of electron bands results from the mixing of the electron envelope functions. In contrast, hole bands depend on the atomic character of the hole states, especially between dots. Antisymmetric interdot mixing of low-energy hole states is favored for widely spaced dots. Symmetric mixing is favored for closely spaced dots. The character of this mixing critically impacts the optical response of these states. Interdot coupling also affects the maximum spin polarization that can be realized in hole states. This polarization mixing has consequences for nano/quantum device applications for the generation of polarized photons, entangled photons, and quantum computing with entangled spins.



Figure 2. Atomic-scale charge density of a typical electronic state in a double-dot molecule.

Nanoscale simulations of optical fields near nanosystems are also being carried out. Results are being used to design nanoprobes and nanocavities for use in precision nano optics metrology. Results are also being used to design and model the nano optics highway, that is, collections of nanoparticles used for nano optical communication to generate, transport and collect photons on the nanoscale, well below the diffraction limit that governs the classical transport of photons. Nano optics highways will be critical for the transport of excitations in quantum devices and in the metrology of these devices.

The optical properties of molecules are dramatically influenced by coupling to plasmon resonances of nearby metallic structures. This can lead to harmful effects such as fluorescence quenching and to useful effects such as surface enhanced Raman scattering. The demonstration

of single molecule sensitivity via SERS has stimulated great interest in using the electromagnetic response of metallic nanoparticles as nanoscale sensors and probes. The extreme near-field enhancements required for single molecule Raman scattering is thought to occur in the gaps between metal nanoparticles. We have studied the optical properties of coupled metallic nanoparticles to investigate their potential in plasmon enhanced spectroscopies and to identify plasmonic nanoprobe structures with optimal response.

We have shown that changing the dimensions of the nanoparticles or increasing local interparticle coupling is a major source of field enhancement. Coupling pairs of nanoparticles generates a redshift of the plasmonic response and an enhancement of the near field signal in the cavity between the nanoparticles. The redshift in pairs of particles is similar to the redshift in an isolated particles with the same total length, but the cause of the shift is different. The redshift in coupled pairs is connected with the coupling at the cavity, while the redshift in isolated particles is connected with depolarization. The local field enhancement at the cavity of a pair is more than an order of magnitude larger than near the end of an isolated particle. We have shown how this field enhancement can be tailored by the particle size and shape, interparticle separation, and the geometry of the particle ends. Such information will greatly aid the design of structures optimal for nanoscale sensing or for nano optical communication.

Precision Metrology for Nanoscale Quantum Technologies

Advanced optical metrology is needed to provide the characterization tools critical for the continuing development of emerging nanotechnologies and quantum (coherent) technologies. We are developing and exploiting precision metrology at the interface between atomic and nanoscale systems, focusing on precision optical metrology and nano optics, to further the understanding of the nano optics and nanomechanical properties of nanoscale and quantum-coherent systems.

John Lawall and Garnett W. Bryant (842)

Accurate measurement of very small distances is essential for characterizing structures used in nano and quantum technologies and for industries such as semiconductor fabrication. For some kinds of measurements, such as those needed in large chip fabrication, the ability to precisely measure distances of centimeters is important. We have been developing advanced, high-precision optical techniques for displacement measurements. We recently demonstrated the ability to measure displacements up to 25 mm with the lowest uncertainty ever reported. To characterize micromechanical (MEMS) and nanomechanical (NEMS) systems, the challenge is even greater. Femtometer displacements at GHz speeds need to be measured.

We have demonstrated a technique for measuring displacements with an accuracy of 10 picometers (about 1/10th the size of an atom) over a range of 25 mm. The corresponding relative uncertainty is 4×10^{-10} , the smallest ever reported. The method employs Fabry-Perot interferometry, and offers unique advantages over approaches previously used. The key idea is that the resonant frequencies of two modes of a scanning Fabry-Perot cavity are measured simultaneously, using optical techniques to measure the absolute frequency and radio-frequency techniques to measure the difference frequency. The associated measurement redundancy imposes a strict bound on many systematic sources of error. In addition, the spatial filtering provided by the resonant cavity provides control over the exact geometry of the laser light that is not possible in more conventional approaches – and is essential when making measurements with this level of accuracy. Another remarkable advantage of the technique is that the light can be extinguished or blocked as the target is moved, which is not the case in the traditional approach where sinusoidal fringes are counted during the motion. Finally, the Fabry-Perot cavity under interrogation is located remotely from the laser

system and coupled via an optical fiber link, making the system particularly attractive for remote sensing applications.

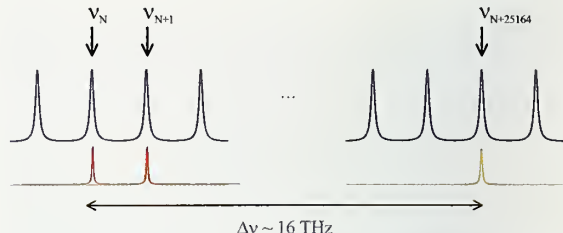


Figure 1. The length of a scanning Fabry-Perot cavity is measured by simultaneously probing three resonances, two at 633 nm (red) and one at 613 nm (orange). In the case illustrated above, the order number N is measured to be $N = 732\,635$, and the difference in order numbers probed by the red and orange lasers is 25 164.

A natural extension of this work relates the displacement measurement directly to the SI definition of the meter via replacement of the iodine-stabilized helium-neon measurement laser with a cesium clock. This effort is a modern realization of an idea, first put forth by Zoltan Bay at NBS in 1970, of using a microwave measurement of the mode spacing within a Fabry-Perot cavity to measure displacements free of the systematic error induced by diffraction. In addition to probing two adjacent modes of a Fabry-Perot cavity with red light at 633 nm, as discussed above, we probe another mode with orange light from a helium-neon laser at 612 nm. A precise measurement of the mode spacing using the light at 633 nm allows us to determine the exact number of modes in the 16 THz interval between the red and orange lasers, as shown in the figure. We then beat light from the helium-neon lasers against light from a visible frequency comb that is locked to a cesium clock. The resulting measurements of the cavity length are not compromised by diffraction, and are related directly to the definition of the second, and by extension the meter.

We are now beginning to exploit advanced optical metrology tools, such as the high precision displacement techniques that we have developed, to probe nanoscale and quantum coherent phenomena that underlie nano and quantum technologies involving nanomechanical systems, nano optical systems, and coupled nano optomechanical systems. Nanomechanical systems are currently used as ultrasensitive force and mass sensors. They offer the potential for imaging large molecules, improving our understanding of quantum measurements, and being used to read out quantum logic gates based on individual magnetic nuclei. We are planning to construct nanomechanical devices at the AML nanofabrication facility and

to explore them in the regime where they exhibit quantum behavior. This will involve initial cooling by cryogenic means and then further cooling by techniques reminiscent of quantum optics. One possible approach exploits both nanomechanical and nanooptical techniques by integrating a quantum dot into the mechanical resonator and effecting sideband laser cooling. Another approach involves coupling the resonator to a Cooper pair box. Both approaches have been predicted to allow cooling to the vibrational quantum ground state of the oscillator. We will pursue the most viable approaches that allow us to reach the quantum limit and begin to probe and exploit quantum effects with nano/mesoscopic structures.

Classical optical metrology and communication use macroscopic source, detectors, lenses, mirrors, waveguides, etc. However, classical optics does not work at subwavelength distances. Nanoscale manipulation of photons for communication in nano/quantum devices and for optical metrology with proximal nano-probes and nanosensors demands very different tools to control and guide photons. Photons will be manipulated on the nanoscale by converting them to material excitations (plasmons in metallic nanoparticles, electronic excitations in quantum dots), transporting the excitations along nanooptical guides made of coupled nanoparticles, and then converting the excitations back to photons.

We plan to develop approaches for nanooptical metrology and communication based on the use of metallic nanoparticles and semiconductor quantum dots as nanocomponents for generating, transporting, guiding, focusing, storing and detecting photons on the nanoscale. This will include exploiting metallic nanoparticles and structures to locally enhance fields, via the plasmonic excitations of the metallic structures, to achieve fields strong enough for high sensitivity single molecule detection and analysis. We will develop nanoantennas and nanoguides, made by integrating metallic nanoparticles, nanocrystals and quantum dots, to controllably transport light from source to nanosample to detector via the material excitations in the nanoantenna or guide. A typical nanoantenna or guide could have metallic nanoparticles to enhance fields, nanocrystals to control excitation transfer and quantum dots to provide single-photon generation and detection.

In the quantum limit, a single photons or plasmon would be used to probe or communicate with individual nanostructures, qubits, atoms, molecules, etc. We plan to pushing nanooptical metrology and communication to this limit. Control of photon and plasmon generation and manipulation down to the single quanta limit will be required. This opens up the ultimate quantum limit

where the coherent evolution of quantum processes can be initiated, probed, or controlled via single photonic or plasmonic quanta without the decoherence due to other quanta as would happen if a classical field were used. Achieving this limit will be critical for the measurement of quantum processes in chemical and biological structures, quantum devices, and quantum information processors.

Control of Cold Quantum Gases for Atomic Clocks and Quantum Information Processing

The need is for greatly improved primary standards for time and frequency and for the development of practical devices that exploit the revolutionary potential of quantum information processing. To achieve these ends, this project will develop theoretical tools and models for characterizing coherent quantum mechanical manipulation of single atoms and their interactions in ultracold quantum gases.

Paul S. Julienne and Eite Tiesinga, PL (842)

Cold gases of neutral atoms offer unprecedented opportunities for ultraprecise control of quantum processes for individual atoms or collections of atoms. Recent experimental progress opens up opportunities for dramatic breakthroughs in atomic clocks and quantum information processing. The task of this project is to develop theoretical modeling and predictive capability for using ultracold quantum gases for these purposes.

Typical atom traps can hold on the order of 1 million atoms at temperatures on the order of 1 μK in a trap of 10 μm to 1 mm in size. It is also possible to use a set of directional laser beams to impose an optical lattice structure on the trapped atoms. Such a lattice, shown schematically in figure 1 below, can confine individual atoms to a volume on the order of 30 nm in single trapping cells spaced a few hundred nm apart. When a quantum gas of bosons undergoes a Mott insulator transition, for example, it is possible to occupy a wide region of the lattice uniformly with exactly one atom per site or, in some cases, two atoms per site.

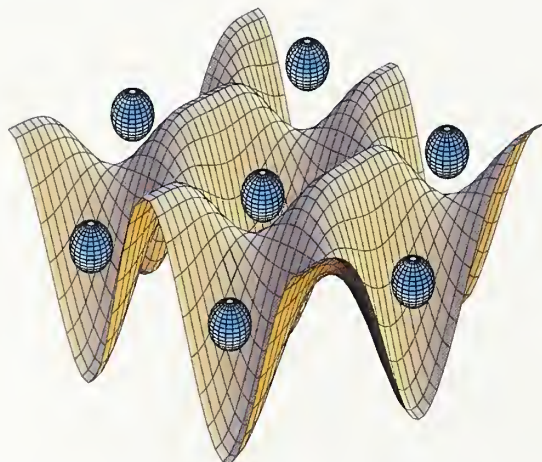


Figure 1. Optical lattice structure imposed on trapped atoms using a set of directional laser beams.

Lattices with no more than one atom per site are very

promising for atomic clocks, since the confinement to a single quantum state completely eliminates the Doppler effect, and single cell confinement eliminates the clock frequency shift due to atomic collisions. Lattices also offer prospects for entangling gate operations for quantum information processing by coherent quantum manipulation of atomic interactions in cells containing two atoms.

The collisions and interactions between cold atoms play a very significant role in cooling and trapping of the gases and in the loading and control of atoms in optical lattices. Some collisions are very beneficial, aiding the cooling of the gas or the control of desired quantum properties. Other collisions are harmful, and result in loss of trapped atoms or the decoherence of quantum properties. The long-term goal of this project is to develop quantitative theory for characterizing the interactions and collisions of specific atomic species that can form cold, neutral atomic gases. These models also characterize how optical and magnetic fields can modify key properties. We have previously developed quantitative models for Li, Na, K, Rb, and Cs atoms, and more recently, have begun work on Cr, Ca, Sr, and Yb. All of these species have been cooled or trapped in the ultracold regime. These models have been developed in conjunction with experimental groups at NIST and other laboratories, and are consistent with all the known data on these systems.

Most recently we have developed quantitative theory to explain and account for the dynamical properties of Feshbach resonance states in the alkali-metal species, both for free-space collisions and for interactions in optical lattice cells. Figure 2 shows a schematic example of a Feshbach resonance for collisions of ^{85}Rb atoms in one of its Zeeman sublevels near a magnetic field of 15 mT. The figure shows how the collision probability varies versus magnetic field strength and collision energy (color contour) and how the binding energy of a molecular bound state of the atom dimer varies (red line). Such magnetically controllable properties have been widely used by experimental groups to control and modify the properties of a variety of species of ultracold bosonic and fermionic quantum gases, for example, to achieve Bose-Einstein condensation or to create a Bose-Einstein condensate of dimer molecules comprised of two fermionic atoms.

One recent project we completed considered a new architecture for quantum information processing using a set of fixed marker atoms individually confined in optical lattice cells. By bringing a movable messenger atom

to a lattice site and performing a two-atom logic gate operation, then moving the messenger atom to other sites, a distant marker atom can be entangled with the original marker atom and used for quantum computation. We showed how the moving and bringing together of the atoms could be done dynamically. We also showed how particular Feshbach resonance states of ^{87}Rb atoms might be used to construct the needed two-atom gate operations. This work was done in collaboration with a group at the University of Innsbruck, Austria.

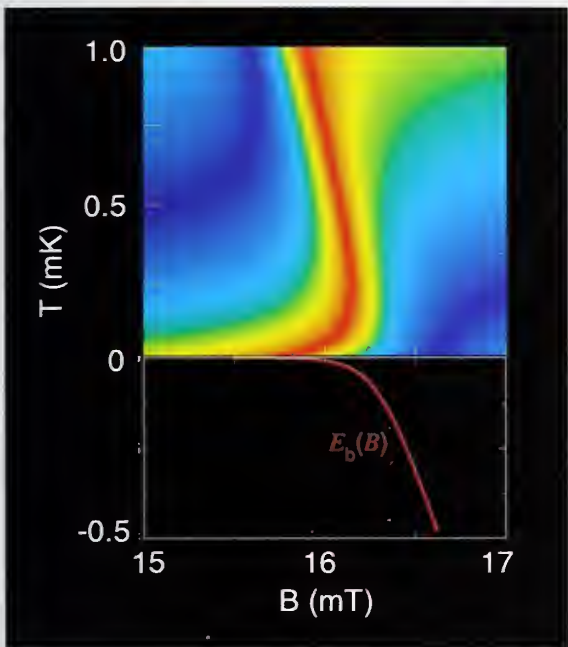


Figure 2. Schematic example of a Feshbach resonance for collisions of ^{85}Rb atoms in one of its Zeeman sublevels near a magnetic field of 15 mT.

It is known that cold, trapped atoms can be combined into molecules by a time-dependent sweep of the magnetic field that moves the field to a domain where there is a bound molecular dimer state. In a collaborative effort with Oxford University, we have developed general models of this process for atoms in free space or in lattice cells. Using the example of the 15.5 mT ^{85}Rb resonance shown in the Figure, we showed how a universal theory of the lifetime of the bound state could be calculated in general from the known parameters of the resonance. The lifetime increases by orders of magnitude when the bound state is very weakly bound close to the point of resonance. Our predictions were verified quantitatively by an experimental study at the University of Colorado.

A Feshbach resonance near 830 mT for fermionic species ^6Li has been used by a number of groups to study the paring of unlike fermionic spin states in a quantum degenerate gas analogous to Cooper pairing and to

switch the gas between such paired states and a molecular Bose-Einstein condensate of dimer molecules. We have worked closely with an experimental group at the University of Innsbruck to interpret and analyze data that allows us to construct a highly quantitative predictive model of ^6Li atom interactions that will be extremely useful to researchers in this field.

The next generation of atomic clocks will be based on optical frequency instead of microwave atomic transitions. This is because of the 10000 times faster oscillation frequency of optical clocks as compared to the present Cs microwave standard. In particular, cold, trapped Ca, Sr, and Yb atoms offer excellent candidates for optical frequency atomic clocks. The alkaline-earth-metal atoms have atom cooling properties very different from the alkali-metal atoms. We have started a program of first principles calculation of the properties of these systems relevant to using them as clocks.

In particular we have calculated the optical spectrum when light is used to photoassociate two Ca atoms to an excited molecular state. The optically allowed atomic transition gives rise to a spectrum similar to that known for alkali-metal atoms, only simpler. However, the Ca atoms have a weak intercombination line transition that is not present for alkali-metal species. This line is the basis for the atomic clock transition in Ca, as is true for the analogous line for Sr or Yb. We have calculated the intercombination line photoassociation spectrum. We also have predicted that the molecular intercombination lines in these species can be used as optically controllable Feshbach resonances that should allow control of scattering properties similar to what has been done with alkali-metal atoms. This is important, since the lack of magnetic structure in the ground state of Ca, Sr, or Yb does not permit magnetic Feshbach control.

One of the largest contributors to the error budget of an atomic clock comes from a shift in the clock transition frequency due to collisions between the atoms. We are initiating a study to understand and calculate the collisional shifts that will affect optical frequency atomic clocks. This includes cataloging the physical processes that will contribute, and identifying the possible magnitude of each. This will guide future experimental studies that will try to quantify the actual magnitude of such shifts, and will aid the development of predictive models calibrated by experimental data.

Quantum Computing with Trapped Ions

This project, part of the NIST Quantum Information Program, strives to demonstrate a working prototype and fully scalable quantum computer of approximately 10 to 20 quantum bits (qubits) using laser-cooled trapped ions. Quantum computing has the potential to revolutionize information processing, with dramatic impacts in such areas as cryptography, database searching, complex systems modeling, and many other applications. Within the past year, this project has successfully demonstrated all the requirements for a fully scalable quantum computer, as well as demonstrating application of quantum computing principles to fundamental metrology. This project serves the interests of the intelligence and defense communities, as well as the longer-term interests of the commercial information technology sector.

David Wineland and Tom O'Brian, PL (847)

The NIST trapped ion quantum computing project is arguably the most successful quantum computing research effort in the world. This project uses the team's long expertise in quantum state engineering and measurement of atomic ions confined in linear electromagnetic traps. Over approximately the past year, the project has demonstrated all the five DiVincenzo criteria for a fully-scalable quantum computer, has achieved several world's first demonstrations of crucial quantum computing achievements such as quantum teleportation of information on massive particles and robust error correction, and has successfully applied quantum computing techniques to enhanced spectroscopy and early demonstrations of a quantum logic atomic clock. The program attracts top researchers and collaborators from across the world, and has received intense interest from the U.S. intelligence and defense communities and from U. S. information technology companies interested in adopting the NIST technology.

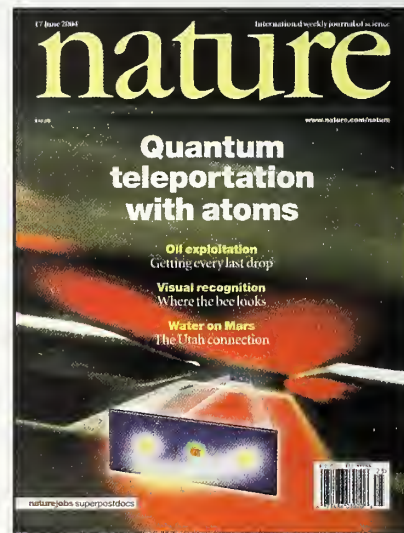
The main thrust of the project is to demonstrate a working, scalable, prototype quantum computer consisting of about 10 to 20 trapped ion qubits. The project currently uses $^{9}\text{Be}^{+}$ ions for most experiments, although other species are used for related experiments. The team is consistently working with collections of four to five ions, with a clear path to scaling to larger numbers of qubits. Over the past two years, the team has achieved all of the DiVincenzo criteria for a practical, scalable quantum computer: a scalable system of well-defined qubits; a method to reliably initialize the quantum system; long

coherence times; existence of universal gates; and an efficient measurement scheme. Most researchers consider the trapped ion approach to have the clear lead in quantum computing research among many other approaches (neutral atoms, superconducting Josephson Junctions, nuclear magnetic resonance, etc.).

This project represents close collaborations between the Time and Frequency Division (experiment) and the Mathematical and Computational Sciences Division (theory), as well as close interactions with the Quantum Electrical Metrology Division on the fabrication of microscale ion traps. The project is funded through internal NIST support and the intelligence community.

Accomplishments

- Demonstration of quantum teleportation of information on massive particles ($^{9}\text{Be}^{+}$ ions), simultaneously with a group from Innsbruck. Previous demonstrations of quantum teleportation used photons. Teleportation of quantum information among massive particles may be a key to efficient transfer of quantum information in large-scale quantum computers – effectively serving as the “wiring” of a quantum computer.



- Enhanced quantum state detection efficiency. A key process in both quantum computing and metrology using quantum information processing is high-fidelity detection of particular quantum states. By encoding the state of one qubit with an additional (ancilla) qubit and measuring both qubits, the state of the original qubit is detected with greater fidelity in the presence of noise. These results suggest that errors in individual qubit measurements need not

limit scalable quantum computers, when the scheme is applied to more ancilla qubits.



Figure 2. Six-zone alumina wafer ion trap. The team is conducting research on developing traps to support two-dimensional ion arrays to support more efficient quantum computing with larger numbers of qubits.

- Demonstration of broadly-applicable robust quantum error correction. Measurement noise is unavoidable in quantum processing for computing and communications. A scalable quantum computer requires techniques to control and correct for the errors introduced by such noise. The team conducted the first experimental demonstration of a robust, scalable quantum error correction scheme using three ${}^9\text{Be}^+$ ions in a linear, multi-zone trap. An encoded one-qubit state is protected against spin-flip errors by means of a three-qubit quantum error-correcting code. In principle, the approach enables a quantum state to be maintained by means of repeated error correction, an important step towards scalable fault-tolerant quantum computation using trapped ions.
- Demonstration of entangled state spectroscopy for three particles. The ultimate Heisenberg limit for measurement on a system of particles is obtainable only when the particles are entangled. Then the sensitivity of the measurement for N entangled particles increases by $N^{1/2}$ compared to unentangled particles. The team entangled three ${}^9\text{Be}^+$ ions and showed that the phase sensitivity increased by the factor of $3^{1/2}$ (within experimental uncertainty) as expected. Such Heisenberg-limited measurements could be used to reduce the required time for averaging atomic clocks

to their ultimate uncertainty by a factor of N when the N particles are entangled. For example, the current NIST primary frequency standard (atomic clock) requires about 10 days of averaging of continual measurements on about one million unentangled cesium atoms to achieve the ultimate noise-limited uncertainty. If the million atoms could be entangled, the measurement time to reach the noise-limited uncertainty would be reduced by about a factor of one million to about one second. While this early demonstration of entangled state spectroscopy on three ions is obviously far removed from routine entanglement of one million atoms, the demonstration clearly points to the value of quantum information processing techniques for fundamental metrology as well as for quantum computing.

- Based on the work described above as well as many other accomplishments in quantum computing and quantum metrology over many years, team leader Dr. Dave Wineland won the Frederick Ives Medal (highest award presented by the Optical Society of America) and the Presidential Rank Award for Distinguished Service presented to the handful of highest-achieving senior professionals in the Federal government.

Selected Publications

1. M. D. Barrett, J. Chiaverini, T. Schaetz, J. Britton, W. M. Itano, J. D. Jost, E. Knill, C. Langer, D. Leibfried, R. Ozeri, and D. J. Wineland, *Deterministic quantum teleportation of atomic qubits*, Nature 429, 737 (2004).
2. T. Schaetz, M. D. Barrett, D. Leibfried, J. Britton, J. Chiaverini, W. M. Itano, J. D. Jost, E. Knill, C. Langer, and D. J. Wineland, *Enhanced Quantum State Detection Efficiency through Quantum Information Processing*, Phys. Rev. Lett. 94, 010501 (2005).
3. J. Chiaverini, D. Leibfried, T. Schaetz, M. D. Barrett, R. B. Blakestad, J. Britton, W. M. Itano, J. D. Jost, E. Knill, C. Langer, R. Ozeri, and D. J. Wineland, *Realization of quantum error correction*, Nature 432, 603 (2004).
4. D. Leibfried, M. D. Barrett, T. Schaetz, J. Britton, J. Chiaverini, W. M. Itano, J. D. Jost, C. Langer, and D. J. Wineland, *Towards Heisenberg-Limited Spectroscopy with Multiparticle Entangled States*, Science 304, 1476 (2004)

Neutral Atom Quantum Computation

Quantum information processing has applications to commercial information transmission, national security intelligence, and advanced device development through secure transmission, decryption, and modeling of quantum systems. We are developing the tools to use neutral atoms as qubits for quantum processing. Optical lattices and optical tweezers are to be used for storage as well as manipulation and processing of the atomic qubits.

William D. Phillips and James Porto, PL
(842)

Quantum information stores and manipulates qubits, which differ fundamentally from the ordinary bits of familiar, classical information. While ordinary information bits can be zero OR one, qubits can be both zero AND one, at the same time in quantum superposition. The possibility of entangling many qubits gives quantum processing a computational power that is exponentially greater than that of classical computing for some problems. For example, the factoring of large integers is a famously hard problem. The time to factor grows as an exponential of the size of the number, so that as far as anyone knows no present or conceivable classical computer could factor a very large number in any reasonable time. By contrast, a large scale quantum computer, if made, could factor numbers, using Shor's algorithm, in polynomial time.

The difficulty of factoring numbers ensures the security of public-key encryption schemes, so the possibility of easy factoring impacts commercial communication as well as national intelligence. Another side of quantum information is that transmission of information as qubits guarantees that the message cannot be intercepted without it being evident to the communicators. Small quantum processors would provide the capability of making quantum repeaters to enable quantum secure transmission over long distances. Finally, quantum information processing allows the efficient simulation of quantum devices that are exponentially difficult to simulate on a classical computer. This would provide an important tool for the design of new devices, and understanding of solid-state systems.

We intend to use single Rb atoms as qubits, with the internal hyperfine states of the atoms being the qubit states. The atoms are first laser cooled to microkelvin temperatures, trapped and further cooled so as to undergo Bose-Einstein condensation, then held in an opti-

cal lattice, (an array of optical microtraps formed by intersecting laser beams) that can hold single atoms at single, addressable locations. Optical tweezers, (single focused laser beams) will move atoms from one location to another, allowing collisional interactions that will entangle the atoms and effect the quantum computation.

So far, we have produced large arrays of atoms, demonstrated the confinement of single atoms on single lattice sites, developed a superlattice method for tightly confining the atoms while keeping them separated by enough to allow individual optical addressing, and demonstrated the ability to move the atoms in a state dependent manner. We are collaborating with an international group of researchers on the theory of realizing atomic quantum processors, and on optical tweezer manipulation, rapid entanglement processes, and the conversion of information from photons ("flying" qubits used for information transmission) to atoms (material qubits used for information processing).



Figure 1. The time-dependence of the diffraction pattern of atoms released from an optical lattice reveals the fidelity of putting atoms into the motional ground state of the individual lattice-site optical traps. The near-constancy of the pattern in time shows that "adiabatic" loading has better than 99.5% fidelity, while deliberately nonadiabatic loading results in a strong time dependence.

Polymer Miscibility of Imidazolium Compatibilized Nanotubes

The conductivity, strength, toughness, and flammability properties of polymers may all be substantially improved by the addition of carbon nanotubes (CNTs). However, the effective utilization of CNTs in nanocomposite applications may depend on the ability to homogeneously disperse them into the polymer matrix. Furthermore, extensive interfacial interaction is required to achieve load transfer across the CNT-polymer interface, to prevent reaggregation during subsequent processing, and to enable other enhanced properties in the nanocomposite. Nanotubes preferentially aggregate into bundles, where adjacent tubes are held together by strong van der Waals attractions.

Jeffrey Gilman, BFRL (866)

One approach to achieving good dispersion of nanotubes in polymers is to take advantage of van der Waals interactions between the aromatic surface of the CNT and compatible hydrocarbon groups on a surfactant. For many applications, this non-covalent compatibilization approach may be a more facile and practical processing method than the alternative, which is to introduce covalently bonded functional groups on the ends and sidewalls of the CNT's. Up to now, two types of surfactants have been studied: non-ionic surfactants used with organic solvents for dispersion in epoxy resins, and ionic surfactants, such as sodium dodecyl sulfate (SDS), which can be used with water soluble polymers. Unfortunately, SDS undergoes acid hydrolysis at 40 °C and has an onset temperature for decomposition of 190 °C; these properties limit its use for melt blend processing, since most polymers are melt processed at 200 °C or above. We have demonstrated that imidazolium salts are excellent cationic treatments for layered silicates (clays); they enable high temperature curing and melt processing of polymer clay nanocomposites due to their high thermal stability and excellent polymer compatibility when one of the imidazolium alkyl groups is a C-16 aliphatic chain. In addition, we have also been investigating the use of imidazolium intercalated graphite to prepare polymer graphite nanocomposites. In this project, we are extending this approach to the study of the miscibility of imidazolium treated nanotubes in commodity polymers. The effect of adding 0.5 % (mass fraction) 1,2-dimethyl-3-hexadecylimidazolium tetrafluoroborate (DMHDIIm-TFB) to PS/CNT is shown in Figure 1. In the TEM image on the left very few unaggregated CNTs can be ob-

served; instead nanotube agglomerates ($\approx 1 \mu\text{m}$) dominate. In contrast, when DMHDIIm-TFB modified CNTs are used, well dispersed single nanotubes can be observed in the TEM (right).

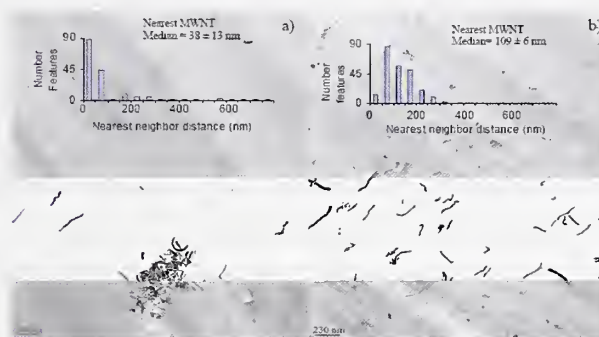


Figure 1. a) TEM images of PS/MWNT (without DMHDIIm) and b) PS/MWNT (1:1) DMHDIIm TFB.

Figure 1. a) TEM images of PS/MWNT (without DMHDIIm) and b) PS/MWNT (1:1) DMHDIIm TFB.

In the process of investigating new approaches to compatibilize nanoadditives, such as clays and nanotubes, to polymers, we have also developed several techniques for monitoring and measuring the degree of dispersion achieved. A laser scanning confocal micrograph of a polystyrene/nanotube nanocomposite is shown in figure 2. A fluorescent dye was blended in the polymer matrix, but the fluorescent intensity is quenched in the vicinity of the nanotubes. Thus, by measuring the spatial variation of the fluorescent intensity we can determine the degree of dispersion of the CNTs in the polymer matrix.

New Materials to Protect Firefighters from Burn Injuries

Firefighters are being seriously burned and fatally injured while wearing their protective clothing system. Nanocomposite fabrics may have the ability to dissipate heat energy away from the skin and protect against burn injury.

Jeffrey Gilman and Kuldeep Prasad, BFRL (866)

Calculations of thermal performance of protective clothing, using a model developed at NIST, have demonstrated that fabrics with unidirectional heat conduction properties have the potential to protect firefighters from serious burn injuries (Figure 1).

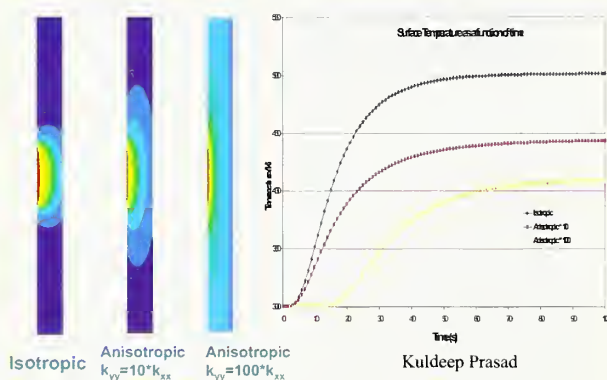


Figure 1. Surface temperature as a function of time.

Estimates of the thermal properties of carbon nanotubes (CNTs) indicate that the ratio of the thermal conductivity along the axis to that across the diameter of the nanotube may be as much as to five orders of magnitude (Table I).

Table I. Comparison of Thermal Conductivity

Material	Thermal Conductivity (W/mK)
CNT	2500 - 37000
graphite	100 - 200
polymers	0.01 - 20

Unfortunately, our preliminary results, obtained using infrared imagery, have indicated that fabrics made from polymer/nanotube composites (containing on the order of only a few percent nanotubes) do not possess the requisite properties to prevent the formation of local hot spots; presumably because the exchange of thermal

energy between the polymer matrix and nanotubes is ineffective (right hand side of Figure 2). On the other hand, our experiments indicate that materials consisting predominately of aligned carbon nanotubes can provide the necessary unidirectional thermal conductivity (left hand side of Figure 2).

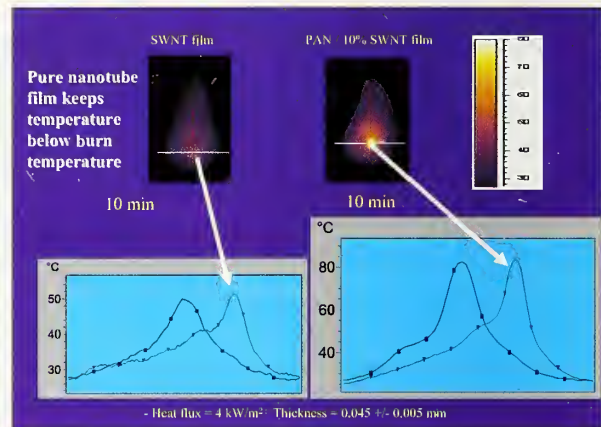


Figure 2. Comparison showing the effect of alignment of carbon nanotubes on unidirectional conductivity

We will use our imidazolium based ionic liquids to prepare nanotube liquid crystal solutions and a highly aligned, naturally occurring polymer (silk) as a spinning dope to prepare nanotube fibers. The general idea is to compatibilize the nanotubes to the silk using the imidazolium treatment developed in our laboratory so that the nanotubes and silk are blended within the fiber structure. The silk will give the flexibility to the thermally conductive nanotube phase in the fiber. Our expectation is that this will allow us to increase the nanotube content of the fibers to the point where a significant enhancement in thermal conductivity can be achieved. We will also investigate the possibility of using -OH and -NH₂ functionalized nanotubes to improve compatibility and, thereby, to enhance the efficiency of thermal energy exchange between the nanotubes and the silk. Once we have perfected the technique for making macroscopic fibers from carbon nanotubes, we will prepare several samples for testing on BFRL's firefighter mannequin. The test materials will be placed on problem areas (where the fabric is forced to bend or crease to conform to the shape of the body) of the mannequin and the temperature distributions will be determined from quantitative analyses of images obtained from IR photography.

Characterization and Photoreactivity of Titanium Dioxide Nanostructures

There is a wide range of photoreactivity observed in TiO_2 nanostructures, depending on the method of preparation. At present, it is difficult to control the photoreactivity of these materials since the properties controlling photoreactivity are not well understood. To compensate for this lack of predictability, each industrial user of TiO_2 has developed qualitative or at best, semi-quantitative methods, to evaluate photoreactivity. Project objectives are to obtain a comprehensive understanding of the fundamental properties and mechanisms controlling TiO_2 photoreactivity using an integrated metrology and scientific approach with facilities and expertise unique to BRFL and NIST.

Stephanie Scierka and Joannie Chin, BFRL (861)

Background

High volumes of semiconductor metal oxides such as titanium dioxide (TiO_2) are utilized each year as fillers and UV absorbers for building materials such as paints, sealants and bulk plastics. A common issue shared by each of the abovementioned applications is that their service life and durability is affected by the photocatalytic properties of these semiconductor metal oxides. This property of TiO_2 nanostructures can also be exploited to deliberately destroy harmful organic materials, such as viruses, bacteria and toxic chemicals.

The major impact of this research would be to establish quantitative, scientifically based techniques for the measurement of photoreactivity in TiO_2 and other semiconductor nanomaterials.

Approach

Techniques for the measurement of photoreactivity that will be developed and investigated in this program include the following:

- Photoconductivity
- Electron Paramagnetic Resonance (EPR)
- Chemical assays and probes, including methyl viologen, horseradish peroxidase and isopropyl alcohol.

Each of these techniques yields specific information on each of the three primary processes in a photocatalytic reaction, which are (a) photo-induced charge carrier

generation in the semiconductor, (b) interfacial charge transfer to surface species on the surface of the semicon-

ductor, and (c) reaction of charge carriers and activated species with adsorbed materials on the semiconductor surface. Information obtained using each of these analytical techniques will contribute toward a more comprehensive understanding of the entire photoreactive process.*

Another thrust in this program involves the characterization of the surface physical and chemical properties of the nanomaterials themselves, particularly that which affects the adsorption of and subsequent reactivity of the nanoparticles with reagents.

Results

An industrial workshop was held in October 2004 with representatives from the coatings, polymers, catalysis, and TiO_2 manufacturing sectors. The workshop discussion highlighted the needs of each industry and resulted in a general proposal to develop a test for both durable and catalytic materials that produces a rating for photocatalytic activity on raw materials. It was determined that each industry would work to develop an industry-wide *performance test*, specific to each application. Experimental results to date show there are differing mechanisms for specific TiO_2 nanoparticles and appear to depend on the method of analysis used. Work is continuing.

Photoconductivity: The measured conductance of a TiO_2 nanostructure film increases upon ultraviolet (UV) exposure. The extent of the increase in conductance depends upon the TiO_2 nanoparticle and surface treatment. Calcination of the TiO_2 nanoparticles caused a decrease in the measured conductance. An optimum amount of humidity is necessary for maximum conductance.

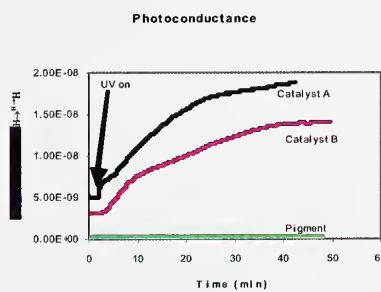


Figure 1. Photoconductance of TiO_2 nanoparticles upon UV irradiation.

Assays: A methyl viologen assay was used to moni-

tor the photoreactivity of several TiO_2 nanomaterials. These results were unlike that obtained from a horseradish peroxidase assay, which measures the peroxide concentration. It appears that the production of peroxide does not correlate directly with electron and hole production. Further interpretation of the results is underway.

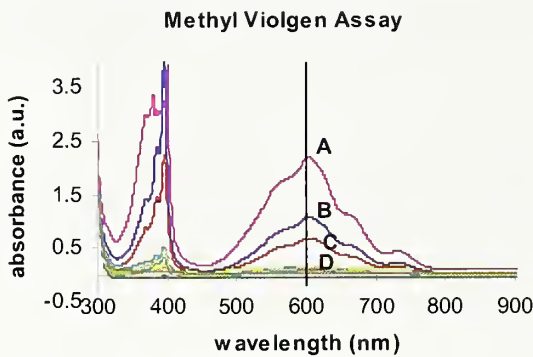


Figure 2. Methyl viologen assay for a series of TiO_2 nanomaterials. The photoreactivity is measured at 602 nm.

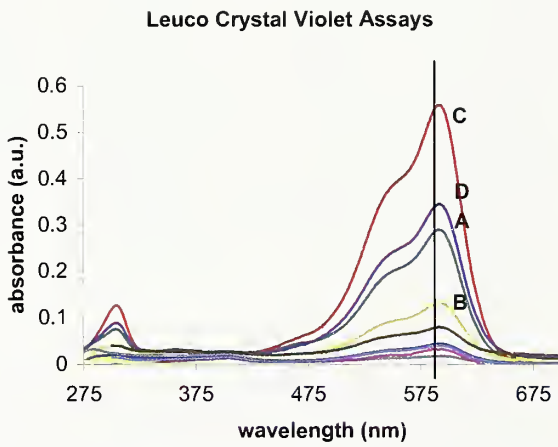


Figure 3. Horseradish peroxidase assay for a series of TiO_2 nanomaterials. Peroxide concentration is measured at 590 nm.

EPR: EPR spectroscopy measures free radicals and their concentrations. Our current experiments are using nitroxide spin traps to titrate the free radicals generated in aqueous TiO_2 suspensions exposed to UV irradiation. Given spin traps are reported to monitor specific free radicals. Preliminary results show that spin traps can follow free radical generation and that free radical generation does vary with TiO_2 nanomaterial. Each spin trap appears to be measure a different free radical or set of free radicals as the shown by the change in the decrease in concentration for given TiO_2 nanomaterials. Experiments are continuing.

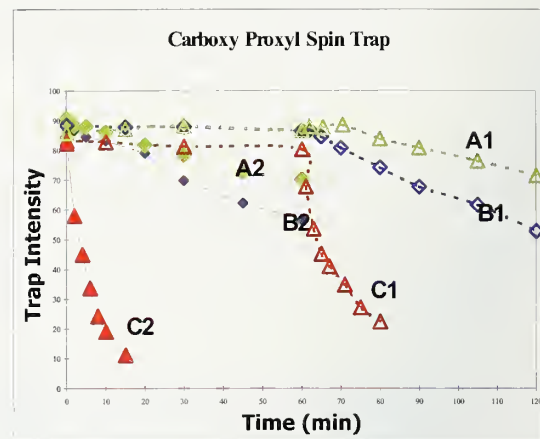


Figure 4. Carboxy proxyl spin trap concentration in TiO_2 suspensions as a function of UV irradiation time.

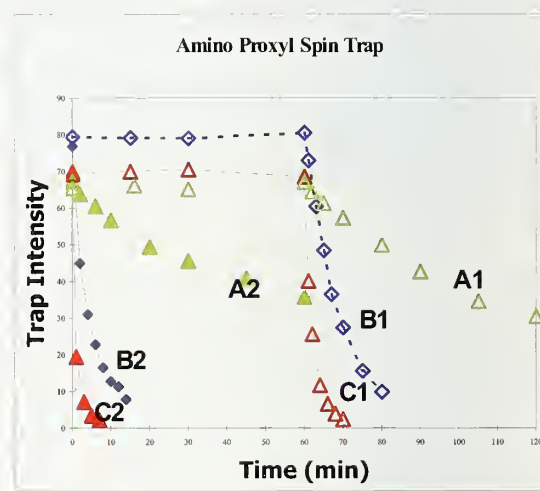


Figure 5. Amino proxyl spin trap concentration in TiO_2 suspensions as a function of UV irradiation time.

Optical Properties of Carbon Nanotubes

The goal is to establish the next generation of standards for optical power measurements at NIST (and elsewhere). The science: to lower barriers to identification of tube size, spacing, species and dielectric function of carbon nanotubes (preferably by rapid, inexpensive, optical techniques).

John Lehman, EEEL (815)

Our group helps industry, defense, and the medical community use lasers safely and cheaply. We have demonstrated the first thermal detectors coated with carbon nanotubes and, in collaboration with the National Physical Laboratory (NPL), measured relevant detector properties for building the next generation of standards for laser power and energy measurements at NIST and elsewhere. Figure 1 depicts a pyroelectric detector coated with carbon single-wall nanotubes (SWNTs). This detector is the first of its kind and allows us to directly measure the optical and thermal properties of various tube compositions and topologies. We have also built the first detectors coated with carbon multiwall nanotubes (MWNTs) grown on the detector platform. Related to this work, we have shown qualitative results for cleaning SWNTs by laser vaporization, and begun fabrication of MWNT-coated coupons for emissivity measurements with the National Institute of Advanced Industrial Science and Technology (AIST).

We have provided pyroelectric detectors to NPL for evaluation of detector properties from $0.8 \mu\text{m}$ to $14 \mu\text{m}$. In collaboration with AIST, we have undertaken measurement of blackbody emissivity at 300 K of MWNT nanotube samples. This work is relevant to optical and thermal properties of CNTs in general, and specifically to the design of robust blackbody emitters. We have undertaken UV-laser damage cleaning studies of SWNT samples for the design of radiometer and thermal detector absorbers. In the past year we have generated three publications (see below) and presented our work at the Conference on Lasers and Electro Optics (CLEO), as well as NSF and NASA workshops.

Thermal-detector coatings based on CNTs will resist damage and aging at shorter wavelengths and higher power and energy. Resistance to aging is particularly important at UV wavelengths, where we plan to support calibration of blue and UV laser sources and detectors for applications such as high resolution DVD and chemical and biological agent detection systems. We have worked collaboratively with NPL, AIST, and NREL and

established ourselves among the leaders in this developing field. Applications range from laser-based manufacturing tools to semiconductor lithography to healthcare and laser surgery.

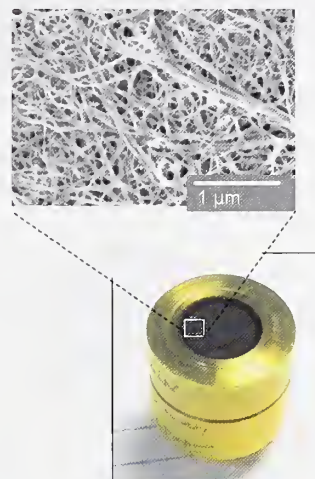


Figure 1. A pyroelectric detector coated with carbon single-wall nanotubes (SWNTs).

Selected Publications

1. J. H. Lehman, C. Engtrakul, T. Gennett, A. C. Dillon, "Single-wall carbon nanotube coating on a pyroelectric detector," *Appl. Opt.*, **44**, 483-488, (2004).
2. J.H. Lehman, R. Deshpande, P. Rice, B. To, A.C. Dillon, "Carbon multi-walled nanotubes grown by HWCVD on a pyroelectric detector, *Infrared Physics and Technology*, in press, accepted Dec 04.
3. A. C. Dillon, A.H Mahan, J. L. Alleman, K.M. Jones, S-H. Lee and J.H. Lehman*, "Hot-wire Chemical Vapor Synthesis for a Variety of Nanomaterials with Novel Applications," *Thin Solid Films*, in press, accepted Dec 04.

Characterization of Single-Walled Carbon Nanotubes

Raman spectroscopy is a powerful tool for the characterization of carbon nanotubes. Phonons, in particular the one corresponding to the radial breathing mode, are now used routinely to determine the diameter of the nanotubes. The resonant character of these modes can be employed to extract the nanotubes chirality. These informations allow a determination of the semi-conducting and metallic properties of the carbon nanotubes.

Angela R. Hight Walker, PL (844)

The multibody effects in the optical spectra of single-walled carbon nanotubes (SWCNT) were investigated by means of resonant Raman spectroscopy. Resonance enhancement of the Raman scattering intensity of the radial breathing mode in SWCNTs is used as a probe of tube diameter and of one-dimensional electronic structure. The newly constructed, confocal magneto-Raman microscope at NIST permits continuously tunable laser excitation from the NIR to the UV. The novel Raman facility consists of a microscope capable of working over a wide range of temperatures ($T = 4.2\text{-}300\text{ K}$) and magnetic fields ($H = 0\text{-}8\text{ T}$) coupled to a triple grating spectrometer with ultimate Raleigh rejection capabilities, thereby permitting low-frequency or Terahertz Raman spectroscopy. From such measurements we have obtained the direct optical transition energies involved in the resonant process. We observe that the measured resonance energy

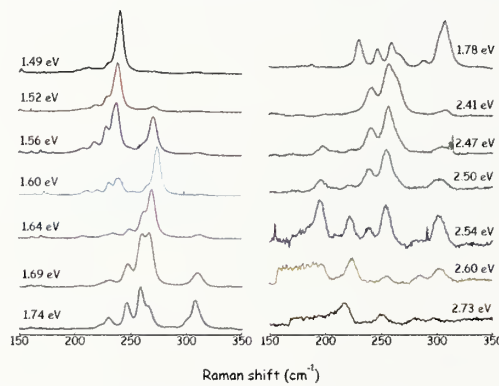


Figure 1. The resonant dependance of the radial breathing mode of SWCNT.

for these modes deviate from the optically-allowed interband transitions predicted by calculation of the single-particle electronic excitations. These results are interpreted as arising from excitonic effects in the resonant Raman scattering of single-walled carbon nanotubes. Our initial investigations were carried out on isolated

and bundles of single-walled carbon nanotubes. We have demonstrated single nanotube sensitivity by resonant enhancement of the Raman scattering from the radial breathing mode.

Measurements are underway to examine the temperature dependence of these Coulomb interactions. The response of the carbon nanotubes with different diameters was observed by varying the incident laser wavelength and as a function of temperature. We observed a temperature dependence of the optical interband transitions in carbon nanotubes that is consistent with theoretical prediction.

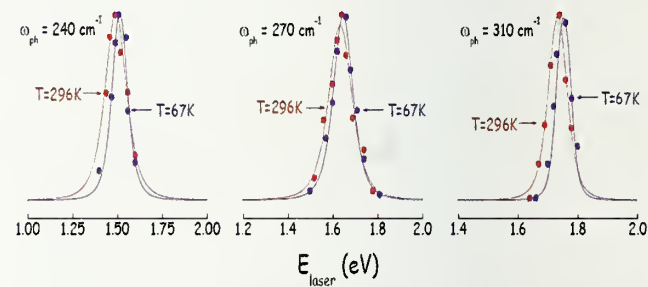


Figure 2. Temperature dependance of optical interband transition.

For future work, we plan to develop the capability to routinely use optical spectroscopic techniques for the characterization of carbon nanotubes. We will continue our exploration of the temperature and magnetic field dependence of the resonant Raman scattering in bundles of carbon nanotubes. We shall extend this to isolated carbon nanotubes to identify those properties that are intrinsic to the carbon nanotubes and those that result from interaction between nanotubes. Diameter-selective DNA-wrapped carbon nanotubes will also be investigated. The use of photocurrent spectroscopy to complement the resonant Raman spectroscopy in probing the one-dimensional electronic structure of the nanotubes will be explored. This latter technique will also find potential applications in the studies of carbon nanotube-base optoelectronic devices.

Stability of Nanowires

Metallic or semiconductor nanowires are important components in many electronic technologies. At small length scales many materials exhibit unusual electrical, chemical, and thermal properties that are not observed in the bulk. Applications include novel electronic devices ranging from high efficiency lasers and detectors to exotic single electron transistors and cellular automata. The tendency of nanowires to fragment into nanospheres due to area-minimizing surface instabilities acts as a limit to the length of nanowires that can be used in nanodevices. This instability can also be used beneficially as a mechanism for the self-organization of chains of nanospheres from unstable nanowires. We have studied analytically the effect of surface tension anisotropy on this instability in order to help understand and control nanowire fragmentation. Our analysis predicts the wavelengths of the instability as a function of the degree of anisotropy of the surface energy of the nanowire.

Geoffrey B. McFadden, ITL (891)

At the small length scales that characterize nanostructures, the importance of surface effects relative to volume effects becomes significant. Typical surface effects that can be important at the nanoscale include surface energy or capillarity, surface diffusion, surface adsorption, and surface stress and strain. In particular, the effects of capillarity must be taken into account in order to understand the tendency of nanowires to fragment when the rate of surface diffusion of atoms is high enough to allow shape changes to occur over practical time scales.

As shown by Plateau in his classical studies of capillary instabilities, a cylindrical interface with an isotropic surface free energy is unstable to volume-preserving axisymmetric perturbations whose wavelength exceeds the circumference of the cylinder. Such perturbations lower the total energy of the cylinder, leading to the breakup of the cylinder into a series of drops or bubbles. The stability of a liquid jet was subsequently studied by Lord Rayleigh, who argued that the length scale of the instability is determined by the perturbations having the fastest growth rate; the phenomenon has generally come to be known as the Rayleigh instability. The Rayleigh instability arises in a number of diverse applications, such as ink jet printing, two-phase flow, quantum wires, fiber spinning, liquid crystals, and polymer blends.

Because of the underlying crystal lattice, the surface

energy of a liquid-solid or vapor-solid interface is generally anisotropic and depends on the orientation of the local normal vector at each point of the interface. The surface energy of a solid-solid interface between two crystals is also anisotropic in general, with the additional complication that the surface energy also depends on the direction cosines that characterize the relative orientations of the two crystals. Here we have considered a model of this type in which the surface energy depends only on the local normal vector.

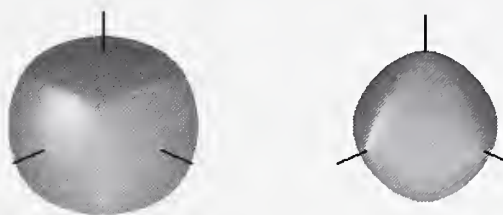


Figure 1. Equilibrium shapes for materials with cubic anisotropy. These shapes are energy minimizing surfaces that are the anisotropic versions of soap bubbles (the isotropic case).

An observation that partially motivates this work is the apparent stability of elongated nanowires that are grown in a bridge configuration or epitaxially on a heterogeneous substrate. The nanowires (alternatively called nanorods or quantum wires) are “one-dimensional” crystals with dimensions as small as one nanometer high, a few nanometers wide, and can be as long as a micron. There are long-standing studies on experimental techniques to grow nanowires, and the stability of these nanowires is beginning to come under study. Another motivation for the work is the recent observation that the Rayleigh instability of a nanowire can be used to produce self-organized chains of nanospheres with interesting electrical and opto-electronic properties. In either case it is desirable to develop models to predict the length scales of the instabilities in order to assess the geometry of the resulting structures.

Continuum modeling of nanowires provides some guidance as to their expected stability, though the strict applicability of continuum models is limited if the length scales approach atomic dimensions. There are a number of possible mechanisms that could stabilize a nanowire, including elastic interactions between the wire and the substrate, quantum electronic shell effects, and surface energy anisotropy. A useful model of the surface energy anisotropy for a cubic material is given by the expression $\gamma(n_x, n_y, n_z) = \gamma_0 [1 + 4 \epsilon (n_x^4 + n_y^4 + n_z^4)]$. In the above figure we show examples of 3D equilibrium shapes cor-

responding to this surface energy. The shapes are smooth for $-1/18 < \varepsilon < 1/12$. For $\varepsilon < 0$, the shapes resemble rounded cubes, with [110] edges first forming at $\varepsilon = -1/18$. As ε decreases below $-1/18$, the edges extend toward the [111] directions, merging to form a corner for $\varepsilon = -5/68$. For $\varepsilon > 0$ the shapes are octahedral, with [100] corners first forming at $\varepsilon = 1/12$. These equilibrium shapes are most easily computed using the ξ -vector formalism of Hoffman and Cahn, which produces a closed-form expression for the equilibrium shape in terms of the surface energy. This is also useful in formulating the variational problem for the stability of a nanowire.

We consider differentiable surface energies with anisotropies mild enough that the surface of the wire is smooth and does not exhibit any missing orientations. In order to examine the stability of the wire using a variational approach, we employ a general energy functional that describes the total surface energy of the system. This expression and the constraint of constant volume of the wire are perturbed about the two-dimensional equilibrium shape. The higher order terms in this perturbation expansion produce a condition for stability. For constant volume, if the perturbation increases the energy, the equilibrium state is stable, otherwise it is unstable.



Figure 2. Capillary instability of a nanowire with an anisotropic surface energy with three-fold symmetry about the wire axis.

For small levels of anisotropy, we evaluate the stability of an isolated nanowire approximately using asymptotics. For larger amplitudes of anisotropy, we compute solutions numerically. We find that surface tension anisotropy can either promote or suppress the Rayleigh instability, depending on the orientation of the nanowire and the magnitude and sign of the anisotropy. For general surface energies we derive an associated eigenproblem whose eigenvalues govern the stability of the wire. The eigenproblem is described by a pair of coupled second-order ordinary differential equations with periodic coefficients, which generally lack closed-form solutions. We have applied the analysis to a number of examples, including the above case of a cubic material. We have

computed the stability of the wire to general perturbations when the axis of the wire is in a high symmetry orientation such as [001], [011], or [111].

In addition to determining the stability of an isolated wire, we have also examined how both the anisotropy of the surface energy of the wire and the interaction of the wire with a substrate affects the stability of the rod. The equilibrium configuration of a wire in contact with a substrate has an elegant description that can be obtained by again appealing to the Hoffman-Cahn ξ -vector formalism. This approach determines the contact angles in terms of the surface energies of the phases that meet at the contact line. Using general anisotropic surface energies we have then derived an associated eigenproblem that describes the stability of the system. The problem is described by a pair of coupled second-order ordinary differential equations with periodic boundary conditions along the axis of the rod and boundary conditions arising from the contact angles between the wire and substrate. We have considered the effects of the overall orientation of the crystal relative to the substrate and examined a range of contact angles. The substrate is assumed to be rigid with an isotropic surface energy.

We applied the analysis to a number of examples, including the case of a cubic material, and compute the stability of the wire to perturbations when the axis of the wire is aligned parallel to the high symmetry orientations [001], [011], and [111]. We assumed a weak anisotropic surface energy to eliminate missing orientations on the wire. The magnitude and the sign of the anisotropy determine the relative stability in comparison to the isotropic case. In general as the contact angle tends to 90 degrees the wire becomes more stable, which is analogous to the stability of a 3D planar film.

Selected Publications

1. K. F. Gurski and G.B. McFadden, The Effect of Anisotropic Surface Energy on the Rayleigh Instability, *Proceedings of the Royal Society (London) A* **459** (2003), pp. 2575-2598.

Semiconductor Quantum Dot Structure Metrology

Self-assembled semiconductor quantum dots (QDs) continue to grow in importance in the optoelectronics marketplace. They have an atomic-like density of states that offers substantial opportunities for unique and improved devices. These include ultra-low-threshold laser diodes with low temperature dependence, semiconductor optical amplifiers with reduced cross-gain modulation and large bandwidth, and mid-wave and long-wave infrared photodetectors. However, there are many aspects of QD growth that are not well understood, in particular dot nucleation, dot size and shape, and the effect of capping the dots. The optical and electrical properties of the QDs and resulting devices depend strongly on the shape and composition. Control over nucleation sites would enable production of regular arrays of QDs. In addition, the lateral uniformity of dot density, which is important for device yield and performance, has not been investigated until now. We have measured many of these structural properties through nanoscale probing using atomic force microscopy (AFM) and transmission electron microscopy (TEM).

Alexana Roshko, EEEL (815)

We performed studies of the shape of InGaAs quantum dots grown on (001) GaAs substrates by molecular beam epitaxy (MBE). Samples were investigated by high resolution TEM and AFM. From cross-sectional TEM, we observed a shape transition for QDs \approx 8.5 nm in height. Dots less than 8.5 nm are pyramidal; taller dots are multifaceted, allowing accommodation of the increased volume without increasing the QD base length. While similar dots have been previously observed for both the InAs/GaAs and InGaAs/GaAs dots, the dot shapes found here do not fit any previous models for the dot facet planes, which we identified as nearly {111} planes. The addition of a 20 nm GaAs cap layer dramatically changed the dot dimensions, increasing the diameter of the dot base by factors of 3 to 5.

We have demonstrated that large lateral variations in dot density and height occur for InGaAs quantum dots grown by both MBE and metal-organic chemical vapor deposition (MOCVD). Atomic force microscopy was used to examine the density and height distributions of self-assembled QDs. AFM images were taken at a programmed array of points on the surface of 50 mm diameter wafers, and systematic analysis of the images was used to determine the average dot density and height

from each image. It was found that an image scan size of $3 \times 3 \mu\text{m}^2$ was optimal for measurements of QD density.

For dots grown by MBE, the standard deviation in dot density was found to vary from 15 to 30 % of the average dot density across the central $26 \times 26 \mu\text{m}^2$ region of the wafers. Investigations of the QD density found variations of up to 25 % for more local length scales on the order of micrometers. These density variations, on both the large and local scales, do not correlate with observable step edges on the sample. Nor do the large-scale variations appear to be due to non-uniformities in temperature, as differences of more than 15 °C across the wafers would be required to produce the observed variations. Also, the variations do not typically follow a concentric pattern across the wafers, as would be expected if they were due to temperature gradients. The standard deviation in dot height was 10 % or less of the average height, which was about 10 nm. Similar results were found for MOCVD-grown QDs. However, MOCVD samples were found to have broader distributions of QD size than those grown by MBE. The majority of MOCVD-grown dots are less than 5 nm in height, but there is a continuous distribution of larger dots, with heights up to 30 nm or more. Dots grown by MBE have nearly Gaussian size distributions and a maximum variation in height of less than 15 nm. An inverse relationship was found between the dot height and density distributions on several MBE samples, suggesting that a uniform distribution of QD material was deposited on the wafers, but that the nucleation of dots was non-uniform. We have also examined the influence of growth temperature, vicinal substrates, arsine partial pressure (in MOCVD), and wafer rotation rate (MBE) on the dot distributions.

The scientific community was surprised at the extent of the density non-uniformity of quantum dots across a wafer revealed by our studies. Work by others had concentrated on the variation in QD density as a function of growth conditions as measured on small specimens, held in the center of the MBE stage during growth. At least one research group made a change in the way they grow quantum dots as a result of our findings. The search for means to control the density and position of QDs remains a dominant theme in the industry, and is part of our further study.

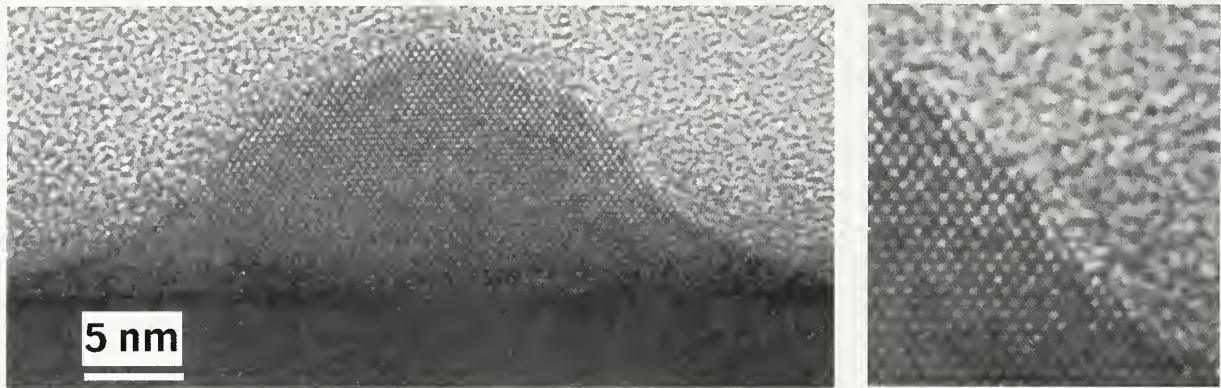


Figure 1. Cross-sectional TEM image of multi-faceted InGaAs/GaAs QD, grown at 540 °C. The entire dot is shown in (a) and a magnified section shows the sidewall facet in more detail in (b).

Selected Publications

1. A. Roshko, T.E. Harvey, S.Y. Lehman, R.P. Mirin, K.A. Bertness and B.L. Hyland, "GaAs Buffer Layer Morphology and Lateral Distributions of InGaAs Quantum Dots", submitted to J. Vac. Sci. Tech. B, 2004.
-

Chemistry and Structure of Nanomaterials

Successful nanoscale materials fabrication is empowered by a detailed knowledge of the chemistry and structure of surface bound molecules; e.g., the optimization of self-assembled monolayers, molecular templates, micro-electro-mechanical system lubricants, and functionalized nanotubes. We have developed Near-Edge X-ray Absorption Fine Structure (NEXAFS) spectroscopy techniques that are ideally suited to the non-destructive measurement of chemical bond concentration, rehybridization and orientation, with sub-monolayer molecular sensitivity in diverse nanoscale materials. Furthermore, NEXAFS can distinguish chemical bonding in the light elements, measure the orientation of interfacial molecules, and measure surface and bulk chemistry independently and simultaneously.

Daniel A. Fischer, MSEL (852)

Materials having low energy surfaces are used in many applications, for example, in non-wetting surfaces or marine coatings for fouling resistance. We have produced a photo-responsive polymer surface by combining the reversible photo-switching properties of azobenzene with the self-assembly behavior and low surface energy properties of semi-fluorinated segments to create a fluoroazobenzene molecule surface. Upon UV exposure, this surface switches between a hydrophobic and a less hydrophobic orientation, as shown in Figure 1 (left upper and lower panels). For such surfaces, one could imagine applications ranging from low cost surface patterning to polymer surfaces that would adsorb biological macromolecules on cue.

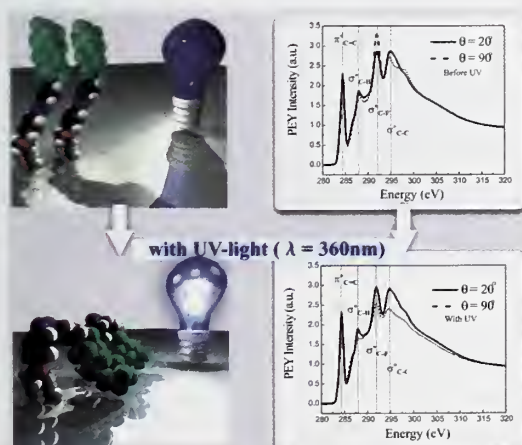


Figure 1. UV light reorients fluorobenzene semi-fluorinated segments (green) downwards, i.e., to a less hydrophobic state.

We have utilized NEXAFS to observe, verify, and quantify the reversible cis-trans molecular conformation transformation from hydrophobic to less hydrophobic states. The right panels of Figure 1 (upper and lower) show the polarization-dependent NEXAFS anisotropy behavior of the C-F and C-C peaks, which reverse with *in situ* UV light exposure, highlighting the reorientation of the semi-fluorinated segments.

Application of NEXAFS spectroscopy to the study of electronic structure and chemical composition is illustrated in Figure 2 for various chemically functionalized, single-walled carbon nanotubes. Upon peroxide functionalization, the C=C ring resonance is greatly diminished on extensive sidewall functionalization, indicating loss of extended conjugation and disruption of nanotube electronic structure. The C=O peak intensity is greatest for peroxide chemistry. NEXAFS spectroscopy supports a model of peroxide functionalization, shown in Figure 3.

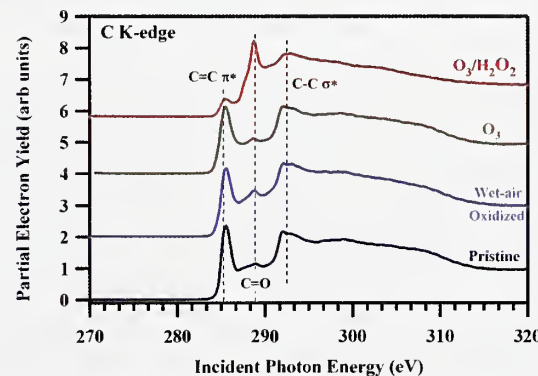


Figure 2. Carbon NEXAFS of oxidized / functionalized nanotubes

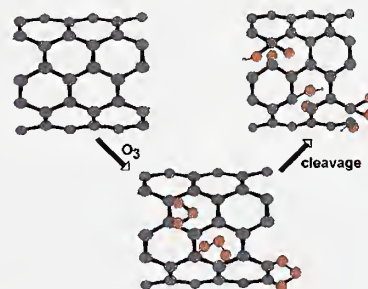


Figure 3. Model of peroxide functionalization of nanotubes.

Mechanical Metrology for Small-Scale Structures

Myriad industrial and biological systems are composed of small-scale structures for which the mechanical behavior is not accurately known. Optimizing the performance and reliability of these systems requires either mechanical property measurements on specimens of these structures harvested from the appropriate phases or interfaces of the system, or the ability to test these structures in situ. We have developed a standardized testing configuration and methodology for localized measurements of strength and fracture toughness of materials and interfaces at the micrometer to nanometer length scale.

Edwin R. Fuller, Jr. and George D. Quinn MSEI
(8520)

This project develops methodology to: (1) measure mechanical properties of microstructures for myriad industrial and biological systems that cannot be fabricated in bulk samples; (2) study small-scale mechanical phenomena that may be controlled by surface effects, e.g., the influence of surface stresses on crack nucleation and extension; and (3) obtain quantitative mechanical property data of materials and interfaces for designing small-scale structures and components and for assessing their mechanical reliability. To address these goals, well characterized testing configurations must be developed for small-scale measurements of strength and crack extension. We are pursuing three tasks: (1) specimen design and finite-element analysis; (2) specimen fabrication; and (3) mechanical testing and fracture analysis (fractography). Work in the Ceramics Division this year has focused on the first and third areas. Two collaborations were established in the fabrication task: one with James A. Beall of the Quantum Electrical Metrology Division (817) in NIST Boulder, and one with Northwestern University.

Significant progress has been made in the design of a compressively loaded test configuration with a well-defined, tensile gage section. Such a specimen can be loaded using a depth-sensing nanoindenter as a universal testing machine, thereby giving a record of both applied force and point displacement. One of these specimens, fabricated by James Beall from a silicon wafer by deep reactive ion etching (DRIE), is shown in the right side of Fig. 1. The configuration is similar to a theta specimen, except that the geometry is hexagonal. When a load (per unit thickness) is applied to the top beam, a uniform uniaxial tensile stress results in the middle gage section.

Finite element analysis gives (horizontal) gage section stresses on the order of 1.25 GPa for 50 mN/ μm of applied load. For a 2 N applied load, these 100 μm thick specimens generate 500 MPa of tensile stress in the gage section. The left side of Fig. 1 shows a reconstructed failed specimen. The insert shows the fracture surface of the gage section, and the two [111] cleavage facets that were formed. Alternate geometries, including a round theta specimen, have also been tested and modeled.

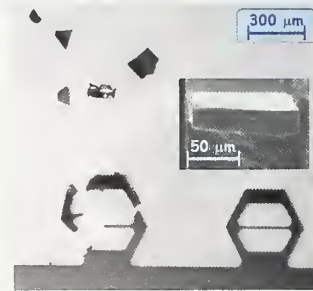


Figure 1: Prototype specimen design.

To extend this technique to a wide variety of materials and systems, general fabrication techniques are being developed. As an example, focused-ion-beam (FIB) milling, performed in collaboration with Northwestern University, has been used to produce hex specimens that are an order of magnitude smaller than the DRIE silicon. Figure 2 shows such a hexagonal theta specimen, fabricated by FIBing, of a lamellar, directionally solidified eutectic (DSE) of $\text{Ni}_{0.5}\text{Co}_{0.5}\text{O}$ and ZrO_2 . When applied to this type of system, the test method enables direct measurement of interfacial mechanical properties between the two DSE phases.



Figure 2: Hexagonal theta specimen of a DSE made by FIBing.

Highly Charged Ion Modified Materials

With the diminishing size of electronic device elements comes the increasing need to precisely and reproducibly control the transport properties of materials at the nanometer scale. This need is a consequence of the fact that the electronic properties of a single device element must be well matched to other components in order to be incorporated into a greater microelectronic circuit. The materials and systems that function at one size scale may not function at another. We are using highly charged ions to modify materials to create new composites in a way that allows us to tune spatial features and transport properties to values that lie in ranges not accessible with traditional materials.

Joshua M. Pomeroy and John D. Gillaspy, PL
(842)

The ability to precisely and reproducibly control the electronic transport properties of a material is paramount to its inclusion in any engineered device or system. It is natural then, that understanding and controlling the electronic properties of materials receives a great deal of attention from researchers in all branches of science. Examples of this need can be found in industries such as storage media where the size of hard drive read elements must shrink below 100 nm in dimension. At this nano-scale dimension, metallic devices have too low a resistance area (RA) product to be successfully incorporated into larger systems, while the RA product of oxide based tunnel junctions is too high. The RA product is a direct indicator of the ability of electrons to flow perpendicular to the plane of a given material. At the NIST Electron Beam Ion Trap (EBIT) Facility, we have designed a way to use highly charged ions (HCl) to create a new type of composite material with a tunable RA product.

Techniques using highly charged ions to create composite materials take advantage of the large damage zones that are localized on the surface. Damage zones from singly charged ions are due to the kinetic energy transfer to the lattice from many collisions distributed in a column that penetrates hundreds of nanometer into the bulk. When highly charged ions are used, a massive charge transfer occurs when the HCl is about 1 nm above the surface, creating a very high density of electronic energy on the surface. This energy disrupts the equilibrium of the lattice and a damage zone is created.

The characteristic properties of the individual damage zones determine the properties of the composite material, and are dependent on the material system, kinetic energy, and ion charge state.

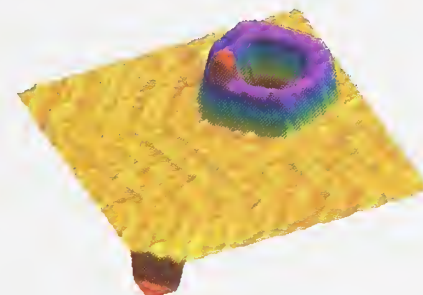


Figure 1. An STM image of a 25 nm feature created on a gold surface with a highly charged xenon ion.

In order to understand the properties of the individual damage zones, we have studied the variation of damage zones on different materials systems as a function of ion kinetic energy and charge state. For example, a feature created by a single xenon HCl on a gold surface is found to displace several thousand of times its own mass (Figure 1). Features of this type provide unique opportunities to study quantum behavior of nanometer sized features critical to efforts in quantum computing and quantum optics without expensive low-yield nano-fabrication techniques.

Immediate technological impact can be achieved by exposing multilayers to HCIs, tuning the size of the damage zones (by controlling charge state) to control transport between the layers. Using data collected from studies of individual damage zones, we have modeled selected materials systems and found that by using carefully selected material-ion combinations, composite materials with tunable electrical transport can be created and easily integrated into existing technologies. Experiments are currently underway to demonstrate this capability by developing a composite material with a tunable RA product, an immediate need for the high-density magnetic storage industry.

Nanoscale Metrology of III-Nitride Semiconductor Films and Nanowires

The III-nitrides comprise the only known semiconductor material system that will enable the development of electrically pumped blue-UV lasers and LEDs. These optoelectronic devices are vital components of systems for a wide range of applications including solid state lighting, detection of chemical/biological agents, cancer diagnoses, and water decontamination. Rf telecommunications and electric power distribution also benefit from the robust nature of III-nitrides to withstand high electrical power and high temperatures. In spite of the promise of these materials, there are complicating issues concerning the impact of nanoscale defects, strains, and phase segregation on their electrical and optical behavior and overall device efficiency. Interestingly, the wide bandgap semiconductors are one of the few instances of a material system where device applications and strong economic demands have emerged even though there is limited understanding of the fundamental structural and electronic properties responsible for their successes. In particular, progress in blue-UV laser development is hindered by the fact that 2D epitaxial growth of III-nitride structures is accompanied by a high density of nanoscale structural imperfections and defects. On the other hand, one-dimensional III-nitride nanowire crystals (50-100 nm in diameter, micrometers to tens of micrometers in length) have recently been shown to exhibit exceptional structural purity and extremely low defect density. Even with the improved crystalline properties that the III-nitride nanowires offer over their thin-film 2D counterparts, the nature of these nanowires makes them extremely challenging to characterize and to fabricate into useful devices. To optimize these materials (2D films and 1D nanowires), this project develops and applies correlated metrology methods to examine the interplay of spectroscopic, structural, and compositional effects on the nanoscale.

Norman Sanford and John Schlager, EEEL
(815)

Due to nonradiative recombination mediated by defects, the external quantum efficiency of LEDs is relatively low. It must be increased for III-nitride technology to truly impact global conversion to solid state lighting. Furthermore, InGaN is a uniquely quantum system

whereby the insolubility of indium results in precipitates of nanocrystalline inclusions of InN that exhibit quantum confinement. These naturally occurring ‘quantum dots’ are thought to be responsible for luminescence and lasing action, *not* the composition of the material. Therefore, understanding the local phase segregation, the composition dependence on InN dot radii, the interaction of carriers with defects and piezoelectric effects, and the pathways of radiative and non-radiative recombination processes are the key issues in optimizing LEDs and lasers.

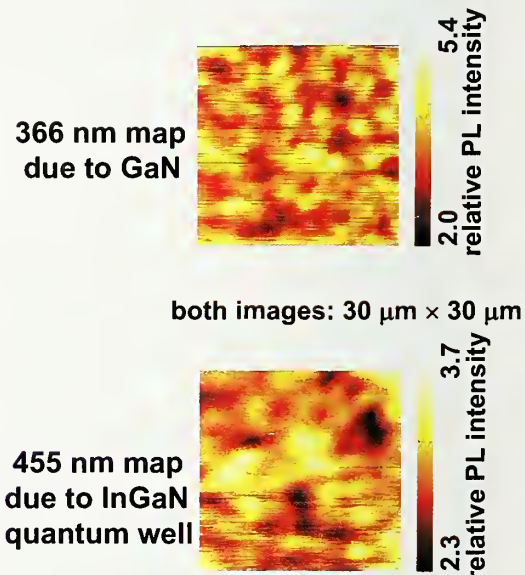


Figure 1. Multiphoton NSOM PL image of buried InGaN quantum well and surrounding GaN.

We developed two complementary techniques for optically probing nanoscale features in III-nitride layers and nanostructures: near-field scanning optical microscopy (NSOM) and confocal photoluminescence spectroscopy, both implementing multi-photon pumping. Multi-photon luminescence (MPL) spectroscopy offers a means by which the uniformity of an active, buried layer, e.g. a quantum well in a laser or LED structure, can be probed regardless of the thickness of the surrounding layers. Standard direct above-bandgap photoluminescence (PL) spectroscopy is problematic since the pump beam could be absorbed elsewhere in the structure before exciting the regions of interest. Using MPL spectroscopy, with ultrafast pumping for photon energies near or above midgap, even embedded structures may be examined, since the surrounding layers are transparent to the pump.

The intense optical field of the ultrafast pump pulses near 800 nm wavelength enables electrons to be promoted to the conduction band via virtual state processes. Subsequent relaxation to the valence band, possibly also involving exciton, donor, acceptor, or defect levels, yields the luminescent output. The NSOM uses a “look through” geometry whereby the pump beam is focused through the bottom of the sample substrate. For data collection, the relative positions of the pump beam and the tapered fiber tip are held constant while the sample is transversely scanned between them. For the present NSOM tips used (tapered UV-transparent optical fibers with aluminum apertures), the spatial resolution is roughly 100 nm. Significant spatial fluctuations (~50%) in the photoluminescence (PL) signatures from both In-GaN (near 400 nm wavelength) and the surrounding GaN (near 360 nm) layers were observed. The PL fluctuations from these two layers (at these two distinct wavelength bands) of the sample are uncorrelated. Follow-up metrology, including correlated cathodoluminescence scans over the same targeted scan areas, is in progress to help pin down the sources of the PL fluctuations.

Multi-photon confocal spectroscopy (MPCS) was also developed in our laboratory, enabling us to probe material samples at cryogenic temperatures and measure the temporal decay of the PL, two features not possible in the NSOM configuration. The spatial resolution of the confocal spectroscopy system is roughly 250 nm or better. Furthermore, the high numerical aperture optics used with MPCS offers high optical throughput and the ability to separately scan depth-resolved spectra. The combination of NSOM with MPCS allows correlation of spatially resolved, time-resolved, and low-temperature spectroscopy to aid in identification and understanding of defects, strains, and alloy fluctuations in both 2D and 1D semiconductor structures.

Wide bandgap semiconductors offer revolutionary improvements to the global utility infrastructure, since adoption of solid state lighting technology by 2025 could reduce by 50% the world’s usage of electricity for lighting, reduce global power consumption by 10%, and vastly reduce power plant emissions and environmental pollutants. The advent of high-purity 1D structures in these materials is also opening up possibilities for entirely new optoelectronic and electronic device applications. The economic and societal impact of a more thorough understanding of nanoscale effects can thus be enormous through the leveraging of increases in device efficiency and consequently reduced time to widespread adoption of solid state lighting.

Selected Publications

1. N. A. Sanford et al., “Fabrication and analysis of GaN nanorods grown by MBE,” *phys. stat. sol. (c)*, DOI 10.1002/pssc.200461602 (2005).
-

Mathematical Modeling of Nanomagnetism

Measurement, understanding, and control of magnetic phenomena at the nanoscale each require the support of mathematical models of the physics involved, and software that correctly implements and makes predictions based on these models. The Object-Oriented MicroMagnetic Framework (OOMMF) project provides this capability in a public domain package of portable software components organized in an extensible framework. OOMMF software is widely used and cited in the physics and engineering literature. Current objectives are to continue to expand the features supported by components in the OOMMF framework, with focus on high priority items, such as thermal effects and spin transfer, motivated by their relevance to nanoscale sensor and spintronics work.

Michael J. Donahue and Donald G. Porter, ITL
(891)

Many existing and developing applications of nanotechnology make use of the phenomena of magnetism at the nanoscale. Some of the most familiar and successful examples are technologies widely used by the information storage industry such as magnetic recording media, GMR sensors for read heads, and magnetic RAM (MRAM) elements. Mathematical modeling and computational simulation continue to support advances in information storage technology such as the advanced patterned magnetic recording media that promise to achieve recording densities of 1 Tb per square inch.

Nanomagnetism modeling is playing a role in other nanotechnology efforts as well. For example, modeling was critical to the development of a fully magnetic logic gate and shift register was accomplished at University of Durham and recognized by the Institute of Physics as one of the top ten stories in physics for 2002. Other efforts aim to develop logic and information processing devices that carry information in the form of the spin of a charge carrier, so called *spintronics* devices. In biotechnology, the use of paramagnetic beads to locate and position biological macromolecules is under study. In materials science, the probing capability of ferromagnetic resonance is used to characterize and measure material properties, where a model-based understanding of nanomagnetodynamics is a key to interpreting experimental results. Also relevant to materials science is the effort to develop improved sensor designs capable of detecting magnetic fields that are both smaller in magnitude and more localized in space.

In each of these areas, the NIST Object-Oriented MicroMagnetic Framework (OOMMF) system is in use to enable nanoscale science and engineering. OOMMF is a public domain package of portable software components organized in an extensible framework to enable computational simulation of magnetic systems.

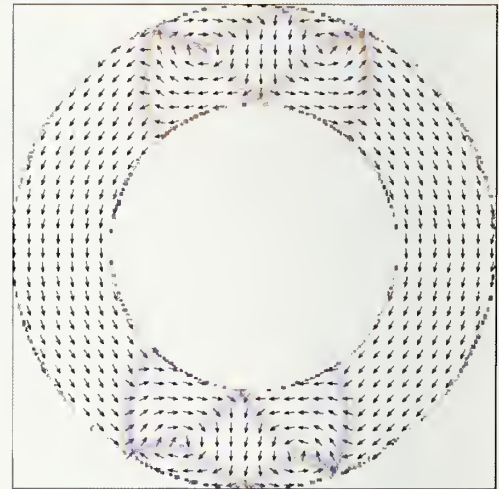


Figure 1. Top: Image of 2000 nm diameter ring of ferromagnetic material produced by a magnetic force microscope. Bottom: Magnetization pattern computed by OOMMF based on known parameters chosen to match the experimental work

One recent example of the use of OOMMF to support nanotechnology R&D is depicted in Figure 1. An image of 2000 nm diameter ring of ferromagnetic material was produced by a magnetic force microscope (MFM). Such ring elements are proposed for both storage and sensor applications, where their utility is critically dependent on their precise behavior. The colors of the image represent the strength of stray magnetic field sensed at each location scanned above the ring. An MFM directly measures

stray field; it does not directly measure the magnetization pattern found in the ring itself. A measured stray field does not uniquely determine what magnetization pattern produced the stray field. Also illustrated is a magnetization pattern computed by OOMMF software based on known parameters chosen to match the experimental work. The pattern of arrows represents the magnetization pattern predicted by the model, and it can be confirmed that the predicted pattern is consistent with the measured stray field. In complementary roles like this, modeling is able to indirectly deduce details of a nanoscale system that are not within the capability of direct measurement.

Many of the equations governing nanomagnetism were established long ago. The notable Landau-Lifshitz equation dates back to 1935, and William Fuller Brown established the fundamentals of *micromagnetic modeling* in articles and books published from the 1940s to 1970s. At that time, the applications of the theory were mostly limited to simple geometries that could be attacked analytically. It was not until the 1990s that the widespread availability of significant and inexpensive computing power made application of micromagnetic modeling to practical problems a reality.

Unfortunately, the accurate solution of the relevant equations in software is a more difficult task than many physicists and engineers first realize. By the mid-1990s, many researchers and their students had produced their own micromagnetic simulation programs to support their own work. While their publications were careful to list details of their experiments and analyses, their home-grown software would typically only merit a high-level description. Usually the equations the software was meant to solve would be noted, but no reports of software testing were provided, and there was no opportunity to review its performance. The problems solved by these computer codes were typically precisely matched to a particular experiment, and it was rare that two independent teams would perform computer simulations of precisely the same scenario to enable comparison.

In 1996, NIST challenged this research community with a *standard problem*, inviting all those with magnetic modeling simulation software to attempt to compute some properties of a magnetization reversal similar to those routinely reported in the literature at the time, but all starting from the same assumptions. The results were alarming. The number of significantly different solutions almost matched the number of programs. Subsequent research has discovered flaws in both the programs and the problem. An important value of OOMMF is that it provides a transparent benchmark against which any research team developing their own magnetic model-

ing software can compare their results.

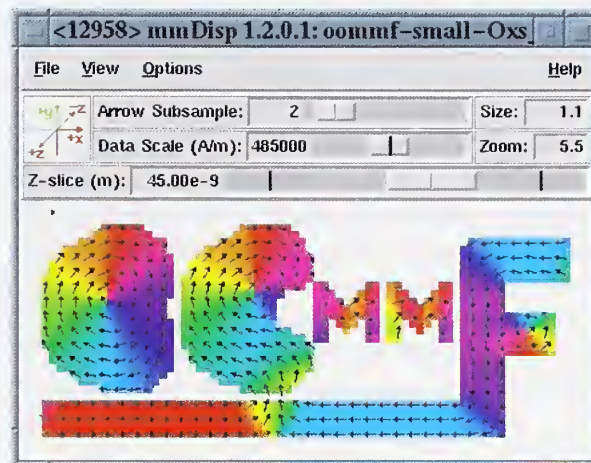


Figure 2. Part of the graphical user interface for OOMMF.

Those researchers for whom OOMMF provides all required modeling capabilities can, of course, can also choose to use OOMMF in place of developing their own software. In addition, OOMMF is structured as an extensible framework of software components, so those users who have needs beyond OOMMF's current capabilities can often extend it to meet their needs without the need to rewrite a new software package from scratch.

OOMMF has been remarkably successful in achieving its objectives. OOMMF software has been downloaded more than 8,000 times. A growing number of peer-reviewed research publications cite use of OOMMF; 185 are listed on the OOMMF web site.

Current plans for OOMMF are to supply additional extension modules and to make improvements to the framework necessary to support the nanomagnetic simulations required in emerging research areas. For example, NIST research in the development of ultra-low field magnetic sensors requires reliable modeling of thermal effects, a component that OOMMF has until now not provided. There is also considerable interest in representing the effects of spin transfer in nanomagnetic systems. In each of these cases, research is active into determining the correct models for these phenomena.

Further information on the OOMMF project, include software downloads, documentation, and extensive references, can be found at <http://math.nist.gov/oommf/>.

Magnetic Materials for Nanoscale Sensors and Ultra-High Density Data Storage

Magnetic sensors play a central role in many important technologies ranging from health care to homeland security. A common need among these technologies is greater sensitivity through nano-structured materials. In ultra-high density data storage, one of the most pressing needs is for nano-structured media that store data at ever-increasing densities. Improved methods for the magnetic isolation of grains in ultra-thin films are a key need. We have initiated research programs in both areas.

William F. Egelhoff, Jr., MSEL (855)

Over the past decade, NIST's Magnetic Engineering Research Facility (MIRF) has made important and widely recognized contributions to the thin magnetic films used as read heads for hard disk drives. MIRF is one of the most versatile facilities in the world for the fabrication and analysis of novel magnetic thin films. This versatility is illustrated by two new areas of research that have recently been initiated. One is magnetic sensors and the other is magnetic media. The common link is that both require nano-structured thin films.



Figure 1. The Magnetic Engineering Research Facility.

We are now 1.5 years into the Magnetic Sensors Competence Program. We have evaluated a series of complex magnetic alloys that in bulk form are very sensitive to small magnetic fields but had not previously been studied in thin-film form (*e.g.*, Ni₇₇Fe₁₄Mn₅Cu₄). Our approach is to carry out the metrology needed to optimize these materials in thin-film form.

We have made several surprising discoveries. First, these alloys are uniformly less sensitive in thin-film form. Second, some of the bulk sensitivity can be recovered by nano-layering the magnetic thin films with non-magnetic thin films. Third, conventional thin-films sensor designs contain a design flaw that allows magnetic irregularities to reduce the potential sensitivity by over a factor of 100. Fourth, we have found a way to use nano-structuring of the thin films to reduce these irregularities sharply and achieve a factor of 40 improvement in sensitivity. Fifth, an analysis of the physics of the nano-structuring immediately suggests that opportunities exist for significant further gains.

In the area of novel magnetic media we have been collaborating very closely with Seagate. Seagate is the world's leading manufacturer of hard-disk drives, and for the past two years they have been sending a physicist from their research labs to work with us, first on ballistic magnetoresistance, and then on novel magnetic media.

We have recently demonstrated a new method for magnetically decoupling grains in layered cobalt-palladium (CoPd) materials, a leading candidate for the next generation of magnetic media. We have found that if we deposit a gold film on top of the CoPd and anneal the sample in air an unexpected phenomenon occurs as a result of rapid diffusion of atoms along grain boundaries. Specifically, Co atoms on the grain boundaries are replaced by gold atoms from the surface. As a result the grain boundaries are demagnetized, and each grain can magnetically switch independently of its neighbors. This method provides the best magnetic isolation of grains to date and may be key to development of future media.

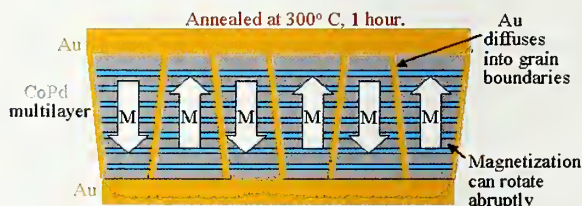


Figure 2. Grains isolated magnetically by Au diffusing into grain boundaries.

Evanescence Microwave Probing and High-resolution Microwave Power Imaging

Evanescence Microwave Probing: The development of new man-made electronic materials with properties not previously seen in nature, in addition to the growing interest in the electrical properties of biological materials, has led to a critical need to develop accurate measurement methods for fully understanding the interaction of these materials with electromagnetic fields. Conventional methods do not have the necessary sensitivity to characterize these materials at the micrometer and nanometer scales, so NIST researchers are developing an evanescent microwave probe system to perform quantitative, high-frequency, dielectric measurements on electronic and biological materials. High-resolution Microwave Power Imaging: NIST is developing metrology for quantitative imaging and measurement of electromagnetic field components and material characterization of nano-scale electrical and magnetic devices by establishing accurate spatially resolved waveform and frequency-domain metrology.

Michael Janezic, James Baker-Jarvis, and Pavel Kabos, EEEL (818)

We have developed a prototype evanescent microwave probe system that can quantitatively measure the complex permittivity of dielectric materials. By making use of evanescent fields, the measurement resolution is dependent on the dimensions of the probing structure, rather than the wavelength of the incident wave. As a result, near-field spectroscopic techniques are capable of both imaging and characterizing the electromagnetic properties of a wide range of materials at small spatial resolutions.

Recent improvements to the evanescent microwave probe system include broadening the frequency range of the method by making use of the probe's higher-order resonant modes. Previously, this method has only been employed at a single frequency, but measurements made on several standard dielectric materials showed that data from the higher-order modes was comparable to other resonator methods.

To improve the resolution of the evanescent microwave probe method, we developed a new theoretical model for needle-type probes. Traditionally, spherical-tipped probes are used as evanescent microwave probes because the interaction between the probe and sample is easy to model. However, spherical probes are difficult to

realize for measurements below 10 micrometers. The alternative is needle-type probe, which can be used below 1 micrometer, but are difficult to model. Therefore we developed a new theoretical model that accurately models the relation between the resonance characteristics of the needle probe and the dielectric properties of the material under test.

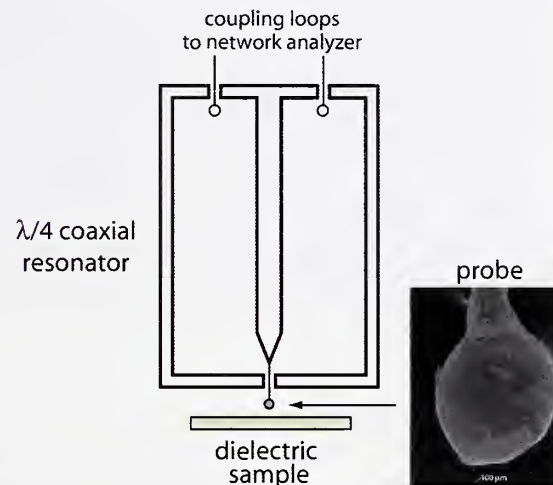


Figure 1. Evanescent microwave probe system.

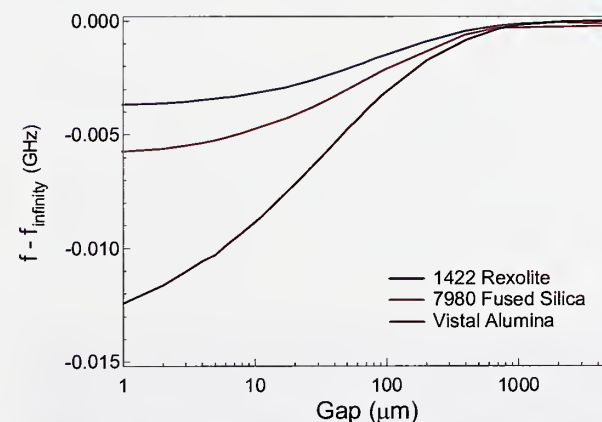


Figure 2. Resonant frequency as a function of the gap between the probe and dielectric material.

Chemical Sensing with Nanowires and Nanotubes

Process control and sensing rely on the ability to detect specific chemical species. The ability to detect and quantify the presence of specific species gives optimal control. Using nanowires and nanotubes as sensing units offers the possibility to build sensors capable of monitoring multicomponent mixtures with compact devices.

Richard E. Cavicchi, CSTL (836)

The novel properties of nanowires and carbon nanotubes show great promise for use in chemical sensing devices. Nanowires have a high fraction of their constituent atoms on the surface and therefore have electrical properties that are especially sensitive to the chemical environment in which they operate. We have been investigating growth and characterization of these materials, as well as implementation into sensing devices.

We have investigated lower temperature growth of tungsten nanowires. Tungsten nanowires are important for field emission and conductivity sensing devices. Existing methods require temperatures in excess of 800 °C to produce nanowires. Lower temperature growth is important for preserving the integrity of process steps for integrated devices, for example the use of aluminum metallization.

We have demonstrated a general method for the fabrication of tungsten nanowires by hydrogen plasma treatment of sputtered tungsten films and metal wire filaments at 500 °C. This work also revealed a surprising nanostructure termed a “nanoduct” consisting of hollow rectangular cross-section tubes of tungsten. These structures were found to grow in confined geometries and a model was proposed for the growth process.

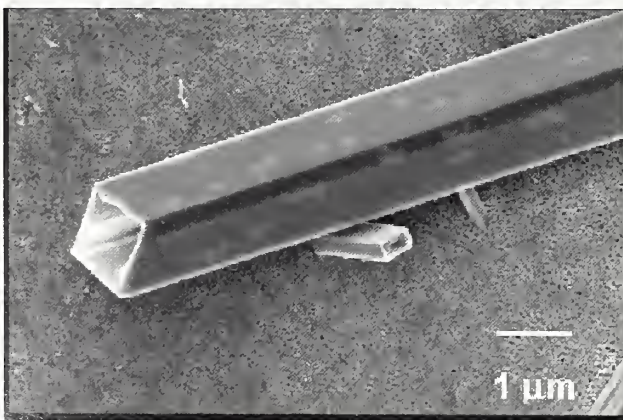


Figure 1. Tungsten “nanoduct” grown in a hydrogen plasma.

ZnO is a promising candidate material for nanolaser devices in which the wavelength of light is comparable to the device size. A nanolaser would detect species adsorbed on its surface by a change in the resonance factor Q of the lasing due to absorption of light. There is also interest in ZnO nanowire field emission and solar cells. Using zinc powder as a source material in a vapor transport growth process, we have grown vertically oriented faceted ZnO nanowires on substrates at temperatures as low as 500 °C, much lower than the 800 °C to 1000 °C of the widely used vapor-liquid-solid growth method. These nanowires could serve as the basis for surface-emitting nanolasers.

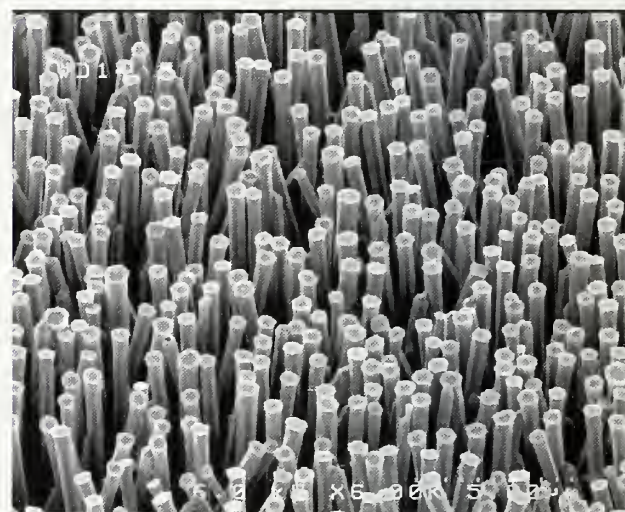


Figure 2. ZnO nanowires grown by vapor transport growth.

Carbon nanotubes have demonstrated high thermal conductivity along the length of the nanotube. Recently we have grown nanotubes on micromachined calorimeter sensors and grown chemically sensitive coatings over the nanotubes. The nanotubes greatly enhance the surface to volume ratio, while maintaining high thermal contact to the sensor.

III-Nitride Semiconductor Nanowires: Growth and Characterization

We are growing nanowires in wide bandgap III-nitride alloys. The eventual goal of this work is the realization of electrically pumped UV lasers and LEDs in these nanoscale structures. In fact, the III-nitrides are the only known semiconductor materials that will enable the development of such devices, which address a wide range of applications including detection of chemical and biological agents, biomedical procedures such as cancer diagnoses and treatment, and compact systems for water decontamination. We are carrying out nanowire growth optimization studies and are pursuing structural and spectroscopic studies to understand defect and recombination effects.

Kris Bertness and Norman Sanford, EEEEL
(815)

We have grown isolated GaN and AlGaN nanowires using gas-source molecular beam epitaxy (MBE). To the best of our knowledge, we are the third group in the world to have done so. The wires exhibited photoluminescence (PL) of comparable intensity to that from bulk free-standing HVPE GaN (indicating very low defect density), a relaxed *c* lattice constant, and the tendency to align in response to external electric fields. The nanowires ranged from 50 to 250 nm in diameter, were well separated, and grew to lengths ranging from 2 to 6 micrometers. They formed spontaneously, without metal catalysts, under conditions of low Ga flux combined with high nitrogen flux (with RF-plasma dissociation) at temperatures near 820 °C. The growth substrates were Si(111) wafers covered with thin AlN buffer layers. The growth axis of the wires oriented along the [0001] direction, and X-ray diffraction using the (0002) reflex yielded a lattice parameter *c* = 0.51852 nm +/- 0.00002 nm, indicating that the wires were fully relaxed. Field-emission scanning electron microscope images showed that the wires had hexagonal cross-sections. Nanowires were harvested and dispersed by immersing as-grown specimens in a toluene bath under ultrasonic agitation and dispensing droplets of the nanowire/bath slurry onto sapphire (or other) substrates. Evaporation of the solvent yielded dispersed nanowires. Unpolarized PL (325 nm cw excitation) at 3 K from both as-grown and dispersed samples showed the donor-bound exciton peak near 3.4723 eV dominating the spectrum, as expected for low-strain GaN. The dispersed NWs displayed a preference for settling on metal patterns versus bare regions of sapphire substrates. Longer wires (roughly 6 μm) re-

quired application of a voltage between metal patterns during dispersal to display alignment. These alignment techniques may prove useful to isolating individual nanowires for optical and electrical measurements.

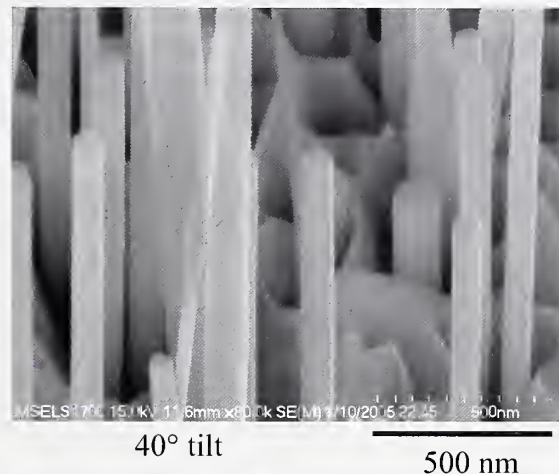


Figure 1. Field-emission scanning electron microscope image of GaN nanowires.

The nanowire topology itself is very attractive for a number of important applications. For example, in near-field scanning optical microscopy (NSOM), nanowire lasers could provide an active tip with unprecedented brightness compared to conventional NSOM that utilizes passive tapered fiber tips (typical tip aperture is roughly 100 nm in diameter), which suffer from unavoidably high optical loss. Additionally, the structure and emission wavelength of the nanowire laser lends itself well to integration with medical catheters for in-vivo cellular imaging technologies and localized photodynamic therapy. In these applications, the UV nanowire emission permits the optical excitation of fluorophore-tagged cancer cells, and the small diameter of the emission aperture affords a high degree of spatial selectivity in locating the cancerous region. Furthermore, ultra compact UV sources are required for homeland security needs in the spectroscopic detection of anthrax and other biotoxins.

Measuring & Understanding Charge Transport in Molecules

Molecular electronics is a field that many predict will have important technological impacts on the electronic and communication systems of the future. In molecular electronic systems, molecules perform the functions of electronic components. We are characterizing the structural properties of, and the conduction mechanisms through, molecules and developing methods that reliably and reproducibly measure the electrical properties of molecular.

Roger D. van Zee, CSTL (836)

The drive to increase electronic device performance, with the associated push to ever smaller device dimensions, has lead industry observers to conclude that silicon-based technology will reach a point of diminishing gains in the near future. This, in turn, has generated interest in alternative technologies. It is hoped that the tremendous flexibility available with organic synthetic chemistry and self-assembly techniques can be harnessed to produce devices comprised of single or small numbers of molecules. The CSTL team of researchers in molecular electronics is integrating a range of techniques that will provide key information on electronic structure and electron transport in molecular electronic systems.

The program takes an integrated approach. The conduction or current-voltage properties of molecule are measured using scanned-probe microscopes for specific molecular species. Spectroscopic measurements are then performed to compare whether these measured current-voltage properties correspond to intrinsic molecular properties. Theoretical calculations are used to interpret the results from both of these experiments. Finally, these composite data are compared to the performance of device prototypes made from similar materials.

Obtaining a detailed understanding of electronic transport properties in molecules requires the ability to correlate structure and transport mechanisms. Here we have used a “standard” test molecule to provide reference measurements. This molecule affords a means of probing the impact of molecular orientation on tunneling behavior. Asymmetry in the current-voltage curves show that, in the case of a “standing up” phase, the tunneling behavior is rectified by the asymmetry of the transport junctions, while in the “laying down” molecule, this asymmetry is almost completely removed (Cf. Figure 1). This can be explained by differences in metal surface potentials of the tip and sample surface.

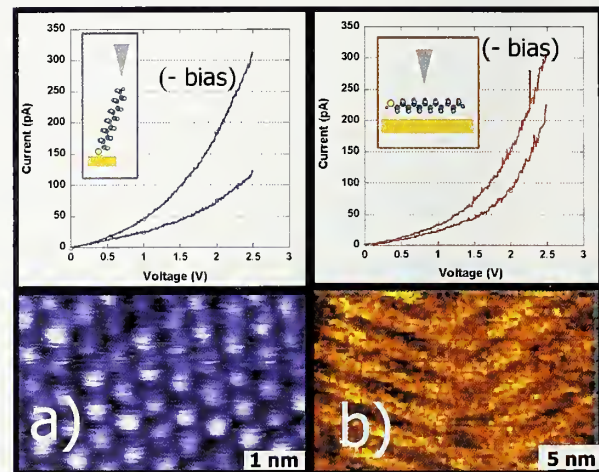


Figure 1. Orientation dependence on tunneling behavior in dodecanethiol showing asymmetric I-V behavior in molecules standing up on the surface (a) vs. more symmetric behavior in molecules laying down

The conductance measurements described above suggested that geometry and conduction were linked. However, molecular conductance should also be linked to the electronic states of the molecules. To investigate whether these electronic structure properties are related to conductance measurements, ultrafast laser spectroscopies have been used to study the geometry and electronic structure of test. These data are used to draw energy level diagrams, such as the example shown below, and also provide prediction of hole- and electron-injection barriers (Φ). Future experiments will compare these optical measurements to device prototype conductance measurements.

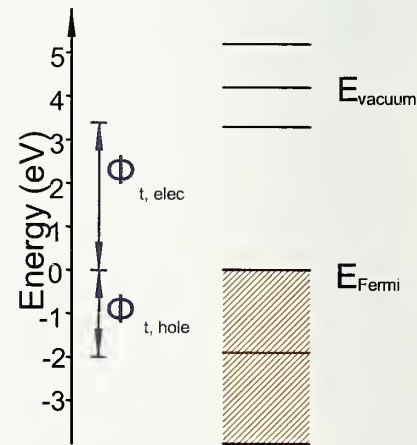


Figure 2. Energy level alignment diagram for oligo(phenyleneethynylene) on gold.

In order to interpret and understand the results from the current-voltage and electronic structure measurements, theoretical calculations are required. Particular attention has been focused to the electrostatics at the molecule-metal interface, which has been found to affect significantly the transport properties of the system. These calculations allow one to visualize how the electrons and fields are distributed along and around the molecule (Cf. Figure 3). This algorithm has been used to study the possible sources that lead to asymmetric current-voltage in a series of organic thiolates connected to gold electrodes. In order to develop efficient and robust models to gather a qualitative picture of electron conductance through molecular bridges, a simple algorithm has been implemented. Results of the calculations are in good agreement with the experimental curves shown in Figure 1.

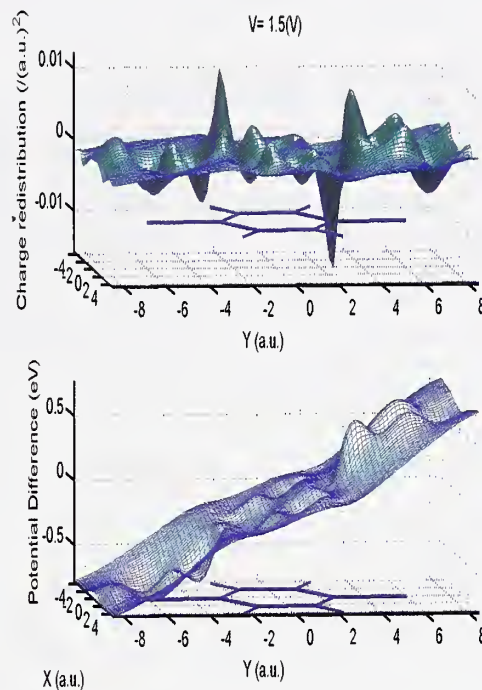


Figure 3. Charge distribution and electrostatic potential profiles for a prototypical molecule (benzene dithiolate) attached to gold electrodes.

MOS Device Characterization and Reliability Project

The CMOS FET (Field Effect Transistor) is approaching physical channel lengths of 10 nm and gate dielectric thickness of 1 nm. To scale to these nanometer dimensions requires new materials such as high permittivity gate dielectrics and metal gate electrodes. The MOS Device Characterization and Reliability (MOS DCR) Project develops the electrical, reliability, and physical characterization techniques necessary to address the metrology issues for CMOS devices posed by these new materials.

John S. Suehle and Eric M. Vogel, EEEL (812)

Introduction

The International Technology Roadmap for Semiconductors (ITRS) states that an effective thickness of 1 nm will be required by 2010. Due to increased power consumption, intrinsic device reliability, and circuit instabilities associated with SiO₂ of this thickness, a high permittivity gate dielectric (e.g. HfO₂) with low leakage current and at least equivalent capacitance, performance, and reliability will be required. Furthermore, because of the depletion of the polysilicon gate associated with the high electric fields in the device, metal gate electrodes will also be required. Electrical, reliability, and physical characterization techniques need to be developed and enhanced to address issues associated with alternate dielectrics and metal gate electrodes.

Electrical Characterization and Reliability

Electrical characterization of Metal Oxide Semiconductor (MOS) capacitors and Field Effect Transistors (FETs) has historically been used to determine device and gate dielectric properties such as insulator thickness, defect densities, mobility, substrate doping, bandgap, and reliability. The strategy of this effort is to develop robust electrical characterization techniques and methodologies to characterize charge trapping kinetics, V_t instability, defect generation rates, and time-dependent dielectric breakdown (TDDB) for both patterned device samples and blanket films obtained from our collaborators. Many issues such as tunnel/leakage current and spatially dependent properties associated with metal oxide and silicate dielectrics are also present in ultra-thin oxide and oxide-nitride stacked dielectrics. Therefore, many of the characterization schemes will first be developed on the simpler ultra-thin oxide and oxide-nitride dielectrics and then be applied to the metal oxide and silicate dielectrics for a variety of high-k samples subject to different deposition and gate electrode processes.

A series of experiments was conducted to characterize the energy dependence of interface trap density in n and p-channel HfO₂ FETs supplied by IBM. The study demonstrated that the mobility reduction observed in n-channel devices is due to positions of interface traps in the upper half of the Si energy band.

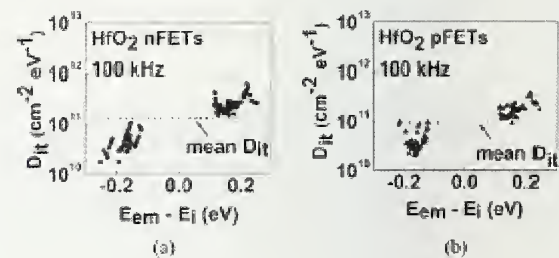


Figure 1. Energy distribution of interface traps as determined by the rise and fall time dependence of charge-pumping currents for HfO₂-gated MOSFETs. (a) n-MOSFET. (b) p-MOSFET.

The JEDEC standard, JESD-92, was published describing several techniques that can be used to detect soft breakdown in ultrathin gate oxides, where detection can be difficult. The standard also includes guidelines for designing test structures and data analysis procedures.

A mechanistic study of progressive breakdown in small area ultra-thin gate oxides was completed. One breakdown mode features a conducting filament that is stable until hard breakdown occurs, and a second mode features a filament that continually degrades with time. The acceleration factors are different for each mode, indicating different physical mechanisms are involved in the evolution and formation of the final hard breakdown event. Unstable filaments that result from the first soft breakdown progressively degrade and change physical structure until their leakage current becomes unacceptably large. A set of voltage and temperature acceleration parameters different from oxide wear-out is necessary to project the leakage current with time.

Reverse short channel effect (RSCE) was observed in high-k (HfO₂ on SiON buffer, Al₂O₃ on SiON buffer) gated submicron n-MOSFETs. SiO₂ or SiON control samples show normal short channel effect (SCE) behavior. The possible causes such as inhomogeneous channel doping profile and gate oxide thickness variation near S/D ends have been ruled out. The results indicate that the channel length dependent interface trap density is the main cause of the RSCE, while oxide charge also plays a role.

Physical Characterization

Project staff are optically characterizing advanced oxynitrides, oxide/nitride stacks, and more complex compounds, such as hafnium silicon oxynitride and hafnium-aluminum silicate using spectroscopic ellipsometry. Because many of these materials have bandgaps just below 6 eV, the measurement range obtainable with the VUV ellipsometer enables the investigation of processing related structure in the index of refraction, which shows up in the absorbing region above the bandgap energy. Project work is directed at determining preferred structural models, spectroscopic index of refraction values, or preferred optical dispersion functions for each of these film systems, and the variability of these parameters due to differences in fabrication processes. Work is also directed at extracting accurate bandgap values and interpreting the processing related structure found in the dielectric function. Analysis has been done primarily with software developed at NIST for SE, which allows the addition of the latest published or custom-developed optical response models for each material system investigated.

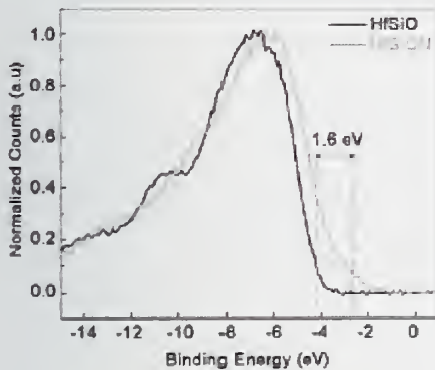


Figure 2. Soft X-ray photoelectron spectroscopy spectra of HfSiO and HfSiON thin films, which gives information about the valence band edge, but not about the full band-gap. Inclusion of nitrogen into the silicate network decreases the valence band offset (about 1.6 eV) by introducing states in the gap. A shift in the O_{2p} edge is also observed.

We develop fundamental understanding of the physical properties of high-k dielectric films via comparison of structural, optical, and electrical characterization. These multimethod studies utilize techniques such as transmission electron microscopy (TEM), soft X-ray photoemission (SXPS), X-ray absorption spectroscopy (XAS), grazing incidence angle X-ray diffraction (GIXRD), capacitance-voltage (C-V) and current-voltage (I-V) analysis, as well as SE, reflectivity, and FTIRATR. The crystalline phase of various high-k dielectric films can depend on film thickness, stress, grain-size, and impurities. The degree of crystallinity, interface roughness, chemical homogeneity, and stoichiometry can have a direct effect on the dielectric properties and the leakage current across such

dielectric layers. Strain, interface properties, and the effects of surface contamination species can also have important effects.

We have begun developing measurement techniques needed to characterize candidate gate metals for next generation CMOS with high-k gate dielectrics. Fabricated test structures and extracted work function values using the internal photoemission, flatband voltage as a function of oxide thickness method, and Scanning Kelvin Probe Microscopy (SKPM). A mask set containing a variety of test structures with which to calibrate and compare these measurement methods has been designed and procured. The test structures contain up to four levels of different interleaved metal layers, MOS capacitors, and sheet resistors.

Selected Publications

1. E. M. Vogel, G. A. Brown, "Challenges of Electrical Measurements of Advanced Gate Dielectrics in Metal-Oxide-Semiconductor Devices," 2003 International Conference on Characterization and Metrology for ULSI Technology, Mar 24-28, 2003, Austin, Texas, pp. 771-781 (30-SEPT.-2003)
2. J.-P. Han, E.M. Vogel, E.P. Gusev, C. D'Emic, C.A. Richter, D.W. Heh, J.S. Suehle, "Asymmetric Energy Distribution of Interface Traps in n- & p- MOSFETs with HfO₂ Gate Dielectric on Ultra-thin SiON Buffer Layer, IEEE, Electron Device Letters, March 2004.
3. J. S. Suehle, B. Zhu, Y. Chen, and J. B. Bernstein, Detailed Study and projection of Hard Breakdown Evolution in Ultra-thin gate Oxides, Microelectronics Reliability, 45, p. 419 2005.
4. N. V. Nguyen, J. E. Maslar, Jin-Yong Kim, Jin-Ping Han, Jin-Won Park, D. Chandler-Horowitz, and E. M. Vogel, "Crystalline Quality of Silicon-On-Insulator Characterized by Spectroscopic Ellipsometry and Raman Spectroscopy," Appl. Phys. Lett., vol. 85, p. 2765, 2004.
5. S-E Park, S. Jeliazkov, J. J. Kopanski, J. Suehle, E. Vogel, A. Davydov, and H-K Shin, "Electrical Characterization of MOS structures and Wide Bandgap Semiconductors by Scanning Kelvin Probe Microscopy", 2005 MRS Spring Meeting, San Francisco, CA.

Nanoelectronic Device Metrology Project

The CMOS FET (Field Effect Transistor), which is the current basis of ULSI (Ultra-Large-Scale Integrated) circuits, is beginning to show fundamental limits associated with the laws of quantum mechanics and the limitations of fabrication techniques. Therefore, it is expected that entirely new device structures and computational paradigms will be required to augment and/or replace standard planar CMOS devices. The Nanoelectronic Device Metrology (NEDM) Project develops the metrology to enable these beyond-CMOS nanotechnologies (such as Si-based quantum devices, and molecular electronics).

Curt A. Richter and Eric M. Vogel, EEEL (812)

Introduction

The NEDM Project investigates and is developing metrology for two specific areas of nanotechnology: (1) Si-based quantum electronics, and (2) molecular electronics. Molecular electronics is based upon bottom-up fabrication paradigms, while Si-based nanoelectronics are based upon the logical continuation of the top-down fabrication approaches utilized in CMOS manufacturing. Organic semiconductors for use in pervasive organic electronics is a third emerging technology under investigation in the NEDM. These technical approaches bracket the possible manufacturing techniques that will be used to make future nanoelectronic devices.

Molecular Electronics

In molecular electronics, our major objective is a NIST standard suite of molecular test structures and a fundamental understanding of charge transport through molecules and molecular ensembles. We are developing robust molecular test structures in order to use them to measure the electrical properties of molecules. Specifically, we are developing nanofabricated test-structures for assessing the electrical properties and reliability of moletronic molecules. These in-house test structures and prototypical ME devices obtained from leading researchers outside of NIST are thoroughly assessed to determine if they are viable test vehicles. In addition to the complexity of the nanofabrication of test structures, the challenges associated with measuring the electrical properties (such as current-voltage and capacitance-voltage as functions of temperature and applied fields) of these small molecular ensembles are daunting. The measured electrical properties will be correlated with systematic characterization studies by a variety of advanced analytical probes and the results used in the validation of pre-

dictive theoretical models.

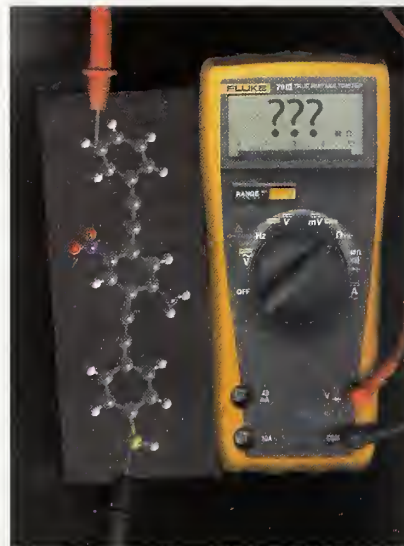


Figure 1. Electrically measuring molecules: the concept.

Two of the most critical elements to forming a successful ME device structure are the formations of a high-quality molecular monolayer and a top-metal/molecule interface. The NEDM is investigating ways to improve the characterization and control of these top and bottom molecular interfaces. To do this, the NEDM is optimizing self-assembly of molecular films onto both metals such as gold and directly onto Si surfaces. The direct attachment of organic molecules to the silicon surface is of increasing importance for emerging molecular electronics applications as devices incorporating molecules chemically bonded to silicon are amenable to integration with existing Si processing techniques. In order to determine optimal top-metallization techniques, we are developing new characterization approaches to determine metal/molecular interactions. Empirically, new deposition techniques and new top-metals (such as organic conductors) are being assessed to determine their viability as top metal contacts.

We have a significant collaboration with Hewlett Packard (HP) Research Labs. By using a crossbar test structure consisting of a molecular monolayer sandwiched between a series of perpendicular metal wires, collaborators at separate facilities recorded nearly identical electrical measurements. This step, along with others taken to eliminate potential sources of error, ensures that the measured behavior is directly attributable to the device and not the experimental set up. Electrical (current-voltage, or IV) measurements of crossbar devices containing eicosanoic acid exhibit a controllable, two-state

switching behavior that is due to the presence of the molecular layer. However, the molecular monolayer is not the sole cause. Rather, the switch-like behavior most likely arises from the interaction of the molecules with the electrodes. This example illustrates that the properties of molecular electronic devices are often determined not by the molecule alone, but by the entire device that consists of both the molecules and the attachment electrodes. This two-state behavior was independently measured in two separate laboratories, indicating that it is not a measurement artifact and illustrating that these devices are robust enough to ship via conventional methods and remain active. In addition to IV measurements, what well may be the first capacitance-voltage (CV) measurements of molecular monolayer-based devices were taken at NIST. These CV curves also show two-state behavior.

We have also developed an improved solution-based method for the direct attachment of long-chain aliphatic molecules to Si. In this method, ultraviolet (UV) radiation is used to assist the attachment of alcohols to the hydrogen-terminated Si(111) surface to form molecular monolayers successfully. To investigate the quality of these organic monolayers, they were physically and chemically characterized with infrared spectroscopy, spectroscopic ellipsometry, and contact angle measurements. The electrical properties of these organic films were probed by using IV and CV measurements obtained from a metal-organic-silicon test structure fabricated by post-monolayer metal deposition. The effect of differing alkane chain length on the electrical properties was investigated, and the CVs are in agreement with traditional theory for a metal-insulator-semiconductor.

Silicon Nanoelectronics

The focus of the Si-based nanoelectronics is the physical and electrical metrology of the basic building blocks of silicon quantum electronic devices (e.g., quantum layers, wires, and dots of silicon surrounded by silicon dioxide). By identifying and addressing the critical metrology issues associated with these basic building blocks, the basis of metrology for future Si-based ULSI nanotechnology will be defined.

A major goal is to fabricate silicon nanowire transistors using both top-down (lithography and etching) and bottom-up (placing grown nanowires using a variety of techniques) processing. These structures will be used to establish the relationship between the key fabrication conditions, physical properties (such as the geometry of the nanowire), and final electrical properties of these silicon devices. We have demonstrated that silicon nanowire (SiNW) field effect transistors (FETs) fabricated by a standard ‘top-down’ approach exhibit substan-

tially enhanced transport behavior. A systematic study of the inversion electron transport properties of SiNWs with different channel geometries has shown that a SiNW device exhibits enhanced inversion channel current density. The extracted electron inversion mobility of the 20 nm width nanowire channel ($1000 \text{ cm}^2/\text{Vs}$) is found to be 2 times higher than that of the reference MOSFET of large dimension ($W > 1\mu\text{m}$). The enhancement is attributed to the possible suppression of inter-valley phonon scattering due to strain in the SiNW FET caused by the oxidation process.

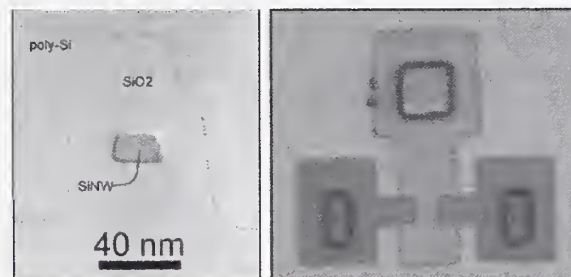


Figure 2. A silicon nanowire transistor.

Selected Publications

1. Richter, C.A., D.R. Stewart, D.A.A. Ohlberg, R.S. Williams,; “Electrical Characterization of Al/AlO_x/Molecule/Ti/Al Devices,” *Appl. Phys. A*, 80, 1355–1362. March 2005.
2. S.-M. Koo, A.-F. Fujuwara, J.-P. Han, E. Vogel, C. Richter, and J. Bonevich, “High Inversion Current in Silicon Nanowire Field Effect Transistors.” *Nano Lett.*, Vol. 4, 2107-2111, Nov. 2004.
3. C. A. Richter, C. Hacker, L. J. Richter, E. M. Vogel, “Molecular Devices Formed by Direct Monolayer Attachment to Silicon,” *Solid State Electronics*, Vol. 48, pp. 1747-1752 (17-JUNE-2004).
4. “Metrology for Emerging Research Devices and Materials,” Eric Vogel, 2005 International Conference on Characterization and Metrology for ULSI Technology, Univ. Texas-Dallas, Richardson, Texas, March 15-18, 2005.

Nanomagnetodynamics: Devices

NIST is developing measurements for magnetic devices used in the magnetic data storage and magneto-electronics industries for advanced magnetic recording systems, magnetic solid-state memories, and magnetic sensors. Broadband electrical measurements are being developed to characterize nanoscale devices based on giant magnetoresistance and spin-dependent tunneling.

Stephen E. Russek, EEEL (818)

The data storage industry is developing smaller and faster technologies that require sub-hundred-nanometer magnetic structures to operate in the gigahertz regime. New techniques are required to characterize these magnetic structures on nanometer-size scales and over a wide range of time scales varying from picoseconds to years. For example, the response of an 80-nanometer magnetic device, used in a read head or a magnetic random access memory (MRAM) element, may be determined by a 5-nanometer region that is undergoing thermal fluctuations at frequencies of 1 hertz to 10 gigahertz. These fluctuations give rise to noise, non-ideal sensor response, and long-term memory loss. Advances in technology are dependent on the discovery and characterization of new effects such as giant magnetoresistance (GMR) and spin-dependent tunneling (SDT). NIST has developed new techniques for characterization of magnetic thin films and device structures on nanometer size scales and gigahertz frequencies.

Device Magnetodynamics — NIST has fabricated test structures that allow the characterization of small magnetic devices at frequencies up to 40 gigahertz. The response of submicrometer magnetic devices such as spin valves, magnetic tunnel junctions, and GMR devices with current perpendicular to the plane (CPP), are measured in both the linear-response and nonlinear-switching regimes. We have measured the sensors using microwave excitation fields and field pulses with durations down to 100 picoseconds. We have compared measured data to numerical simulations of the device dynamics to determine the ability of current theory and modeling to predict the behavior of magnetic devices. We are developing new techniques to control and optimize the dynamic response of magnetic devices. These include the engineering of magnetic damping by use of rare-earth doping and precessional switching, which controls switching using the timing of the pulses rather than pulse amplitude.

Magnetic Noise and Low-Field Magnetic Sensors — NIST has developed new techniques to measure both the low-frequency and high-frequency noise and the effects of thermal fluctuations in small magnetic structures. Understanding the detailed effects of thermal magnetization fluctuations will be critical in determining the fundamental limit to the size of magnetic sensors, magnetic data bits, and MRAM elements. High-frequency noise is measured in our fabricated structures and in commercial read heads. High-frequency noise spectroscopy directly measures the dynamical mode structure in small magnetic devices. The technique can be extended to measure the dynamical modes in structures with dimensions as small as 20 nanometers. The stochastic motion of the magnetization during a thermally activated switching process is measured directly, which will lead to a better understanding of the long-time stability of high-density magnetic memory elements.

In-Situ Magnetoconductance and Quantitative Magnetometry — NIST has developed new techniques to measure the electronic and magnetic properties of magnetic thin-film systems *in situ* (as they are deposited). One such technique, *in-situ* magnetoconductance measurements, can determine the effects of surfaces and interfaces on spin-dependent transport in a clear and unambiguous manner. The effects of submonolayer additions of oxygen, noble metals, and rare earths on GMR are being studied.

Magnetoresistive Scanning System Implemented

We built a high-frequency magnetoresistive (MR) scanning system to probe high-frequency electric and magnetic fields above high-speed circuits. The system can use either commercial recording heads or NIST-fabricated high-frequency MR sensors. The spatial resolution can be as small as 100 nanometers depending on the type of probe. A special set of high-frequency structures — which included co-planar waveguide tapers, shorts, and opens — were fabricated to allow imaging of structures that had spatially varying microwave fields in three dimensions. The structures were imaged in three modes: low frequency magnetic fields (1 kilohertz), high-frequency electric fields (1 to 4 gigahertz), and high-frequency magnetic fields (1 to 4 gigahertz).

Low-Frequency Noise Measurements on Commercial Magnetoresistive Sensors

Low-frequency noise was measured in the frequency range from 0.1 hertz to 10 kilohertz on a variety of

commercially available magnetic sensors. The types of sensors investigated include those implemented with anisotropic magnetoresistance (AMR), giant magnetoresistance (GMR), and tunnel magnetoresistance (TMR) effect devices. The 1/f noise components of electronic and magnetic origin were identified by measuring sensor noise and sensitivity at various applied magnetic fields. For the GMR sensors, both electronic and magnetic components contribute to the overall sensor noise. Maximum noise occurs at the bias field that gives maximum sensitivity. The noise of TMR-based sensors is primarily due to resistance fluctuations in the tunnel barrier, having little to no field dependence. The best low-field detectivity of the sensors that has been measured is on the order of 100 picotesla per root-hertz at 1 hertz. These magnetic sensor noise data are part of a database of low-field sensor performance.

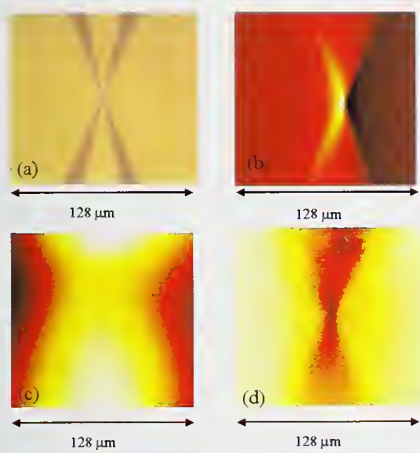


Figure 1. Image of fields above a coplanar waveguide obtained using a high-bandwidth spin-valve recording head: (a) optical image, (b) low-frequency magnetic image, (c) 1 gigahertz capacitive image, (d) 1 gigahertz magnetic image.

In-Situ Observation of Nano-Oxide Formation in Magnetic Thin Films

In-situ conductance and reflection high-energy electron diffraction (RHEED) measurements were taken during the oxidation of 20-nanometer-thick Co and Co-Fe layers. The conductance shows an initial drop with exposure to oxygen followed by a period of increasing conductance, indicating an increase in specular reflection of electrons at the oxide interfaces. RHEED measurements show a blurring of the (111) face-centered-cubic (FCC) texture with exposure to oxygen, indicating the formation of an amorphous oxide during the initial conductance drop and conductance increase. After the conductance begins to decrease again, a new diffraction pattern appears in the RHEED data, indicating the formation of CoO with a FCC (111) texture but with a different lattice spacing. These studies shed light on the physical mecha-

nisms for the giant magnetoresistive effect used in magnetic sensors.

Current Density Distribution Determined through *In-Situ* Conductance Measurements

The sheet conductances of top-pinned spin valves and single-material films were measured *in situ* as the thin-film layers were grown. The data were fit to a Boltzmann transport calculation. The electrical conductivity and electron mean free paths were determined for each material by measuring the *in-situ* conductance of thick, single-material films. The electron transmission probabilities were deduced for each interface from the theoretical fits to the multilayer data. From these interfacial transport parameters the ratio of current density to electronic field, or effective conductivity, was calculated as a function of position for the completed spin valve. The distribution of current in the spin valve was not very sensitive to the overall amount of diffuse scattering at the interfaces. Spin valves are used in modern magnetoresistive read heads in disk drives.

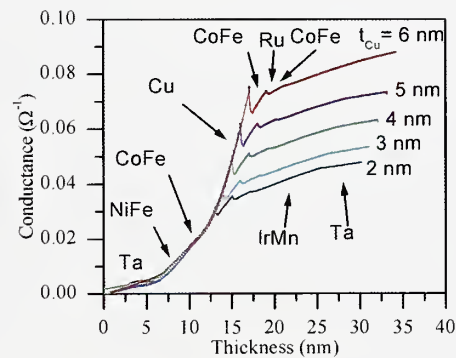


Figure 2. *In-situ* conductance measurements of a spin-valve taken during growth. The data can be fit to determine the local current density.

Selected Publications

1. N. Stutzke, S.E. Russek, D.P. Pappas, and M. Tondra, "Low-Frequency Noise Measurements on Commercial Magnetoresistive Magnetic Field Sensors," *J. Appl. Phys.*, in press.
2. A. McCallum and S.E. Russek, "In-Situ Observation of Nano-Oxide Formation in Magnetic Thin Films," *IEEE Trans. Magn.* **40**, 2239-2241 (July 2004).
3. A. McCallum and S.E. Russek, "Current Density Distribution in a Spin Valve Determined Through *In Situ* Conductance Measurements," *Appl. Phys. Lett.* **84**, 3340-3342 (April 2004).

Nanoscale Engineered Magnetic Sensors

In 2004 we embarked on an interdisciplinary program on low-noise, nanoscale magnetic sensors with improved detection levels. The program includes development of new amorphous and nanocrystalline materials, imaging of magnetic domains, noise measurement in sensor devices, and micromagnetic modeling.

David P. Pappas, EEEL (818)

Magnetoresistive magnetic field sensors have wide application in research and industry. Currently, cryogenic superconducting quantum interference devices are used for the measurement of ultra-low magnetic fields. They provide important information in many areas of basic research, medical magnetic field monitoring, and security. However, it is necessary to develop devices operating at room temperature that are scalable, linear, and have comparable sensitivity to realize the maximum benefit of such devices. The most promising candidates for development are magnetoresistive technologies. Magnetic noise is a critical problem in the development of these devices; such noise can be two orders of magnitude higher than the intrinsic Johnson, shot, and 1/f noise of the device. New materials, measurement techniques, and device architectures are required to characterize and reduce the effect of low- and high-frequency magnetic fluctuations.

New Zigzag Magnetoresistive Field Sensors

We developed new “zigzag” magnetoresistive sensors that, because of their shape, are sensitive to magnetic fields parallel to their axes but insensitive to fields perpendicular. The sensors are made of thin films of Ni-Fe, 35 micrometers long and 5 micrometers wide, with nanoscale design elements at the edges. The devices sense magnetic fields using a small current down their centerlines. They are able to distinguish positive and negative fields because their resistance is an odd function of field.

In general, anisotropic magnetoresistive sensors must be biased, with their magnetization at an angle with respect to the current direction. The new sensors are fabricated in a zigzag pattern that pins the magnetization at alternating positive and negative 45 degrees to the direction of the current flow. This novel approach provides a built-in magnetization bias determined by the corrugation of the edges. Since the angle of magnetization of the magnetic domains is controlled only by the sensor shape,

and not by adjacent biasing fields, the devices may be scaled to nanometric dimensions.

When the sensor is exposed to a magnetic field oriented in the direction of the current, the angle of magnetization relative to the current in both sets of the domains decreases. This results in an increase of electrical resistance in each domain and in the entire device. For magnetic fields in the negative current direction, the magnetization angle increases and the resistance decreases. For magnetic fields in the perpendicular axis, the magnetization angle increases in one set of magnetic domains and decreases in the other, resulting in no net change in device resistance.

The sensors are simpler in design and likely will be cheaper to make than conventional magnetic sensors used in portable devices, which typically include multiple aluminum strips that alternate diagonally across the sensor. The new zigzag sensors are expected to have less electronic noise by confining the current to the center of the device and by eliminating edge imperfections that can result in nanoscale magnetic fluctuations.

Such sensors could be used to measure magnetic fields in applications such as compasses, weapons detection, medicine, and non-destructive evaluation of structural materials.

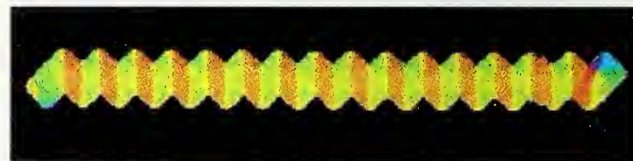


Figure 1. Micrograph of a zigzag magnetoresistive element obtained by use of a scanning electron microscope with polarization analysis (SEMPA). With respect to the long axis of the sensor (the axis of current), green indicates magnetization at an angle of +45 degrees, orange at an angle of -45 degrees. The magnetic domain patterns were also accurately modeled with NIST's Object Oriented MicroMagnetic Framework (OOMMF).

Magnetodynamic Imaging

New techniques are being developed to dynamically image magnetic nanostructures. We have successfully used Lorentz microscopy to image the magnetic structure in a spin-dependent tunneling device. We are extending Lorentz imaging to allow dynamical observation of the magnetic structure in magnetic films and active devices at frequencies from 1 hertz to 10 kilohertz. Fluctuations in the magnetic structure, which often correspond with defects in the device, give rise to noise and stochastic behavior that can limit their performance as sensors and

memory elements.

We designed a new scanned-probe-imaging system based on dynamic ballistic electron magnetic microscopy that will be able to image fluctuation in magnetic structures on sub-nanometer length scales. This technique uses spin-dependent scattering of the electrons emitted from a scanned tunneling tip to detect local magnetic structure. This technique is capable of imaging buried magnetic structures and fluctuations in active giant-magnetoresistive and spin-dependent tunneling devices.



Figure 2. Lorentz microscopy image of a 100-micrometer Ni-Fe/Co-Fe tunnel junction. Disorder in both the magnetically hard Co-Fe layer and the magnetically soft Ni-Fe layer can be observed.

Nano-magnetic Imaging for Forensic Applications

Magnetic tapes are still the prevalent method for storing audio and video data in much of the world. Examination of media from tape media for authenticity and validation is critical in a wide range of investigations, including criminal and terrorism, for example. In this work, we have built a system that can image both audio cassette and VHS tapes in real time (i.e. as the tape is being played back) with sub-micrometer resolution downtrack.

This allows investigators to identify whether or not tapes are copies or if they were altered after the recording in question. An image of a typical recording stop event on a cassette tape is shown in the Figure 3, illustrating the high resolution of this technique and also the capability to recover the data along a given piece of the track. The short burst of high frequency occurs as the tape slows down, and then the gradual lowering of the head back onto the tape can be seen near just after. These images are taken with a 256 linear array of sensors that glide just above the tape to map out the magnetic fields. The sensors are nano-engineered to have low noise and a



Figure 3. This figure illustrates the high resolution of this technique and also the capability to recover the data along a given piece of the track.

dynamic range that corresponds to that needed for these tapes. In addition, the magnetic response of each of the 256 sensors has been individually calibrated. This results in a very accurate image that allows for unprecedented accuracy in the analysis of entire tapes, computerized screening, and data recovery of partially erased data.

Selected Publications

1. F. C. S. da Silva, W.C. Uhlig, A.B. Kos, S. Schima, J. Aumentado, J. Unguris, and D. P. Pappas, "Zigzag-Shaped Magnetic Sensors," *Appl. Phys. Lett.* **85**, 6022-6024 (December 2004).

Single Photon Sources and Detectors

Emitters and detectors of single photons on demand are important for low light level metrology and quantum key distribution, a secure form of communication. They are also critical components of quantum computing systems and experiments that will test the fundamental limits of precision in optical metrology. Epitaxial InGaAs/GaAs quantum dots are attractive as single photon emitters for their ease of fabrication and inclusion with monolithic microcavities, short spontaneous emission lifetimes, and the possibility of electrical injection. We are developing single photon emitters based on InGaAs quantum dots (QDs), with the ultimate goal of electrically pumped operation. We are also developing QD-based single photon detectors.

Richard Mirin, EEEL (815)

For practical implementation, single photon sources should operate at high temperatures. We have demonstrated photon antibunching from a single, self-assembled InGaAs quantum dot at temperatures from 5 K up to 135 K, and single photon emission up to 120 K. We grew InGaAs quantum dots using molecular beam epitaxy and isolated single dots with etched mesas. The second-order intensity correlation $g(2)(0)$, which is a measure of the independence of single photon emitters, was derived by measuring the coincidence photon counts in a Hanbury Brown-Twiss interferometer. For temperatures up to 100 K, $g(2)(0)$ was measured to be approximately linear with temperature and less than 0.26. At 120 K, $g(2)(0)$ increases to about 0.47, which is slightly less than the second-order intensity correlation expected from two independent single emitters. At 135 K, $g(2)(0)$ was 0.67, which still indicates nonclassical light emission that is equivalent to having three independent single emitters. Contributions to the emission other than that from the uncharged single exciton were separated by analysis of additional peaks in the photoluminescence spectra. If we were able to eliminate the contribution due to the additional peaks, we would obtain a $g(2)(0)$ value of 0.087 at a quantum dot temperature of 100 K.

There are two reasons why the single InGaAs quantum dot decreases in emission at higher temperatures, thereby requiring higher pump intensities and subsequently degrading the performance as a single photon source. Experiments suggest that carrier transfer to the wetting layer is a contributing factor, which can be mitigated using larger quantum dots with less quantum confinement energy or wider bandgap barriers. Secondly, optical phonon scattering becomes more pronounced as

the temperature increases. The problem could be lessened by promoting faster radiative recombination times of the quantum dot excitons by the use of a microcavity. Single electron-hole pair injection by electrical means should improve the performance of an InGaAs quantum dot single photon source by removing the possibility of charged exciton or biexciton formation. The photon repetition rate of the electrically pumped source will be controlled by the frequency of an applied AC voltage, allowing precisely defined emission of single photons.

The results above represent the highest reported temperature for non-classical light emission from the InGaAs/GaAs system. The single photon source is being developed for applications including ultra-secure communication, the testing of fundamental theories of quantum optics, and high-accuracy radiometry in which optical power and energy measurements are calibrated by counting photons.

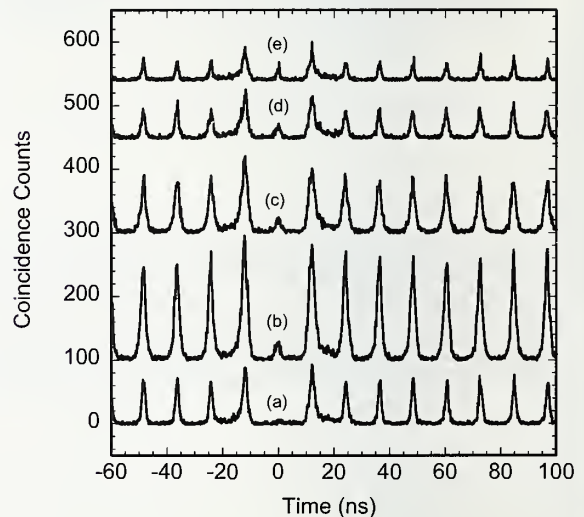


Figure 1. Second-order intensity correlation of single photon source measured as a function of temparture. (a) 5 K, (b) 50 K, (c) 100 K, (d) 120 K, and (e) 135 K.

We are also developing a type of single photon detector that is based on a quantum-dot, optically gated field-effect transistor in III-V semiconductor material. It will be able to operate at temperatures that are obtainable with solid state cooling, unlike the state-of-the-art single photon detectors based on superconductors. Such a device has the potential for high quantum efficiency (> 90%) and low noise, and it is compatible with conventional semiconductor fabrication and processing methods. In our device, the barrier material adjacent to the

QD is optically excited to create electron-hole pairs. A hole is captured by the QD and stored there. In effect, the QD is an engineerable trap and can store charge for a long time. We have observed persistent photoconductivity in our detectors at very low light levels. Next generation devices are in fabrication and testing.

Selected Publications

1. R. Mirin, "Photon antibunching at high temperature from a single InGaAs/GaAs quantum dot," *Appl. Phys. Lett.* **84**, 1260 (2004)
-

Terahertz Technology

We develop metrological methods, components, and technology for imaging and spectroscopy from about 100 GHz to several terahertz (THz). We fabricate our own nanoscale detectors that we invent, engineer, and evaluate.

Erich Grossman and Robert Schwall, EEEL (815)

Imaging in the approximately 100 GHz to 2 THz range offers the possibility of detection of concealed weapons and remote detection of contraband (e.g., explosives under clothing) without the use of ionizing radiation. Spectroscopy in this frequency range has additional applications in industrial processing and remote identification of chemicals. We have developed unique capabilities in detectors, optics, and metrology methods. These capabilities are being used to construct improved imaging systems and to provide government agencies with unbiased evaluations of systems and components developed in industry.



Figure 1. An optical image of a representative hand gun used in test.

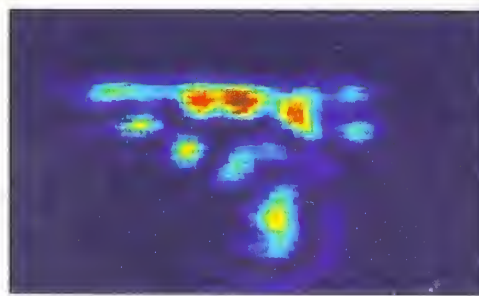


Figure 2. An active mm-wave image of the representative hand gun.

Accomplishments

- *Real-Time Imaging with Slot-Ring Antenna-Coupled Uncooled Millimeter-Wave Bolometer Arrays — Imaging*

applications in the terahertz spectral range require large numbers of pixels, and an appropriate balance between sensitivity and cost. One approach to achieving all three goals simultaneously is to use lithographic antennas to couple the radiation into nanometer-sized detectors. In this case, the antenna engineering challenge is to develop an array-compatible antenna with the highest possible directivity in a completely planar monolithic structure. This is the motivation behind a new antenna design we have developed, in which slot-ring antennas with finite ground planes are patterned on electrically thin substrates. Because the application is imaging, sensitivity to radiation from only one side of the substrate is desired, so a planar backshort is employed to reflect radiation from the backside of the substrate into the forward direction. With the backshort at the proper position behind the plane of the slot-ring antenna, constructive interference occurs between the directly received radiation and that reflected by the backshort, increasing the directivity. Measured beam patterns are highly circular and exceptionally narrow (22° at -3 dB) from a completely planar antenna. They can be arrayed at a spacing of 1.5 wavelengths with negligible measured effect on performance. A 120-element array for 95 GHz has been fabricated and used to obtain real-time images.

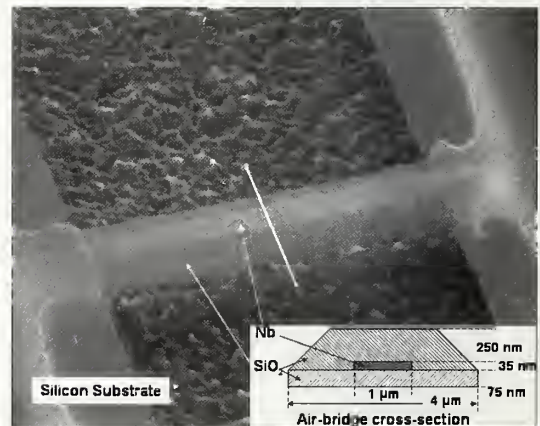


Figure 3. Scanning electron micrograph of SiO_2 encapsulated Nb microbolometer. The figure insert shows a schematic of the cross-section of the bolometer and the encapsulating oxide.

- *Actively Illuminated Scanned 40k pixel 95 GHz Imaging System — Fundamental considerations dictate the use of actively illuminated imaging systems for indoor applications, and active illumination favors a scanned architecture. We have completed design and fabrication of all the major components — line source, detector array, lenses and scanner of a real-time whole-body imaging system. System test will commence in late 2004 and continue through 2005.*

- *Characterization of Sb-Heterostructure Quantum Tunneling Diodes as Submillimeter Wave Detectors — We*

have measured the diode I(V) and noise of Sb-heterostructure quantum tunneling diodes fabricated from epitaxial layers of InAs and AlGaSb by an industrial collaborator. These devices exhibit exceptionally high nonlinearity in the I(V) characteristic, which produces the rectification without bias. Thus the device does not suffer from the 1/f noise associated with a dc bias. Our measurements indicate that these devices have sensitivity that challenges that of other existing room-temperature detectors in this frequency range, and that they could be attractive candidates in the millimeter and submillimeter wave region.

Selected Publications

1. A. Luukanen, E. N. Grossman, H. P. Moyer, and J. N. Schulman, "Low-frequency noise properties of quantum tunneling Sb-heterostructure millimeter wave diodes," submitted to *Appl. Phys. Lett.* (2004).
2. A. Luukanen, E. N. Grossman, H. P. Moyer, and J. N. Schulman, "Noise and THz rectification characteristics of zero-bias quantum tunneling Sb-heterostructure diodes," Submitted to *Int'l. J. High Speed Electronics* (2004).
3. A. J. Miller, A. Luukanen, and E. N. Grossman, "Micromachined antenna-coupled uncooled microbolometers for terahertz imaging arrays," *Proc. of SPIE*, 5411, pp. 18-24 (2004).
4. E. N. Grossman, A. Luukanen, and A. J. Miller, "Terahertz active direct detection imagers," *Proc. of SPIE*, 5411, pp. 68-77 (2004).
5. A. Luukanen, R. H. Hadfield, A. J. Miller, and E. N. Grossman, "A superconducting antenna-coupled microbolometer for THz applications," *Proc. of SPIE*, 5411, pp. 121-126 (2004).
6. A. Luukanen, A. J. Miller, and E. N. Grossman, "Active millimeter-wave video rate imaging with staring 120-element microbolometer array," *Proc. of SPIE*, 5410, pp. 195-201 (2004).
7. E. N. Grossman, T. E. Harvey, and C. D. Reintsema, "Controlled barrier modification in Nb/NbO_x/Ag metal insulator metal tunnel diodes," *J. Appl. Phys.* 91(12), pp. 10134-10139 (June 15, 2002).
8. S. Nolen, T. E. Harvey, C. D. Reintsema, and E. N. Grossman, "Properties of cavity-backed slot-ring antennas at 95 GHz," *Proc. SPIE* 4373, pp. 49 (2001).
9. E. N. Grossman, S. Nolen, N. G. Paultre, and C. D. Reintsema, "Concealed weapons detection system using uncooled, pulsed, imaging arrays of millimeter-wave bolometers," *Proc. SPIE*, 4373, pp. 7 (2001).
10. N. G. Paultre, E. N. Grossman, G. N. Stenbakken, B. C. Waltrip, S. Nolen, and C. D. Reintsema, "Design of an active mm-wave concealed object imaging system," *Proc. SPIE*, 4373, pp. 64 (2001).

Nanoscale Fabrication

Our goal is to maintain state-of-the-art nanofabrication capabilities in NIST Boulder facility for the use of the NIST staff and collaborators.

James Beall, EEEL (817)

Our facilities for fabricating integrated circuits are essential to nearly all of the work in the Group. We maintain a research-class facility specialized in the fabrication of complex nanoscale superconducting circuits, nanoscale electronics and MEMS structures. Beginning with computer-aided design, we use our electron-beam and optical lithography to make structures smaller than 40 nm and complex circuits containing as many as 107,000 Josephson junctions. Our tools are housed in 200 m² of "class 100" clean room space, which was improved greatly in 1999. We have recently added tools for fabricating MEMS that are essential for the creation of many of our ultra-sensitive instruments, and for micromachined ion traps for quantum computing and future atomic clocks.



Figure 1. Maggie Crews inspects a mask generated in our optical pattern generator.

Our facilities are used for a variety of diverse projects including those by most of the NIST organizations in Boulder. They include the fabrication of Josephson ar-

ray voltage standards, a prototype capacitance standard based on single electron tunneling, prototype Johnson noise thermometry, microcalorimeters for materials analysis and space observation including the most complex superconducting system ever made, quantum computing using Josephson phase qubits, quantum computing using ion traps, miniature atomic clocks, terahertz imaging systems for homeland security, revolutionary single photon counters for fundamentally secure communications, and novel nanoscale magnetic imaging probes.



Figure 2. View of clean room lithography bay with digital pattern generator and wafer stepper recessed into the wall on the right and wet processing on the left. Optical lithography produces linewidths smaller than 500 nm and is often combined with electron beam lithography for structures as small as a few tens of nm.

Our facilities are available as an "open-shop" operation. After appropriate training, all of our staff can personally use them to fabricate the devices needed for their research. We keep the facility and the processes flexible and under the control of each individual user to avoid constraining research and to allow maximum creativity. Our past accomplishments are testimony to the success of this approach.

In the past two years we have upgraded our optical pattern generator to a modern instrument capable of making masks with feature sizes of 1.5 micrometers. Having this

in-house mask-making facility allows very rapid turn-around, which improves productivity and encourages creativity. This capability is rare for a facility of this size and sophistication. For patterning at the $0.5\text{ }\mu\text{m}$ scale, we use optical lithography in a recently acquired I-line stepper and a UV contact aligner. Electron-beam lithography enables registration and patterning at less than 50 nm . Our capability in electron beam lithography is being enhanced with the addition of a field emission scanning electron microscope with wafer-scale stages and load lock.

Our thin-film deposition and etching tools are similar to those found in a semiconductor fabrication facility, but they have been optimized for normal and superconducting metal fabrication. We have general purpose and dedicated sputtering and e-beam systems to deposit multilayers of metals. We use electron cyclotron resonance (ECR) plasma-enhanced chemical vapor deposition (CVD) of SiO_2 for circuit insulation. Dry etching is performed in standard RIE and plasma etching tools.

etch tools for micromachining of Si. We use xenon difluoride gas to rapidly and isotropically etch silicon for a sacrificial layer release of surface micromachined structures. A deep reactive ion etch system allows highly anisotropic etching of Si for through-wafer etching and definition of high aspect ratio Si structures.



Figure 3. Access bay for diffusion furnaces used to fabrication many MEMS structures for integrated structures that make state-of-the-art standards and measurement technologies possible.

We have tools necessary to fabricate structures for microelectrical-mechanical systems (MEMS). We use a set of research-scale tube furnace reactors (5'' capable), for wet and dry silicon oxidation, solid-source diffusion of boron, low-stress silicon nitride/polysilicon low-pressure chemical vapor deposition (LPCVD), and LPCVD of low-temperature oxide. We have added two silicon dry-

Johnson Noise Thermometry

We use a nanoscale quantum-based voltage source to reduce the uncertainty of Johnson noise thermometers, with the ultimate goal of creating an intrinsic quantum-based electronic temperature standard for use by the NIST Chemical Science and Technology Laboratory. The quantum-based pseudorandom noise sources that we use are fabricated with nanoscale dimensions in our laboratory.

Wes Tew, CSTL (836), Sam Benz, EEEL (817), and Sae Woo Nam, EEEL (815)

Gas-based and fixed-point methods of precision thermometry are either limited to specific fixed temperatures or require considerable effort to reduce uncertainties below parts in 10^5 . An electronic quantum-based method would provide another approach as well as advantageous features such as improved linearity of temperature calibrations. It would also provide an improved realization of the Kelvin thermodynamic temperature scale, and a direct link between temperature and electrical standards, possibly providing a route to a redetermination of the Boltzmann constant. More importantly, this quantum-based Johnson noise thermometry (JNT) method is a new paradigm to realize the thermodynamic temperature scale through electrical and quantum-based standards. This JNT approach to create an “electronic Kelvin” is analogous to the NIST watt-balance program to realize an “electronic kilogram.”

Our customers and collaborators include the NIST Chemical Science and Technology Laboratory, the temperature calibration laboratories of other national measurement institutes, and industrial applications requiring long-term temperature stability or with temperature sensors in difficult or remote locations.

In order to meet these needs and to create a quantum-based electronic temperature standard, we have developed new technology in a number of different areas. We have constructed low-noise cross-correlation electronics, developed a nanoscale quantum voltage noise source (QVNS) specifically for this application, and performed the first calibrations of the electronics using the QVNS. We have compared the QVNS synthesized pseudo-noise voltage waveforms with the voltage noise of resistors in triple point cells of both gallium and water. We have also devised a novel ratiometric method that uses the QVNS to compare the voltage noise of resistors at different temperatures.

Accomplishments

- NIST has performed many comparisons between the Johnson noise voltage of a resistor in a gallium cell and the synthesized pseudo-noise waveforms of the quantum voltage noise source. Similar measurements have been done with a water triple-point cell. Measurements were made using the custom built cross-correlation electronics system. The computer-controlled optically-interfaced system correctly sampled at the 50 MHz sampling rate and stored and processed the waveforms in real time. This correlation electronics is different from other systems because we digitally process the signal in an FPGA before sending it to a computer. This is necessary to reduce the data rate to the computer.

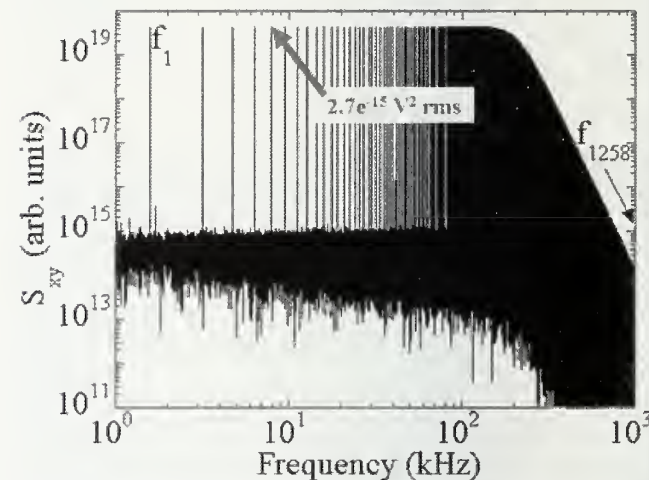


Figure 1. Log-log plot showing the measured spectrum of a QVNS-synthesized pseudo-noise waveform. The spectrum was measured with the JNT cross-correlated electronics and shows the power ($\langle V^2 \rangle$) spectrum S_{xy} of the 1258 tones synthesized by the QVNS. Each bin has a width of 1 Hz and is an average of 200 samples. The power spectrum is in arbitrary units based on the digitizer bins.

- NIST fabricated numerous circuits specifically to improve the performance and optimize the circuits for the JNT program. We have tested the circuits with appropriate pseudo-noise waveforms and demonstrated proper cross-correlation using an FFT spectrum analyzer. Benz also performed extensive measurements of input-output coupling for the JNT circuits and devised a novel unipolar bias method to decrease the coupling by about 40 dB. These results allowed us to take the next step and measure the arrays at much smaller voltages and higher bandwidth using cross-correlation electronics.
- NIST has continued development of the Johnson noise thermometry system. Unwanted distortion was observed when the Josephson signal was measured with the cross-correlation electronics. We were able to significantly reduce

this distortion by using inductive chokes on the input of the electronics. The cause of the distortion appears to be mixing in the first FET amplifier stage of 100 MHz to 400 MHz delta-sigma modulator tones synthesized by the Josephson array. With this dramatic improvement, the Josephson synthesized noise waveform and the gallium and water triple point cells were directly compared. We found agreement to 2 parts in 10^3 with a 1s uncertainty of 1×10^{-3} between the voltage noise of a 100 W resistor in a triple-point gallium cell ($T_{90} = 302.916$) and a pseudo-noise waveform with the same average power that is synthesized by a quantized voltage noise source. We estimate the temperature of the resistor to be $302.5 \text{ K} \pm 0.3 \text{ K}$ (1σ uncertainty based on the uncertainty from the cross-correlation). With better characterization of our JNT system, we expect to achieve relative accuracies of parts in 10^5 for arbitrary temperatures in the range between 27 K and 1000 K.

- We have proposed using a new “ratiometric method” that takes advantage of the linearity of the Josephson waveforms to independently compare different noise powers. The Johnson noise power at a known temperature is first balanced with a synthesized noise power from the QVNS. The process is then repeated by balancing the noise power from the same resistor at an unknown temperature. When the two noise power ratios are combined, a thermodynamic temperature can be derived where the scaling is accomplished by the ratio of the two QVNS spectral densities. Using this method, preliminary results of the ratio between the gallium triple point and the water triple point were used to demonstrate the accuracy of the measurement system with a standard uncertainty of 0.04 %.
- This year we have been able to measure the ratio of the gallium and water triple-point temperatures to within an accuracy better than $100 \mu\text{K/K}$ using the ratiometric method. This was accomplished by making improved Josephson circuits with smaller common mode signals, using flip-chip on flex packaging developed by the Quantum Voltage Project, and improving the output transmission lines and electrical connections in the electronics by eliminating distortion-producing poor contacts. Future efforts will focus on understanding the frequency dependence of the absolute measurements, which probably are due to the frequency response of the transmission line. These errors should be correctable or able to be reduced significantly. In the next year we also plan to perform more absolute and relative mode measurements at higher temperatures (273 K to 1000 K) through comparisons with an ITS-90 calibrated platinum resistance thermometer.

Selected Publications

1. S. Nam, S. Benz, P. D. Dresselhaus, W. L. Tew, D. R. White, and J. M. Martinis, “Johnson noise thermometry using a quantum voltage noise source for calibration,” Digest 2004 Conference on Precision Electromagnetic Measurements, 27 June – 2 July 2004, London, England, pp. 664-665 (2004).
2. S. Nam, S. Benz, P. D. Dresselhaus, and J. Martinis, “Johnson noise thermometry measurements using a quantized voltage noise source for calibration,” IEEE Transactions on Instrumentation and Measurement, 52, 2, pp. 550-554 (April 2003).
3. S. P. Benz, P. D. Dresselhaus, and J. Martinis, “An AC Josephson source for Johnson noise thermometry,” IEEE Trans. Instrum. Meas., 52, 2, pp. 545-549 (April 2003).
4. S. W. Nam, S. P. Benz, J. M. Martinis, P. D. Dresselhaus, W. L. Tew, and D. R. White, “A ratiometric method for Johnson noise thermometry using a quantized voltage noise source,” *Temperature: Its Measurement and Control in Science and Industry*, 7, (1), pp. 37-42, Dean C. Ripple Ed., Proc. The Eighth International Temperature Symp., AIP Conf. Proc. 684, New York: Melville (2003).
5. S. P. Benz, J. M. Martinis, S. W. Nam, W. L. Tew, and D. R. White, “A new approach to Johnson noise thermometry using a Josephson quantized voltage source for calibration,” Proc. TEMPMEKO 2001, the 8th Int'l. Symp. on Temperature and Thermal Measurements in Industry and Science, B. Fellmuth, J. Seidel, and G. Scholz, Eds., Berlin: VDE Verlag, pp. 37-44 (April 2002).

Quantum Communications

We develop and apply single-photon detectors (optical/infrared) for metrology and science. Our work is based on nanoscale detectors fabricated in our own laboratory.

Sae Woo Nam, EEEL (815)

New quantum-based communication and measurement systems that use single and correlated photons have been developed; however, the current tools to calibrate the components in these systems are inadequate for the emerging applications. For accurate calibration, a detector capable of determining the number of photons in a single pulse of light is needed. We are developing high-efficiency detector systems with this capability in the three telecommunication windows (850 nm, 1310 nm, and 1550 nm). These new instruments will also aid in the understanding and advancement of new photon sources such as the single-photon turnstile (SPT). They can be used as a spectroscopic diagnostic tool or characterization tool for optical elements, optical materials, and optical systems at ultra-low light levels. A near-term use of the detectors is for initial research in Quantum Key Distribution, a method of communication where security is assured by the laws of quantum mechanics rather than by mathematical complexity.

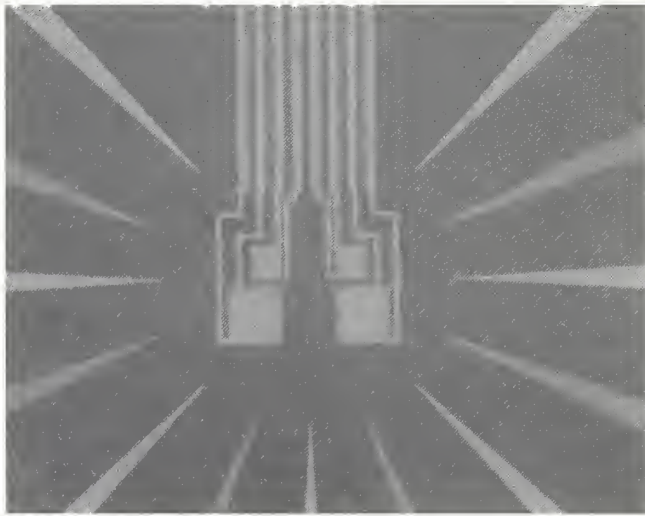


Figure 1. Array of four transition edge sensor (TES) singlephoton detectors. The larger squares are 50 μm on a side and the smaller ones are 25 μm . The arrows are for alignment.

Two distinct strategies are being pursued in this project. The first, which is best suited for counting photons at telecommunication wavelengths or measuring the energy of a single photon, is a refinement of superconducting

transition-edge sensor (TES) detector technology that was previously developed by the Quantum Devices Group and researchers at Stanford University. In this device a thin film of tungsten is cooled to its superconducting transition temperature (~ 100 mK). The tungsten is biased at its transition from the normal to superconducting state such that the input of a small amount of heat from the arrival of a single infrared photon, dramatically changes in the tungsten resistance. The change in resistance is proportional to the heat absorbed.

These TES detectors can be operated in two distinct modes, depending on the photon source properties. For single-wavelength (monochromatic) sources such as lasers and spontaneous parametric down-conversion (SPDC) crystals (used for quantum information and metrology) the sensor response is directly proportional to absorbed photon number (photon number discrimination mode). For broadband sources (such as white-light or multiple fluorescence emissions) the energy-resolving ability of the TES devices allows photon-counting spectroscopy to be performed across the entire near infrared/optical band (2 μm to 200 nm). In this mode, the photon number is discarded in favor of determining the energy (i.e., color) of the incoming photons (spectroscopic mode).

Over the past year we have increased the quantum efficiency of the TES detector system from less than 20 % to over 80 %. This was done by incorporating the tungsten film in a carefully designed “optical cavity” that prevents the incident photon from passing through the detector or reflecting off its face and increases the probability that a photon incident on the detector will be absorbed in the tungsten. Additional work is underway to eliminate losses in the fiber optic components that couple photons to the detector, made to increase the system detection efficiency. Our goal is to get as close as possible to 100% efficiency.

Conventional semiconductor-based single-photon detectors suffer from high rates of “dark counts” (false positives), at the communication wavelengths of 1300 nm and 1550 nm, which severely limit single-photon applications. The TES detectors have no intrinsic dark counts, allowing them to be operated at much lower light levels than any existing metrological instrument. As the efficiency of TES systems has increased this has led to the investigation of previously unknown sources of dark counts in fiber optic systems. One such source at 1,550 nm is now thought to be the black body radiation incident on a fiber at room temperature.

Their unparalleled sensitivity allows these detectors to be a significant tool in the development of quantum-based communication protocols and the evaluation of the security of optical quantum cryptographic systems.

The second technical strategy involves the use of a different type of superconducting detector. These detectors, called superconducting single photon detectors, or SSPDs, have been previously investigated at the University of Rochester. They incorporate a very narrow (~100 nm) serpentine line of metallic superconductor such as Nb or NbN carrying a bias current very close to its critical current. When a photon strikes the superconductor a small “hot spot” is created locally, reducing the critical current to a value below the bias current. This develops a voltage across the superconductor that can easily be detected. While the detector is not photon-number resolving (one or more photons will create the hot spot), it is extremely fast, producing pulses of order a few tens of picoseconds. Such a device would be potentially very useful in a quantum communication system. At the present time, these devices have very low quantum efficiency (a few percent) and are incapable of long-term unattended stable operation. We are initiating work to address both of these issues.

Accomplishments

- *Development of a process for reliably fabricating thin film tungsten detectors with a controllable transition temperature* — Previously tungsten films for TES had been successfully made at Stanford, at Munich Technical University, and at NIST, but only with low yield and widely varying properties. During 2004 a development program using statistical process control methodology was completed that enables us to deposit films with high yield and controllable T_c .
- *Increase in speed of TES detectors by 2 to 3x* — Improvements in the etching process used to pattern the TES detectors has resulted in improved edge definition and devices that are 2 to 3 times as fast as earlier-generation sensors.
- *Increase in TES system quantum efficiency from <20% to >80 %* — The reliable process for fabricating tungsten films has enabled us to explore a variety of configurations for increasing quantum efficiency. A structure incorporating a metallic mirror and dielectric layer below the tungsten and an anti-reflection layer on top has yielded 93 %+ absorption of 1,550 nm photons in the tungsten and an overall system efficiency over 80 %.
- *Fabrication of thin, high- T_c NbN films* — The development of SSPDs has been limited by the availability of thin (~4 nm) high T_c (~10 K) films. Previously these films were available from only one institution in Mos-

cow, Russia. In 2004 we succeeded in fabricating a series of films which initial tests indicate have large area T_c , equivalent to those from Moscow.

Selected Publications

1. S. Nam, A. J. Miller, and D. Rosenberg, “Low-temperature optical photon detectors for quantum information applications,” Nuclear Instruments and Methods in Physics Research A 520, pp. 523–526 (2004).
2. D. Rosenberg, S. W. Nam, A. J. Miller, A. Salminen, E. Grossman, R. E. Schwall, and J.M. Martinis, “Near-unity absorption of near-infrared light in tungsten films,” Nuclear Instruments and Methods in Physics Research A 520, pp. 537-540 (2004).
3. G. DiGiuseppe, M. Atatüre, M. D. Shaw, A. V. Sergienko, B. E. A. Saleh, M. C. Teich, A. J. Miller, S. W. Nam, and J. Martinis, “Direct observation of photon pairs at a single output port of a beam-splitter interferometer,” Physical Review A (Atomic, Molecular, and Optical Physics) 68(6): pp. 1 63817-1-4, (December 2003).
4. A. J. Miller, S. W. Nam, J. M. Martinis, and A. V. Sergienko, “Demonstration of a low-noise near-infrared photon counter with multiphoton discrimination,” Appl. Phys. Lett., 83 (4): pp. 791-793 (28 July 2003).
5. J. M. Martinis, “Electronics for arrays of transition edge sensors using digital signal processing,” IEEE Transactions on Applied Superconductivity 13(2): pp. 618-21, (June 2003).
6. B. Cabrera, J. M. Martinis, A. J. Miller, S. W. Nam, and R. W. Romani, “TES spectrophotometers for near IR/optical/UV,” Proc., 9th Int'l Workshop on Low Temperature Detectors, 22- 29 July 2001, Madison, WI, pp. 565-570 (2002).

Quantum Computing Using Superconducting Phase Qubits

We develop techniques for making highly coherent quantum systems using integrated circuits. This includes developing new high-fidelity measurement techniques for quantum systems. Ultimately, we would intend to help make large-scale quantum information processing systems a reality. All of the nanoscale circuits for our work are made in our laboratory.

Ray Simmonds, EEEL (817)

The integrated circuit components of classical computers are rapidly approaching the so-called “quantum limit.” Instead of avoiding quantum effects, we have the opportunity to exploit them as a means for more effective computation. A quantum computer has the ability to use the intrinsic properties of quantum systems to naturally perform parallel processing during a calculation. This allows a quantum computer to solve problems considered intractable for classical computers. Three such problems have been of considerable interest: discrete logarithms, factorization, and search algorithms for large databases. The practical significance of building a successful large-scale quantum computer is tremendous. It could

- Provide a powerful tool for encryption. A quantum computer is seen as the only instrument that could break the most secure encryption codes in use today. This is an immensely important subject for national security.
- Solve highly complex (many-body) problems in a reasonable amount of time. This will become increasingly important for the chemical and biological sciences.
- Provide rapid search engines to help navigate us through the information age.
- Allow us to simulate large quantum systems efficiently.

In a conventional computer, information is often stored as electrical charge on tiny capacitors. The presence or absence of charge stored on a single capacitor represents a (classical) bit, which can represent two (classical) information states “0” and “1.” All logical computations are done using groups and combinations of this binary information. A quantum bit or “qubit” is described in terms of two quantum states denoted by “|0>” and “|1>”. Remarkably, a quantum bit can be placed in a state that is a mixture of both “|0>” and “|1>”! Even more remarkable is the fact that multiple qubits can be placed in a massive mixture of all combinations of their possible states, a phenomenon known as entanglement.

Entanglement is the “magic” of quantum mechanics and allows a quantum computer to stir up quantum information in order to produce a meaningful calculation with incredible speed. Whether or not quantum computing becomes practi-

cal, our work will produce new knowledge for the precise measurement of quantum systems. Through our research with quantum-mechanical superconducting circuits, we are learning how to directly control and measure quantum systems in new ways. We have already shown (as described below) the ability to detect previously unknown nanoscale quantum systems that could never be seen before. By gaining the ability to control quantum systems directly, we are exploring untouched regimes of nature and may find ways to direct unforeseen advancements in nanotechnology.

Although this project began only three years ago, we have made significant progress over this short period. The first qubit design used a current-biased Josephson junction made from niobium with an amorphous aluminum-oxide tunnel barrier. It was successful in showing Rabi oscillations by varying the power of the microwave drive. The energy relaxation time was 300 ns, and the Rabi decay time was estimated to be 10 ns. The next qubit showed a reduction in excess tunneling events caused by quasiparticle heating.

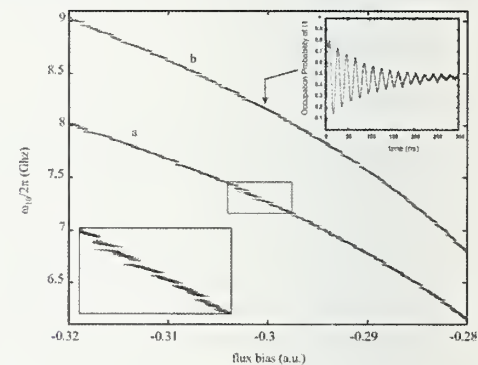


Figure 1. An example of qubit spectroscopy for qubits (a) and (b) showing the transition frequency ω_{10} for various flux biases to the qubit loop. Notice the small “splittings” indicative of microscopic quantum systems residing within the tunnel junction coupling to our superconducting quantum bit. Top inset shows Rabi oscillations away from resonators.

Accomplishments

- *Developed a New Flux Biased Josephson Phase Qubit* — We developed a new qubit design that is well isolated from the external environment while still providing an extremely sensitive readout. In addition, this qubit does not generate quasiparticles during measurement. This system has shown Rabi oscillations with up to 75 % visibility with 100 ns decay times. We have also seen energy relaxation times as long as 500 ns.
- *Discovered Spurious Resonators Within Josephson tunnel Junctions* — Using our new improved qubit we have developed spectroscopic measurements of the qubit transition frequency over a wide range of possible operating flux

biases. In doing so, we discovered nanoscopic spurious resonators within the tunnel junctions of the qubit. Elimination of these resonators in future Josephson junctions could improve the performance of *all* superconducting devices.

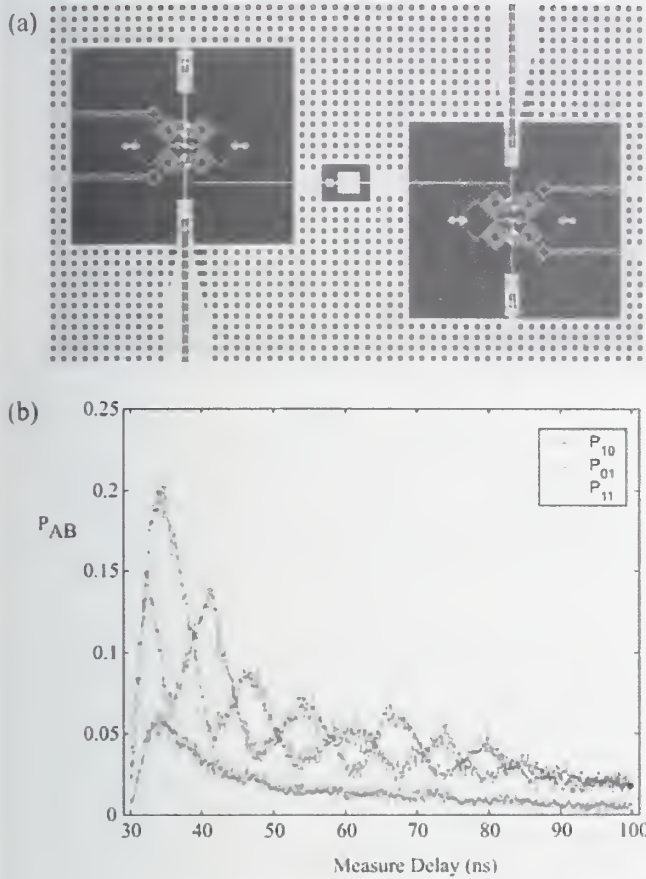


Figure 2. (a) A fabricated coupled qubit circuit. (b) Simultaneous measurement of two coupled qubits during state oscillations.

- *Developed a Method for Characterizing Tunnel Junctions and Phase Qubits* — Using a low frequency nonlinear current bias, we have developed an effective way to measure extremely small quasiparticle currents in the current-voltage characteristics of tunnel junctions fabricated using various novel methods. These measurements are then correlated with qubit spectroscopy, Rabi oscillations, and energy relaxation times in order to characterize the performance of these new tunnel junctions and the qubits that incorporate them.

- *Developed a New, Faster Method to Read Out the Phase Qubit* — We have implemented a new qubit state-measurement technique that is a faster order of magnitude than our former method. In this new method, with a temporal resolution of less than 5 ns, a flux bias pulse is applied to the qubit so that the $|1\rangle$ state, if occupied, is suddenly presented with a very small energy barrier, through which it rapidly tunnels. This new advance has allowed us to monitor rapid qubit state variations, opening the door to tracking

strongly coupled interactions between phase qubits and other quantum systems.

- *Observed Quantum Oscillations Between a Josephson Phase Qubit and a Nanoscopic Resonator* — We have detected coherent quantum oscillations between Josephson phase qubits and two-level resonator within the tunnel barrier of a superconducting phase qubit. These results reveal a new aspect of the quantum behavior of Josephson junctions, and they demonstrate the means to measure two-qubit interactions in the time domain. The junction-resonator interaction also points to a possible mechanism for decoherence and reduced fidelity in superconducting qubits.

- *Coupled-Qubit Interactions* — Through the first ever simultaneous measurement of two superconducting qubits, we have recently witnessed two coupled phase qubits entangle themselves by performing coherent state oscillations. This is a tremendous step forward! Soon, we hope to have the ability to perform simple logic operations between two qubits, the building blocks for a full scale quantum computer.

Selected Publications

1. K. B. Cooper, M. Steffen, R. McDermott, R. W. Simmonds, S. Oh, D. A. Hite, D. P. Pappas, and J. M. Martinis, “Observation of quantum oscillations between a Josephson phase qubit and a microscopic resonator using fast readout,” cond-mat/0405710 accepted by Phys. Rev. Lett. (2004).
2. R. W. Simmonds, K. M. Lang, D. A. Hite, D. P. Pappas, J. M. Martinis, “Decoherence in Josephson phase qubits from junction resonators,” Phys. Rev. Lett. 93, 077003 (2004).
3. J. M. Martinis, S. Nam, J. Aumentado, K. M. Lang, C. Urbina, “Decoherence of a superconducting qubit due to bias noise,” Phys. Rev. B 67, 094510 (2003).
4. J. M. Martinis, S. Nam, J. Aumentado, and C. Urbina, “Rabi oscillations in a large Josephson-junction qubit,” Phys. Rev. Lett. 89, 117901 (2002).

Quantum Sensors

NIST has developed detector systems that are redefining the measurement abilities of currently available technology, often by orders of magnitude, and continues to develop groundbreaking detector systems for both industry and research groups. Our sensors are based on quantum phenomena for spectroscopy, imaging, and other precision measurements for wavelengths from dc through gamma rays. We integrate these sensors with custom superconducting and room temperature electronics, cryogenic structures and software to create complete measurement systems. Applications of this measurement capability include materials analysis, astronomy, and homeland defense. We design some of our sensors to make them capable of chemically analyzing samples smaller than 100 nm.

Kent Irwin, EEEL (817)

By operating at temperatures below 1 K, a new generation of photon detectors is achieving unparalleled sensitivity in measuring very small differences in the energy of photons. At these low temperatures, they are able to take advantage of quantum phenomenon, including quantum interference (SQUIDs), quantum phase transitions (superconducting transition-edge sensors), and quantum tunneling (normal-insulator-superconductor tunnel junctions). As a world leader in developing these new detector systems, NIST has developed transition edge sensor (TES) bolometers for use in a variety of applications. These devices utilize a strip of superconducting material, biased in its transition from normal to superconducting states, as an extremely sensitive thermometer. This thermometer is attached to an absorber that is isolated from a cold (~ 100 mK) heat sink by a micromachined structure. The heat deposited by incident photons is then measured to accurately determine their energy.

Applications of our nanoscale sensors include ultra-high-resolution X-ray spectroscopy for materials analysis for the semiconductor industry, and the development of large scale arrays of quantum sensors for high-throughput imaging and spectroscopy of electromagnetic radiation for materials analysis and astronomy. In the International Technology Roadmap for Semiconductors, improved X-ray detector technology is identified as one of the most important metrology needs for the semiconductor industry to help address analysis requirements for small particles and defects. NIST's TES microcalorimeter X-ray detectors have been identified as a primary means of realizing these detector advances, which will greatly improve in-line and off-line metrology tools that currently use semiconductor energy-dispersive spectrometers (EDS). In addition, the astronomy community has an ever increasing need for instruments

capable of supplying extremely high energy-sensitivity coupled with large-format arrays for imaging and photon collection. TES detector arrays promise to greatly expand the abilities of astronomers to study objects ranging from solar flares to supernova remnants to the formation of galaxies. The Quantum Sensor project has formed collaborations to transfer our TES technology into astronomical instruments with several institutions, including NASA, Stanford University, the Lockheed-Martin Solar Astrophysics Laboratory and the UK Astronomy Technology Center.

Accomplishments

- NIST has developed x-ray detectors of extremely high energy resolution and demonstrated a complete x-ray spectroscopy system. This detector and spectrometer have been made possible by our broad expertise in such fields as superconductivity, device fabrication including silicon micromachining, superconducting electronics, cryogenic engineering, and low-noise, room temperature electronics.

A significant accomplishment has been to demonstrate world-record energy resolution for an EDS detector of 2.4 eV at 5900 eV (see Figure 2), which is over 30 times better than the best high resolution semiconductor-based detectors currently available. We have used the system to identify nanometer particles of materials such as W on Si substrates, an identification problem that is impossible with standard EDS detectors and of great importance to the semiconductor industry. It has also demonstrated energy shifts in the EDS X-ray spectra of materials such as Al, Fe, and Ti, depending on their chemical bonding state, thus allowing differentiation between a particle of Al and Al_2O_3 , for example.

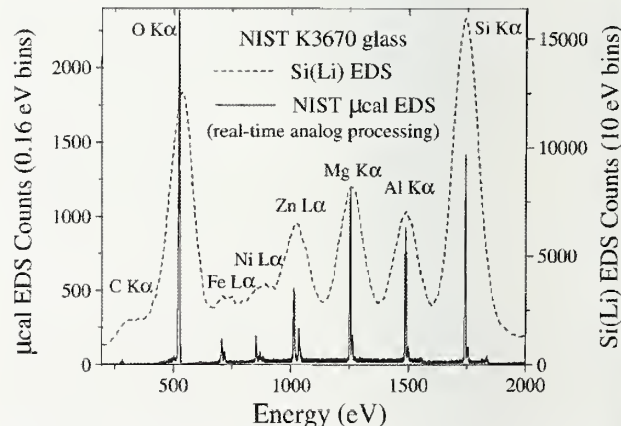


Figure 1. Comparison of resolutions of NIST microcalorimeter EDS to standard semiconductor EDS.

- We have made significant progress towards fabricating a practical on-chip, solid-state microrefrigerator using Normal metal – Insulator – Superconductor (NIS) tunnel

junctions. Presently, cryogenic instruments that operate near 100 mK use complex, expensive adiabatic demagnetization refrigerators and dilution refrigerators. The thin-film microrefrigerators are compact and readily integrated on-chip with devices requiring sub-kelvin cooling such as microcalorimeter X-ray spectrometers for X-ray microanalysis. We have fabricated an NIS refrigerator designed to operate at bath temperatures of 300 mK, which is accessible with relatively simple and inexpensive ^3He refrigerators. These are the largest working NIS refrigerators made to date and the only ones fabricated with photolithographic techniques.

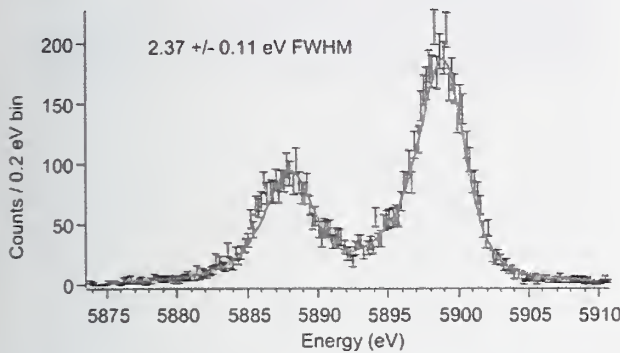


Figure 2. World-record 2.4 eV energy resolution achieved with NIST microcalorimeter at 6 keV.

- We have demonstrated the first multiplexed readout of an X-ray microcalorimeter array, using time-division SQUID multiplexing to read out many detectors through a single amplifier. This breakthrough establishes a clear path to the instrumentation of kilopixel microcalorimeter arrays, which will have wide-ranging implications for fields as diverse as materials analysis and X-ray astronomy. In the experiment, the multiplexed TES detectors measured the energy of 5.9 keV X-rays emitted from an ^{55}Fe source with an average resolution of 6.94 ± 0.05 eV, which represents only a small and well-understood degradation in resolution from the non-multiplexed performance of the detectors. We believe that we can multiplex 32 detectors with an energy-resolution degradation of only 0.1 eV. This would allow a square, 1024-detector array to be read out with only 32 signal channels.

- We have demonstrated the first microwave SQUID multiplexer. This breakthrough opens a path to reading out very large arrays of SQUIDs for magnetoencephalography and non-destructive evaluation, and CCD-scale arrays of low-temperature detectors. In this circuit, the outputs of many SQUID amplifiers are simultaneously monitored by a single high electron mobility transistor (HEMT) amplifier channel. Each SQUID amplifier is placed in a high-Q resonant circuit with a different resonant frequency, and excited by a comb of microwave signals at each of the resonant frequencies. The amplitude of the reflected microwave signals at each frequency is a function of the input signal at each SQUID. In an initial experiment, we demonstrated the

low-noise readout of SQUIDs using this microwave reflectometer approach, and multiplexed two SQUIDs simultaneously near 500 MHz. Future work will focus on operation at 5 GHz and developing technology for much larger SQUID arrays. Because of the large bandwidth available with microwave measurements, it should be possible in the future to read out many thousands of SQUIDs in a single coaxial cable, and to instrument arrays of SQUIDs with thousands or millions of pixels.

- We have developed a surface micromachining method for producing freestanding pixels above the surface of a silicon wafer. This process has been integrated into the X-ray TES fabrication process, and TES devices have been produced and cooled down.
- We have delivered a full, 1,280-pixel multiplexed submillimeter bolometer array to the SCUBA-2 project. This is the first true submillimeter camera available to the community.

Selected Publications

- A. M. Clark, A. Williams, S. T. Ruggiero, M. L. van den Berg, and J. N. Ullom, "Practical electron-tunneling refrigerator," *Appl. Phys. Lett.* 84 (4): pp. 625-627; 26 (January 2004).
- J. N. Ullom, W. B. Doriese, G. C. Hilton, J. A. Beall, S. Deiker, W. D. Duncan, L. Ferreira, K. D. Irwin, C. D. Reintsema, and L. R. Vale, "Characterization and reduction of unexplained noise in superconducting transition-edge sensors," *Appl. Phys. Lett.* 84(21): pp. 4206-4208 (May 24, 2004).
- J. P. Pekola, R. J. Schoelkopf, and J. N. Ullom, "Cryogenics on a Chip," *Physics Today* 57(5): pp. 41 (May 2004).
- K. D. Irwin and K. W. Lehnert, "Microwave SQUID multiplexer," *Appl. Phys. Lett.* 85 (11): pp. 2107-2109 (2004).
- W. B. Doriese, J. A. Beall, S. Deiker, W. D. Duncan, G. C. Hilton, K. D. Irwin, C. D. Reintsema, J. N. Ullom, L. R. Vale, and Y. Xu, "Time-division multiplexing of high-resolution TES X-ray microcalorimeters: Four pixels and beyond," *Appl. Phys. Lett.*, 85: 4762 (2004).
- J. Beyer, D. Drung, and K. D. Irwin, "Bias conditions of DCSQUID for a time-domain SQUID multiplexer," *Review of Scientific Instruments*, 75, pp. 502 (1994).

Single Electronics for Standards and Metrology

NIST has developed novel integrated circuits for standards and metrology based on the unique properties of electronic devices that can manipulate and detect individual electrons. In our laboratory we fabricate these circuits that have all three dimensions on the nanoscale.

Mark Keller and Neil Zimmerman, EEEL (817)

This project addresses three different needs: a fundamental representation of capacitance, a fundamental representation of electrical current, and general applications of nanoscale single-electron tunneling (SET) devices, with a particular emphasis on future integrated nanoelectronics.

For the first need, NIST is developing intrinsic standards based on fundamental physical principles, such as the volt, based on the Josephson effect, and the ohm, based on the quantum Hall effect. The present representation of the SI farad is through silica-based artifact capacitors. Although these capacitors are of high quality, they are susceptible to drift in time and may depend on other parameters such as temperature, pressure, and frequency. The metrology community needs a capacitance representation that is based on fundamental physical principles rather than on properties of individual physical artifacts.

For the second need, at present, there is no fundamental representation of current; the representation of current is via the representations of voltage and resistance. Though these representations are based on fundamental physical principles and are of high quality, the representation of current is dependent upon them. An independent representation of current could provide significant additional confidence in the coherency of the representations of the SI electrical units through closure of the “metrology triangle” $V = I R$ with all measurements based on fundamental constants.

For the third need, various classes of future nanoelectronics beyond CMOS are projected to work with one or a few electrons. These include molecular electronics, semiconductor-based integrated circuits using single-electron memory or logic, and quantum computing (QC). We are using our expertise to elucidate properties of transfer of superconducting “Cooper pairs,” which are the basic mechanism for one realization of QC circuits. We are also addressing an endemic problem in single-electron logic, the “charge offset” phenomenon, which makes it difficult or impossible to integrate multiple SET-based devices together.

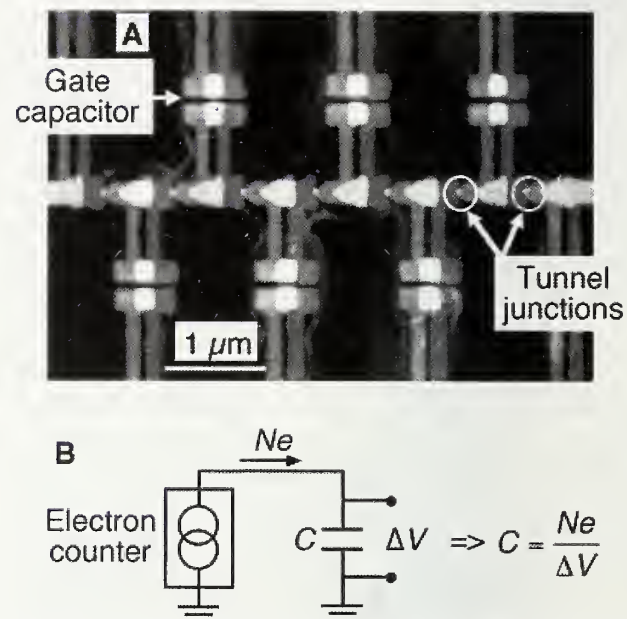


Figure 1. Atomic force microscope image of an electron counter, the heart of a new capacitance standard based on counting electrons. The standard, shown in the schematic, consists of the electron counter, a capacitor, and a single-electron electrometer (not shown) to monitor the process. The electron counter, based on seven nanometer-scale tunnel junctions in series, can “pump” electrons onto the capacitor with an error rate of less than 1 electron in 10^8 .

Accomplishments

- Electron Counting Capacitance Standard Demonstrated—The components of the prototype ECCS standard demonstrated by NIST are illustrated in the figure. The electron counter can “pump” electrons onto the capacitor with an error rate of less than one electron in 10^8 . The electron pumping is monitored with an SET-based electrometer fabricated on the same chip as the pump, with a charge sensitivity better than 10^{-2} electrons. The capacitor operates at cryogenic temperatures and uses vacuum as the dielectric, resulting in a frequency-independent measure of capacitance. To operate the ECCS, approximately 100 million electrons are placed, singly, on the capacitor. The voltage across the capacitor is measured, resulting in a calibration of the cryogenic capacitor. This capacitance can then be transferred to room temperature by use of a standard ac bridge measurement technique. The result is a value of capacitance with a repeatability of one part in 10^7 .
- Quasiparticle Poisoning in Cooper Pair Transistors—In collaboration with Professor Michel Devoret (Yale), we have experimentally verified a model for erratic quasiparticle tunneling in superconducting Cooper pair transistors (these are the superconducting versions of the SET). This phenomenon, quasiparticle “poisoning,” will limit the operation of the superconducting Cooper pair pump as well as

charge-based qubits. Our work showed that the gap energies in the leads versus the island played a significant role in determining these poisoning rates. In addition, we have confirmed a “remote poisoning” phenomena, whereby a voltage-biased junction device can cause poisoning in other devices on the same chip, even if it is electrically isolated. This has important implications for the electrometry that we will use in the Cooper pair pump, as well as in charge-based qubits.

- rf-SET demonstrated — NIST has demonstrated operation of a rf-SET, a version of an SET electrometer read out by microwave reflectometry. This approach greatly increases the bandwidth of the electrometer (to 3 MHz in our present setup) and improves the charge resolution (to 50 $\mu\text{e}/\text{Hz}^{1/2}$). This is the basic technology we will use to perform the passive electron counting experiments. Future work will focus on expanding the bandwidth and narrowing the charge resolution to perform better than the quantum limit.

- SET Electronics Developed to Probe GaAs Quantum Dots for Single Photon Source* — The past two years have produced significant progress towards the development of a single-photon turnstile, a device designed to generate single photons on demand using semiconductor quantum dots (QD) and single-electron principles. A key step towards this goal is to measure the tunneling of single electrons onto individual quantum dots. We have succeeded in making these measurements by integrating an SET electrometer over a low density field of GaAs quantum dots. A schematic cross-section of the device is shown below, along with a scanning electron micrograph of the SET electrometer. Using these devices, we have clearly identified the addition of single electrons onto single quantum dots located below the SET. We have counted up to 3 electrons added to a single dot, and have measured the energy spectrum associated with adding electrons on this dot.

- Si-based Pumps Turnstiles, CCDs Demonstrated* — Our work in collaboration with a group in NTT, Japan, has made a great deal of progress in investigating Si-based devices that can control the motion of single electrons. In the past two years, we have demonstrated such control in three different types of devices: pumps, turnstiles, and CCDs. The most promising device for the future is the CCD, both because we have recently demonstrated in subsequent work that such devices can be made with improved reliability and homogeneity, and because we demonstrated that this device has the potential to run at higher speed. In one of our publications we showed that the CCD can pump single electrons at rates as fast as 100 MHz, corresponding to 15 pA; this is an improvement by about a factor of 5 over previous results in metal-based pumps. However, we have to note that we were not able to measure error rate in detail in the CCDs; this work is now in progress.

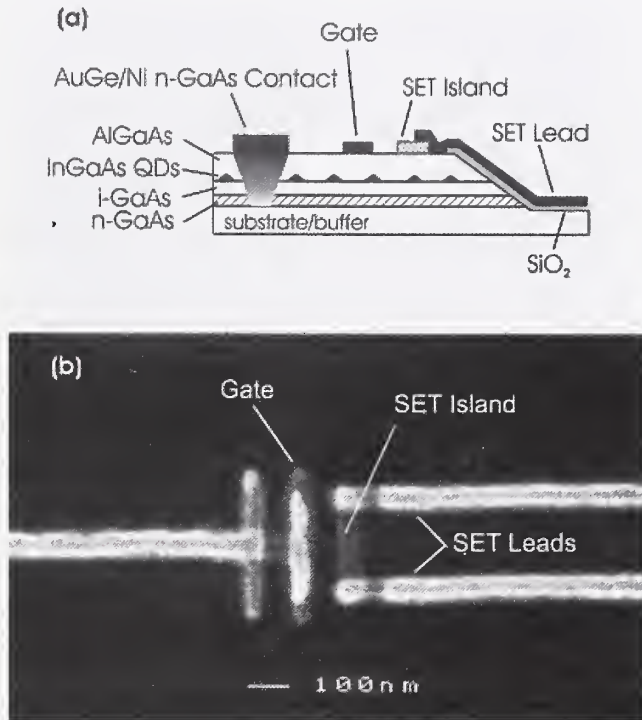


Figure 2. (a) Schematic cross-section of our SET electrometer integrated on a GaAs chip containing self-assembled quantum dots. (b) SEM micrograph of an SET electrometer. We have identified single-electron tunneling events into individual quantum dots located beneath the electrometer.

Selected Publications

1. X. Jehl, M. W. Keller, R. L. Kautz, J. Aumentado, and J. M. Martinis, “Counting errors in a voltage-biased electron pump,” Phys. Rev. B 67, 165331-1 - 165331-9.
2. N. M. Zimmerman, M. A. El Sabbagh, and Y. Wang, “Larger value and SI measurement of the improved cryogenic capacitor for the electron-counting capacitance standard,” IEEE Trans. Instrumentation and Measurement 52, pp. 608-11 (2003).
3. A. Fujiwara, N. M. Zimmerman, Y. Ono, and Y. Takahashi, “Current quantization due to single-electron transfer in Si-wire charge-coupled devices,” Appl. Phys. Lett. 84, pp. 1323 (2004).
4. K. D. Osborn, M. W. Keller, and R. P. Mirin, “Single-electron transistor spectroscopy of InGaAs self-assembled quantum dots,” Physica E 21, pp. 501-505 (2004).
5. J. Aumentado, M. W. Keller, J. M. Martinis, and M. H. Devoret, “Nonequilibrium quasiparticles and 2e periodicity in single-Cooper-pair transistors,” Phys. Rev. Lett. 92, pp. 066802 (2004).

Quantum Voltage Metrology

NIST is meeting the nation's voltage metrology needs by developing state-of-the-art precision dc and ac voltage standard systems and by providing high-performance voltage measurements founded on nanoscale quantum-based superconducting circuit and system technology. In our facility we fabricate for our standards the most complex superconducting nanoscale circuits in the world.

Samuel Benz and Yi-hua Tang, EEEL (817)

An international agreement signed in 1990 redefined the practical volt in terms of the voltage generated by a superconductive integrated circuit developed at NIST and the Physikalisch-Technische Bundesanstalt in Germany. This circuit contains thousands of superconducting Josephson junctions, all connected in a series array and biased at a microwave frequency. The voltage developed by each junction depends only on the frequency and a fundamental physical constant; thus, the circuit never needs to be calibrated. This allows any standards or commercial laboratory to generate highly accurate voltages without the need to calibrate an artifact standard. This advance has improved the uniformity of voltage measurements around the world by about a hundred-fold. These systems are rapidly becoming essential for meeting legal and accreditation requirements in commercial, governmental, and military activities.

The U.S. electronics instrumentation industry maintains its world-leading position through the development and deployment of accurate, flexible, and easy-to-use instruments. This increasingly sophisticated instrumentation places mounting demands for higher accuracy voltage metrology both in calibration and testing laboratories and on production lines and factory floors. NIST meets this need by providing some customers who need immediate realization of the highest possible in-house accuracy with their own quantum voltage standard systems, and other customers with a calibration service for their Zener voltage references. NIST provides the foundation for voltage metrology that enables the U.S. electronics instrumentation industry to compete successfully in the global market. Through this strong voltage metrology foundation, NIST also supports scientific research in high accuracy voltage measurements for the standards and superconductive electronics communities and the U.S. military.

Accomplishments

- In early 2004, the NIST voltage metrology laboratory moved into the new Advanced Metrology Laboratory (AML) to take advantage of its superior control of environmental parameters such as temperature and humidity. This challenging move demonstrated that our nanoscale quantum-based voltage measurement system is very robust and we verified that its performance was equivalent to that in the existing measurement laboratory.
- NIST has increased by tenfold the junction density of Josephson arrays. This was achieved by vertically stacking 10 superconducting Josephson junctions on top of each other at a spacing of 45 nm. The biggest challenge was to vertically etch the stacked thin films so that the junctions in the stacks have the same area and achieve the same electrical characteristics. This was achieved and demonstrated by measuring the electrical characteristics of 1000 stacked arrays with and without a 9 GHz microwave bias. The resulting voltage steps were flat; that is, they produced a precision constant voltage, based on the Josephson effect, over a large current range of 1 mA. This large operating range indicates impressive uniformity for these nano-stacked arrays and significant progress toward our goal of using nanotechnology to increase the performance of ac and dc voltage standard systems. Higher junction density is required to increase the output voltage as well as the operating bandwidth of the superconducting circuits whose quantum mechanical properties enable precise synthesis of arbitrary waveforms.
- Using nano-stacked Josephson junction arrays, NIST has more than doubled the precision stable output voltage for programmable voltage standard circuits. The stacks are made by alternately sputtering multiple normal metal layers of molybdenum disilicide between superconducting niobium layers. The stacks are then interconnected in series with superconducting wiring in order to create a long series-connected array of junctions for the maximum output voltage. For the past few years, the record output voltage for programmable Josephson voltage standards has been limited to about 1 V. These new fabrication techniques have allowed us to double and triple the number of junctions in the circuit, which, combined with a small increase in the drive frequency from 16 GHz to 19 GHz, has allowed us to reach 2.5 V maximum output voltage. The circuit can produce precision output voltage over a current range of 1 mA and over a frequency range from 14 to 19 GHz. The operating current and frequency ranges are also large compared to previous programmable circuits and indicate good uni-

formity for the 67,410 total junctions. This is the first successful application of stacked Josephson junctions, and the results suggest that further output voltage improvements may result from taller stacks and larger arrays.

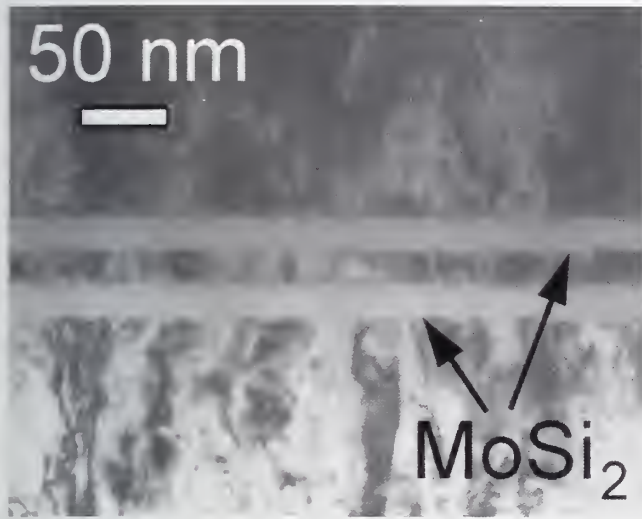


Figure 1. Transmission electron microscope (TEM) image of a two-junction stack with molybdenum-disilicide barriers and niobium outer and middle electrodes. The image shows that the MoSi_2 deposits uniformly the niobium, even when the niobium is as thin as 20 nm. (Image by John Bonevich-MSEL, NIST)

- This year we have developed and combined three new technologies to create an improved, more robustly packaged programmable voltage standard with higher performance. First, we built a new circuit that produces 50-times higher voltage resolution. We also developed a flexible, microwave-compatible cryopackage that improves electrical contact reliability. By combining these two breakthroughs with previously demonstrated stacked-junction fabrication technology, we have assembled a robust, cryopackaged programmable voltage standard that produces a record 2.6 V output with $77 \mu\text{V}$ resolution using the same electronics. The new standard will replace an older programmable circuit in the voltage calibration lab that was capable of 1 V output and 4 mV resolution. The novel superconducting integrated circuit of this new system uses a ternary-logic design to achieve the increased voltage resolution. As compared to previous double-stacked circuits and the older non-stacked programmable circuit, the double-stacked junction uniformity was improved, effectively increasing the operating margins two-fold to 2 mA for full chip operation.

The new cryopackage uses a “flip-chip on flex” technology that we hope will improve the service life and reliability of our Josephson systems, because directly soldered connections to the chip replace less reliable press contacts. The system is currently being implemented in the voltage calibration service.

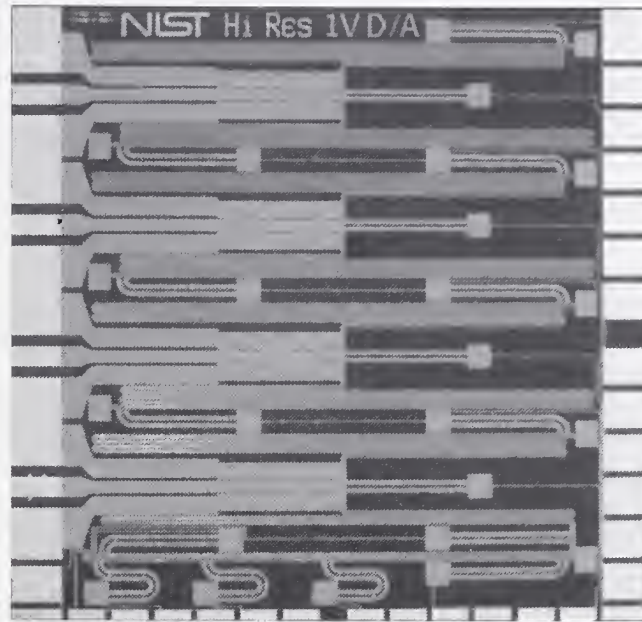


Figure 2. A 1 cm \times 1 cm superconducting integrated circuit with 67,406 double-stacked SNS Josephson junctions for the 2.6 V high-resolution PJVS operating at 18.5 GHz.

Selected Publications

1. S. P. Benz and C. A. Hamilton, “Application of the Josephson effect to voltage metrology,” invited paper, Proc., IEEE 92, (10) (October 2004).
2. M. Ishizaki, H. Yamamori, A. Shoji, P. D. Dresselhaus, and S. P. Benz, “A programmable Josephson voltage standard chip using arrays of $\text{NbN}/\text{TiN}/\text{NbN}/\text{TiN}/\text{NbN}$ double-junction stacks operated at 10 K,” Digest, 2004 Conference on Precision Electromagnetic Measurements, 27 June–2 July 2004, London, England, pp. 8-9 (June 2004).
3. Y. Chong, P. D. Dresselhaus, and S. P. Benz, “Thermal transport in stacked superconductor–normal metal–superconductor Josephson junctions,” Applied Physics Letters 83, (9), pp. 1794-1796 (1 September 2003).
4. P. D. Dresselhaus, Y. Chong, J. H. Plantenberg, and S. P. Benz, “Stacked SNS Josephson Junction Arrays for Quantum Voltage Standards,” IEEE Trans. Applied Superconductivity, 13, (2), pp. 930-933 (June 2003).
5. C. J. Burroughs, S. P. Benz, and P. D. Dresselhaus, “AC Josephson voltage standard error measurements and analysis,” IEEE Trans. Instrumentation and Measurement, 52, (2), pp. 542-544 (April 2003).

Architectures for Fault-tolerant Quantum Computing

In theory, quantum computers can efficiently simulate quantum physics, factor large numbers and estimate integrals, thus solving computational problems that are otherwise intractable. In practice, quantum computers must operate with noisy devices called “gates” that tend to destroy the fragile quantum states needed for computation. The goal of fault-tolerant quantum computing is to compute accurately even when gates have a high probability of error each time they are used. We are developing architectural concepts and error remediation strategies which will enable the development of practical quantum computing devices.

Emanuel Knill, ITL (891)

Research in quantum computing is motivated by the great increase in computational power offered by quantum computers. There are a large and still growing number of experimental efforts whose ultimate goal is to demonstrate scalable quantum computing. Scalable quantum computing requires that arbitrarily large computations can be efficiently implemented with little error in the output.

One of the criteria necessary for scalable quantum computing is that the level of noise affecting the physical gates is sufficiently low. The type of noise affecting the gates in a given implementation is called the *error model*. A scheme for scalable quantum computing in the presence of noise is called a *fault-tolerant architecture*. In view of the low-noise criterion, studies of scalable quantum computing involve constructing fault-tolerant architectures and providing answers to questions such as the following:

Q1: Is scalable quantum computing possible for error model E?

Q2: Can fault-tolerant architecture A be used for scalable quantum computing with error model E?

Q3: What resources are required to implement quantum computation C using fault-tolerant architecture A with error model E?

To obtain broadly applicable results, fault-tolerant architectures are constructed for generic error models. In such cases, the error model is parameterized by an error probability per gate (or simply error per gate, EPG), where the errors are unbiased and independent. The fundamental theorem of scalable quantum computing is the *threshold theorem* which answers question Q1 as

follows:

If the EPG is smaller than a threshold, then scalable quantum computing is possible.

Thresholds depend on additional assumptions on the error model and device capabilities. Estimated thresholds vary from below 10^{-6} to 3×10^{-3} , with 10^{-4} often quoted as the target EPG for experimental realizations of quantum computing.

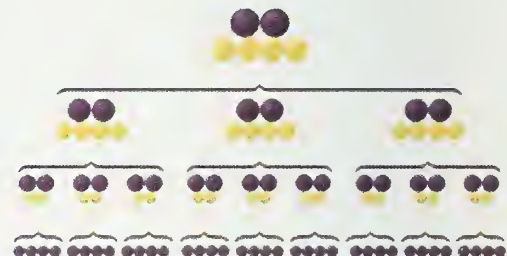


Figure 1. The new NIST architecture for quantum computing relies on several levels of error checking to ensure the accuracy of quantum bits (qubits). The image above illustrates how qubits are grouped in blocks to form the levels. To implement the architecture with three levels, a series of operations is performed on 36 qubits (bottom row) each one representing a 1, a 0, or both at once. The operations on the nine sets of qubits produce two reliably accurate qubits (top row). The purple spheres represent qubits that are either used in error detection or in actual computations. The yellow spheres are qubits that are measured to detect or correct errors but are not used in final computations.

Many experimental proposals for quantum computing claim to achieve EPGs below 10^{-4} in theory. However, in the few cases where experiments with two quantum bits (qubits) have been performed, the EPGs currently achieved are much higher, 3×10^{-2} or more in ion traps and liquid-state nuclear magnetic resonance (NMR) experiments, for example.

In our work we have provided evidence that scalable quantum computing is possible at EPGs above 3×10^{-2} . While this is encouraging, the fault-tolerant architecture that achieves this is extremely impractical because of large resource requirements. To reduce the resource requirements, lower EPGs are required.

We have developed a fault-tolerant architecture, called the *C₄/C₆ architecture* that is well suited to EPGs between 10^{-4} and 10^{-2} . We have analyzed the resource requirements for this architecture and compared it to the state of the art in scalable quantum computing.

The Architecture

Fault-tolerant architectures realize low-error qubits and gates by encoding them with error-correcting codes. A standard technique for amplifying error reduction is concatenation. Suppose we have a scheme that, starting with qubits and gates at one EPG, produces encoded qubits and gates that have a lower EPG. Provided the error model for encoded gates is sufficiently well behaved, we can then apply the same scheme to the encoded qubits and gates to obtain a next level of encoded qubits and gates with much lower EPGs. Thus, a concatenated fault-tolerant architecture involves a hierarchy of repeatedly encoded qubits and gates. The hierarchy is described in terms of levels of encoding, with the physical qubits and gates being at level 0. The top level is used for implementing quantum computations and its qubits and gates are referred to as being *logical*. Typically, the EPGs decrease superexponentially with number of levels, provided that the physical EPG is below the threshold for the architecture in question.

The C₄/C₆ architecture differs from previous ones in five significant ways. First, we use the simplest possible error-detecting codes, thus avoiding the complexity of even the smallest error-correcting codes. Error correction is added naturally by concatenation. Second, error correction is performed in one step and combined with logical gates by means of error-correcting teleportation. This minimizes the number of gates contributing to errors before they are corrected. Third, the fault-tolerant architecture is based on a minimal set of operations with only one unitary gate, the controlled-NOT. Although this set does not suffice for universal quantum computing, it is possible to bootstrap other gates. Fourth, verification of the needed ancillary states (logical Bell states) largely avoids the traditional syndrome-based schemes. Instead, we use hierarchical teleportations. Fifth, the highest thresholds are obtained by introducing the model of postselected computing with its own thresholds, which may be higher than those for standard quantum computing. Our fault tolerant implementation of postselected computing has the property that it can be used to prepare states sufficient for (standard) scalable quantum computing.

The properties of the proposed architecture were determined with several months of calculations and simulations on large, conventional computer workstations. Although the new architecture has yet to be validated by mathematical proofs or tested in the laboratory, it provides some evidence that scalable quantum computation may be closer to our reach than previously believed.

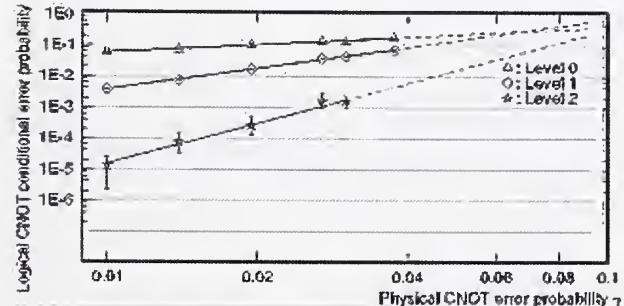


Figure 2. Errors for a CNOT gate implementation at levels 0, 1 and 2. The errors are conditional on no faults having been detected. The error bars are 68% confidence intervals. As can be seen, errors decrease rapidly with increasing level at EPGs of 3% or below. Extrapolation suggests that this behavior persists for even larger EPGs. At high EPGs, the “no fault” condition happens rarely. Nevertheless it is possible to complete a quantum computation with polynomial overhead by using many trials to prepare relatively error-free states that can then be used to implement error-corrected logical gates with high success probabilities.

Summary

We have given evidence that accurate quantum computing is possible with error probabilities above 3% per gate, which is significantly higher than what was previously thought possible. However, the resources required for computing at such high error probabilities are excessive. Fortunately, they decrease rapidly with decreasing error probabilities. If we had quantum resources comparable to the considerable resources available in today's digital computers, we could implement non-trivial quantum computations at error probabilities as high as 1% per gate.

Selected Publications

1. E. Knill, Quantum Computing with Realistically Noisy Devices, *Nature* **434** (03 March 2005), pp. 39-44.
2. <http://www.nature.com/nature/links/050303/050303-4.html>
3. <http://math.nist.gov/quantum/>

Synthesis of Quantum Logic Circuits

Design automation is an important technique for finding efficient classical circuits. Given a specification of the Boolean function which the target circuit should implement, a synthesis program automatically determines a sequence of gates realizing this function.

Quantum logic synthesis aims to build a similar tool-set for quantum circuits, seeking the fewest number of one and two-qubit processes to achieve a target quantum computation. We have developed a technique of automatic quantum circuit synthesis for unstructured qubit evolutions improving a construction from the mid 1990s by a factor of more than one hundred. In addition, we have shown the new construction to be within a factor of two of optimal. For multi-level quantum logics (qudits) similar advances have led to the first circuits ever with optimal asymptotics.

Stephen S. Bullock, ITL (891)

While classical computers manipulate bits which carry values of 0 or 1, quantum computers manipulate quantum bits (qubits) which are state vectors of two-level quantum systems. If the quantum computer is not exchanging energy with the outside environment, these qubit state vectors are rotated during the computation. Typical quantum algorithms call for implementing such a rotation, mathematically a unitary matrix, and then observing the qubits. Thus, while efficient Boolean circuits realize complicated functions on bits using a small number of logic gates, efficient quantum circuits break complicated unitary matrices into a small number of simple factors. These factors (quantum gates) typically correspond to manipulating one or two quantum bits.

The past two years have seen marked advances in the design of universal quantum logic circuits. Such circuits implement any possible unitary evolution by appropriately tuning their gate parameters. The new techniques are also overtly constructive. Unitary matrices implementing nontrivial quantum computations are large, e.g. requiring $2^n \times 2^n$ matrices for n qubits. The new quantum circuit synthesis algorithms rely on well-known matrix decomposition such as QR or the Cosine Sine Decomposition. For ten qubits, commercial software on a 2.5GHz PC requires a few seconds for these factorizations.

We illustrate basic quantum circuit design with an example. Each circuit in the figure below applies the same two-qubit computation, namely multiplying the 01

and 10 states by the complex number i while leaving 00 and 11 unchanged. Each qubit is represented by a single line or rail in the circuit. The boxes denoted S and H indicate single qubit operations, i.e. particular 2×2 unitary matrices. The gate spanning both qubits is a quantum controlled not, or CNOT. CNOT flips the target qubit (carrying the inverter) when the control qubit (black slug) carries 1, so that these down-target CNOTs exchange 10 and 11.

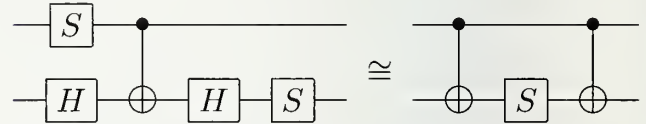


Figure 1. Two quantum circuits for performing the same task.

Although their target computation is the same, either diagram might be better suited to a given implementation of quantum computing. For example, if CNOTs are costly while one-qubit gates are implemented more easily, then the circuit at left is preferable. Alternately, if one-qubit gates are expensive but CNOTs are cheap, then the circuit at right is preferable. In practice, CNOTs tend to be more expensive than one-qubit rotations, and three-qubit gates tend to be more rare and difficult to implement than CNOTs. Further, while it is possible to build any unitary using exclusively one qubit gates and CNOT, simply employing one-qubit gates does not suffice. Thus, the following discussion of universal quantum circuits focuses on minimizing CNOT counts.

In fact, it is not obvious that CNOT and one-qubit gates suffice to build any unitary evolution. This was settled in 1995 in a landmark paper of Barenco, Bennett, Cleve, DiVincenzo, Margolus, and Shor. If n is the number of qubits on which the unitary operator acts, then these authors showed that $48n^34^n$ CNOTs suffice, in addition to many one-qubit gates. Shortly thereafter, Knill argued that some multiple $C4^n$ gates must be required for reasons of dimension. The result has a parallel in classical circuits. Namely, given a random bit-valued function on n bit strings, approximately $2^n / 2$ strings will take on a value of 1. Thus, we expect $2^n / 2$ gates are required to distinguish for which bit strings the circuit should return a nonzero value.

A Unitary-Universal n Qubit Circuit

In summer of 2004, we discovered a new unitary-universal n qubit quantum circuit requiring roughly $(1/2)4^n$ CNOTs, an improvement by a factor of two

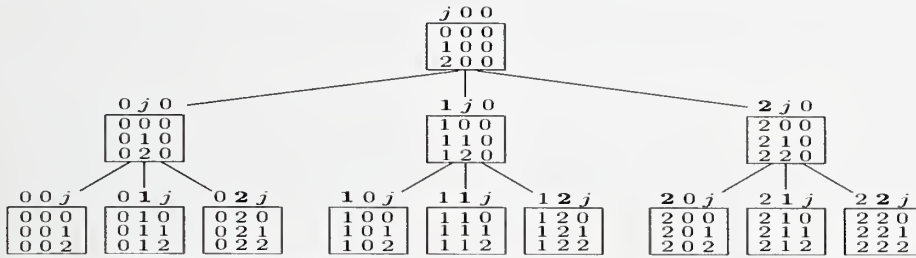


Figure 2. Recursively generated tree for automated quantum circuit synthesis for three qutrits.

over the best known circuit at the time and a factor of $100 n^3$ over the 1995 circuit. Moreover, work from the summer of 2003 had sharpened Knill's bound, actually valid for any two-qubit gate, to a specific bound of $(1/4)^{n/2}$ CNOTs. Hence, the present circuit may never be improved by more than a factor of two.

The outline for deriving the circuit is as follows. The key step is to use the Cosine-Sine Decomposition (CSD) for matrices. The CSD splits any unitary matrix into three factors; the circuit elements outlined in the box below represent the first and last. The slash in the circuit represents a multi-line carrying an arbitrary number of qubits, meaning U may be any unitary matrix on any number of qubits. Moreover, the circuit elements having the square box controls correspond to uniformly controlled rotations, a circuit block for which particularly CNOT-efficient circuits are known. Hence, the diagram employs the CSD to reduce construction of the n qubit U into four simpler $n - 1$ qubit unitaries V_1, V_2, V_3 , and V_4 . This allows for a recursive construction which terminates with hand-optimized two-qubit circuits.

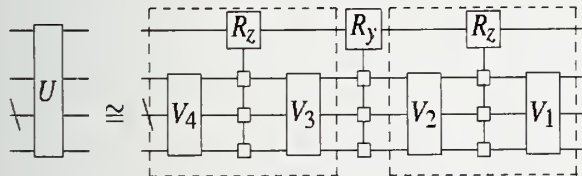


Figure 3. Basic quantum circuit synthesis decomposition.

Circuits for Quantum Multi-Level Logics

In addition, the efficiency of the circuit for quantum multi-level logics (qudits, $d = \text{level}$) has improved. One may think of a qudit by way of analogy: a qubit state is a quantum superposition of 0 and 1, a qudit state is a quantum superposition of $0, 1, \dots, d - 1$. Knill's lower bound also stated that Cd^{2n} two-qudit gates were required for any generic $d^n \times d^n$ unitary U . Yet the best known constructive procedure required $Cn^2 d^{2n}$ gates. In fall of 2004, we produced a new Cd^{2n} construction, closing this gap. The circuit exploits a variant of the QR matrix decomposition. The original asymp-

totically optimal qubit circuits, due to researchers at the University of Helsinki, also leaned on a QR technique and a Gray code cancellation. Rather than generalize the Gray code cancellation to base d numbers, the new circuit relies on a recursively generated tree. This tree describes which entries of the unitary matrix to construct with quantum gate elements at which time. A sample tree, for 3 qutrits (i.e., $d = 3, n = 3$) is shown above.

Lessons Learned

These specialized techniques for generic unitary matrices might help in optimizing other quantum circuits.

- Just as Boolean factorizations are important for classical circuit design, so too matrix decompositions are important in quantum circuit design.
- It is possible to exploit parallels to classical logic synthesis. For example, one may view the side factors of the CSD as multiplexors, applying an $n - 1$ qubit unitary matrix dependent on the most significant qubit.
- Novel aspects of quantum circuits must be explored thoroughly. For example, at the heart of the qudit circuit is a subcircuit capable of solving the hard problem of initializing a generic quantum memory state. In contrast, the classical problem of initialization trivially requires at most n bit flips.

Selected Publications

1. V. Shende, I. Markov and S. Bullock, A Practical Top-down Approach to Quantum Circuit Synthesis, <http://www.arxiv.org/abs/quant-ph/0406176>.
 2. S. Bullock D.P. O'Leary and G. Brennen, Asymptotically Optimal Quantum Circuits for d-level Systems, <http://www.arxiv.org/abs/quant-ph/0410116>.
-

Quantitative Single-Molecular Pair Fluorescence Resonance Energy Transfer

*Recently available single-molecule sensitive optical diagnostics have tremendous impact on our understanding of disease and the basic processes of life, but are limited by artifacts and significant uncertainties in the measurement process. We demonstrate a quantitative method for the measurement of single molecular-pair fluorescence resonance energy transfer (*spFRET*) that enables us to elucidate molecular structures on a length scale of 2 nm to 8 nm.*

Lori S. Goldner, PL (844)

Tremendous technical developments have recently made it possible to detect, identify, track, and manipulate single biomolecules in an ambient environment or even in a live cell. Single molecule approaches have changed the way many biological problems are addressed and are leading daily to new insights in the basic processes of life. The ability of single molecule approaches to avoid ensemble averaging and to capture transient intermediates and heterogeneous behavior renders them particularly powerful in elucidating mechanisms of molecular machineries: what they do, how they work individually, how they work together, and finally, how they work inside live cells

Fluorescence resonance energy transfer, or FRET, is a technique widely utilized to elucidate molecular structure and dynamics and is especially noted for its sensitivity to inter or intra molecular distances. Indeed, the term “spectroscopic ruler” has often been applied to this technique, in which a change in the distance between two fluorophores (donor and acceptor dyes) changes the spectroscopic properties of the dyes in a calculable fashion. It is widely appreciated that FRET also depends on the relative orientation of the two dyes, but since the relative orientation is often unknown or fluctuating in time, this dependence is also widely ignored. The result is that FRET, which in principle might provide a highly accurate measurement of either distance or relative orientation of a single dye pair, in practice provides neither accurately and is generally only used for observing structural changes.

In this work [1], we describe how accurate single molecular-pair FRET (*spFRET*) measurements can be used to directly validate or identify specific molecular structures. This is a two part problem: first, we show how to accurately measure the probability of energy transfer, E . This problem is, in principle, already solved in the literature but we give a specific recipe for accurate measure-

ment of E , enabled by single molecule techniques, that has not been used before in this context. Once E has been measured, there is still the problem of calculating or measuring the dependence of E (for a specific dye pair) on the inter-dye distance and relative orientation. This involves knowing the spectral overlap of the two dyes and the quantum-yield of the donor dye, both of which are notoriously difficult to measure with high accuracy. Here we demonstrate a single-molecule technique for solving this problem accurately and *in situ*.

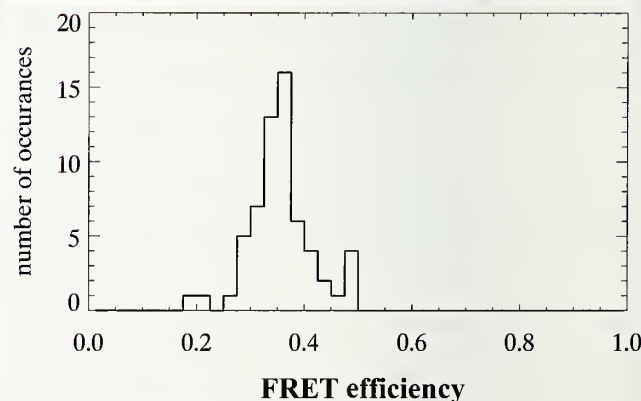
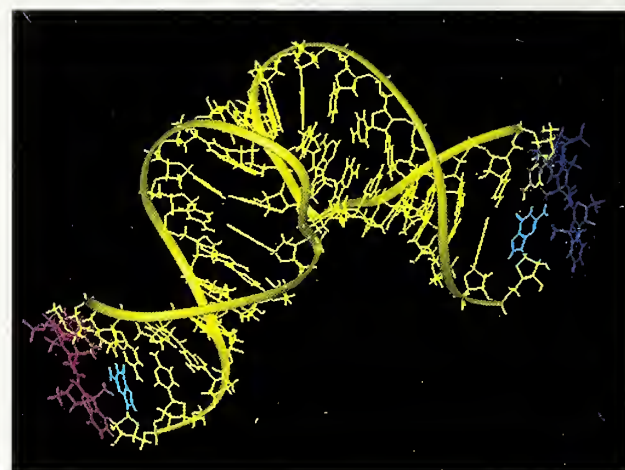


Figure 1. Top: An average “bent helix” structure of RNA complex under study here, determined from 8 minimum-energy NMR structures. Dyes molecules are shown in blue (donor) and magenta (acceptor) attached on the 5' ends of the RNA. Bottom: A histogram of average *spFRET* efficiencies showing structural heterogeneity.

These two problems, (1) accurate measurement of E and (2) accurate determination of the spectral overlap and donor quantum-yield have been widely discussed in the literature, so that the requirements for accurate measurements are well understood and straightforward; the problem is that these measurements are sufficiently diffi-

cult and time-consuming that the experimentalist often settles for a simple qualitative observation of structural change. We have developed an *in situ* solution that permits highly accurate measurements of E for individual FRET pairs and a method for direct comparison with structural models.

We demonstrate our technique with a study of an RNA complex that regulates the replication of a DNA plasmid in the bacteria *E.-coli*. For this system, NMR structural data gives 8 possible structures; using this new technique, we can distinguish between these structures and determine if there are conversions between structures or if the structures are static.

This work will be extended to include the study of HIV-genome/drug interactions and other RNA/DNA/protein complexes for which an improved understanding of structure and dynamics will enable rational design of drugs or more accurate understanding of basic biological processes.

Selected Publications

1. Yim, P. B., Zhang, Z., DeJong, E. S., Carroll, J. M., Marino, J. P., and Goldner, L. S. Single RNA Kissing Complexes Studied by Fluorescence Resonance Energy Transfer. Proc. SPIE, in press. 2005. Biomedical Optics.
-

Bacteriophage/Quantum-Dot Nanocomplex to Detect Biological Target in Clinical or Environmental Isolates

In a time of bio-terrorism threats it is necessary to have new methods available for specifically targeted biological pathogens. Different challenges need to be addressed when trying to identify pathogens in the outside environment. A detection system needs to be rapid, highly sensitive, and specific.

Jeeseong Hwang, PL (844)

Currently, the most advanced technique to detect bacteria relies on the labeling of targets with green fluorescence protein (GFP) gene. For instance, Oda *et.al.* used GFP genes to express and fluorescently detect *E. coli* (M. Oda, M. Morita, H. Unno, Y. Tanji, *Applied and Environmental Microbiology* **70**, 527-534,2004). This procedure requires expensive laboratory equipment and expertise in molecular biology laboratory. In addition, the difficulty in detecting bacteria with this approach occurs when the expression of GFP expression is low, requiring very costly high-sensitivity fluorescence detection techniques, such as single molecule imaging. Furthermore, GFP photobleaches rapidly, allowing fluorescence measurements for only a few seconds to a minute under ordinary microscopy conditions. When the minimum number of phage per bacteria to cause infection is only a few, bacterial detection with GFP expression will be very difficult due to the low fluorescence signal and fast photobleaching rate of GFP.

Researchers at NIST and NIH have developed a new technique to detect bacteria strains using fluorescent

quantum dots (QDs) and genetically engineered bacteriophage. The technique centers on combining functionalized (e.g. surface-coated with specific proteins, peptides, etc.) QDs with modified bacteriophage genetically engineered to express surface-coat-molecule(s). These modified bacteriophage are also adapted to be highly specific to given target biological samples, for instance strains of bacteria. The novel combination of phage quantitatively labeled with QDs will enable the detection and quantification of low abundance targets present down to the single copy level of target biological samples from clinical or environmental isolates. The unique optical characteristics of QDs such as photostability, size-dependent spectral properties on the same nanometer scale as its linked bacteriophage makes the combination highly suitable for imaging and discovery of single pathogenic targets including deadly bacterial strains and tumor cells.

Selected Publications

1. J. Hwang, R. Edgar, M. McKinstry, G. Giulian, C. Merrill, and S. Adhya, Invention Disclosure, "Bacteriophage/Quantum-Dot Nanocomplex to Detect Biological Targets in Clinical and Environmental Isolates," NIST Docket #05-007 (2005).

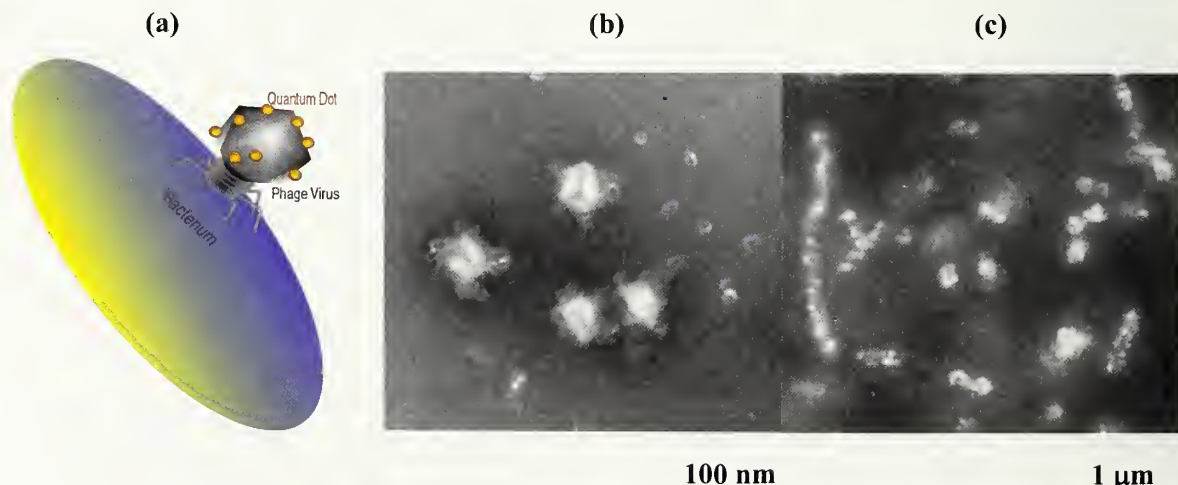


Figure 1. (a) A schematic of the detection concept. The capsid region of a bacteriophage virus is genetically modified to express biotin moieties to conjugate with streptavidin QDs. (b) TEM image of phage/QD complexes. Multiple QDs are bound to phage viruses. (c) Fluorescence image of bacteria targeted with phage/QD nano-complexes. Quantitative analysis of the results evaluates the specificity of the T4 phage viruses to a *E. coli* bacterial strain.

Chemical Sensor Microscopy for Nanotechnology

Nanoscale chemical mapping has immense potential as a device and materials characterization tool for current and developing nanotechnologies. However, techniques used to achieve nanoscale chemical imaging are still in early stages of evolution. This research combines Chemical Force Microscopy (CFM) and moisture-enhanced probe-sample interactions as a viable method for measuring the surface chemical properties of materials with nanometer spatial resolution.

Tinh Nguyen and Xiaohong Gu, BFRL (861)

Nanometer scale chemical mapping has immense potential as a materials characterization tool for current and emerging nanotechnologies. Despite this critical need, techniques to achieve nanoscale chemical information are still in infancy stage. The use of chemically-functionalized probe in an AFM, called Chemical Force Microscopy (CFM) has been shown as an excellent approach to characterize chemical heterogeneity at the nanoscale spatial resolution. Much of current research using CFM has been performed in solvents. However, for polar polymeric materials and biomaterials, solvent is not a desirable medium. By using a combination of hydrophilic AFM tips and elevated relative humidity (RH) at the tip-sample environment, we have successfully developed a method to image materials chemical heterogeneity in air at a nanoscale spatial resolution.

The first example to demonstrate this method is shown in Figure 1, which was highlighted in Today's Chemist at Work in 2003. The sample was a patterned self-assembled monolayer (SAM), consisting of COOH regions (thin stripes) and CH₃ matrix material. These are height and phase images taken by tapping mode AFM using a NIST-patented RH chamber attached to the AFM and an unmodified Si tip. Under normal ambient conditions, SiO₂ on Si surface is fully hydroxylated (approximately 5OH groups per nm²). Therefore, Si tips should be regarded as OH-terminated probes. Except for the high spots of the surface defects, the height images are essentially featureless at low or high RHs. However, the phase images at different RH levels reveal the bright COOH regions separated by the CH₃ areas. Further, the image contrast difference increases with increasing RH.

Figure 2 presents another example of using the present approach to enhance AFM phase image contrast



Figure 1. Height and phase AFM images of a patterned SAM, showing the effect of RH on the phase image contrast. (In each RH, height image is on the left and phase image is on the right.)

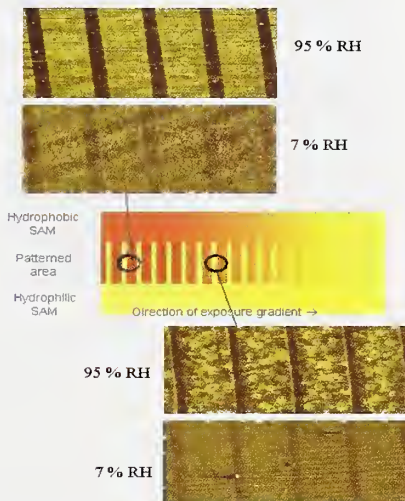


Figure 2. Effect of RH on phase image contrast for different hydrophilic/hydrophobic gradients; (unmodified Si tip; stripe: hydrophilic; matrix: hydrophobic).

of chemically-heterogeneous samples. These images were taken using tapping mode AFM for a gradient-patterned SAM sample, whose schematic is included for clarity (center illustration). The thin stripes are the hydrophilic COOH regions and the matrix (thick stripes) is the chemical gradient material. These images were also obtained using tapping mode AFM and an unmodified Si tip. At low RH, the phase contrast between the stripes and the matrix is poor, even for the regions that have the highest surface free energy differences. However, the contrast between the same two regions is greatly increased at 95 % RH. At high RH, the contrast even in the regions having small surface free energy difference can also be observed. Because the chemical structure and

chain lengths of the stripe and the matrix are similar, the contrast observed in Figures 1 and 2 is believed to be due mainly to the hydrophilicity difference between the two regions.

The use of functionalized carbon nanotube (CNT) tip to probe chemical heterogeneity using the present approach is illustrated in Figure 3. These are AFM phase images taken at four different RHs for a SiO₂/ODS (n-octyldimethylchlorosilane) pattern SAM using oxygen-plasma treated CNT tip and unmodified Si tip. In this figure, the darker stripes are the SiO₂ material and the lighter matrix is the hydrophobic CH₃, and all images were taken at the same location.

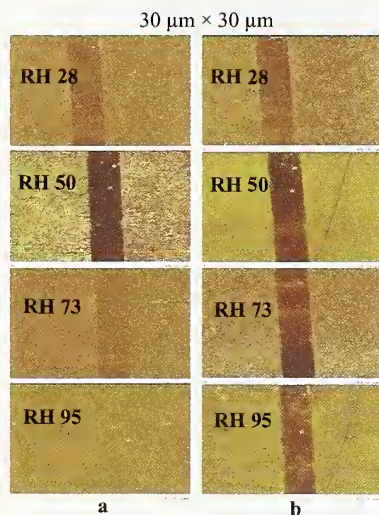


Figure 3. AFM phase image contrast as a function of RH for plasma-treated CNT tip (a) and Si tip (b) on a SiO₂-Si/CH₃-terminated patterned SAM; stripe is Si-SiO₂ substrate and matrix is CH₃-terminated SAM.

Clearly, the image contrast obtained by the plasma-treated CNT tip is greatly enhanced at 50% RH but drastically decreases at 73 % or 95 %RH. For the Si tip, the RH-enhanced contrast remains high even at high RHs.

The use of this approach for chemical imaging by contact mode AFM is shown in Figure 4. The sample was a SiO₂/ODS patterned SAM and the probe was an unmodified Si₃N₄ tip. Data on the adhesion force as a function of RH for the SiO₂ substrate and CH₃-terminated SAM are included for comparison. The image contrast is greatly enhanced at 53 % RH and decreases slightly at 90 % RH, consistent with adhesion force data.

One example on the use of this method to probe chemical heterogeneity in polymeric materials is shown in Figure 5. These are images taken using tapping mode AFM of a cryo-fractured PS-PEO (polyethylene oxide) block copolymer surface. The dark domains are the hydrophilic PEO material and the bright areas are the hy-

drophobic PS. The phase images clearly show that high RH not only enhances the contrast between the hydrophilic and hydrophobic regions but also enlarges the hydrophilic areas.

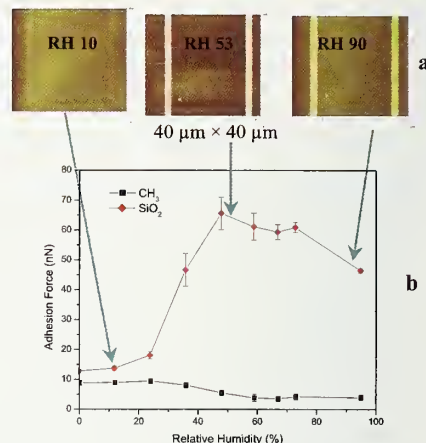


Figure 4. Effect of RH on image contrast (a) and adhesion force (b) obtained by AFM contact mode for a SiO₂/OTS patterned SAM; stripe is the SiO₂ substrate and matrix is ODS.

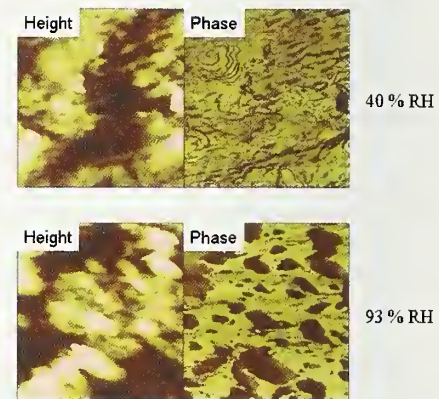


Figure 5. AFM height and phase images of PS/PEO block copolymer fractured surface at two RH levels.

The above examples and additional data obtained by both functionalized and unfunctionalized tips firmly demonstrate that the approach of using elevated RH in the tip-sample environment and hydrophilic AFM tips is a viable method to probe materials chemical heterogeneity in air.

Nanomechanical Properties of Polymer Thin Films

There are numerous drivers for the use of ultrathin polymeric films, most notably the microelectronics industry where feature sizes of 22 nm are anticipated by 2010. However, the ability to measure the physical and mechanical properties of polymeric materials on this length scale remains a daunting task. We employ our buckling-based metrology to measure the elastic modulus (resistance to deformation) of nanostructured thin films as well as ultrathin polymer films.

Christopher M. Stafford, MSEL (854)

Nanotechnology promises to revolutionize a growing set of materials applications ranging from electronics to drug delivery to ballistic protection. However, the quest to engineer materials on the nanoscale (e.g., in the form of ultrathin films) is met with the daunting task of measuring the physical and mechanical properties of these systems. Understanding the mechanical properties of nanofilms is especially critical in the fabrication of MEMS, NEMS, and electronic devices. Current methodologies such as indentation can probe the bulk mechanical properties of materials but are challenged by thin polymer films as well as multilayered structures.

We have established a buckling-based metrology that measures the elastic modulus of relatively stiff polymers films supported on soft elastic substrates. This metrology exploits a buckling instability that occurs in laminates upon compression. The wavelength of the instability, d , can be related to modulus ratio of the film and substrate, E_f/E_s , through the following equation:

$$\lambda = 2\pi h \left[\frac{1-\nu_s^2}{3(1-\nu_f^2)} \frac{E_f}{E_s} \right]^{1/3}$$

This year, we applied this metrology to measure the mechanical properties of nanoporous low- k dielectrics in development for semiconductor applications. The modulus of these low- k films has been well correlated with their resilience to the chemical mechanical polishing (CMP) used during processing. The materials studied have pores (air) ranging in size from 5 nm to 50 nm encapsulated in a continuous matrix of organosilicate (MSSQ). The modulus of the series of nanostructured films decreases monotonically with increasing porosity (Figure 1), and these data agree with semi-analytical models describing the porosity dependence of a materials' modulus.

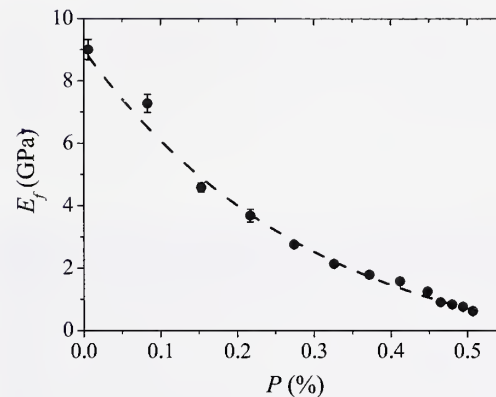


Figure 1. Modulus (E_f) as a function of porosity (P) for a series of nanoporous organosilicate films.

We also applied this metrology to measure the elastic modulus of ultrathin polystyrene (PS) films. The data are shown in Figure 2. For $h > 30$ nm, the apparent modulus is constant; we observe a transition in the modulus as a function of film thickness that occurs at $h \approx 30$ nm. We have generated several arguments for the observed decrease in mechanical integrity of ultrathin polymer films. Regardless of the origins of this transition, the data alone are compelling and need to be accounted for in future theories and models for how fundamental physics of polymer thin films impacts their mechanical properties. The data also highlight issues concerning the fabrication and stability of sub-30 nm features patterned in thin polymer films

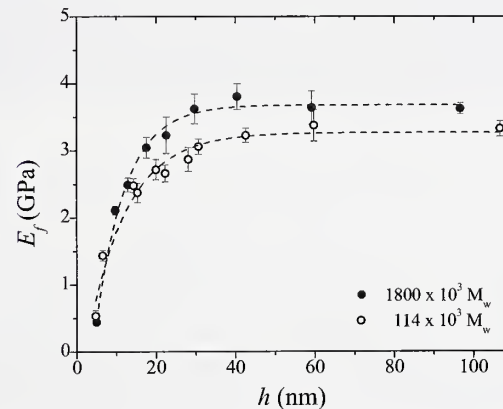


Figure 2. Modulus (E_f) as a function of thickness (h) for PS films of two different molecular mass.

Nanomechanical Metrology

The need for reliable, standardized mechanical test methods applicable to nanometer-scale volumes of material has grown dramatically in recent years. Nanoindentation has become the method of choice for quantitative determination of mechanical properties of small volumes of material, but standardization efforts have lagged far behind the application of the technique. Over 1000 commercial nanoindentation instruments are currently in use, with no traceable force calibration and an extremely limited choice of standardized test methods. We develop standard reference materials (SRMs), traceable calibration transducers, and robust, reliable methods for obtaining, analyzing and modeling nanoindentation data.

Douglas T. Smith and Lyle E. Levine, MSEL (852)

Nanoindentation is the most commonly used method for determining hardness and elastic properties of small volumes of materials. In this technique, a diamond indenter is pushed into a specimen surface, and the force on and displacement into the surface are recorded. The technique is capable of providing information on the elastic and plastic deformation of a specimen for indentations as shallow as a few nanometers, and requires minimal specimen preparation effort. However, there are only a very limited number of accepted test methods available, and no means to traceably calibrate or verify the performance of nanoindentation instruments. This leads to large interlaboratory variations in results, and a dearth of reliable data for understanding or predicting nanoscale mechanical behavior.

In many mechanical test methods, including nanoindentation, a force is applied to a specimen, and displacement is measured. Traceable displacement measurement by interferometry is well established. Force measurement is more problematic, because the SI unit for force is still based on an artifact kilogram mass. The Microforce Competence Program at NIST has developed a primary realization of force, traceable to electronic and length SI units, for force calibration in the range 1 mN to 10 nN. Transfer force cells have now been developed that allow force calibration, traceable to NIST, for commercial nanomechanical test equipment such as nanoindentation instruments and atomic force microscopes. One such cell, shown in Figure 1, was calibrated against the NIST primary force balance to an uncertainty less than 0.5 % for forces in the range 0.05 mN to 5.0 mN.

That cell was then mounted, as if it were a specimen, in several popular commercial nanoindenter instruments. For forces above 2 mN, the recorded nanoindenter force was within the 1 % uncertainty required by most draft standards for nanoindentation machines. However, for lower applied force, the error increased dramatically, and at 0.05 mN, the recorded force was almost 18 % below the actual applied force.



Figure 1. SI-traceable force cell.

In addition, mechanics at the nanoscale is inherently difficult to model accurately. Finite element modeling (FEM) can effectively capture the elastic behavior of macroscopic structures but includes no accurate failure criteria, since this depends upon atomic-scale behavior. Classical atomistic simulations can handle enough atoms (millions to billions) to model such events but their potentials are inaccurate for large strains. Quantum-mechanics-based simulations using density functional theory (DFT) are extremely accurate and handle the chemistry exactly, but such simulations are so CPU intensive that they can handle only a few hundred atoms. A combination of all three techniques is required to accurately model mechanical behavior at the nanoscale.

Over the past year, we have developed techniques to handle such multiscale modeling for quasistatic applications such as nanoindentation. At the macroscale, FEM is used to simulate the elastic behavior of a nanomechanical system. The FEM mesh is fine enough to use the predicted elastic displacement fields to generate boundary conditions and initial atom positions for an atomistic simulation using classical potentials. The use of classical potentials in a large simulation cell allows us to correctly propagate the long range stresses to the critical regions where bond distortions are large or where chemistry effects need to be explored. In these critical regions, we embed a DFT simulation.

Improving Image Resolution in Nanotechnology

Current nanoscale electron microscopy images remain of relatively low quality. To address this issue we are developing improved mathematical tools for image analysis, and the use of such tools to provide measurable increases in resolution in state-of-the-art scanning electron microscopy. One very major difficulty lies in the large image sizes, often on the order of 1024x1024 pixels, or larger. This presents formidable computational challenges. Many new techniques are based on nonlinear partial differential equations, and typically require thousands of iterations, and several hours of CPU time, to achieve useful results. Real-time image processing algorithms are exceedingly rare and very highly sought after.

Alfred Carasso, ITL (891)

A fundamental problem in scanning electron microscopy (SEM) is the fact that the shape of the electron beam that produced the image is seldom known to the microscopist. Therefore, image deblurring must proceed without knowledge of the actual point spread function that caused the blur. Such so-called *blind deconvolution* is fraught with difficulty, and little authoritative discussion of this subject is to be found in most image processing textbooks.

Nevertheless, in recent years, considerable progress was achieved at NIST in developing mathematical technologies that lead to real-time image processing algorithms. In addition, a unique new capability has been created, the so-called *APEX method*, that can achieve useful blind deconvolution of 1024×1024 SEM imagery in about 60 seconds on current workstations. Because of its manifold applications, this technology is the subject of intense and continuing research and development.

The APEX Method

The APEX method is an FFT-based direct blind deconvolution technique that can process complex high resolution imagery in seconds or minutes on current desktop platforms. The method is predicated on a restricted class of shift-invariant blurs that can be expressed as finite convolution products of two-dimensional radially symmetric Lévy stable probability density functions. This class generalizes Gaussian and Lorentzian densities but excludes defocus and motion blurs. Not all images can be enhanced with the APEX method. However, we have shown that the method can be usefully applied to a wide variety of real blurred im-

ages, including astronomical, Landsat, and aerial images, MRI and PET brain scans, and SEM images. APEX processing of these images enhances contrast and sharpens structural detail, leading to noticeable improvements in visual quality.

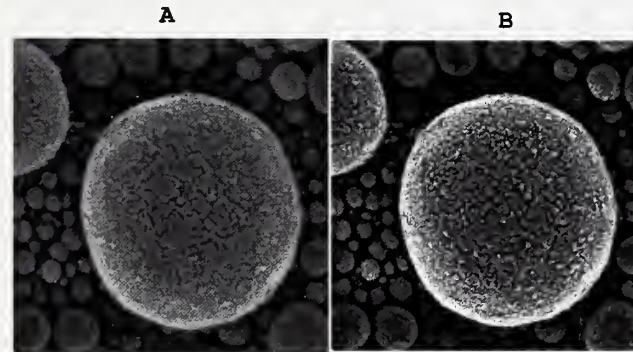


Figure 1. APEX blind deconvolution of state of the art Scanning Electron Microscope imagery produces measurable increases in sharpness. (A) Original 1024x1024 Tin sample micrograph has Lipschitz exponent $\alpha = 0.40$ and TV norm = 13000. (B) Sharpened image has $\alpha = 0.29$ and TV norm = 34000.

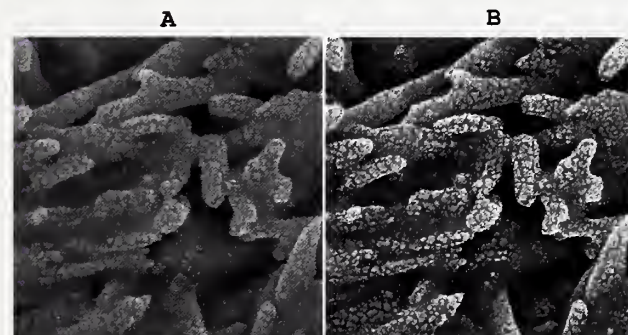


Figure 2. APEX sharpening of SEM imagery. (A) Original 1024x1024 Magnetic Tape sample has $\alpha = 0.35$ and TV norm = 14000. (B) Sharpened image has $\alpha = 0.26$ and TV norm = 39000.

Application to SEM Imagery

Recently, a new Hitachi Scanning Electron Microscope was acquired by the NIST Nanoscale Metrology Group, capable of producing higher quality imagery than had previously been possible. A major challenge for our deconvolution algorithms was to demonstrate measurable increases in sharpening of such state of the art imagery. Two sharpness measures were used, the image Lipschitz exponent α , and the image discrete *total variation* or TV norm. Image sharpening increases the TV norm, due to the steepening of gradients, while it decreases the Lipschitz exponent as finer scale features become resolved. Examples of such sharpening are shown in Figures 1 and 2. In Figure 1A, the original

1024x1024 Tin sample micrograph has TV norm of 13000 and Lipschitz exponent $\alpha = 0.40$. The APEX-sharpened Figure 1B has TV norm = 34000 with $\alpha = 0.29$. In Figure 2A, the original 1024x1024 Magnetic Tape sample has TV norm = 14000 with $\alpha = 0.35$. The APEX-processed Figure 2B has TV norm = 39000 with $\alpha = 0.26$. These very substantial sharpness increases are typical of those obtained in numerous other test images.

Measuring Image Smoothness

Most commonly occurring images $f(x,y)$ are not differentiable functions of the variables x and y . Rather, these images display edges, localized sharp features, and other fine-scale details or *texture*. Many digital image-processing tasks require prior specification of the correct mathematical function space in which the true image lies. If an image is incorrectly postulated to be too smooth, the processing algorithm may produce an overly smoothed version of the true image in which critical information has been lost.

During the last 10 years, a very considerable amount of image analysis research has been based on the assumption that most images belong to the space of functions of bounded variation. However, it has been subsequently discovered that such so-called total variation (TV) image processing sometimes results in unacceptable loss of fine-scale information. This phenomenon is now known as the *staircase effect*. In papers published in 2001, French researchers Gousseau, Morel, and Meyer, showed that most natural images are, in fact, not of bounded variation, and that TV image-processing techniques must inevitably smooth out texture.

Correct characterization of the lack of smoothness of images is a fundamental problem in image processing. It turns out that so-called *Lipschitz spaces* are the appropriate framework for accommodating non-smooth images. The L^P Lipschitz exponent α for the given image, where $0 < \alpha < 1$, measures the fine-scale content of that image, provided the image is relatively noise free. Heavily textured imagery has low values for α , while large values of α indicate that the image is relatively smooth. Estimating an image's Lipschitz exponent is a delicate problem. We have developed a new, computationally efficient, method for estimating α . It merely requires blurring the image by convolution with a specific singular integral kernel, and evaluating the discrete L^P norm of the difference between the blurred and original images. The rate at which this L^P norm tends to zero, as the kernel approaches the Dirac δ -function, is directly related to the Lipschitz exponent α . Since the required convolutions can be accomplished by FFTs, very minimal computational effort is thus needed to implement the resulting procedure. In addition, this approach has the advantage

of allowing consideration of substantially wider Lipschitz spaces than is mathematically possible with existing procedures, thereby encompassing a much wider class of images.

Significant potential applications of this technology include the routine monitoring of image sharpness and imaging performance in electro-optical imaging systems, the performance evaluation of image reconstruction software, the detection of possibly abnormal fine-scale features in some medical imaging applications, and the monitoring of surface finish in industrial applications. In addition, specifying the correct Lipschitz space wherein an image lies can be used to solve the blind image deconvolution problem in a way that preserves texture, i.e., fine detail, in a recovered image. We recently have developed a new method, the Poisson Singular Integral (PSI) method, which yields an excellent approximation to optimal image filtering for a very wide class of images.

Selected Publications

1. S. Carasso, The APEX Method in Image Sharpening and the Use of Low-exponent Lévy Stable Laws, *SIAM Journal on Applied Mathematics* **63** No. 2 (2002), pp. 593-618.
2. S. Carasso, D. S. Bright and A. E. Vladar, The APEX Method and Real-time Blind Deconvolution of Scanning Electron Microscope Imagery, *Optical Engineering* **41** No. 10 (2002), pp. 2499-2514.
3. Carasso, Singular Integrals, Image Smoothness, and the Recovery of Texture in Image Deblurring, *SIAM Journal on Applied Mathematics*, **64** (5), (2004), pp. 1749-1774.

Optical Metrology for Nanolithography

Responding to a NIST proposal, the semiconductor manufacturing industry is seeking new, high-index lens materials for 193 nm immersion lithography in order to achieve features sizes as small as 32 nm. The materials must have high indices of refraction, have isotropic optical properties, have transmission cutoff wavelengths shorter than 193 nm, and have high optical quality. NIST first identified several promising classes of materials, and is pursuing a project to optically characterize candidate materials in these and related classes that meet these specifications. This is a joint experimental and theoretical effort.

John H. Burnett, PL (842), Simon G. Kaplan, and Eric L. Shirley (844)

The Rayleigh criterion for resolution in optical systems is $k_1\lambda/NA$, where k_1 is a prefactor (≥ 0.25) that depends on optical engineering, λ is the wavelength of light, and $NA = n \sin \theta$ is the numerical aperture, involving n , the index of refraction in, and θ , the half-cone angle for light incident at the focus. For conventional optical lithography these parameters have been pushed to near their theoretical limits, with the exception of the index. To drive resolution further, the industry has now turned to increasing the index. While the index in the above resolution criterion is that at the image in the photoresist, as shown in Figure 1 the NA is limited by the smallest index of the resist, of the fluid above the resist, and of the last lens element.

We were the first to point out that the index of the last lens element is the key bottleneck for decreasing feature sizes. We initiated a program to identify potential high-index optical materials and to establish their feasibility for incorporation in lithography tools. The industry now accepts our claim that these materials could potentially enable one further generation of feature sizes, to 32 nm, using conventional optical lithography.

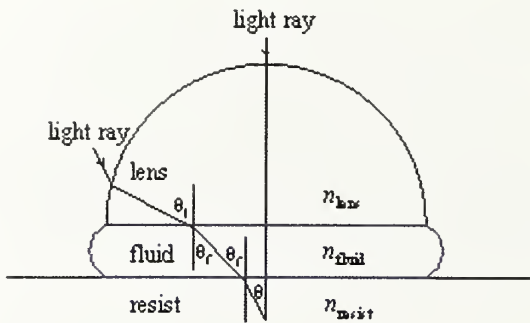
On theoretical grounds, wide-band-gap optical materials are limited to Group-I or Group-II oxides and fluorides. Our calculations and measurements show that the indices of fluorides are too low to be useful. However, we have established that the alkaline-earth oxides, magnesium aluminum spinels, and several other related oxide compounds have the requisite high indices and band gaps. As a result of our identification of these promising classes of high-index oxide materials, the semiconductor lithography industry is considering redesigns of the lithography tools to take advantage of the improved reso-

lution that could be achieved.

Although we have identified these classes of materials for the industry, a wide variety of materials within these classes remain to be explored. To be useful, the optical properties of the materials must meet certain tight specifications on, e.g., the absorption, index, index dispersion, thermal optical coefficient, stress-optical coefficients, and intrinsic birefringence. The material classes we have proposed permit wide compositional variations involving stoichiometry, atomic substitution, and solid solutions of related materials. Thus these material systems offer substantial phase space to potentially tailor optical properties to meet the requirements.

Because there exist little or no experimental or theoretical data on the optical properties of these materials at deep ultraviolet wavelengths, this project is in its infancy. However, the required state-of-the-art facilities to make these measurements have been developed for this and related projects. Preliminary results for some of these materials indicate that their properties may be in the acceptable ranges. In association with the semiconductor industry, we are working with ultraviolet materials suppliers to explore the full range of these materials to identify the most promising candidates and demonstrate feasibility.

The most quantitative output of our work must come from measurement, but measurement results are interpreted and/or confirmed using parallel theoretical simulation and modeling. As a simple example, Figure 2 illustrates theoretical results for the index of refraction as a function of photon energy for magnesium, calcium, strontium and barium oxide. While the results differ somewhat from experimental values, the trends and approximate values of the indices of refraction illustrates the use of a theory that can operate independently from experimental input. This is valuable for searching through the large phase space of possible new materials and material combinations for promising candidates to attempt to grow. One multi-dimensional region that we intend to search next is in magnesium aluminum spinels with varying degrees of magnesium versus aluminum richness and degrees of inversion.



$$\text{NA} = n_{\text{resist}} \sin \theta_i = n_{\text{fluid}} \sin \theta_f = n_{\text{lens}} \sin \theta_i$$

$$n_{\text{resist}} > n_{\text{fluid}} > n_{\text{lens}}$$

Figure 1. Schematic of light rays traveling through final lens element, immersion fluid, and resist. The NA is limited by the smallest index.

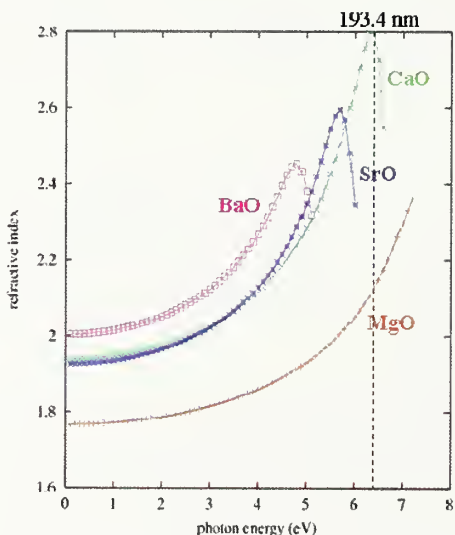


Figure 2. Theoretical indices of refraction versus photon energy for magnesium, calcium, barium and strontium oxide. The down-turn indicates the onset of absorption. The photon energy corresponding to 193.4 nm is indicated.

True Three-Dimensional Tomography Utilizing Bayesian Statistical Inference

Scanning Transmission Electron Tomography (STEM) has the capability of producing projected images based on more than a single axis of rotation. In order to take advantage of this feature, Bayesian statistical methods need to be extended from the current practice of reproducing a series of two-dimensional slices with ad hoc post-processing, to producing directly true three-dimensional images using the STEM projections to determine the smoothness of the 3D image. This goal is achieved by developing software based on 3D geometry and extending current 2D Bayesian methods to 3D. In addition, full Bayesian inference, necessitating Monte Carlo methods, is utilized to assess the final quality of the reconstructed image.

Donald Malec and Juan Soto, ITL (898)

The Scanning Transmission Electron Microscope (STEM) offers the possibility of obtaining high-resolution, three-dimensional image reconstruction of material or biological samples at the nanometer scale. Image reconstruction is based on using a series of two-dimensional projections obtained as entry and exit energy differentials of electron beams aimed through a sample at various tilt angles. At NIST, there are a number of ongoing projects associated with both overcoming problems and capitalizing on unique features of STEM in order to convert these projections back into images. This project entails extending Bayesian two-dimensional image methods to three-dimensional and providing associated estimates of precision.

Bayesian methods in the literature are based on reproducing two-dimensional images (slices) from projections based on rotating a projection bed (an array of detectors) around a single axis of rotation. By obtaining a grid of these points, pseudo three-dimensional images can be reconstructed based on a series of stacked slices as in medical imaging from CAT scans. These slices can be further processed to fill in the gaps based on judgment. Forming two-dimensional slices is the current level of practice. These methods are based on two-dimensional geometry and cannot be trivially extended to 3D. Imaging directly into three dimensions has several advantages. Among them is a more direct use of the nearby continuity of nearby features of a solid and, most importantly, the ability to use novel or unsystematic tilt series angles.

This project achieves three aims:

1. To extend state-of-the-art Bayesian methods of image estimation from two-dimensional slices to true three dimensions.
2. To obtain measures of precision of areas of these images using full Bayesian inference methods.
3. To implement and develop more efficient geometrical algorithms needed to implement the full-Bayes approach

The following example illustrates the issues dealt with here. Consider a fictitious solid that contains the letters of word “FOCUS” in two orientations (see Figure 1). The left half of this figure represents the first layer of the solid’s depth and the right half the second layer.



Figure 1. A fictitious solid containing the letters of the word “FOCUS” in two orientations. The left image represents the first layer of the solid’s depth and the right image the second layer.

Suppose that this solid is covered by an opaque, uniform layer of a known substance, rendering its interior invisible. An ideal electron beam (i.e., when multiple scattering can be ignored) can be aimed through the substance as a way of visualizing the underlying structure without destroying the coating or the solid. In an ideal setting a series of tilt angles results in a series of projected images at each angle. The image in Figure 2 is a simulation of the solid based on 121 tilt series of 11 equi-spaced tilt-angles, between 0 and π , around the depth and height axes. For each tilt series, the energy degradation is captured on a 100×100 grid. The degradation of the energy is based on both the underlying geometry due to the letters and Poisson noise based on a dosage of 10^6 electrons per pixel.

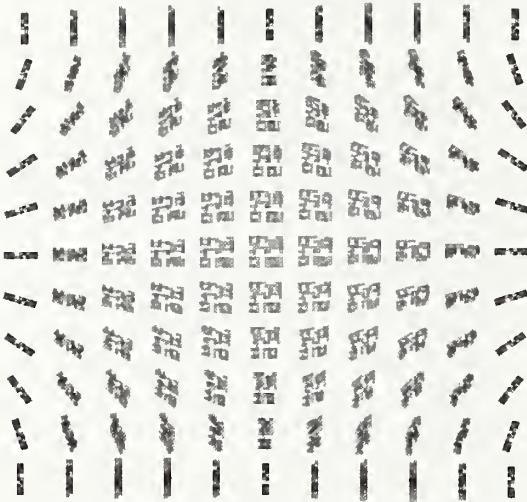


Figure 2. Simulation of the solid based on 121 tilt series of 11 equi-spaced tilt-angles, between 0 and π , around the depth and height axes.

The original solid can be faithfully recaptured using the high-quality sample images above. More realistically, available projections may be of lower quality and resolution, possibly because of the fragility of material or the time and expense of collecting detailed projections. The next simulation is a result of projecting the same solid onto an 11×5 series of tilt angles equi-spaced between 0 and π . The projection bed in this case consists of only a grid of 7 by 7 sensors. In addition, the dosage is only 1000 resulting in much more noise due to Poisson error. A realization is given in Figure 3.

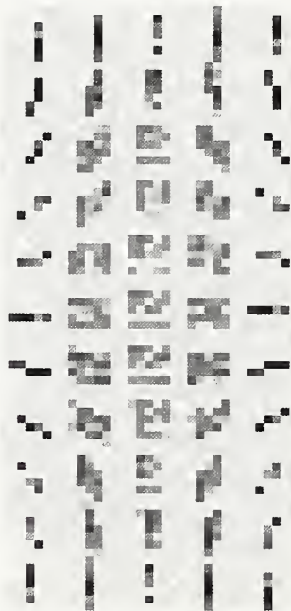


Figure 3. Simulation based on projecting the same solid onto an 11×5 series of tilt angles equi-spaced between 0 and π . The projection bed consists of a grid of 7 by 7 sensors. Also, the dosage is only 1000 resulting in much more noise due to Poisson error.

Using this information as input, the 3D Bayesian method can still produce an estimated image. Doing so results in the image of Figure 4 using the posterior mean.



Figure 4. 3D Bayesian estimate based upon simulation results of Figure 3.

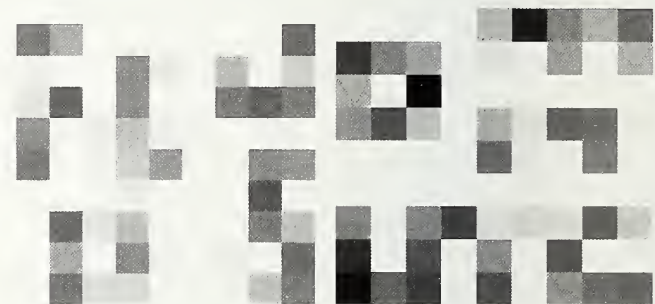


Figure 5. Posterior standard errors for each voxel in the example. Dark shade indicates a relatively larger error.

As mentioned, estimates of the accuracy of the image can also be made based solely on the projected data with no knowledge of the true image. For this example, the resulting posterior standard errors for each voxel are shown in Figure 5, where a dark shade indicates a relatively larger error. As can be seen, in general the edges are less accurate than the center. This is to be expected since all angles of rotation are about the center resulting in more data that incorporates the center voxels. However, the interaction between the letters and surrounding space is clearly evident in the accuracy estimates. Obtaining these estimates can be used informally, or perhaps with additional methodological development, as a way of determining where to obtain more projections to most efficiently reduce error.

Structure and Dispersion Measurements of Polymeric Building Materials

Almost all commercially viable polymeric construction products have nanoscale pigments dispersed throughout the polymeric matrix. Poor dispersion of these pigments is qualitatively known to adversely affect the appearance, service life, and mechanical properties of these products. Current methods for assessing pigment dispersion in industry are subjective, indirect, unreliable, and limit to large micron-size aggregate dilute suspension. The objective of this project is to develop non-destructive, light scattering techniques for characterizing nanoscale pigment dispersion in liquid (uncured) and in solid (cured) polymeric matrices and relate these dispersion properties to the appearance and weathering service life of polymeric materials.

Li-Piin Sung, BFRL (861)

We have developed methodologies for quantitative assessment of pigment dispersion using small angle neutron scattering (SANS) beam in NCNR's cold neutron facility. To develop a more practical and non-destructive method for characterizing the dispersion of pigments in uncured and cured polymeric materials, a state-of-the-art light scattering materials characterization laboratory was established. By correlating with the SANS measurements and microscopy measurements, an efficient and accurate measurement using light scattering metrology will be developed. Collaboration with theoreticians from university especially in applying particle dispersion theory is ongoing to derive a quantitative dispersion parameter.

With the completion of BFRL light scattering materials characterization laboratory (FY04), we now have the new capabilities of characterizing the morphology (nano-domain due to dispersion in mixing or phase separation) and measuring structure dispersion for various processing conditions in uncured and cured coatings. Current research efforts will focus on metal oxide nanoparticulate systems because of their importance to a range of industries, but the methods developed will be generic in nature. In this way, we will establish a framework for determining structure-property relationships for nanoparticles and nanoparticle-polymer systems.

We have conducted a series of particle dispersion measurements using small angle neutron scattering (SANS), angular-resolved static and time-resolved dynamic light scattering (SLS & DLS) techniques. Studied particle size ranges from 20 nm to 800 nm, and two major types of particles (TiO_2 and polymer spheres) were

examined. Several trials have attempted to improve nanoparticle dispersion by chemical surface treatments /physical mixing of nano- TiO_2 . Figure 1 shows parts of SLS and DLS results. From SLS results, the dispersion parameters such as particle cluster size and the interactions of particle-particle and particle-matrix can be determined. From DLS, autocorrelation function and relaxation time of the nanoparticle in solvent matrix can be characterized in different dispersion states. Data analysis is in progress and more experiments are underway to better understand the dispersion kinetics/dynamics.

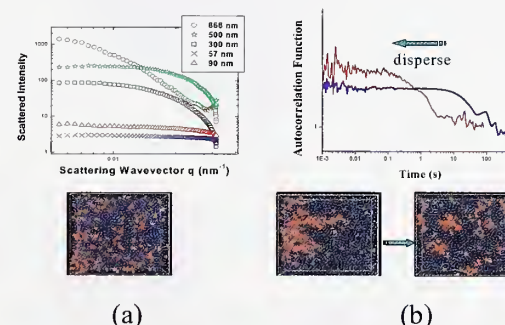


Figure 1. (a) SLS Results of various nanoparticles suspense. (b) DLS results for nano- TiO_2 pigments dispersed in the toluene.



Figure 2. Examples of different pigment dispersion due to different annealing conditions. Slow and quench indicated slow and fast cooling conditions. Image size: 60 $\mu m \times 60 \mu m$.

In addition to studying the particle dispersion in suspension state, we have also studied particle dispersion and microstructure/morphology of pigmented coatings under different processing conditions and the effect of dispersion and microstructure on the durability (UV degradation). The controlled parameters are cooling rate, particle size, mixing time, pigment volume concentration, mixing chemistry...etc. Figure 2 shows pigment dispersion of two types of pigmented PVDF coatings (blue and black pigments) under different annealing conditions. The white dots in the confocal images are the

pigments, and the images clearly show that different cluster sizes and spatial distribution of particles. Figure 3 shows SANS studies of nanostructure for different chemical and physics mixing of polymer coatings and the UV degradation results. Detailed information can be found in the recent publications. Dispersion and microstructure play a big role on durability (UV degradation).

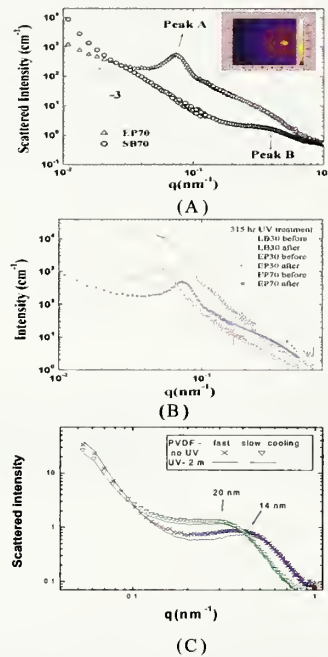


Figure 3. (a) SANS results of PVDF coating by different mixing methods. (B) UV degradation results on three coatings with different microstructures. (C) SANS results of PVDF coatings under different annealing conditions and UV degradation results (lines) after two-month indoor UV degradation.

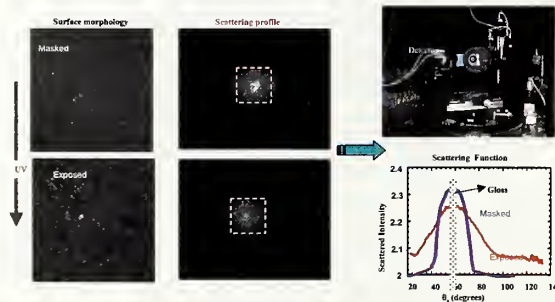


Figure 4. Surface morphology and light scattering profiles from masked and exposed PVDF coatings. The 5-axis sample stage of LS-I is also shown here.

We have also investigated the nano- to micro size surface morphology changes of coatings with different particle dispersion due to the UV degradation and scratch test. Figure 4 shows an examples of surface morphology changes after 12 years exposed in the Florida and its corresponding surface scattering feature using the new light scattering instrument (LS-I). The LS-I pro-

vides the capability of probing surface and subsurface microstructure changes due to UV degradation.

With the capability of accurate dispersion measurements, we can provide the direct link between these dispersion properties (particle and cluster size, interactions, degree of dispersion) to the appearance (surface roughness and gloss) and weathering service life of polymeric materials. In addition to the dispersion characterization measurements, the newly developed LS instrument (LS-I) characterizes surface roughness and microstructure of polymer films, and will have a full capability of color and gloss measurement upon acquiring a customized Scanning Wavelength (White light) Illumination System. The techniques and measurement methods developed in this study will support dispersion measurements in the BFRL nanoscale metrology project and the characterization of polymer surface project.

This project, which is strongly supported by the industry (members of NIST/Industry Polymer Interphase Consortium and NIST/Industry Service Life Coating Consortium), provides essential scientific-base data for the development of methodology and measurement protocols that can be used for evaluating surface appearance, dispersion state of coating constituents. A successful development of these methods will greatly improve the commerce and reliability of products that depend on surface appearance, dispersion state of coating constituents, including the automotive industry, coatings and other building polymeric materials.

Design and application of this instrument were presented in the Inter-Society Color Council (ISCC) and Council for Optical Radiation Measurement (CORM) jointed Technical Meeting in May 10-14 2004. Parts of the results have been presented at Rohm & Haas Chemical Company, and a coating international meeting (FSCT/ICE) in October 2004.

Selected Publications

1. L. Sung, S. Vicini, D. L. Ho, L. Heddle, C. Olmstead, and K. A. Wood, *Polymer* **45**(19), 6639-6646 (2004).
2. J. Faucheu, L. Sung, J. W. Martin, K.A. Wood, *FSCT-ICE 2004 Proceedings of the 82th Annual Meeting Technical Program*, McCormick Place North, Chicago, IL, October 27-29, (2004); *in press*, JCT Research (2005).

Synthetic X-ray Spectrum Images for 3D Chemical Imaging at the Nanoscale

Synthetic “phantom” x-ray spectrum image datasets are needed to develop and test reconstruction algorithms, visualization tools, and metrology software for 3D chemical imaging. By generating simulated observables (X-ray spectra) from samples constructed in silico with exactly known composition and geometry, this project seeks to provide test data to judge the efficacy and accuracy of data processing systems attempting to reconstruct the unknown 3D distribution of elements within real samples from measured X-ray spectrum images.

John Henry J. Scott and Nicholas Ritchie CSTL
(837)

In the last 30 years, analytical electron microscopy (AEM) and scanning electron microscopy with x-ray microanalysis (SEM XM) have advanced steadily via innovative electron optics, better spectroscopic detectors, improved computer control, and multi-modal data acquisition technology. The analyst now has access to a wealth of high-quality, multidimensional data about the sample. As a result, the challenge now is to devise schemes to manage and exploit this flood of raw data and to synthesize the results into meaningful solutions to real-world problems. Recently, researchers have begun to explore the possibility of chemical tomography in the AEM, the determination of 3D elemental distributions in the sample based on tilt-series of electron energy-loss (EELS) and X-ray emission data. One of the chief barriers to this work is that for thicker samples EELS maps can show non-monotonic relationships between the observed signal in the 2D tilt images and the concentration of the analyte in that projected pixel. This violates the projection requirement, a key assumption in many 3D reconstruction algorithms. Because of this, most successful work to date has been limited to systems that (at least approximately) meet this requirement and do not exhibit the full complexity of interactions possible in the AEM or SEM. To get past this hurdle, it is necessary to construct new models for 3D reconstruction in the AEM and SEM that explicitly account for effects such as beam spreading, multiple scattering, and through-sample self-absorption.

Following the lead of the medical imaging community, one useful step towards the creation of 3D reconstruction algorithms is the analysis of synthetic datasets from phantoms with known properties. Figure 1 shows the results from 3D Monte Carlo simulations of three

cylinders (Cu, Al, and SiO₂), each 600 nm

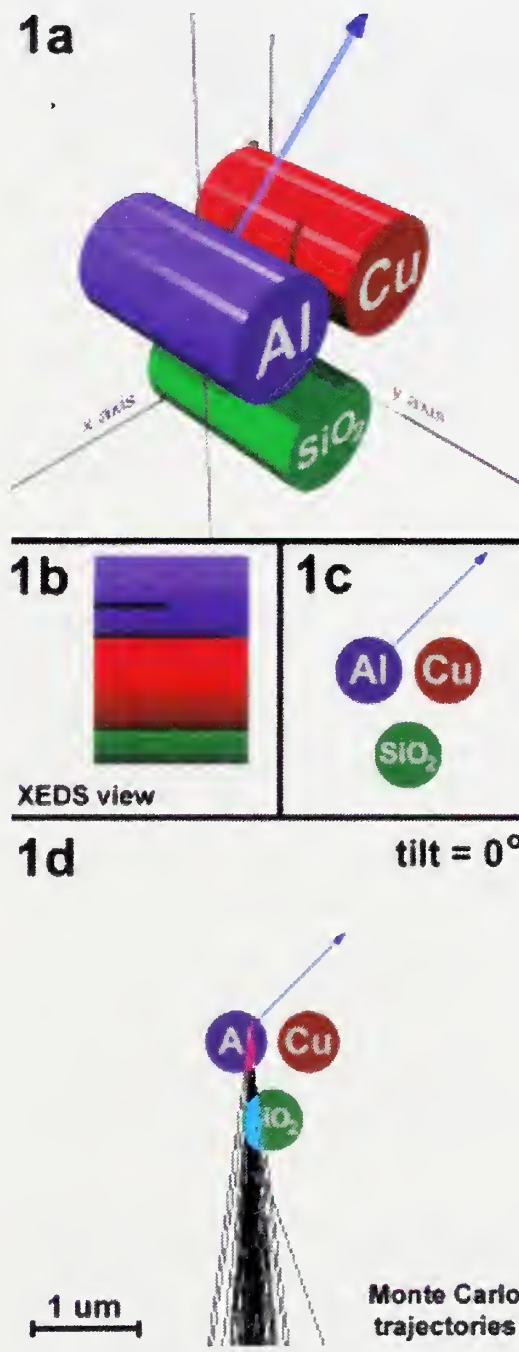


Figure 1. (a) AEM cylinder phantoms (600 nm diameter by 1 mm long) shown in orthographic projection while at zero tilt; the blue arrow points toward the X-ray detector. (b) the same phantoms as seen from the perspective of the X-ray detector, showing how some cylinders eclipse others during tilting. (c) view along the tilt axis, perpendicular to the incident electron beam; the blue arrow points toward the X-ray detector. (d) 300 keV Monte Carlo electron trajectories. 100 incident electrons shown striking the sample at 1 of 32 horizontal beam raster locations with the sample at zero tilt.

in diameter and 1 μm long. The electron beam (purple line) was rastered over 32 pixels parallel to the x-axis and the resulting X-ray spectra at the XEDS detector were calculated, resulting in spectrum-line profiles for each tilt from 0° to 180°. From the 5,760 spectra calculated, chemical sinograms were extracted by summing the intensities in 130 eV wide windows over the Cu K α , O K α , and Al K α peaks. These data display both beam broadening and self-absorption effects, but do not include Bragg scattering or dynamical interactions, two other effects that plague 3D AEM.

Figure 2 shows how a similar dataset was generated for an even more complex sample, a 3D “Rubik’s cube” of various elements. Unlike the dataset shown in Figure 1, this dataset consists of a complete 2048-channel X-ray spectrum at each pixel in a 2D array. Thus while this second dataset does not exhibit a tilt variable, it comprises a 2D image instead of a series of 1D line profiles. Both types of dataset are important in refining a practical 3D reconstruction algorithm.

The elemental map in Figure 2 (top right) shows many of the desired physical effects that complicate 3D reconstruction from electron-excited X-ray emission data. As the primary electrons interact with the surface of the sample at each pixel, they spread outward laterally and downward vertically into the different phases in the cubes. Since the electron range for a 20 keV incident beam in these materials is large compared to the size of the subcubes, the resultant excitation volume is expected to extend into neighboring cubes. To further complicate the analysis and eventual 3D reconstruction, after the X-rays are generated by the inelastically scattered electrons, they are differentially absorbed on their way out of the sample toward the X-ray detector. For soft X-rays, such as the N K α X-rays shown in blue in Figure 2 (top right), this self-absorption effect can be quite large. It is visible as a gradient of detected intensity, increasing from the bottom of the image (farther from the detector, longer escape path length) to the top (shorter escape path length).

Although this project was begun just a few months ago, it has already yielded several important datasets that have revealed the complex and dynamic nature of observed X-ray spectra in 3D samples and tilt series. Efforts are underway (in collaboration with the NIST Mathematical and Computational Sciences Division) to produce parallelized versions of these simulators that would allow us to scale up the synthesis of phantom datasets to more pixels and more tilts. In addition to the preliminary publications listed below, this work has been presented at invited talks at multiple universities and at national microanalysis meetings.



Figure 2. (top left) Phantom sample consisting of a “Rubik’s cube” of aluminum, silicon, silicon dioxide, titanium nitride, and copper. This fictional sample contains many of the materials used in modern semiconductor devices, admixed and juxtaposed on the nanoscale to simulate the complexity of true 3D chemical imaging problems. Each of the 27 smaller cubes is 100 nm on an edge, so the entire assembly is 300 nm on an edge. The beam (purple vertical line) is shown striking the sample in the center of the SiO₂ subcube. (top right) 3-color X-ray elemental map showing quantitatively the detected X-ray intensities for the Cu K α X-ray emission line (red), the Si K α X-ray emission line (green), and the N K α X-ray emission line (blue) after excitation with a 20 keV incident electron beam. Note the differential absorption of the Nitrogen K line from bottom to top (the X-ray detector is off the top of the image) and the bleeding of excitation near the phase boundaries. The X-ray map is 300 nm on a edge. (bottom) The same cube shown with the top, middle, and bottom layers vertically expanded and horizontally translated to reveal the 3D structure more clearly.

Selected Publications

1. N. W. M. Ritchie, “A New Monte Carlo Application for Complex Sample Geometries”, submitted to *Surface and Interface Analysis*, 2004.
2. J. S. Villarrubia, A. E. Vladár, B. D. Bunday, and M. Bishop, *Proc. SPIE* **5375**, 199-209, (2004).

Carbon Nanotube Metrology

Characterization of individual carbon nanotubes is required to ensure that these unique materials meet the demanding requirements of future electronic, optoelectronic, chemical sensing, and biomedical applications. A principal challenge associated with isolated tube characterization is optimization of the connection between the nanotube and the test platform. To address this issue, we are developing techniques to manipulate and attach carbon nanotubes to specially designed test structures in the scanning electron microscope. In addition, for biomedical applications, preliminary studies on cell-nanotube interactions are underway to explore the viability and affect of in-vivo probes, sensors, and scaffolds based on carbon-nanotubes.

Paul Rice and Tammy Oreskovic, MSEL (853)

We are developing techniques to measure mechanical and electrical properties of isolated carbon nanotubes. Figure 1 shows a test device fabricated to measure the electrical characteristics of an individual multi-walled carbon nanotube. The nanotube was attached, or welded, to the device in the scanning electron microscope using an accepted technique referred to as electron beam deposition. In this example, a single tube extends from one electrode to the other.



Figure 1. SEM image of carbon nanotube test device for electrical measurements. The nanotube extends across a 2 μm gap.

Understanding the properties of the contact requires visualizing its structure on the atomic scale. Using high-resolution microscopy, we have seen some interesting new structures of the weld. Previously, it was assumed that the weld was a uniform material composed of amorphous carbon. Using atomic force microscopy and transmission electron microscopy, we have seen spurious deposits of carbon far outside the weld. Figure 2 shows a nanotube welded to a chromium film with residual carbon covering almost everything. Further work is

planned to measure contact resistance within the weld and resistance changes due to distortions during welding.

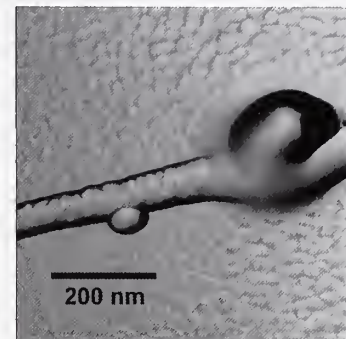


Figure 2. AFM image of a multi-walled carbon nanotube welded to a chromium film. The surface texture is residual carbon from the weld process.

In addition to contact issues, preliminary studies have been conducted to assess nanotube biocompatibility. Cells were exposed to nanotube suspensions and entangled mats. Figure 3 shows proliferation assay results, indicating reduction in growth and metabolic activity for cells grown directly on nanotubes. These results indicate that cell attachment may not be as strong in regions of high nanotube density. However, when the nanotubes were coated with a biologically compatible surfactant, cell growth was not noticeably affected.

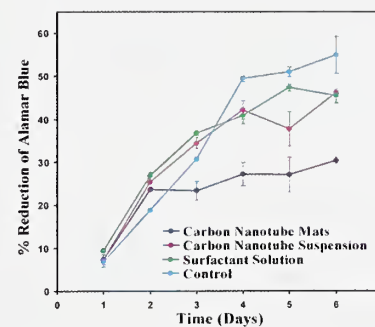


Figure 3. Results from alamar blue assay test for cell growth and proliferation. As the cells grow and divide, they metabolize the Alamar blue compound, changing the medium in which the cells are growing from a blue color to clear. Greater percent reduction indicates more vigorous cell growth.

Nanotribology and Surface Properties

Accurate adhesion and friction measurements at the nanoscale are emerging as critical issues in device industries and nanotechnology. Working with device and magnetic storage industries and other agencies, we have designed and built instruments to meet these needs. These instruments are housed in NIST's new Advanced Measurement Laboratory(AML). This state-of-the-art facility features vibration isolation, class 1000 clean room standards, and temperature control.

Stephen Hsu, MSEL (852)

The Nanotribology and Surface Properties Project was initiated as a part of the MSEL Nanotechnology Initiative. The project develops measurement capability for adhesion, friction, and surface forces at the nanoscale. Working with instrument makers, the Nanotribology Group has designed and built a remarkable facility featuring equipment and instrumentation that establishes a new state of the art for conducting measurements and observations of nanoscale events. Included in this facility are a nanoadhesion apparatus, a dual white light interferometer microscope, a multiscale friction tester, and a multifunction apparatus combining an ultrahigh vacuum scanning tunneling microscope with an atomic force microscope (UHV STM/AFM). Together, these instruments allow us to image, manipulate, and measure adhesion, friction, and other nanomechanical properties of materials from the microscale to the nanoscale.

To resolve some of the instrumental challenges, we have engaged instrument makers, such as Hysitron, Veeco, and others, to solicit their input and collaborations. At the same time, we have established our own capabilities in tip fabrication, cantilever spring constant calibration, and tip characterization. Three new instruments were successfully installed as a result of these collaborations: the NIST-Hysitron multiscale friction tester, the NIST nanoadhesion apparatus, and the first prototype of an interferometer microscope from Veeco. We are continuing to work with our partners to develop next-generation instruments, as suggested by the Nanometrology Grand Challenge Workshop (NIST, January 2004).

Adhesion is an important issue in nanotechnology as well as in device manufacturing industries. Conventional adhesion measurement relies on large contact areas and the accurate positioning of two surfaces. Force measurements typically are performed by strain gauges and transducers with force sensitivities in the newton and

millinewton ranges. These conventional instruments are unsuitable for nanoscale contacts. To resolve this issue, the newly designed NIST apparatus, Figure 1, allows adhesion force measurements between two surfaces at the nanoscale level. In this device, capable of nanonewton force resolution, laser light is piped through an optical fiber and directed at a quadrant photodetector. Because the length and stiffness of the fiber can be modified easily, a wide range of spring constants can be obtained, and the measurement of adhesion forces can be achieved at multiple force levels. Thus, the NIST apparatus has established an exciting new opportunity to measure the influence of surface forces on adhesion, molecular interactions, and the compliance of surfaces, all critical data to device manufacturing industries.

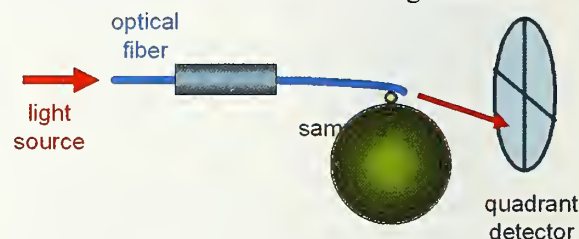


Figure 1. Schematic operation of the NIST nanoadhesion apparatus.

With our new adhesion and nanofriction instruments, we are quantifying the effects of plowing and electrostatic charge on measurements. We continue to work with our external academic under the Nanotechnology Extramural Initiative to develop friction measurement via three approaches: friction-measuring MEMS devices, AFM's, and ultrahigh vacuum friction measurement. These efforts have been successful, and we have gained considerable understanding of how meniscus forces and electrostatic forces can exert significant effects on nanofriction measurements.

Enhanced by the superior vibration isolation and clean room environment in NIST's new Advanced Measurement Laboratory (AML), our UHV STM/AFM system provides atomic imaging and force measurement with an unprecedented resolution and accuracy. Combined with our conventional AFM, we are able to image and manipulate surface features and measure a wide range of material characteristics and properties important in nanodevice operation.

Neutron Reflectometry for Highly Accurate Nanometer Metrology

To provide researchers with state-of-the-art nanometer metrology using neutron reflectometry methods.

Joseph A. Dura, MSEL (856)

Nanotechnology research requires accurate measurements of features on the nanometer level. We report a comparison of techniques for measurements of 1.5 nm to 8 nm SiO₂ films on Si at state-of-the-art precision and accuracy. SiO₂ on Si is a well-understood system for which high quality ultra-thin samples are available. It is technologically relevant since at this thickness it serves as a gate oxide in Si electronics. The International Technology Roadmap for Semiconductors (ITRS) states the need for such measurements at a standard uncertainty of $\approx 1\%$. The present comparison was organized under the auspices of the Consultative Committee for Amount of Substance (CCQM), the body authorized under the International Committee for Weights and Measures (CIPM) to oversee the framework for the SI system for amount of substance. Neutron reflectometry (NR), grazing incidence x-ray reflectometry (GIXRR), x-ray photoelectron spectroscopy (XPS) and ellipsometry were found to be the most accurate and precise methods.

Sets of ten samples for (100) and (111) orientation Si were prepared by thermal oxidation. A sample of each wafer was characterized at the National Physical Laboratory (NPL) by XPS under carefully established reference conditions. Ellipsometry, providing relative differences in thickness across the wafer, was used to adjust the XPS data to determine the reference thickness d_{RT} for each sample. The SiO₂ thicknesses determined by each technique at a given laboratory, d , were analyzed through the equation $d = md_{RT} + c$. Here, m scales the measurement against the XPS result, whereas c represents an offset that incorporates the thickness of a contamination layer containing adsorbed carbonaceous matter and water. In techniques that take into account the contamination, e.g. GIXRR and NR, c can represent a misrepresentation of the contamination layer. XPS is unique in that the contamination has no effect on the result and c should be zero. It is also unique in that while being linear, its length scale has a high uncertainty and needs calibration. This calibration was an essential part of the study and showed that a 1.4 % correction was required. For all techniques, the RMS scatter of the data about the linear fit is an indication of precision. Accuracy is indicated by consistent m values near 1 and c values near 0.

NR was measured on 4 samples with d as follows: 1.65 ± 0.15 nm, 2.00 ± 0.05 nm, 5.55 ± 0.03 nm, and 8.04 ± 0.01 nm. The uncertainties encompass the full range of acceptable fits and therefore represent a 95 % confidence level. Fig. 1 shows the reflectivity vs. momentum transfer, $Q = 4\pi \sin\theta/\lambda$, for the 8 nm sample, the best fit (blue), and two poorer but acceptable fits.

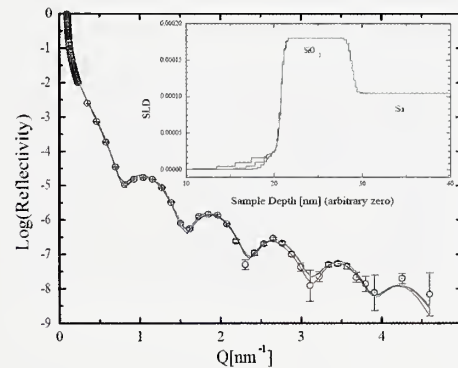


Figure 1. Neutron Reflectivity vs. Q . The inset is the scattering length density profile determined by each fit.

XPS measurements from the 13 additional laboratories achieved excellent reproducibility when employing the reference geometry; the RMS scatter about the linear fit vs. d_{RT} ranged from 0.019 nm (NPL) to 0.136 nm. NR had the next lowest scatter of all measurements (0.026 nm), indicating high precision. For comparison, data from all techniques achieved mean RMS scatters of 0.15. A plot of m vs. c for all laboratories is reproduced in Fig. 2. The high apparent accuracy of both NR and XPS is indicated by their proximity to $m = 1$, $c = 0$.

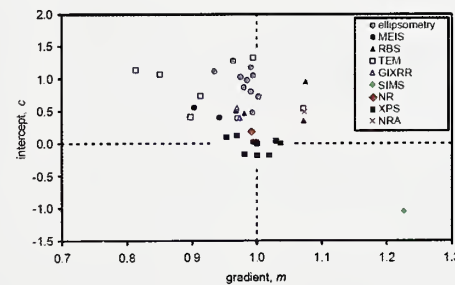


Figure 2. Plots of m and c obtained from various techniques (from Fig. 2A of Ref [1]).

Selected Publications

1. M. P. Seah, et al., Surface and Interface Analysis (in press).

Gradient Reference Specimens for Advanced Scanned Probe Microscopy

Engineering of nanomaterials, biomaterials, and nano electro-mechanical systems hinges on techniques for imaging complex nano-structures. In this respect, new Scanned Probe Microscopy (SPM) methods promise nano-scale mapping of chemical, mechanical and electro-optical properties, but these techniques generally offer qualitative information. Through a suite of reference specimens fabricated with a combinatorial design, we aim to calibrate image data from emerging SPM methods, thereby advancing these nanometrology tools.

Michael J. Fasolka and Duangruth Julthongpuit, MSEL (854)

Recent years have seen the development of a new generation of SPM techniques, which intend to measure chemical, mechanical, and electro/optical properties on the nanoscale. However, contrast in new SPM images is difficult to quantify since probe fabrication can be inconsistent and probe/sample interactions are not understood. Our research at the NIST Combinatorial Methods Center (NCMC) aims to provide a suite of reference specimens for the quantification of next-generation SPM data. By design, our specimens will gauge the quality of custom-made SPM probes, calibrate SPM image contrast through "traditional" surface measurements (e.g., spectroscopy, contact angle) and provide information for understanding complex probe/sample interactions. Our specimens are produced with bench-top microfabrication routes and combinatorial gradient methods developed by the NCMC. Here, combinatorial methods are key, since they enable the fabrication of specimens that vary properties that govern SPM image contrast in a systematic, independent manner. Moreover, as opposed to traditional reference specimens, combinatorial samples provide not one, but a multitude of calibration conditions.

Figure 1 illustrates principles of our specimen design through a specific case useful for quantifying chemically sensitive SPM techniques such as friction-force SPM, or Chemical Force Microscopy, which employs a custom-made probe. The crux of this specimen is a "gradient micropattern" ($\nabla\text{-}\square p$): a series of micron-scale lines that continuously change in their chemical properties (e.g., surface energy) compared to a constant matrix. Two "calibration fields" adjacent to the $\nabla\text{-}\square p$ directly reflect the chemistry of the lines and the matrix. Thus, traditional measurements (e.g., contact angle) along the calibration fields (1) gauge local chemical differences in the $\nabla\text{-}\square p$ and thereby (2) calibrate contrast in SPM im-

ages acquired along the $\nabla\text{-}\mu p$.

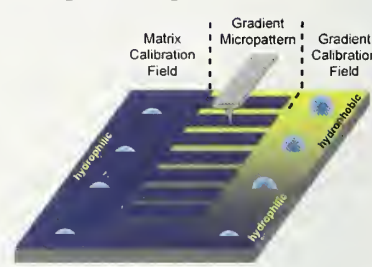


Figure 1. Schematic illustration of our gradient reference specimen for chemically sensitive SPM techniques.

Figure 2 demonstrates use of this specimen for calibrating friction force SPM image contrast. We fabricate this specimen via microcontact printing of a chlorosilane self assembled monolayer (SAM) on a SiO_2 matrix. The chemical gradient is achieved via a graded UV-ozonolysis of the SAM. The plot abscissa gives the difference in friction force (contrast) between the lines and matrix for SPM images collected along the $\nabla\text{-}\mu p$. The ordinate expresses the corresponding surface energy (γ) data (from contact angle measurements) collected along the calibration fields. Thus, from a single specimen we create a comprehensive calibration curve that relates SPM friction force to differences in surface energy. Moreover, the plot neatly illuminates the smallest γ difference sensed by the probe (red arrow), which is useful for gauging the quality of custom-made probes.

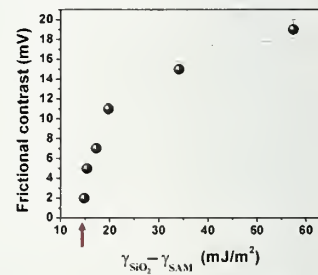


Figure 2. Preliminary calibration curve relating friction force SPM image contrast to differences in surface energy (γ), as determined from a single gradient reference specimen. The minimum contrast point (red arrow) illuminates the sensitivity of the probe.

Currently, we are refining this reference specimen design, and we are developing similar designs for other advanced SPM methods.

Quantitative Nanomechanical Properties

We are developing AFM-based methods to measure mechanical properties on the nanoscale. Atomic force acoustic microscopy provides elastic-modulus values either at a single point or as a map of local property variations. The results further our understanding of surfaces, thin films, and nanoscale structures.

Donna C. Hurley, MSEL (853)

New measurement tools are needed in the burgeoning field of nanotechnology. In particular, information about mechanical properties is critical in many applications. To meet this need, we are developing methods based on the atomic force microscope (AFM). Atomic force acoustic microscopy (AFAM) involves the vibrational modes of the AFM cantilever when its tip is in contact with a sample. With AFAM, the indentation modulus M of a material can be determined. The small tip radius ($\sim 5\text{-}30$ nm) enables images with nanoscale spatial resolution.

In FY04 we examined several issues concerning quantitative AFAM. In one effort, we measured M for three nickel films about 50, 200, and 800 nm thick. M ranged from 210 GPa to 223 GPa, lower than that for polycrystalline nickel. Scanning electron microscopy (SEM) showed nanocrystalline microstructure (grain diameter <30 nm). The reduction in M can be attributed to an increase in intercrystalline material. Furthermore, the average values of M for all three films were the same within measurement uncertainty ($\sim 10\%$). Thus AFAM results were not influenced by the elastic properties of the substrate, even in a 50-nm film. This contrasts with nanoindentation, which must account for substrate properties to accurately measure submicrometer films.

We also investigated relative humidity (RH) effects on AFAM measurements. We created a RH-controlled chamber and used it on patterned self-assembled monolayers (SAM) of n-octyldimethyl-chlorosilane on silicon (Si) substrates. An AFM topography image and AFAM relative-stiffness image are shown in Fig. 1. The hydrophobic SAM stripes are all but invisible in the high-resolution topography image (10 nm full scale), but are clearly seen in the AFAM image. Regions covered by the SAM appear more compliant (lower contact stiffness) due to AFAM's sensitivity to variations in the tip-sample adhesion. Further experiments with similar samples will quantify humidity and adhesion effects.

We also performed AFAM experiments to examine how the tip radius R changes with use. Tests were made with multiple cantilevers on a sample with known elastic

properties. The load was successively increased (up to $\sim 5\text{ }\mu\text{N}$) to break or plastically deform the tip. Values of R measured from high-resolution SEM images (Fig. 2) were compared to values obtained from AFAM data using a Hertzian contact-mechanics model. The AFAM values of R were consistently smaller than the SEM values. Further analysis and experiments are underway to clarify this issue. The knowledge gained will refine our understanding of AFAM contact mechanics and thus improve measurement accuracy and repeatability.

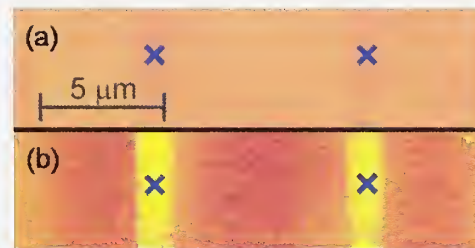


Figure 1. (a) AFM tapping-mode topography and (b) AFAM relative-stiffness images of Si with n-octyldimethylchlorosilane SAM.

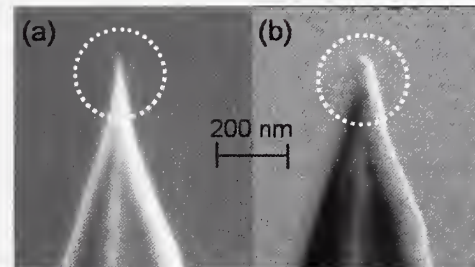


Figure 2. SEM images of AFM tip (a) before use and (b) after repeated AFAM experiments. Circled regions indicate tip wear.

The above results involve either *quantitative single-point* measurements or *qualitative imaging*. In FY04, we worked to realize *quantitative nanomechanical mapping*. This involved a new frequency-tracking circuit to find the contact-resonance frequencies at each pixel. The circuit uses a digital signal processor that enables rapid data acquisition (typically ~ 20 min. for a 256×256 image). We have obtained resonance-frequency images for a variety of materials. Future work will focus on issues related to quantitative image interpretation (e.g., calibration, tip wear, and contact-mechanics models).

Highly Charged Ions in EUV Lithography

International SEMATECH has asked NIST to help in the extension of photolithography to circuit dimensions of 30 nm and below through studies of photon emission efficiency and surface damage from highly charged ions. We have deployed the NIST Electron Beam Ion Trap Facility to complete these tasks.

John D. Gillaspy and Joshua M. Pomeroy, PL
(842)

Despite considerable interest in the development of exotic nanotechnologies, the extension of conventional photolithography to extreme ultraviolet (EUV) wavelengths is the mainstream technique selected by the semiconductor industry to continue miniaturization deeply into the nano-regime (beyond the so-called “32 nm node”). Highly charged ions (HCIs) figure prominently in the list of fundamental physics issues that contribute to both the promise and the potential downfall of EUV lithography.

On the positive side, HCIs show promise for providing an efficient source of the 13.5 nm light that is necessary for EUV lithography to become cost effective for mass manufacturing. On the other hand, HCIs are the most reactive form of matter on earth, so the potential damage they could cause to critical materials in lithography tools is high. NIST was asked to deploy its Electron Beam Ion Trap (EBIT) Facility for Highly Charged Ion Research to assist the large team of experts who are working on these issues around the world.

One key issue was determining the fundamental physical limit in the light source efficiency. At the beginning of the NIST work, prototype light sources developed by industry and the National Laboratories had obtained very high power outputs, but were still over an order of magnitude away from the efficiency needed for practical viability. Because the efficiency obtained in the prototypes was so high already, there was serious concern that further increases might be limited by fundamental physics. Industry planning (and R&D spending on the order of \$1B/year) was proceeding based on predictions of complex plasma models that were virtually untested by well-characterized laboratory experiments. Researchers at NIST provided benchmark test data and coordinated worldwide fundamental data activity for the industry in this area.

Our work was communicated through approximately 1,000 pages of internal reports to industry, periodic tele-

conferences, several peer-reviewed journal and book articles, and a number of invited talks at international meetings of EUV lithography researchers. Our work on this topic led the leader of the NIST Plasma Radiation Group to become chair of the International SEMATECH Fundamental Data Working Group, and co-organizer (with Intel) of the first in a series of EUV Source Modeling Workshops.

This research ended with the conclusion that the source models were indeed accurate in all areas tested, and that further significant gains in efficiency were possible, particularly if tin atoms are used instead of xenon atoms. The validated theories have been able to confidently guide light source development companies in improving the efficiency of the photon production by the plasma. The success in this area has been such that at the most recent International EUV Lithography Symposium (Fall 2004), the source efficiency problem was officially moved from the #1 spot on the list of critical problems, to a spot that is so low on the list that it is no longer even assigned a numerical ranking. The EUV light source problem has been essentially solved.

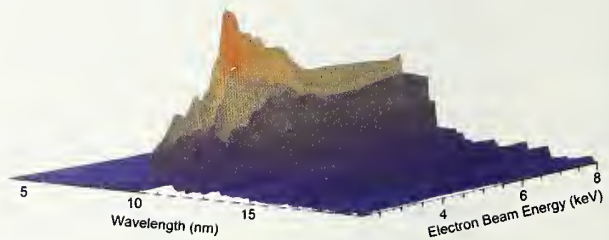


Figure 1. Light emission intensity, taken at the NIST EBIT facility, as a function of photon and electron energy; the red peak moves into the desired photon energy range when tin ions are substituted for xenon ions.

Because of fundamental science studies undertaken earlier, the NIST Plasma Radiation Group was familiar with a peculiar type of surface damage that is significant only when the ion charge state is high. This “potential energy mediated damage” grows with ion charge, and can become so large that it dominates the kinetic energy damage by a large factor. At the beginning of NIST’s work on the light source efficiency problem, it became clear that this exotic ion damage mechanism was largely unknown by the semiconductor industry. NIST brought this to the attention of the community, and embarked on a directed study to investigate the magnitude of the mechanism on samples of actual EUV lithography multi-layer optics and other materials that were expected to be used in the construction of the lithography tools.

In a form of “high precision accelerated testing”, we

used the NIST EBIT facility to dose the materials with small but well-characterized amounts of HCIs, and then applied ultra-sensitive reflectivity and scanning tunneling microscopy measurements to observe the collective damage from non-overlapping ion impacts, and even for some materials the effect of individual ions. This technique has the advantage over conventional high-dose accelerated testing of being able to reveal relatively clearly the fundamental ion damage effects and mechanisms. This work revealed that the highly charged ions used in xenon based light sources will cause over an order of magnitude more damage than singly charged ions. At the most recent International EUV Lithography Symposium, the problem of damage of source materials was officially advanced to the #2 spot on the critical items list.

In summary, NIST's specialized capabilities in the area of highly charged ion physics played a role in a much larger worldwide effort which, together, brought many pieces of a complex puzzle together to essentially eliminate one critical problem, while elevating the significance of a different, previously underappreciated, problem. The shift in priorities allows industry to better allocate resources to focus on the problems that are truly most important in order to improve the probability of making EUV lithography a cost-effective tool for mass manufacturing devices at length scales of 30 nm and below.

Electrical Test Structure Metrology

A central goal of this project is to fabricate, calibrate, and document a selection of Critical Dimension (CD) reference materials with calibrated values as low as 70 nm and having designated reference features with an expanded CD uncertainty less than ± 3 nm.

A second area of research is a focus on lower-resistance interconnect material, in particular copper which exhibits lower resistance and improved reliability over aluminum.

Michael Cresswell and Richard Allen, EEEL
(812)

Technical Approach

The key issues which, in the past, have prevented us from providing well-characterized and useful critical dimension (CD) reference materials to the semiconductor industry were our inability to produce reference features with 1) acceptable uniformity and 2) acceptably narrow dimensions. In this project our goal was to produce reference materials that meet both of the requirements. To achieve this goal we replicated the CD reference features in the device layer of a 150 mm (110) Si-MOX (Separation by Implantation with Oxygen) wafers with a device layer thickness of 150 nm. This device layer is electrically isolated from the remaining thickness of the substrate by a 390 nm thick buried oxide created by oxygen implantation.

An image of the test chip, containing candidate reference features, is transferred into a silicon dioxide film that serves as a hard-mask. The edges of the features are aligned as close as possible to the <112> lattice directions. This allows for the etching of the features in the silicon to be performed using a lattice-plane selective etch, tetra-methyl-ammonium hydroxide (TMAH), which etches (111) silicon-lattice planes at a rate 10 to 50 times more slowly than it etches other planes, such as the (110) surface of the wafer. Thus the (111) planes of the reference-feature sidewalls behave as lateral etch stops. Since these (111) planes are perpendicular to the (110) surface, the reference features have planar, vertical, (111) sidewalls.

We used a combination of two metrologies to achieve acceptable uncertainties in the CD: these are lattice plane counts, as revealed by High Resolution Transmission Electron Microscopy (HRTEM), and Atomic Force Microscopy (AFM). We used a CD-AFM, which is specialized for CD measurement in that it uses what is re-

ferred to as a “boot shaped” tip. This allows for imaging of the sidewalls of a vertical feature as well as the surfaces. This technical approach to CD calibration has not been implemented previously, as far as we know. Following a screening procedure using optical and scanning electron microscopy, AFM images of the each of the selected reference features is performed. Following AFM imaging, a selection of features is chosen for HRTEM imaging. HRTEM cannot be performed on all of the reference features as the preparation needed for HRTEM by necessity destroys the features. From the lattice-plane count, a curve showing the relationship between the CD as measured by the AFM and the CD as revealed by the silicon lattice is acquired. CDs are assigned to the remaining chips from this curve.

As a result of this procedure, CD reference features with dimensions between 40 nm and 100 nm were produced with the unprecedented expanded uncertainties of less than 2 nm.

Interconnect fabrication processes involve a sequence of several tens of lithographic operations, each requiring close alignment of the patterned resist to features that have been etched after the previous such operation. Successful manufacturing typically requires alignment and overlay accuracies in the low several nanometers range

Challenges associated with advanced interconnect include the understanding of charge transport in very narrow features. The charge transport is affected by the interaction of the charge carriers with grain boundaries and sidewalls. When the size of either the grains or lines is significantly larger than the mean free path of the electrons, the conductivity of the wires is similar to that of bulk. However, when these dimensions are less than or equal to the mean free path, the conductivity is expected to increase significantly. There are two “features” of conventional copper interconnect systems that complicate any experiments. The first feature is the barrier layer that is needed to keep the copper from diffusing into the surrounding insulator and silicon layers. This barrier layer is usually comprised of a metal, such as tantalum, which is a poor conductor. The second feature is that the planarization in the damascene patterning process can lead to dishing or erosion, which leads to the sheet resistance being a very non-linear function of dimension. Decoupling the contributions to a measured sheet resistance of these two effects is difficult, if not impossible.

We are taking several approaches to address these issues. The first approach is to develop a model from

which the sheet resistance can be calculated for an arbitrary set of dimensions, grain sizes, and scattering coefficients. The results from this model will be compared with measurements of patterned and unpatterned copper films at a range of temperatures. To simplify analysis of the material, we will initially measure copper films with no barrier layer and later extend the measurements to films with barrier layers.

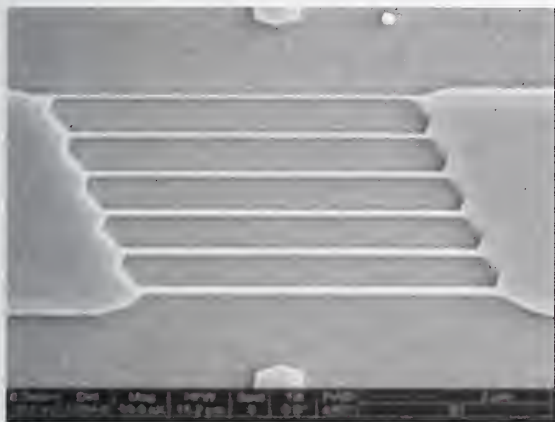


Figure 1. SEM image of the new test structure. (Lengths of the lines shown are approximately 10 µm, and the widths range from about 45 nm to 210 nm.)

Accomplishments

Delivered to ISMT, in collaboration with NIST's Manufacturing Engineering Laboratory (MEL) and Information Technology Laboratory (ITL), ISMT, and VLSI Standards, ten chips containing NIST calibrated CD reference features. These chips, which have been distributed to ISMT's ten member companies, including Intel, IBM, TI, AMD, and Freescale/Motorola, were delivered with sub-100 nm CDs and expanded uncertainties of 1.5 nm. This represents a major improvement over a prior delivery of reference materials from this project with a minimum of 15 nm uncertainty. The improvement in uncertainty resulted from the implementation of a new type of HRTEM-target test structure, an improved lattice-count/CD extraction procedure, the extensive use of SEM inspection to identify targets with superior CD uniformity, and the use of advanced AFM to serve as the transfer metrology.

Held a public meeting at which time these results were presented to SEMATECH, the SEMATECH member companies, and other interested parties. At that time, SEMATECH indicated some interest in pursuing this area of research.

CD reference materials team (with ITL leadership) awarded ATP funding to extend work to non-semiconductor industry related nanotechnology applications. Four papers describing aspects of this work are

being presented at conferences.

Selected Publications

1. N. Guillaume, W. K. Kahn, R. A. Allen, M. W. Cresswell, M. E. Zaghloul, "Application of Conformal Mapping Approximation Techniques: Parallel Conductors of Finite Dimensions," IEEE Transactions on Microwave Theory and Techniques, Vol. 53, No. 3, pp. 812-821 (01-JUN-2004).
2. R. A. Allen, M. W. Cresswell, C. E. Murabito, R. Dixson, E. H. Bogardus, "Critical Dimension Calibration Standards for ULSI Metrology," Characterization and Metrology for ULSI Technology: 2003, International Conference on Characterization and Metrology for ULSI Technology, Mar 24-28, 2003, Austin, Texas, pp. 421-428 (30-SEP-2003).
3. R. A. Allen, B. A. am Ende, M. W. Cresswell, C. E. Murabito, T. J. Headley, W. F. Guthrie, L. W. Linholm, C. H. Ellenwood, E. H. Bogardus, "Test Structures for Referencing Electrical Linewidth Measurements to Silicon Lattice Parameters Using HRTEM," IEEE Transactions on Semiconductor Manufacturing, Vol. 16, No. 2, pp. 239-248 (01-MAY-2003).

Molecular Nanomagnets

New methods are being developed to quantitatively determine the high-frequency properties of molecular nanomagnets for potential use in nanoscale magnetic data storage and biomedical imaging.

Brant Cage and Stephen E. Russek (EEEL)

Many technologies require or are enabled by the use of magnetic nanostructures such as molecular nanomagnets. The study of magnetic nanostructures will enable data storage on the nanometer scale, a better understanding of the fundamental limits of magnetic data storage, and new biomedical applications.



Figure 1. Brant Cage next to a magnetometer modified to simultaneously measure magnetic moment and high-frequency EPR spectra on nanomagnets.

We are developing new methods to characterize the magnetic properties of nanomagnetic structures such as molecular nanomagnets. One method is high-frequency electron paramagnetic resonance (EPR), based on a superconducting quantum interference device (SQUID) magnetometer, which can simultaneously measure low-frequency magnetic properties and high-frequency characteristics, such as resonant absorption/emission of microwaves in the frequency range of 95 to 141 gigahertz over a temperature range of 1.8 to 400 Kelvin. Molecular nanomagnets, which are the smallest well defined magnetic structures that have been fabricated, exhibit quantum and thermal fluctuation effects that will necessarily be encountered as magnetic structures shrink into the nanometer regime. These systems, which contain from 4 to 19 transition-metal atoms, form small magnets with blocking temperatures of 0.1 to 5 Kelvin. We are investigating new methods of manipulating these nanomagnets by varying the ligand structure and binding them to various films. We are looking at new applications by incorporating the nanomagnets into molecular devices and exploring how the nanomagnets relax nu-

clear spins in biological systems.

Broadband SQUID-Detected Electron Paramagnetic Resonance Probe

High-frequency electron paramagnetic resonance (HF-EPR) is a powerful technique for the characterization of magnetic materials. Measurements at 100 gigahertz and above allow greater resolution in the determination of magnetic energy levels, which are useful for the development of new materials for nanomagnetic data storage, spin electronics, and biomagnetism. However, a serious shortcoming of conventional HF-EPR is its inability to quantitatively measure magnetic moment. We have developed a new technique to make quantitative measurements using a commercial SQUID magnetometer.

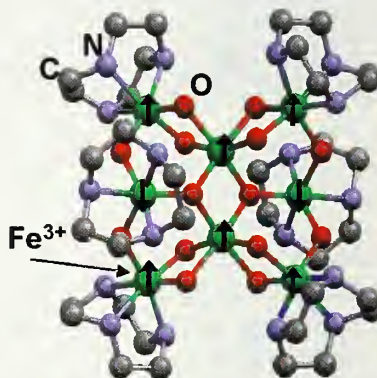


Figure 2. Structure of Fe-8 molecular nanomagnets, after R. Sessoli and D. Gatteschi, *Angew. Chem. Int. Ed.* **42**, 268-297 (2003).

We are able to directly measure the change in magnetic moment of a specimen as microwave stimulation causes resonance at different values of applied magnetic field. The apparatus uses a 95 or 141 gigahertz klystron microwave source followed by an isolator, an attenuator for saturation studies, and a directional coupler. A detector/mixer monitors the frequency and both reflected and incident power. A square-to-round waveguide transition to thin-wall tubing is used to deliver the microwaves to a sample located inside the magnetometer. The probe assembly and sample are mechanically oscillated through the SQUID pick-up loops to obtain the magnetic moment. Quantitative measurement of the degree of saturation at any value of magnetic field allows spin-lattice relaxation times to be calculated in the low-power, saturation regime. (Conventional EPR studies require approaching or exceeding the high-power, nonlinear regime.) This is important at high frequencies where the available microwave power is usually limited.

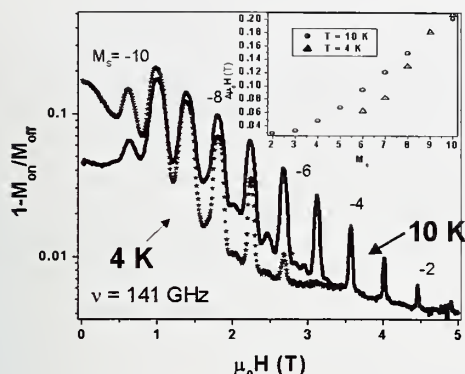


Figure 3. SQUID high-frequency EPR spectra of Fe-8 showing resonant absorption corresponding to transitions between the quantized energy levels.

Characterization of Energy Levels and Saturation in Fe-8 Molecular Nanomagnets

We completed a study of Fe-8 molecular nanomagnets using SQUID HFEPR. This work is the first to quantitatively measure the magnetization suppression of molecular nanomagnets under microwave illumination. By resonantly pumping low lying energy levels at 95 gigahertz it was possible to suppress the magnetization by 80 percent, indicating the presence of an efficient “spin cascade” that allows energy to be efficiently transported from the low-lying spin levels to high-energy levels. The exact mechanism of this spin cascade is still under investigation.

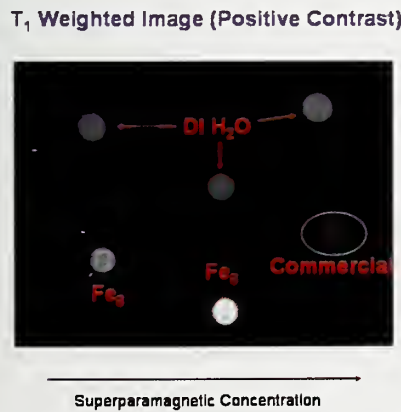


Figure 4. MRI cross-sections of Fe-8 solutions in water, along with pure water and standard Gd-based contrast agents. The variation in intensity from that of the water samples indicates that Fe-8 effectively varies T_1 . Work is done in collaboration with Denver Children's Hospital and University of Colorado.

Development of Molecular Nanomagnets for MRI Contrast Agents

On potential application of molecular nanomagnets is for magnetic resonance imaging (MRI) contrast agents.

The fluctuating moment of a molecular nanomagnet can have a large effect on the nuclear magnetic resonance (NMR) energy relaxation time (T_1) and dephasing time (T_2) of the surrounding protons in water or biological tissue. The local changes in the relaxation times can be used to highlight different tissues, the vascular system, tumors, or neurological activity. Measurements of the effects of Fe-8 on the NMR signal of protons in biological solutions have shown that Fe-8 can effectively modify both T_1 and T_2 . The detailed understanding of the magnetic properties and fluctuations of nanomagnetics will lead to more effective contrast agents and new MRI imaging modalities.

Selected Publications

1. B. Cage and S. E. Russek, “Design for a Multifrequency High Magnetic Field Superconducting Quantum Interference Device-Detected Quantitative Electron Paramagnetic Resonance Probe: Spin-Lattice Relaxation of Cupric Sulfate Pentahydrate ($\text{CuSO}_4 \cdot 5\text{H}_2\text{O}$), *Rev. Sci. Instrum.* **75**, 4401-4405 (November 2004).
2. B. Cage, S. E. Russek, D. Zipse, and N. S. Dalal, “Advantages of SQUID-Detected Magnetic Resonance Over Conventional High-Frequency EPR for Characterization of Nanomagnetic Materials,” *J. Appl. Phys.*, in press.
3. B. Cage, A. Barker, S. E. Russek, C. Stoldt, C. Lanning, G. Ruchiera, R. Shandas, D. Zipse, and N. S. Dalal, “Single Molecule Magnets Hold Promise as Water Soluble Iron-Based MRI Contrast Agents of Size less than 5 nm,” submitted.
4. B. Cage, S. E. Russek, D. Zipse, J. M. North, and N. S. Dalal, “Determination of the Spin-Lattice Relaxation Time of Individual m_s Levels of the Molecular Nanomagnet Fe-8 using SQUID Detected High Frequency EPR,” submitted.
5. B. Cage, B. F. Riddle, J. R. Baker-Jarvis, S. E. Russek, C. M. Ramsey, J. M. North, D. Zipse, and N. S. Dalal, “A Compact, Inexpensive, High-Frequency (50 GHz) Electron Paramagnetic Resonance (EPR) Probe Design for Materials Characterization,” submitted.

Nanomagnetic Measurements

We develop micro-electromechanical systems (MEMS) for nanomagnetic research. Microcantilever-based applications include scanned-probe microscopy; ultra-sensitive magnetometers with sub-monolayer sensitivity; torsional oscillator magnetometry and ferromagnetic resonance spectroscopy of submicrometer magnetic dots; and scanned probes for measuring microwave power above circuits.

John Moreland, EEEL (818)

The Information Storage Industry Consortium's recording-head metrology roadmap calls for high-resolution, quantitative magnetic microscopes and magnetometers that go beyond the limitations of current technology. Magnetic measurement systems have become increasingly complex. Our expertise in magnetism, probe microscopy, and cleanroom microfabrication techniques helps move instruments from the development stage to routine operation in the industrial laboratory and on the factory floor.

In order to improve upon magnetic microscopes, we are focusing on specialized magnetic-force-microscope (MFM) tips for imaging heads and media. New approaches based on MFM imaging are being developed to go beyond the current MFM resolution of 10 nanometers. We are developing ways to attach submicrometer magnetic resonance particles to ultra-sensitive cantilevers and to position particles a few nanometers from the sample surface.



Figure 1. Dong-Hoon Min preparing resonant cantilever for measurement of absolute magnetic moment of a magnetic thin film.

We are developing new tools for measurements of nanoscale magnetic phenomena and representations of magnetic units for the next generation of data-storage devices. We are developing MEMS magnetometers with integrated magnetic samples that can offer tremendous

gains in magnetic-moment sensitivity. Our micro-machining facility is at the state of the art, providing the tools necessary for bulk and surface micromachining on Si wafers. In the near future we plan to demonstrate new metrology instrumentation based on MEMS devices that will enable us to create instruments that have superior performance compared to current magnetic-measurement methods based on macroscopic modalities.

We are developing micro-electromechanical systems (MEMS) technology for micrometer- and submicrometer-scale magnetic samples. Nanoscale samples are a challenge for conventional magnetometers, and new methods are being employed to probe magnetism on this scale. Normally, measurements are made on arrays of micromagnetic dots. Due to fabrication limitations, the results are clouded by statistical variations in dot shape, size, and spacing. More sensitive detectors are needed that can measure magnetic properties of individual dots.

In particular, there is a need to understand atomic-scale spin damping in ferromagnetic systems in order to improve the switching speed of magnetic devices. For example, data-transfer rates for commercial disk drives will soon require operational bandwidths in excess of 1 gigahertz. For switching times less than 1 nanosecond, gyromagnetic effects dominate. One way to understand damping is to investigate size effects as magnetic devices are reduced to submicrometer dimensions. Studies of magnetic nanodots give a better understanding of spin damping and aid in development of faster disk drives.

We will provide new magnetometers based on highly specialized MEMS chips fabricated at NIST. The instruments will be inexpensive, since MEMS can be batch-fabricated in large quantities. Large-scale magnetic wafer properties can be transferred to smaller MEMS magnetometers so that nanometer-scale measurements can be calibrated with reference to fundamental units. Our focus is on developing torque and force magnetometers, magnetic-resonance spectrometers, and magnetic-resonance imaging (MRI) microscopes on MEMS chips. We expect that this technology will lead to atomic scale magnetic instrumentation for the measurement and visualization of fundamental magnetic phenomena.

In order to improve upon scanning probe microscopes, such as MFM, and keep pace with industry needs, we are focusing on specialized MFM tips for imaging heads and media. Ultra-small tips are currently being developed for magnetic-image resolution of 20 nanometers. We are looking at new technologies for fabricating, controlling and measuring nanometer-scale

magnetic structures near the probe tip. In particular, MFM resolution can improve only with the development of more sensitive cantilevers for measuring the small magnetic forces associated with nanometer-scale magnetic probe tips. Conventional MFM is not an intrinsically quantitative technique. Quantitative field mapping can be done with tiny field probes based on mechanical detection of magnetic resonance in the probe. We are developing ways to fabricate small magnetic-resonance particles on ultra-sensitive cantilevers and position the particles a few nanometers from the sample surface for field mapping with one-nanometer resolution.

Frequency Modulation Detection in MEMS *In-Situ* Magnetometer

We have improved our in-situ magnetometer for monitoring the magnetic properties of thin-film multilayers during deposition. By tracking the frequency shift we can separate the magnetic signal from the mass loading and thermal effects. The demonstrated sensitivity for a Ni-Fe film deposition is less than 0.1 nm. This is sufficient for fundamental studies of thin-film interface magnetism and magnetic exchange interactions in multi-layer structures.

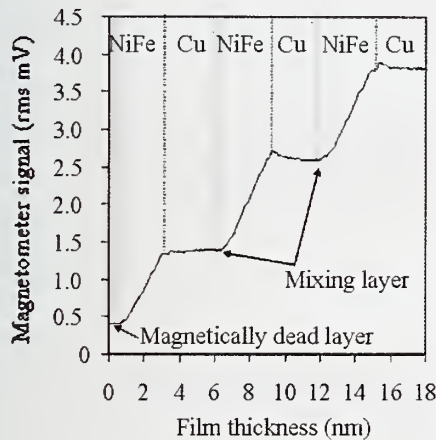


Figure 2. Magnetometer response as a function of film thickness measured with a quartz crystal micro-balance for $\text{Ni}_{0.8}\text{Fe}_{0.2}$ (3 nm)/Cu(3 nm) multilayer film.

Absolute Magnetic Moment

We have demonstrated the concept for an ultra-small magnetic moment standard reference material based on a thin magnetic film deposited onto a cantilever detector. We performed microtorque magnetometry measurements on a series of cantilevers with thin Permalloy ($\text{Ni}_{80}\text{Fe}_{20}$) samples deposited onto them. These cantilevers and the Permalloy samples have been optimized for moments on the order of a nano-joule per tesla. The method has promise for relating all critical measurements pertaining to the determination of the magnetic moment to fre-

quency, which can be determined accurately with a frequency source based on an atomic clock.

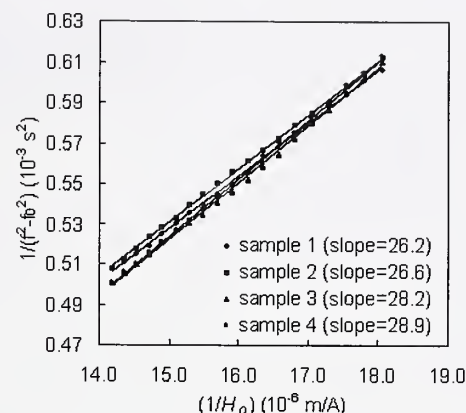


Figure 3. Plots of $1/(f^2 - f_0^2)$ as a function of reciprocal magnetic field $1/H_0$ for 4 samples of $\text{Ni}_{0.8}\text{Fe}_{0.2}$, 500 nanometers thick. The inverse of the slope of the line is proportional to the magnetic moment, and the inverse of the intercepts is proportional to the anisotropy energy. The average values obtained for the samples are respectively 4.67 ± 0.46 nanojoules per tesla and 143.7 ± 6.4 joules per cubic meter.

Selected Publications

1. D. H. Min, A. McCallum, S. E. Russek, and J. M. Moreland, "Sub-Monolayer In-Situ Micromechanical Torque Magnetometer with Integrated Fiber Optic Interferometer for UHV Applications," *J. Magn. Mater.* **286**, 329-335 (February 2005).
2. L. Gao, D. Q. Feng, L. Yuan, T. Yokota, R. Sabirianov, S. H. Liou, M. Chabot, D. Porpora, and J. M. Moreland, "A Study of Magnetic Interactions of $\text{Ni}_{80}\text{Fe}_{20}$ Arrays Using Ultra-Sensitive Microcantilever Torque Magnetometry," *J. Appl. Phys.* **95**, 7010-7012 (June 2004).
3. M. D. Chabot, J. Moreland, L. Gao, S. H. Liou, and C. W. Miller, "Novel Fabrication of Micromechanical Oscillators with Nanoscale Sensitivity at Room Temperature," *J. MEMS*, in press.
4. D. H. Min and J. Moreland, "Quantitative Measurement of Magnetic Moments with a Torsional Resonator: Proposal for an Ultra-Low Moment Reference Material," *J. Appl. Phys.*, in press.

Nanoparticle Measurements for Biological Applications

We are developing techniques for magnetic manipulation and measurement of single molecules and radio-frequency tags for magnetic resonance imaging.

John Moreland, EEEL (818)

Measurement tools and methods are needed for isolating, manipulating and probing the behavior and structure of single molecules. The semiconductor electronics industry has driven the development of fabrication tools that are capable of patterning structures on the order of 100 nanometers, smaller than cellular dimensions. Using micro-electromechanical systems (MEMS), we can create three-dimensional structures that are commensurate with the size of biomolecules. Interactions of single molecules with nanoscale mechanical structures, restriction elements, and other single molecules are probed by magnetic, electronic, electromechanical and optical techniques.

This interdisciplinary NIST effort will result in a well characterized platform integrated with atomic force microscope (AFM), fluorescence resonance energy transfer (FRET), optical microscopy, and electronics, thereby enabling a wide variety of single-molecule studies. Determination of DNA structure will be performed by directly interrogating ordered bases as they are threaded through a well characterized nanopore.



Figure 1. Elizabeth Mirowski characterizing spin-valve magnetic traps for microfluidic magnetic bead capture and sorting.

Instrumentation is being adapted to a new class of microwave probe stations that use micromachined probe chips to extend voltage and current probe measurements on microwave circuits with submicrometer spatial resolution in the 100 gigahertz range. We are extending this technology to biological and medical applications in an effort to develop applications-specific magnetic particles

as well as highly specialized microchips. For example, we are currently developing a chip-scale MRI system for ultra-high-resolution MRI of cell organelles.

High-Throughput Lab-on-Chip for Sorting Biologically-Compatible Magnetic Particles

We have integrated a novel microfluidic magnetic trap platform with an external magnetic force microscope (MFM) to capture and sort magnetic particles into discrete positions in an array. The principle of the platform is to sequentially flow magnetically modified biological samples into the array and to sort them to produce a matrix reference. The matrix can then be transported to a location where each individual magnetic particle — and hence biological sample — can be probed to obtain details about its medical or forensic functions, such as gene sequence or physical structure in different physiological environments. Alternatively, the array can be used to sort particles of varying sizes and magnetic susceptibilities, thereby providing standards for magnetic particles used in medical applications such as contrast enhancers in magnetic resonance imaging or to coax together severed nerve cells so that they can repair themselves and restore mobility to limbs.

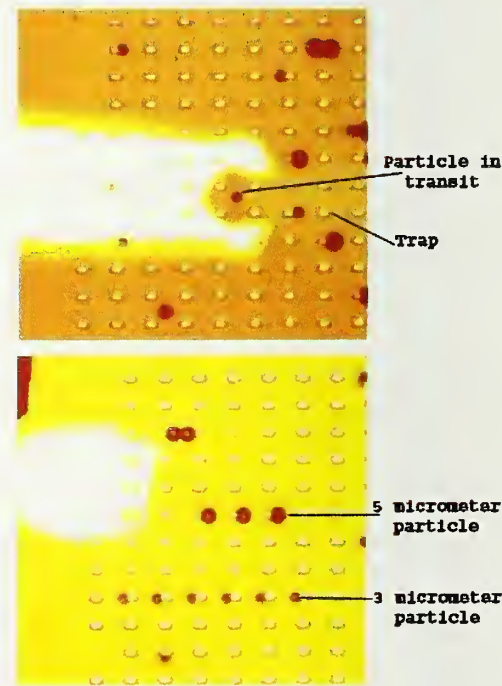


Figure 2. An array of traps (1 micrometer \times 3 micrometer rectangles) and randomly distributed magnetic particles (3 micrometer and 5 micrometer diameters). The white area is the magnetorobotic arm. The top image is before sorting and the bottom is after sorting.

The platform consists of an array of magnetic trapping elements separated from the fluid sample by an optically transparent thin membrane. The magnetic particles are trapped by the local field gradients produced by the magnetic element with a force of approximately 100 piconewtons, which can ensure that the particle remains in the desired position through rigorous transport. The cobalt-coated MFM cantilever serves as a magnetorobotic arm that provides a translatable local magnetic field gradient that captures and moves the particles with nanometer precision. We integrated the electronics of the magnetorobotic arm with a digital camera and programmed it to sort an initially random distribution of particles by moving them within the array of magnetic trapping elements. The forces acting on a 1 micrometer diameter particle were measured by viscous drag in the fluid to be on the order of 50 piconewtons, thereby allowing a sorting rate of approximately 1200 particles per minute. Release of the particles from the cantilever is achieved by retracting the arm, leaving the particles in the solution, retained by the transparent membrane.

Modeling of MRI images for Single-Particle RF Tag Applications

We developed a computer program for calculating the static field profile near microscopic magnetic particles with different magnetic moments. The program is based on solving Maxwell's equations with given boundary conditions. The program also predicts the effect of the field profile on MRI images for different imaging scenarios (phase versus frequency encoding). The program goes beyond previous calculations to include the limit below one volume pixel (voxel). Typical minimum voxel sizes for MRI instruments are around 300 micrometers. However, even if a magnetic particle is much smaller than a voxel, as is the case for micrometer-sized particles, its influence on the applied magnetic field locally can be significant several voxels away due to the narrow line width of the proton nuclear magnetic resonance of water. By developing particles with specific shapes and sizes and materials with nanometer dimensional control, very distinct changes in the MRI image will occur and can be detected with research-grade MRI systems used in medical centers today. The particles would be used as tags for individual cells in the body to monitor in-vivo cell functionality.

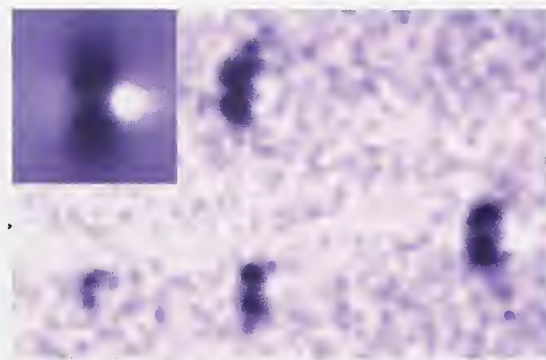


Figure 3. MRI image distortion due to the presence on individual magnetic polystyrene spheres about 1 micrometer in diameter. The data were taken at the Laboratory of Functional and Molecular Imaging at the National Institute of Health (NIH) and modeled at NIST (inset).

Selected Publications

1. E. Mirowski, J. Moreland, S.E. Russek, and M.J. Donahue, "Integrated Microfluidic Isolation Platform for Magnetic Particle Manipulation in Biological Systems," *Appl. Phys. Lett.* **84**, 1786-1788 (March 2004).
2. E. Mirowski, J.M. Moreland, A. Zhang, S.E. Russek, and M.J. Donahue, "Manipulation and Sorting of Magnetic Particles by a Magnetic Force Microscope on a Microfluidic Magnetic Trap Platform," submitted.

Imaging Methods for Nanoparticle and Cell Systems to Investigate Toxicity

Cost-effective and accurate imaging methods are needed to support studies of nanoparticles and cell systems. This need spans a scale from a few nanometers to many tens of micrometers and may include living tissue. The capabilities of conventional optical microscopy combined with recent advances in desktop computing power, were applied to nanoparticle location in human cells, ultimately to aid in the selection and development of the most suitable imaging methods for nanoparticle toxicity studies.

Cynthia J. Zeissler and Peter E. Barker, PL (837)

Little is known about the toxicity of nanoparticles, despite the rapid emergence of nanotechnology products. The potential ability for nanoparticles to pass through skin, and possible consequences, are of interest to manufacturers and users alike. Studies of nanoparticle transport in skin tissue are being developed at NIST, for which imaging capabilities and limitations will be of paramount importance.

Nanoparticle and cell systems can be studied using strongly fluorescent nanoparticles called quantum dots, typically 1 nm to 20 nm in size. The fluorescence emission of quantum dots is readily detected by optical microscopy, however the ability to locate quantum dots to a precision below the diffraction limit of light is a problem. Resolution limitations due to the diffraction of light can be approached by other methods such as transmission electron microscopy (TEM), but with trade-offs. Specialized approaches such as optical superresolution are in development.

A variety of methods may be employed in a complementary fashion to try to address all imaging needs ranging from the nanoscale to the scale of relatively large organic systems of many tens of micrometers. Factors involved in the decision point for selecting conventional optical, specialized optical, or electron methods for nanotechnology research and development in general, have bearing on more than just the basic imaging capabilities. These may include instrumentation costs, the extent to which live-cell system experiments are possible, which imaging artifacts may be present, whether or not chemical measurements can be included, timing considerations, and other factors.

To demonstrate recent computing advances and for comparison to current and future advanced imaging methods that may be employed in the toxicity program, a

capability baseline was explored. This involved a simple optical system, combined with three-dimensional reconstruction methods utilizing recent desktop computing power improvements. Phase contrast and confocal methods were not applied, so that full resolution, simplicity, and low cost could be demonstrated.

Test specimens were created by culturing SK-BR-3 and MCF-7 human cancer cells with various combinations of streptavidin-conjugated quantum dots having emission bands of 585 nm, 605 nm, 655 nm and 705 nm. Samples were fixed prior to imaging.

Optical sectioning was performed, which simply takes advantage of the narrow depth of field inherent in high-resolution optical systems, and does not harm the specimens. Optical sections were three-dimensionally reconstructed, using a desktop Pentium 4 2.8 GHz processor, 512 MB RAM and 32 MB video RAM system. As computer speed and memory improve, the ability to image larger sections of tissue at once while retaining full spatial resolution is expected to improve also.

Figure 1 is an example of a single optical section of an SK-BR-3 cell, taken of 412 nm transmitted light from a 100 W tungsten-halogen lamp using a 30 second exposure time. This demonstrates that dominantly blue or intense laser sources were not necessary to achieve resolution slightly better than 300 nm, except possibly for future time-resolved live-cell studies.

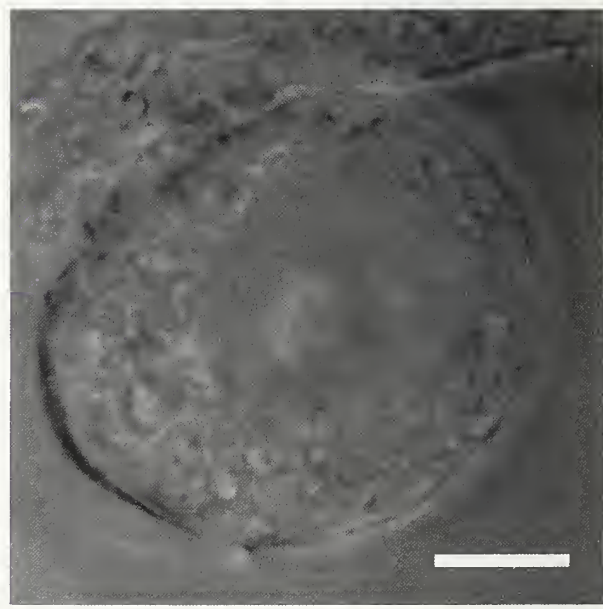


Figure 1. Optical section of an SK-BR-3 cell cultured with nanoparticles. The white scale bar is 5 μm long.

Nanoparticle positions were localized relative to cell features by combining the transmitted light images with epi-fluorescence images of the quantum dots. After reconstruction and surface-modeling, images such as those shown in Figure 2 were used to distinguish and locate nanoparticles outside and inside of the cells. Figure 2 mostly depicts a single cell, although with sufficient computer memory and speed, multiple cells can be evaluated at once, of advantage to skin tissue studies.

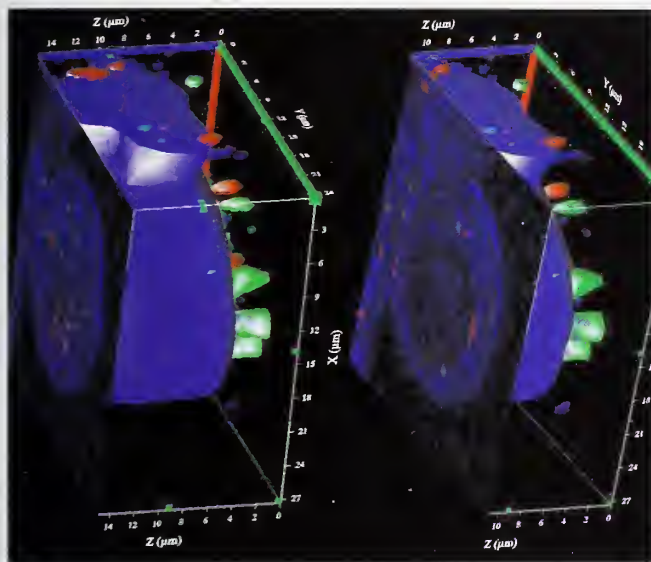


Figure 2. Cross section through 3-D reconstructed cell (blue) showing internal arrangement of two different types of nanoparticles (red and green). To aid visibility, the z-axis has been exaggerated by about 2.5x and surface modeling has been applied causing quantum dot locations on the cell exterior to be represented by red and green balloons. The field of view is nominally $25 \mu\text{m} \times 25 \mu\text{m} \times 6 \mu\text{m}$.

Figure 3 shows a virtual cross-section through a three-dimensionally reconstructed image of an area inside of a single cell, showing an example of the dimensions of the feature produced by quantum dot fluorescence. Each voxel is $47 \text{ nm} \times 47 \text{ nm} \times 50 \text{ nm}$. Voxel interpolation may be able to achieve a precision in quantum dot location close to the size of the quantum dot diameter, notably well below the optical resolution limit. The value of such precise quantum location by optical methods relative to the diffraction-limited location of cell features remains to be seen, since to utilize this information with regard to subcellular components, combination with TEM methods may be required. Future studies including focused ion beam (FIB) specimen preparation combined with TEM are planned.

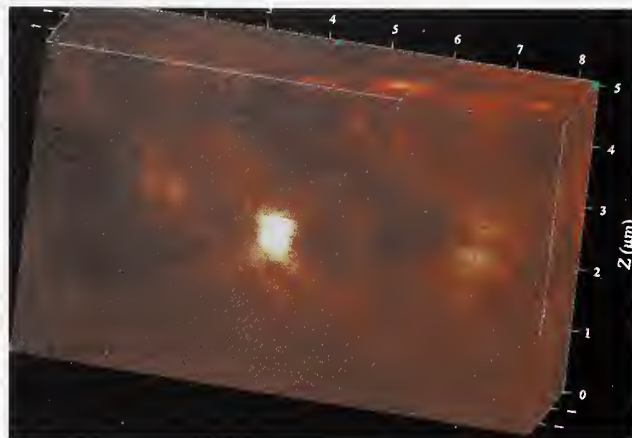


Figure 3. Cross section through quantum dot fluorescence (white) within a cell (red). Each voxel is $47 \text{ nm} \times 47 \text{ nm} \times 50 \text{ nm}$. The slice shown is $5 \mu\text{m}$ high, nominally $8 \mu\text{m}$ wide and $2 \mu\text{m}$ thick.

These results demonstrate that a simple optical microscope using inexpensive white-light sources combined with a liquid crystal tunable filter, and 3-D reconstruction on a modern desktop system, can be used to image the location of quantum dot nanoparticles outside and inside cells with a resolution of slightly better than 300 nm, consistent with the expected Rayleigh resolution limit for the conditions used. However, also suggested is that voxel interpolation may improve quantum dot location precision to less than 50 nm, below the diffraction limit. This presents a simplified but effective approach applicable to imaging nanoparticle and cell systems.

The next testing phase will include skin cells such as keratinocytes and fibroblasts on scaffold systems, and may include live systems, both of which are expected to offer special imaging challenges.

Selected Publications

4. Y. Xiao and P.E. Barker, Semiconductor nanocrystal probes for human chromosomes and DNA, *Minerva Biotech.* **16** (2004) *in press*.
5. Y. Xiao and P. E. Barker, Semiconductor nanocrystall probes for human metaphase chromosomes, *Nucleic Acids Research* **32**:3(2004):1-5.

Development of High-resolution Variable Pressure Reference Scanning Electron Microscope

High-resolution scanning electron microscope (SEM) imaging and metrology of nanostructures need the best available instrumentation. The structures are very small, comparable with the size of the imaging electron beam or the excited volume; therefore SEMs need to be pushed to their maximum capabilities. A reference metrology SEM is currently under development to meet the requirements of the emerging nanotechnology and the semiconductor industry. This new instrument is equipped with a field-emission electron gun and a special electron optical column to provide well-focused electron beam in every working mode. It has a custom-designed high-resolution laser interferometer sample stage. Highly accurate metrology techniques, including model-based metrology methods are currently under development.

Andras E. Vladar, Michael T. Postek and John S. Villarrubia, MEL (821)

There is currently no metrology SEM that exists, which is fully characterized, capable of measuring full-size wafers and photomasks, has low measurement uncertainty and capable of serving as a Reference SEM. NIST is now developing such an instrument. It is based on a new Variable Pressure SEM instrument, which is located in the new Advanced Metrology Laboratory. It has a thermal field emission electron gun with 1 to 3 nm spatial resolution, large (200 and 300 mm wafer and 6 and 9 inch photomask) sample measurement capability, and high-resolution laser interferometer stage. It works with variable electron landing energy and variable vacuum pressures. Its development and deployment of the Reference SEM is planned by CY 2006, to provide highly accurate, traceable 2-dimensional size and 3-dimensional shape e-beam measurements.

Traceability will be facilitated with a laser interferometer sample stage characterized with fast and smooth motion and very high resolution (<0.2 nm) with very fast (>2 million data points/s) positioning readout. It will have two image scanning modes: standing e-beam with scanned stage and standing stage with scanned e-beam. These will allow for the best calibration settings for large and small distances, and sizes. It will have a variety of possible signals and detectors and will work in oil-free, clean vacuum. The instrument will be located on a vibration isolation platform, i.e., on a heavy concrete slab, which floats on air springs. The laboratory will be in a new, clean laboratory with 0.25 °C temperature and 1 %

humidity control.

Development is needed to turn this instrument into one of the best dimensional metrology SEMs in the world. Hence, it will be highly scrutinized. This is necessary to find the best measurements settings and parameters, a thorough investigation of combined measurements and optimization of the SEM itself will be carried out. An assessment of resolution, e-beam and signal transfer characteristics, distortion and noise characteristics in various working modes will be performed. Full measurement uncertainty, accuracy & precision will be documented. The accurate top-down and cross sectional imaging and dimensional measurements will be supported by extensive Monte Carlo modeling of SEM images of all measured structure. The modeling accurately accounts for the physical properties of 2- and 3-dimensional sample structures and the signal generation, including instrument-dependent modeling of signal collection, amplification and noise characteristics. All these lead to, advanced and optimized edge algorithms and to highly accurate shape and size determinations.

The work in this project is in progress. It has been shown that the variable vacuum capability, as it was recently published, gives unprecedented image quality and resolution on otherwise difficult-to-image photomasks. Figure 1 shows two images of the same location of a Cr on quartz photomask. The image on the left is the evidence for severe sample charging in high-vacuum mode even at low, 800 V accelerating voltage, the right one in low vacuum at a much higher, 3.4 kV accelerating voltage. Even so, it shows much less sample charging. Note the slight contamination mark left during the previous high-vacuum imaging.



Figure 1. Severely charging image taken in high vacuum (left). The image on the right was taken in low vacuum with no apparent charging (right).

Figure 2 shows two high-magnification images of the same photomask. Note the excellent resolution; even the Cr grains are well visible. These are excellent inputs for dimensional measurements. The left, tilted-view image reveals the layered structure of the Cr film. The right image shows significant edge roughness, some contamination and other defects.

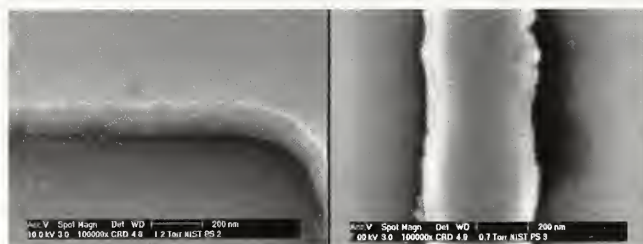


Figure 2. High-resolution tilted (left) and top-down-view (right) images of a Cr photomask.

The reference SEM, as one of the best SEMs existing today has a specification for the highest achievable spatial resolution close to 1 nm. In many cases the spatial resolution, i.e., the smallest resolvable distance between features in the SEM image of these microscopes is not limited by the focusing ability of the electron optical column. Sample stage vibration and drift, electromagnetic fields, including charging, the extent of the information volume (that part of the excited volume where the signal is coming from), and other factors limit the resolving power. Techniques that allow for imaging and measurements at the best resolution are becoming important when the potential advantages of further improvements in the focusing ability of the instrument cannot be realized due to the above problems.

As the electron beam scans the sample in the X and Y directions, the electronics of the microscope collects the signal intensity for certain short periods of time (pixel dwell time) and generates a two-dimensional intensity distribution, a matrix, which can be viewed as an image. The image produced by a sharply focused beam is a good representation of the sample as long as the sample is sufficiently motionless and the beam scans linearly. This is never the case with real microscopes when the images are taken at the highest resolution, because the electron beam and the sample stage always have unintentional motions; both have low frequency drift and other, higher frequency motion. The result is a complex, compound distortion that is present in most real-life SEM imaging and measurements. Barring other potentially significant problems, like charging, contamination, noise, focusing, this distortion could be the most difficult to get rid of. If the compound motion of the electron beam and sample is mostly low frequency (drift), then linear and non linear distortions dominate the problems with the resulting image. If the compounded motion of the electron beam and sample is mostly high frequency and covers a larger area than the size of the finest focus's spot, then the image is blurred, just like when an image was taken with a not fully focused beam.

The short-term drift of the electron beam is typically very small, but external electromagnetic fields could move the beam and as a result, the edges of sharp objects

might show characteristic jaggedness. The sources of these external electromagnetic fields can be found and the fields can be reduced at their origin. It is also possible to get satisfactory remedy through the use of high magnetic permeability metal shields and compensatory techniques.

Figure 3 shows the SEM sample stage motion during a short (5 μ s) period of time tracked by laser interferometer. The approximately 160 pm resolution shows in details that the stage is not completely motionless at nanometer levels it covered a 1.7 nm by 1.7 nm area, while staying most of the time in a 1 nm² area which was not centered at the intended relative X0,Y0 coordinates.

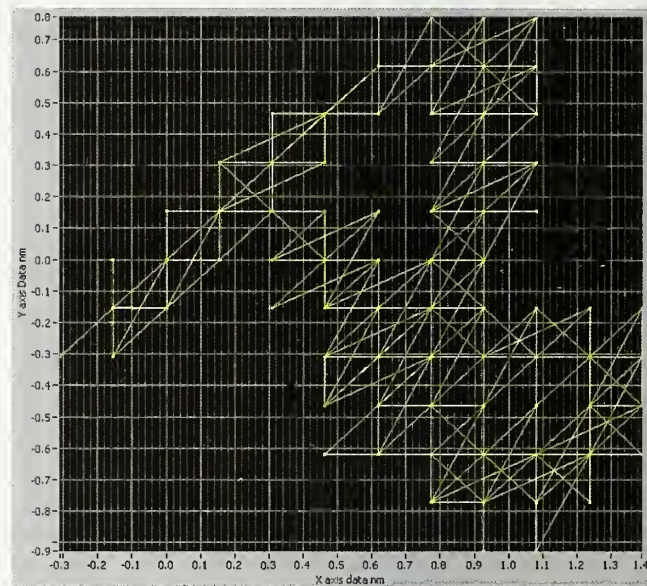


Figure 3. Short-time SEM sample stage motion tracked by laser interferometer.

This denotes an error that is in the size and location of the information volume of the collected data, because without further information the best bet is to assign the data to their intended location. The knowledge of the stage position at these levels allows for compensation for stage drift and vibration and therefore considerable spatial resolution improvement.

These and other advanced and highly accurate metrology techniques, including model-based metrology methods are currently under development and will be implemented quickly when the new SEM arrives at NIST.

Scanning Probe Microscopy for Nanoscale Measurements

Industrial users of scanning probe microscopy need accuracy in dimensional measurements at the nanometer scale. They rely on calibration standards to achieve this. Therefore, we are developing world class traceable calibrations of scanning probe microscopes with nanometer and sub-nanometer uncertainties. We focus here particularly on two recent advances in linewidth measurement, one of them having uncertainty at the nanometer level, for semiconductor and nanomanufacturing applications.

Ronald Dixson, Joseph Fu, George Orji, and Theodore Vorburger, MEL (821)

The NIST response to the need for traceable scanning probe microscope (SPM) calibration standards is cross-cutting and involves the development of special in-house metrology instruments as well as methods for commercially available instruments and collaborations with external partners. One component is the development of the calibrated atomic force microscope (C-AFM). This instrument incorporates displacement interferometry to achieve traceability to the SI meter. The C-AFM uses conventional conical tips and is thus best suited for pitch and height measurements, which are the appropriate measurands for scale calibration standards. This instrument provides traceable pitch and height measurements for nano-scale applications. Pitch ranging up to 20 μm has been measured. The standard uncertainty u_c ranges from $\sim 0.5 \text{ nm}$ at smaller scales to $\sim 0.1 \%$ at the largest scales. Step height, ranging from a few nanometers up to several hundred nanometers, can be measured with u_c on the order of 0.5 % at the largest scales. We expect the fourth generation instrument, recently reassembled with a new scanner, to exhibit even lower uncertainties.

For measurement of linewidth, especially on near-vertical structures, a critical-dimension AFM (CD-AFM) is more appropriate. This type of instrument uses flared tips and two dimensional feedback to image near-vertical sidewalls. These instruments are typically used in semiconductor manufacturing. As part of our collaboration with SEMATECH, the leading semiconductor industry consortium, NIST was able to acquire a Veeco SXM320. A complementary approach involving carbon nanotube tips on a conventional AFM combined with image stitching is also being developed. Recent accomplishments in both of the areas are rapidly advancing the state of linewidth metrology with nanometer level uncertainties.

NIST and SEMATECH have effectively worked to-

gether on linewidth standards. One component of this cooperation has been the single crystal critical dimension reference materials (SCCDRM) project initiated by NIST researchers in EEEL (Cresswell and Allen). The 2004 release of SCCDRM samples to the SEMATECH Member Companies was recently completed, and CD-AFM dimensional metrology played a central role. The measurements on the SCCDRM samples were performed by NIST scientist Ronald Dixson during his tenure as a Guest Scientist at SEMATECH. A Veeco Dimension X3D, the current generation CD-AFM, was used for the SCCDRM measurements. Prior to the measurements, the X3D was characterized and calibrated, and implemented as a reference measurement system (RMS) for traceable measurements of pitch, height, and width. High resolution transmission electron microscopy (HRTEM) was used as an indirect method of tip width calibration for the SCCDRM samples. The AFM and HRTEM results that were used for the tip calibration are shown in figure 1. Features on the distributed samples ranged in width from approximately 50 nm to 250 nm with expanded uncertainties of about 2 nm ($k=2$) on most features. As a result of this project, CD-AFM linewidth measurements can now be performed with a 1 nm ($k=1$) standard uncertainty.

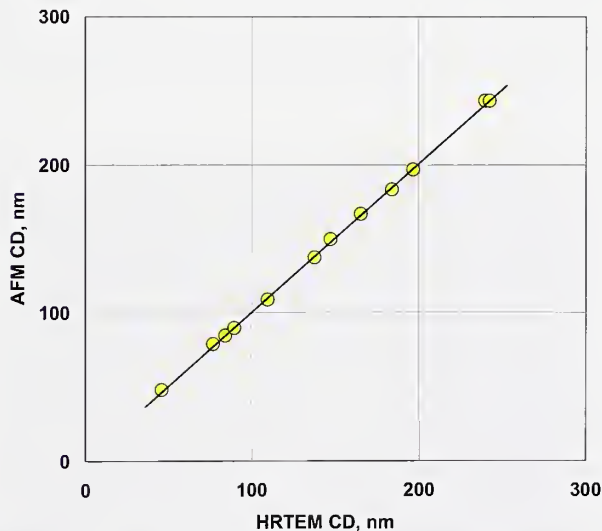


Figure 1. Regression of CD-AFM width values on HRTEM values. The observed slope is consistent with unity – indicating that the two methods have consistent scale calibration. The average offset between the results was used to correct the tip width calibration.

Carbon nanotubes, with small dimensions and excellent wear resistance, offer considerable potential as AFM tips. For linewidth metrology of nano-scale structures, however, nanotube tips have an important

limitation. The nanotubes are mounted at a non-normal angle with respect to the surface. Therefore, for features with near-vertical sidewalls, the tip will only be able to accurately image one sidewall at a time. One possible solution to this is to image a specimen in two orientations – one at 180 degrees with respect to the other – such that each sidewall of the feature is accessible in one of the images. If such images can then be merged with sufficient accuracy, the composite image may have metrological value.

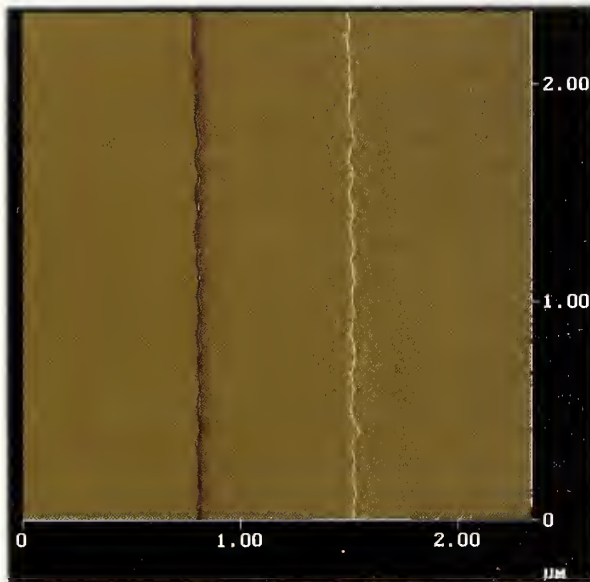


Figure 2a. Conventional AFM slope image using nanotube tip taken on a near-vertical structure in initial orientation. Only the right sidewall can be imaged accurately, as seen by the relative sharpness of the two edge regions. The arrow shows the location of a defect.

While image stitching is a well known technique, it has not been applied to scanning probe dimensional metrology. We are exploring the use of image stitching for linewidth metrology using nanotube tips. We have completed two comparisons of stitching results with calibrated CD-AFM width measurements. The results agreed within the estimated 40 nm expanded uncertainty of the stitching measurement. Our initial results, illustrated in figures 2 and 3, were obtained using tips having sub-optimal length, radius, and mounting angle. We are collaborating with suppliers to refine the carbon nanotube tips and are working on a new generation of this experiment. Publications at the SPIE Microlithography Conference in both 2004 and 2005 and at the 2005 ULSI Conference have resulted from this work.

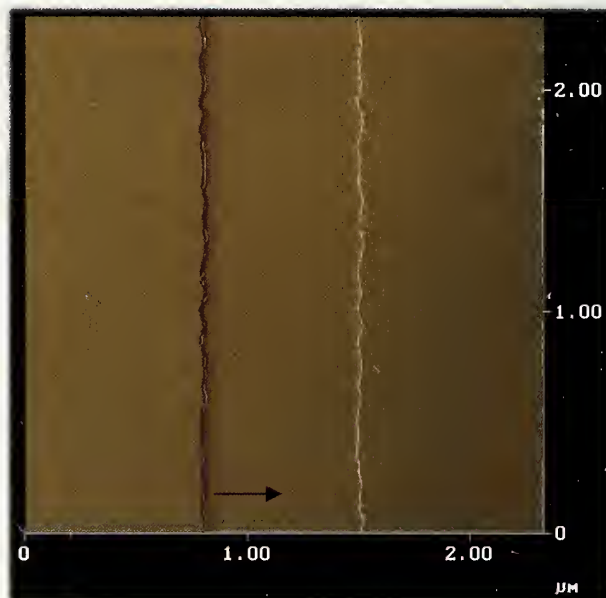


Figure 2b. Conventional AFM slope image using nanotube tip taken on a near-vertical structure after the sample has been rotated by 180 degrees. The apparent right sidewall, which corresponds to the left edge of the structure in the original orientation, can now be imaged accurately. The arrow shows the location of the same defect identified in figure 2a.

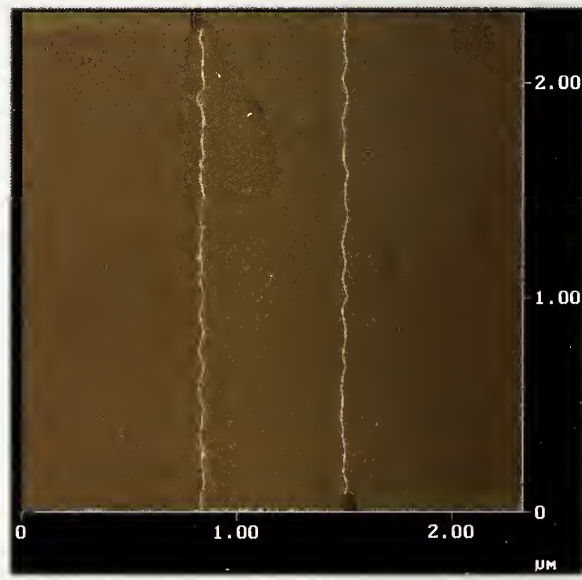


Figure 3. Composite image stitched together from the images in Figures 2a. and 2b. Both edges of the structure are now sharp.

Scanning Probe Microscopy for Nanoscale Measurements: Atom-Based Height Standards

Industrial users of scanning probe microscopy (SPM) need accuracy in dimensional measurements at the nanometer scale. They rely on calibration standards to achieve this. We are developing procedures for using atom-based step height standards for calibrating the z-scale of scanning probe microscopes at the highest levels of resolution of these instruments. A draft documentary standard developed under an ASTM Subcommittee is the final piece in the chain of developments to accomplish this with picometer (pm) scale uncertainties.

Joseph Fu, Ronald Dixson, George Orji, and Theodore Vorburger, MEL (821)

The semiconductor and other nanotechnology industries require physical standards with nanometer and sub-nanometer uncertainties for calibration of the scanning probe tools they use to measure the spacings, linewidths, and heights of the components they fabricate. We have been developing procedures and standards to provide the calibrations needed for all these quantities. Step heights in particular need to be measured to sub-nanometer uncertainties, but until recently traceable step height standards were only available commercially down to heights of about 7 nm.

We have developed procedures for industry to calibrate the z-scale of their probe microscopes with pm-level uncertainties using the 0.3 nm single-atom step heights found on the (111) lattice plane of Si. This development has taken place systematically over several stages. Initially, we collaborated with the University of Maryland to fabricate a number of prototypes of the Si(111) steps using a process pioneered by them. We then performed an independent, traceable calibration of the average Si(111) step height using the NIST calibrated atomic force microscope (C-AFM). This instrument incorporates displacement interferometry in all three axes of motion to achieve traceability to the SI meter. An image of a Si(111) sample taken in the C-AFM is shown in figure 1. Our result of 304 pm agreed within 10 pm of the accepted value of determined from x-ray diffraction of the bulk Si material.

We then developed a recommended value for the surface step height based on these two methods and on results from electron and surface x-ray diffraction. The value recommended was $312 \text{ pm} \pm 12 \text{ pm}$, with a coverage factor $k = 2$.

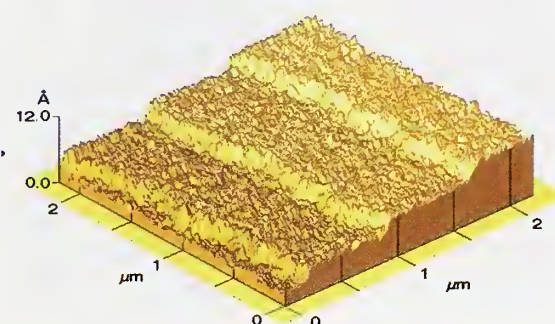


Figure 1. Image of Si(111) step height sample with native oxide taken on the C-AFM.

This work was performed at about the same time as an industrial comparison of five laboratories, including NIST with a proposed calibration procedure using the Si(111) steps as a standard. The data were provided to NIST by the laboratories and the step height results were calculated by us using a single step-height algorithm and associated software. The goal here was to investigate the internal variability of the industrial and NIST measurements to determine if that variability would be consistent with the pm-scale uncertainties desired for this type of measurement. The results from the laboratories showed that the industrial data coupled with a straightforward step height algorithm from NIST could yield calibrations of SPMs using the 312 pm step heights with uncertainties of several percent. Images obtained from industrial participants during this comparison are shown in figures 2 and 3.



Figure 2. An AFM image of single atomic step on Si (111) taken as part of the industrial comparison.

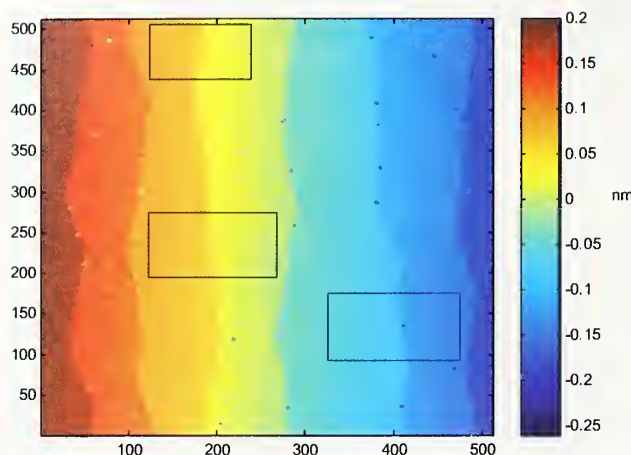


Figure 3. Another AFM image of single atomic step on Si(111) taken as part of the industrial comparison. The boxes drawn on the image illustrate the selection of measurement areas to calculate the step height.

Lastly, we have led the development of a documentary standard that describes the experimental approach and the step height algorithm needed to produce stable results for the measured step height. This standard is being developed under ASTM Subcommittee E42-14. The document, entitled “Standard Practice for Calibrating the z-magnification of an Atomic Force Microscope at Sub-nanometer Displacement Levels Using Si(111) Single Atom Steps”, with ASTM Work Item # 7322, has undergone several drafts and is now being reviewed by ASTM committee members.

Selected Publications

1. R. Dixson et al., Silicon Single Atom Steps as AFM Height Standards, Proc. SPIE **4344**, 157 (2001).
2. J. Fu et al., Algorithms for calculating single-atom step heights, Nanotechnology **10**, 428 (1999).
3. N. G. Orji et al. Traceable pico-meter level step height metrology, Wear **257**, 1264 (2004).

Atom-Based Dimensional Metrology

Customer needs and project objective: NIST is responsible to U.S. industry for the development of length intensive measurement capabilities and calibration standards in the nanometer scale regime. The new class of scanned probes have unparalleled resolution and offer the most promise for meeting these future needs of the evolving nanomanufacturing and semiconductor industry. One important application of the high-resolution SPM methods is in the development of linewidth standards whose dimensions can be measured and traced directly to the crystal lattice. These artifacts are intended to be dimensionally stable to allow transfer to other measurement tools which can measure the artifacts with dimensions known on the nanometer scale.

Richard Silver, MEL (821)

This project is developing atom-based linewidth measurement techniques and artifact standards to assist in the calibration of linewidth metrology tools and the development of unique interferometry capabilities which can be used in conjunction with accurately measured tips to measure feature position and dimensions. The research is intended to enable the accurate measurement of dimensions by counting the atom spacings across a feature in a controlled environment or by measurements based directly on the intrinsic crystal lattice spacing. The technique is compatible with subsequent transfer of artifacts to other measuring instruments after the atomic-scale measurements have been completed.

The technical work is focused in a few related thrust areas. The first area is the development of lithographically patterned three-dimensional structures using SPM methods in UHV. These structures must be in written so that they may be found and measured in other tools. Macro vision systems are a key aspect to enable interconnection to the macro world. A significant part of this effort is focused on preparing substrates for both imaging and fabrication at this scale. Wet chemical processing methods are used to prepare atomically ordered Si surfaces at ambient temperatures.

A second research thrust is the development of techniques for the preparation of SPM tips with reproducible geometries and the characterization of the tip dimensions on the atomic scale. These well characterized tip probes can be used to pattern samples which may be etched and processed at a subsequent step.

The remaining thrust is for the development of new interferometric techniques for sub-nanometer resolution measurement. The new approach to interferometry enables measurements in the 20 picometer resolution range with accuracy in a similar range. The interferometry system is also designed for use directly on the STM to enable atomic scale measurements with new levels of accuracy.

An essential element of this project is the fabrication of test artifacts and structures for the development of high resolution imaging methods. It is imperative to enable fabrication methods for sub-10 nm sized features. Several recent developments in optical microscopy, scatterometry and SEM metrology require test samples with critical dimensions below 10 nm. These test structures are simply not available at this time. In this project we are developing the methods for fabrication of sub-10 nm sized features and etching methods to transfer these patterns into the silicon substrates.

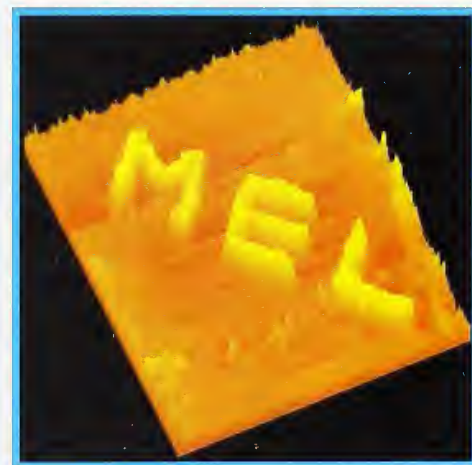


Figure 1. 10 nm features prepared using a UHV STM.

Although the new class of scanned proximal probes have unparalleled resolution and offer much promise for meeting the high resolution imaging and fabrication needs of nanomanufacturing, the substrates onto which the features are fabricated or imaged plays an essential role. Before this resolution can be translated into precise, accurate dimensional measurement capabilities and atom-based standard artifacts, the methods for preparing atomically flat substrates with atomic order need to be made routine and robust. Significant effort has resulted in major accomplishments in this area of research which were published in Applied Physics Letters.

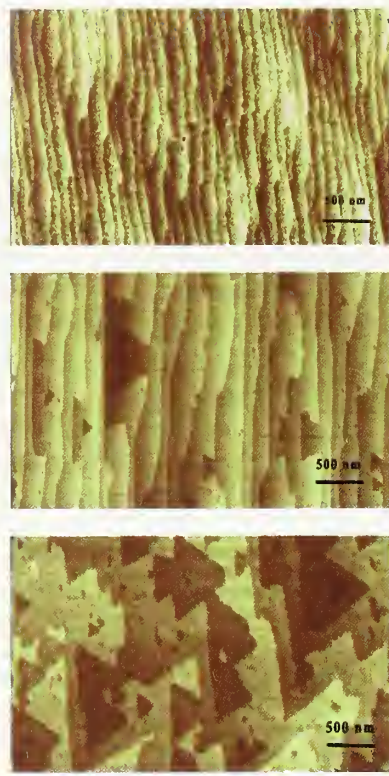


Figure 2. This figure above shows AFM images of Si substrates having three different miscut angles. The miscut angle plays a central role in the final morphology.

One key to accurate metrology at this scale is the development of methods for the production of reproducible tip shapes, the accurate measurement of tip geometry, and models which interpret imaging data to extract real feature dimensions. NIST has developed the means for the reproducible production and characterization of SPM tips, using tools such as field-ion-field-electron microscope (FIFEM).

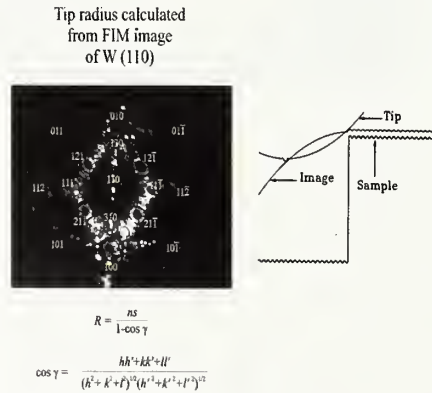


Figure 3. Atomic resolution FIM image of an STM tip.

The FIM instrument can also be used for field evaporation which produces tips with controlled microscopic geometries. One focus of this project is the preparation

of tips optimized for STM measurements and fabrication on atomically ordered surfaces.

The verify the atomic spacings at the surface and to enable traceable measurements of sub-50 nm sized features, a new interferometry capability has been developed. This new approach uses a constant number of wavelengths in the measurement path and continuously changes the interferometer wavelength using a tunable diode laser as the reference mirror is scanned. The laser frequency is constantly tracked and measurements with 20 picometer resolution have been demonstrated.

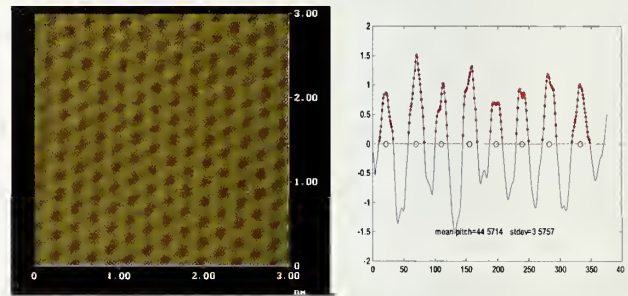


Figure 4. These data are an STM image acquired synchronously with the new diode laser interferometry system. The profile on the right shows the atoms with their interferometer readings.

Recent research is focused on using the new Omicron UHV scanning tunneling microscope to extend the lithography processes described here to the atomic domain. In this recent work, atomic resolution images of hydrogen terminated Si surfaces were obtained using only room temperature processes. The research is to extend the sub-10 nm lithography process to individual atoms.

Selected Publications

1. J. Fu, H. Zhou, and R. M. Silver, "Dependence of Morphology on Miscut Angle for Si (111) Etched in NH₄F", *Applied Physics Letters* **82**, No. 18. 2003.
2. R. M. Silver, S. Gonda, J. Jun, L. Howard, and C. Jensen, "Atomic Resolution Measurements with a New Tunable Diode Laser Interferometer", *Optical Engineering* **43**, No. 1, 2004.
3. P. V. M. Rao, C. Jensen, and R. M. Silver, "A Generic Shape Model for STM Tip Geometry," *JVST B*, Mar/Apr (2004).

Critical Dimension Metrology using Scanning Electron Microscopy and a Model-Based Library

Tolerances for measurement accuracy and repeatability for transistor gates are below the spatial resolution of the scanning electron microscope. This results in measurement artifacts that can only be remedied by accounting for the sample-instrument interaction. We have implemented a model-based library approach that is proving to be more accurate and less sensitive to secondary sample characteristics than the existing measurement methods.

John S. Villarrubia and András E. Vladár, MEL (821)

Transistor gates are typically the smallest manufactured features in an integrated circuit. As such, they tend to be the most sensitive to manufacturing faults. Moreover, their size is closely linked to important device properties, like speed, packing density, and off-state leakage current. Accordingly, manufacturers measure these “critical dimensions” (CDs) in order to monitor for drifts or faults in the manufacturing process. Transistors with CDs of 30 nm are in mass production in 2005.

In a scanning electron microscope (SEM) secondary electron image, the edges of the gate appear bright. (See the intensity peak in the blue curve in Fig. 1.) The usual measurement procedure is to assign edge positions at the location of these bright, so-called edge blooms. Edge assignment is traditionally done using image processing criteria, such as an intensity threshold crossing or the position of the maximum slope in the intensity curve.

Measurements must have accuracy and repeatability small compared to the device dimensions. In 2005, the specifications require measurement bias below 3 nm and repeatability better than 1 nm. However, the edge bloom region is anywhere from a few nanometers to tens of nanometers wide, owing to the finite spot size of the incident beam and, often more importantly, scattering of electrons within the sample (Fig. 1 again). This means the required accuracy and repeatability are smaller than the spatial resolution of the measuring tool. Under this circumstance, not only is the accuracy of an image processing assignment of edge position suspect, but even the repeatability of such an assignment becomes sensitive to small changes in the instrument condition or secondary characteristics of the sample (e.g., wall angles or rounding of corners), changes that alter the shape of the intensity in the bloom even when they do not alter the actual edge position.

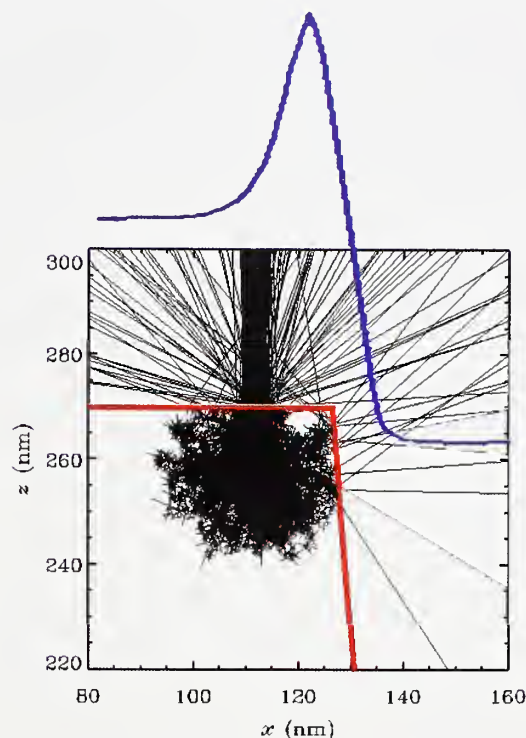


Figure 1. Simulation of electron trajectories in the sample. The sample boundaries are indicated by the red line. Incident electrons scatter within the sample creating an extended “interaction volume,” indicated by the black trajectories. Intensity variation (blue) as the incident beam is scanned across the edge is a consequence of the different numbers of secondary electrons produced at different landing positions.

To perform such measurements, we have developed an alternative to the traditional measurement algorithms. This approach, a model-based library (MBL) method, has 3 components. The first is a physics-based model that permits calculation of the image for a given sample and imaging conditions specified by parameters. This model uses a time-consuming Monte Carlo simulation of electron trajectories. The second component is software that can search, and if need be interpolate, a library of precomputed model results (Fig. 2). This allows fast computation of model results once a library has been constructed. The final component is a nonlinear least squares algorithm that solves for the set of parameters that produces the best least squares match between measured and calculated images. The parameters determined in this way include the edge positions, from which the desired feature size can be determined. As a bonus, other aspects of the feature shape (e.g., sidewall angles) that affect the image can also be determined.

The accuracy of the MBL technique was assessed by

comparing results determined by MBL from top-down images (the usual industrial imaging configuration) with cross-section SEM measurements. Initial tests were performed at NIST using our laboratory SEM, measuring first isolated and then later dense (i.e. closely spaced) polycrystalline Si lines. Agreement between the two techniques was better than 2 nm for linewidth and 0.2° for sidewall angle (Fig. 3a), differences that could be accounted for by line edge roughness.

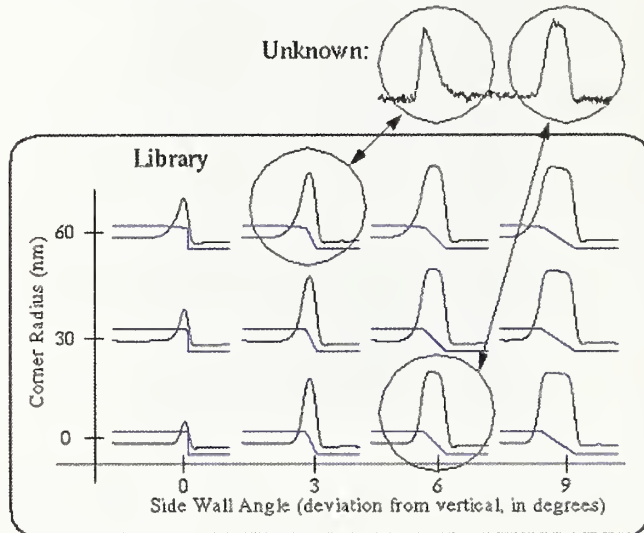


Figure 2. Schematic of the MBL method. A “library” of edge shapes (blue) and their corresponding computed images (black) is constructed ahead of time. A measured unknown is compared to images in the library. The library is interpolated if necessary to obtain the best match. The parameters of the matching shape are attributed to the unknown.

In a collaboration with International SEMATECH, test patterns were fabricated in resist and polycrystalline silicon, measured top-down in an industrial CD-SEM, cross-sectioned, and remeasured in a laboratory SEM. MBL analysis of the top-down images was performed. Comparison with the cross section results indicated substantial agreement (see Fig. 3b and 3c), although there was some evidence of electron-beam induced resist shrinkage similar to that observed by others.

MBL linewidth measurements at a given position on a line were as much as 3 times more repeatable than linewidths determined from the same images by regression to baseline (one of the traditional methods). The improvement is attributed to the fact that MBL is a fitting method that uses the intensity at many pixels to determine an edge position, while the standard image processing methods typically restrict consideration to a smaller set of pixels.

The major manufacturers of CD-SEMs have been given free access to our simulation codes. Soliris, Inc.

announced a product using their own implementation of the MBL method at SEMICON West 2003. Hitachi, Ltd. sent an engineer to work with us for a year as a guest researcher. This collaboration has resulted in a publication (*Proc. SPIE*, in press) showing that MBL is less sensitive than existing methods to SEM focus variation near best focus.

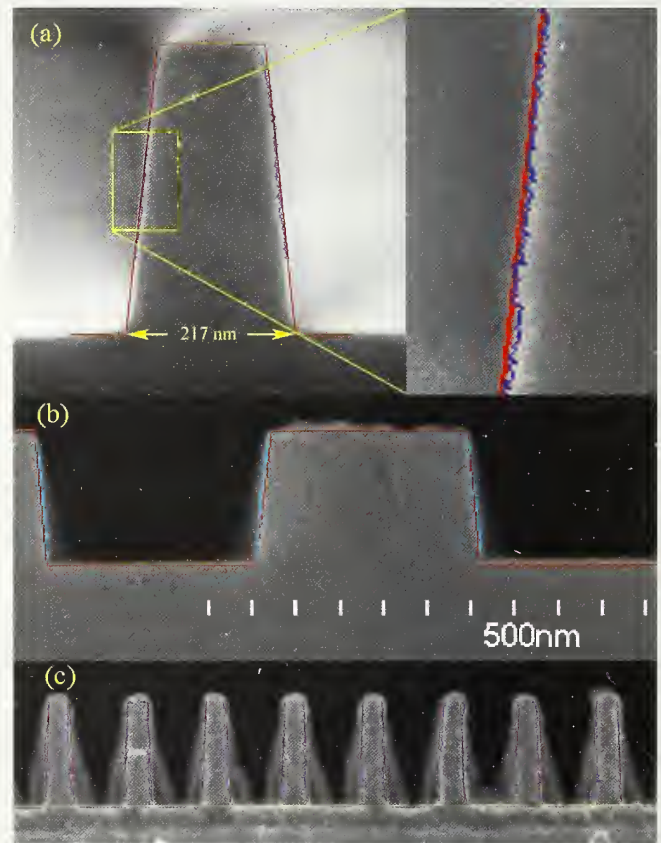


Figure 3. Agreement between MBL and cross-section measurements (a) for isolated polycrystalline (“poly”) Si lines in which top-down measurements were performed with a laboratory SEM, (b) for dense poly lines measured with a commercial CD-SEM, and (c) for dense UV resist lines measured with a commercial CD-SEM. In all cases the red lines are the cross sections predicted by the MBL technique based upon top-down measurements, and the blue lines are edges assigned based upon the cross-sections.

Selected Publications

1. J. S. Villarrubia, A. E. Vladár, J. R. Lowney, and M. T. Postek, *Proc. SPIE* **4689**, 304-312 (2002).
2. J. S. Villarrubia, A. E. Vladár, B. D. Bunday, and M. Bishop, *Proc. SPIE* **5375**, 199-209, (2004).

SI traceable force for scanning probe microscopy and instrumented indentation

A dizzying variety of small-scale force measuring instruments are routinely employed by industrial and government laboratories to evaluate the mechanical performance of thin-film metal, ceramic, and polymer coatings, microelectromechanical systems, and a host of biological processes and functions. Forces as small as a single atomic bond can be detected and are used to help manufacturers choose materials and processes that makeup everything from next generation semiconductors to next year's automobiles. Until recently, these force measurements were considered largely qualitative. Now, the NIST small force metrology lab has begun to put these precise measurements on a firm quantitative basis, having developed new methods and instruments that allow SI traceable calibration of forces below 10^{-5} N.

Jon R. Pratt, MEL (822)

The lowest force traceable to a NIST deadweight force machine is 44 N. Below this value in the United States, secondary laboratories, industrial metrologists, and others responsible for ensuring force traceability purchase or fashion their own primary standards of force; a task most simply accomplished by obtaining traceable mass artifacts. To date, this hierarchical structure has been satisfactory in the United States; however, there is a growing push for standardization in the field of nanomechanical testing (ASTM, ISO, and VAMAS all have working groups on the subject), where forces are two to three orders of magnitude smaller than the deadweight force produced by even the smallest available traceable mass artifact in the United States, or 0.5 mg (approx. 5 μ N). NIST is leading the way in the development of new standards to meet this challenge.

A new hierarchy of small force at NIST

In principle masses smaller than a milligram can be calibrated by NIST, but such artifacts are difficult to handle, and the trend is for their relative uncertainty to increase in proportion to the decrease in mass. In fact, their uncertainty could very well be as large as the force for a deadweight producing 1 nN. A more convenient basis for small force standards is desired.

To realize the unit of force using the SI definition of the Newton, the force must be expressed in terms of measured quantities that are themselves expressed in terms of some combination of the SI base units. Deriving a unit from realizations of the base units is typically

the path of least uncertainty (e.g., kg, m, s), but this needn't always be the case. For instance, electrical forces may be measured in terms of the SI unit of length in combination with appropriate electrical units. Electrical units are themselves derived units in the SI, but they may also be linked to practical representations of the volt and ohm based on the Josephson and quantized Hall effects. Because of this, they may be measured through a large dynamic range with little loss of relative uncertainty, unlike the situation in mass. The block diagram of Figure 1 lays out the new hierarchy of NIST small force metrology—one where the dynamic range of electrical quantities is exploited to produce a primary realization of force based on a combination of length, capacitance, and voltage for forces below 10^{-5} N.

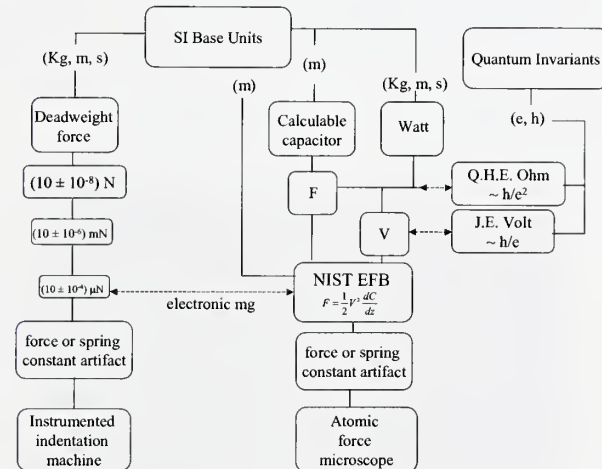


Figure 1. SI traceability in the NIST small force metrology laboratory.

A Primary standard of small force between 10^{-8} N and 10^{-4} N: The NIST Electrostatic Force Balance

At NIST, we can now realize a primary standard of small force from electrostatics, and have constructed a series of increasingly refined systems to realize force using a coaxial cylindrical capacitor arrangement. The present version of this primary standard, referred to as the NIST Electrostatic Force Balance, or simply the EFB, is shown in the photo of Figure 2.

The EFB consists of an electrostatic force generator that acts along a vertical axis (z-direction) aligned to local gravity within a few milliradians. Forces are generated when voltages are applied to a pair of nested, coaxial cylinders. The outer high-voltage cylinder is fixed while the inner electrically-grounded cylinder is free to translate along a z-axis, varying the degree of overlap. The capacitance of this geometry is a linear function of

this overlap, and the electrical force is directed solely along the cylinder axis.

The EFB operates as an electronic null balance and generates electrical forces that may be calculated from

$$F = \frac{1}{2} \frac{dC}{dz} (U_1^2 - U_2^2 + 2V_s(U_1 - U_2))$$

where F is the force in nN, dC/dz is the capacitance gradient in pF/mm, U_1 is the voltage applied to the outer electrode in V before loading, U_2 is the voltage applied to the outer electrode in V after loading, and V_s is the potential difference between the electrodes resulting from surface field effects. Rather than directly measure V_s , we reverse the polarity of the applied voltage and take the mean of the computed electrical forces.

Interestingly, the EFB could be used to redefine a mass artifact in terms of electrical and length units. Recently we used a nominally 2 mg mass artifact as a 20 μN deadweight. One standard deviation of the electrical force data was 0.7 nN, for a relative standard uncertainty better than 4×10^{-5} , which is at the same level as that achieved by conventional mass calibration.

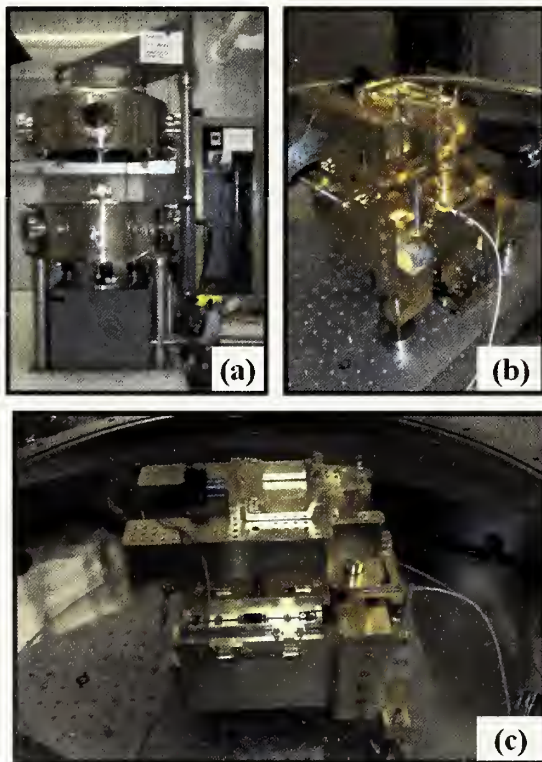


Figure 2. The NIST electrostatic force balance (a) outside view of vacuum system (b) front corner view of balance (c) side view of balance

Force calibration of an SPM

At conventional force levels, force cells are equipped with strain gage transducers that convert changes in mechanical force to changes in electrical resistance. At the force levels considered here, SPM cantilevers can be doped with piezoresistive patterns that achieve the semiconductor equivalent of a strain gage transducer, so that these cantilevers are functionally equivalent to a force cell. We probed the EFB with just such a cantilever, recording its change in resistance as a function of the null force. The relative standard uncertainty of the sensitivity for this device was less than 1%.

Typical SPM cantilevers are passive devices; force induced deflections are measured using an optical lever that is part of the microscope, not part of the cantilever. Because of this, force calibration by direct comparison to the EFB is impractical, but an indirect comparison to a piezoresistive cantilever is quite practical, and a scheme is illustrated in Figure 3. As shown, the SPM simply probes the piezoresistive cantilever as if it were a specimen, and the calibrated force readout is used to calibrate the output of the microscope's optical lever.

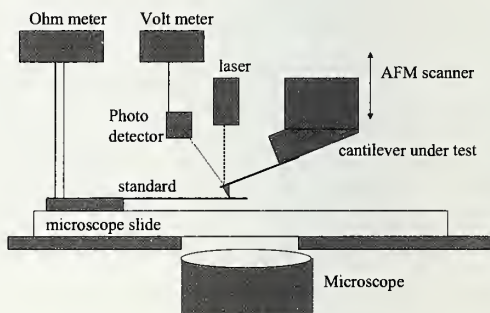


Figure 3. SPM force calibration using a piezoresistive reference cantilever. Micronewton force calibration has been achieved with relative standard uncertainty less than 5%.

Selected Publications

1. J. R. Pratt, D.T. Smith, D.B. Newell, J.A. Kramar, and E. Whitenton, 2004, "Progress towards Systeme International d'Unites traceable force metrology for nanomechanics", *Journal of Materials Research*, 19(1), pp. 366-379.

Phase-sensitive Scatterfield Optical Imaging for sub-10 nm Dimensional Metrology

Customer needs and project objective: There is a substantial need for high resolution, low cost, yet high throughput metrology capability in nanomanufacturing. This project proposes to advance optical microscopy to unprecedented levels of performance through theoretical and experimental development of a new technique we call "scatterfield optical imaging". This new method promises to make possible optical measurements of nanometer-sized features using high-throughput, low cost optical methods with the potential for a significant impact on innovation and quality control in semiconductor manufacturing and nanotechnology as well as providing the measurement basis for new nanometer-scale calibration standards well beyond the state-of-the-art.

Richard Silver, MEL (821)

Although optics are often thought to lose its effectiveness as a metrology tool beyond the Rayleigh resolution criterion, there is now evidence that optics can be used to image and measure features smaller than 10 nm in dimension. The resolution obtained by conventional optical microscopy is usually considered to be limited to approximately half of the wavelength of the light used for illumination. However, another optical metrology method, interferometry, can routinely achieve sub-nanometer resolution using visible light. The key to understanding the difference between these two methods is related to the complexity of the electromagnetic fields (illumination) and the targets used in the measurement. In the case of interferometry, single plane waves, that is, waves having a simple sinusoidal oscillation in space and time, are reflected from planar, mirrored surfaces, with the phase information preserved. For microscopy, the illuminating fields are much more complicated and the samples often have significant three-dimensional character.

Optical imaging and metrology with resolution well beyond the wavelength is a possibility as a result of a new optical configuration and design, increased computation speed, high-resolution CCD array technology, improved signal processing of large arrays, and reliable theoretical scattering models. The ability to "engineer" the illuminating field is key to this advanced measurement technique. It involves low numerical aperture (NA) illumination optics and polar illumination schemes with

high angle to on-axis plane wave illumination. Another key technological advance is the realization that phase information, accessible by stepping through the ideal focus, provides a sensitive, complex optical signature for a given sample and optical configuration. The sample or target design also plays a central role in the ability to increase optical sensitivity to dimensional changes. A target structure which enhances the amplitude of the scattered fields and accessible information content can be optimized with accurate simulation tools.

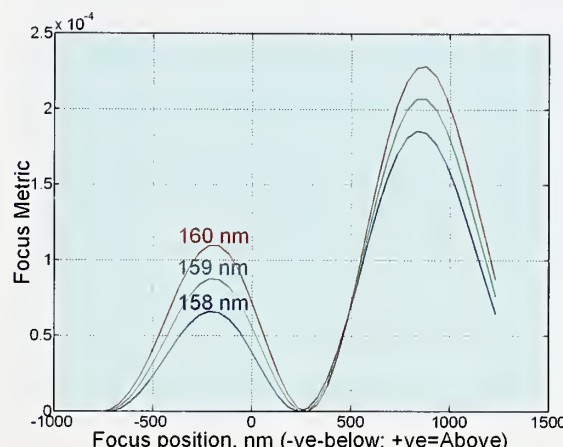


Figure 1. Through focus focus metric profiles showing nanometer sensitivity to linewidth.

A key enabling technology that these improvements rely upon is the unprecedented accuracy by which we can now calculate the electromagnetic scatter from features. The exact profile of the scattered field is extremely sensitive to small changes in the shape and size of the scattering feature. Once one can accurately calculate the scattering function and propagate it in the optical system, one can in principle measure features near to nanometer dimensions. It is no longer necessary to be limited by the concept of image-based edge detection microscopy in optically-based dimensional metrology. This is a radical departure from traditional methods of optical imaging.

This project is now designing a new optical instrument with a key design element being access to the rear focal plane of the objective lens. An open or flexible optical layout has been designed which places an accessible conjugate back focal plane not in the imaging path. This will enable specific, complex fill factors for the pupil plane which then determines the angles and intensities of the Köhler illumination. The instrument will also take advantage of the obvious gains obtained when using shorter illumination wavelengths such as 193 nm

illumination.

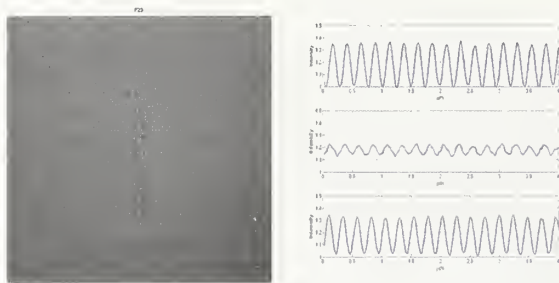


Figure 2. CCD image of a 39 nm CD array with a cross section profile shown on the right.

The sample plays an essential role in the resulting scattered intensity profile. Complex scattering profiles or “signatures” can be created or enhanced in a fundamental way by varying the sample geometry and spatial frequency content. An important aspect in the advance of these optical methods is the possibility of providing the nanomanufacturing and semiconductor industries with the capability of making simultaneous critical dimension and overlay measurements. This would have an enormous impact on the quality, productivity, and cost of layer to layer lithography type manufacturing processes.

The impact from the successful implementation and development of this new measurement science will be significant. Optics has some significant advantages over other high resolution imaging techniques such as scanning electron microscopy (SEM) and atomic force microscopy (AFM). SEM requires high vacuum, is a serial scanning technique, with expensive instrumentation and can be destructive in making measurements. AFM has significant throughput, reliability, and cost of ownership challenges. Optical metrology, on the other hand, is massively parallel, with high throughput, relatively low instrumentation cost, and is non-destructive. The demonstration of accurate sub-10 nm feature measurements with nm sensitivity to changes in shape will be substantial.

The key deliverables of this project include a new measurement technique capable of imaging sub-10 nm sized features with sensitivity to nm scale geometrical changes. The method will be developed for specific applications in the nanomanufacturing and semiconductor industries, as well as core applications in high-level measurements for NIST standards. The fundamental optical limits are being explored and documented in a systematic way. A new optical instrument is now being developed with 193 nm measurement wavelength capabilities. A parametric exploration of the sample and optical illumination space is underway, currently using simulation tools and to be followed up with experimental

confirmation. This work is being performed to define the key target and optical parameters which maximize sensitivity to the sample properties of interest followed by the optimization of those parameters.

Selected Publications

1. R. M. Silver, R. Attota, M. Stocker, M. Bishop, J. Jun, E. Marx, M. Davidson, and R. Larrabee, “High-resolution Optical Overlay Metrology”, SPIE Vol. 5375 P. 78, 2004.
2. R. Attota, R. M. Silver, M. Bishop, E. Marx, J. Jun, M. Stocker, M. Davidson, R. Larrabee, “Evaluation of new in-chip and arrayed line overlay target designs”, SPIE Vol. 5375 P. 395, 2004

Advanced Control Systems and Positioning for Nanoscale Measurements and Standards

Advance control and positioning systems are needed for high precision nanoscale measurement, manipulation, assembly and standards. We are experimenting with arrays of high precision MEMS positioning stages for scanning electron and scanning probe microscopy; multi-degree-of-freedom nanometer resolution optic displacement sensors; automated manipulation and assembly of micro and nano scale component; advance mathematical modeling and optimization; control algorithms and performance measures.

Nicholas G. Dagalakis, MEL (823)

Methods to build high precision complex three-dimensional nanoscale structures, sensors and devices using techniques that allow scale-up is a central challenge of nanomanufacturing. Parallel operation nanomanufacturing of these devices must be explored and standardized in order to allow for the economy of scale needed for successful production. This project will advance the science of manufacturing high precision 3D nanoscale devices and metrology sensors by developing mathematical modeling, simulation and optimization tools, manipulation and metrology tools, control algorithms and performance measures, standards and fabrication techniques.

Project objectives:

- To develop mathematical modeling, simulation and optimization tools.
- To develop manipulation and metrology tools.
- To develop control algorithms and performance measures.
- To develop standards and fabrication techniques.

With collaboration from RPI/CAT researchers, one degree of freedom and two degree of freedom arrays of planar high precision MEMS micro/nano positioners have been designed and fabricated based on NIST macro and meso scale designs (see Figures 1 and 2). These devices have various sizes and design flexures, thermal actuators and two different moving mechanism stage thicknesses.

With collaboration from RPI/CAT researchers we have developed mathematical models of advanced MEMS mechanisms and conducted various optimization studies (Figures 3 and 4). Finite Elements models have

been developed and were used to conduct stiffness, displacement and stress analysis studies (see Figures 3 and 4). Experimental test results are being used in order to develop accurate mathematical models and controllers.

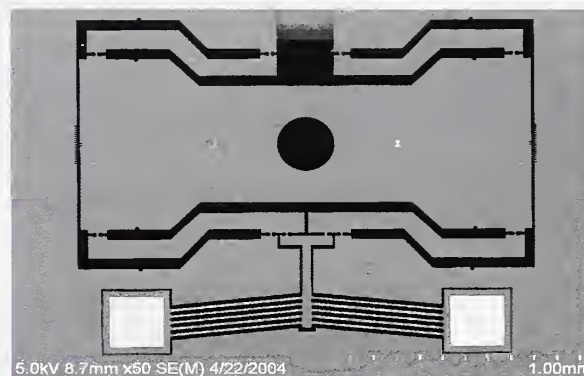


Figure 2. Scanning Electron Microscope picture of a MEMS Scale, Dual Parallel Cantilever Micro/Nano Positioner. The external size is approximately 1.8 mm by 1.8 mm, the thickness is 10 micrometers, all circular notch flexures have a width of 7 micrometers.

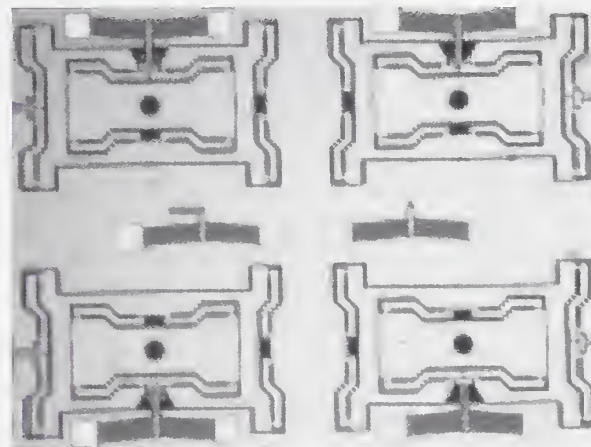


Figure 2. Light microscope picture of a 2x2 array of MEMS scale X-Y axes Dual Parallel Cantilever Micro/Nano Positioners.



Figure 3. Finite elements model simulation of the stage displacement, of a MEMS Scale Dual Parallel Cantilever Micro/Nano Positioner, due to an input force.

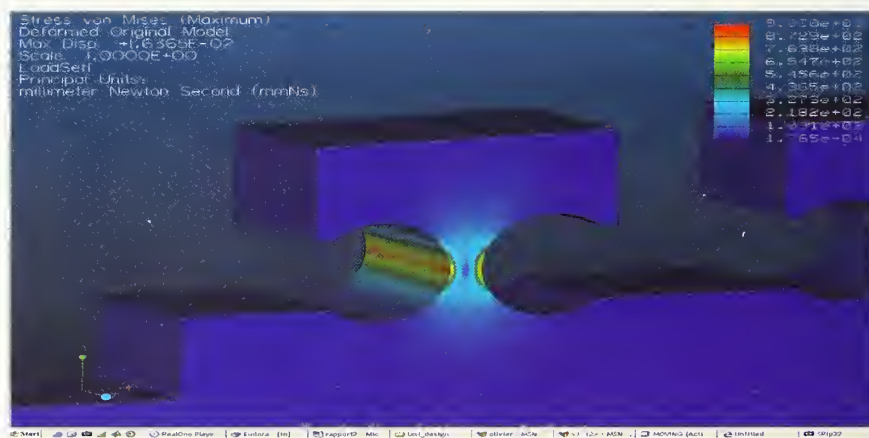


Figure 4. Finite elements model simulation maximum von Mises stress concentration, at the outer surface of the pivot circular notch of a Micro/Nano Positioner, due to an input force.

Molecular Measuring Machine

Nanometer accuracy and resolution metrology over technically relevant areas is becoming a necessity for the progress of nanomanufacturing. We are developing the Molecular Measuring Machine (M^3), a scanned probe microscope (SPM) and Michelson interferometer based metrology instrument, designed to achieve nanometer measurement uncertainty for point-to-point measurements over a 50 mm by 50 mm working area. Both long-range measurements of sub-micrometer pitch gratings over a distance of 10 mm, and short-range, high-resolution measurements of a molecular crystal lattice have been accomplished.

The estimated relative measurement uncertainty so far attained for pitch measurements is 6×10^{-5} , coverage factor $k = 2$. We have also utilized the SPM probe tip positioning accuracy of M^3 along with scanning probe oxidation lithography to create some simple nanometer dimension patterns that could serve as prototype calibration standards for disseminating the SI unit of length at this scale.

John A. Kramar, MEL (821)

Interest abounds and much hope has been placed in the current explosion of research efforts in nanotechnology and nanomanufacturing. Incredible devices have been proposed in fields as diverse as medicine, information technology, and military applications. Several novel devices have been demonstrated in prototype form or limited initial production, for example artificial noses, molecular electronics memory and logic elements, and biological probes including medical diagnostics and therapeutics. For these impressive early ideas and successes to mature into a widespread, stable, and profitable economic sector requires that the infrastructural base of dimensional metrology be extended into this nanoscopic regime. Metrology is also needed in commerce or trade for quality assurance and communication of specifications and capabilities. *Mass production requires process control; process control requires accurate metrology.*

The Molecular Measuring Machine (M^3) is a metrology instrument designed to achieve sub-nanometer resolution with both the probe system and the metric, with the goal of achieving 1 nm uncertainty for point-to-point measurements within its 50 mm by 50 mm working area. The probe system is a scanning probe microscope (SPM) and the metric is a Michelson interferometer. The instrument embodies a realization of the International System (SI) unit of length, since the frequency of the light

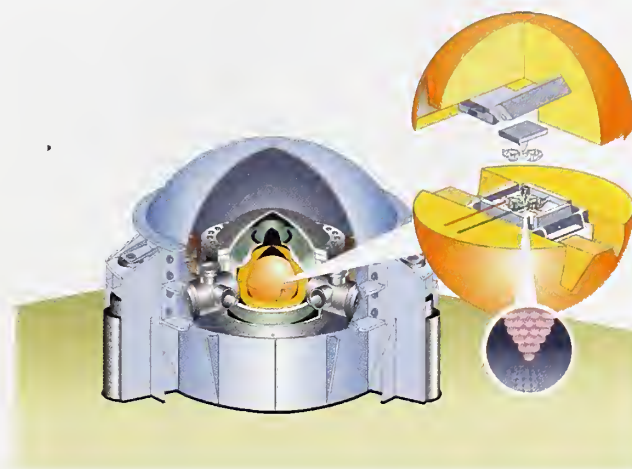


Figure 1. Cut away view of M^3 .

source for the interferometer is measured relative to a recommended radiation. In order to achieve the desired motion resolution simultaneously with a large operating range, piezoceramic-driven, flexure-guided fine-motion stages are stacked on long-range, slideway-guided carriages. The range of the fine motion stages is 10 μm while the range of the coarse motion is 50 mm. The interferometer system measures the combined motion of the coarse and fine stages. The instrument is isolated from environmental fluctuations and noise by temperature control, vacuum, and vibration isolation systems (Fig. 1).

This instrument has been applied to the measurement of submicrometer pitch gratings. This application makes use of the SPM probe to resolve the sub optical wavelength features and the long distance, high resolution and high accuracy metrology system to produce precise, low uncertainty measurements. For example, the pitches of nominal 200 nm and 400 nm gratings were measured with uncertainty as small as 10 pm (coverage factor $k = 2$) to serve as reference standards for the production of diffraction gratings for the x-ray spectrometer of the space-borne Chandra Observatory. Single SPM traces 10 mm in length were acquired in these measurements.

At the small end of the scale, lattice constants of a molecular crystal have also been measured. In this case, the challenge was to minimize noise from vibrations and the control electronics, and from the heterodyne Michelson interferometer. Figure 2 is an image of the organic conductor $(\text{TEET})[\text{Ni}(\text{dmit})_2]_2$ acquired under closed loop servo control based on the interferometer measurements. The measured lattice parameters were within the experimental uncertainty, dominated by the nanometer-level periodic uncertainty in the interferometers.

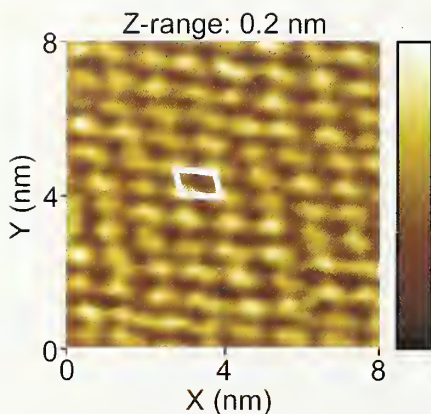


Figure 2. Metrology image of (TEET)[Ni(dmit)₂]₂, an organic conductor, acquired with M³.

Using the interferometer-controlled tip positioning capability of M³, nanometer accuracy calibration artifacts can be made. An example of this is the use of scanned probe oxidation lithography to create 70 nm wide lines on a silicon substrate (Fig. 3). The writing process itself creates lines with approximately 3 nm height, but the features can be transferred into the silicon producing up to 20 nm relief by using reactive ion etching. The ability to create such artifacts provides a means for disseminating the measurement traceability embodied in M³ to customer metrology instruments. It is envisioned that nanoimprint lithography may enable the efficient and cost effective replication of such artifacts, once the scale fidelity of the replication process is verified.

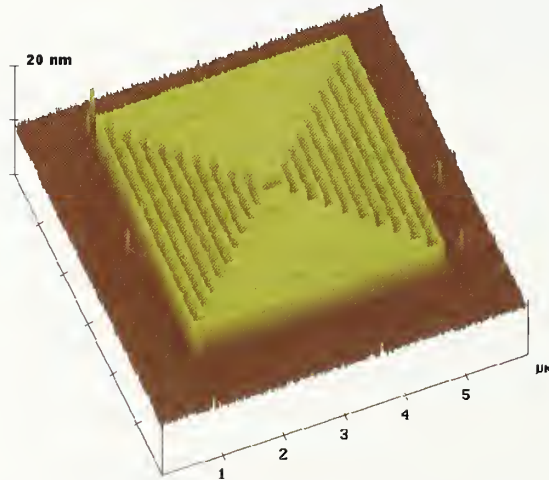


Figure 3. Prototype calibration artifact made by M³ using scanned probe oxidation lithography and reactive ion etching.

Selected Publications

1. John Kramar, Edward Amatucci, David Gilsinn, Jau-Shi Jun, William Penzes, Fredric Scire, E. Clayton Teague, and John Villarrubia, "Toward Nanometer Accuracy Measurements," *Proceedings of the SPIE Conference on Metrology, Inspection, and Process Control for Microlithography XIII*, SPIE Vol. 3677, pp. 1017–1028 (1999).
2. J. A. Kramar, J. S. Jun, W. B. Penzes, F. E. Scire, E. C. Teague, and J. S. Villarrubia, *Recent Advances in Metrology*, "Grating Pitch Measurements with the Molecular Measuring Machine," *Characterization, and Standards for Optical Digital Data Disks*, Proceedings of SPIE, Vol. 3806, pp. 46–53 (1999).
3. J. A. Kramar, Jay Jun, W. B. Penzes, V. P. Scheuerman, F. E. Scire, and E. C. Teague; "Molecular Measuring Machine Design and Performance," *Proceedings of the 16th Annual Meeting of the American Society of Precision Engineering*, Vol. 25, pp. 19–22 (2001).

Agile Nanoassembly to Prototype, Test, and Manufacture Functional Nanodevices

Today little ability exists to directly manipulate and assemble nanoscale components, despite rapid advances in imaging, measurement, and fabrication at the nanoscale. This limits the ability to prototype and test many classes of nanodevice, and is a significant obstacle worldwide to both R&D and commercial production of these devices. We are developing laser tweezer-based systems to control the position and orientation of nanocomponents and enable nanoassembly from prototype to production. Natural, heuristic operator interfaces are a key part of the nanoassembly system, as is automation for efficient production.

Thomas W. LeBrun, MEL (821)

Light beams exert small forces on material objects, and for objects smaller than tens of micrometers the forces can be designed to effectively “grip” a particle in an optical beam and move it to a desired position. To be useful for nanoassembly this elementary ability to grasp point-like particles must be extended to allow full manipulation (position and orientation) of nanoscale components with a range of shapes, sizes, and material properties — and with other components in close proximity. The technique also offers a number of unique advantages over material probes: multiple particles can be simultaneously controlled because beams do not obstruct each other, the number and behavior of the particles manipulated can be changed dynamically, particles can be manipulated in real-world environments such as aqueous solutions or *in-vivo*, and the process can be made parallel.

To perform agile nanoassembly we have developed a scanning Optical Tweezer (OT) instrument that traps and manipulates multiple particles simultaneously by time-sharing — rapidly moving a single trap beam between multiple particles. As the trapping beam rests on each particle it is dithered at high speed to effectively draw a trap that fits the shape of the particle being manipulated, moving the trap moves the particle accordingly.

The position and orientation of each trap is controlled in software and the operator uses a CAD-like graphical user interface (GUI), shown in figure 1, to control each particle independently. Note that objects smaller than a few hundred nanometers can be imaged but not well resolved using traditional optical microscopy, so we have used 3 micrometer spheres in fig. 1. Using the GUI, the operator can draw a number of shapes such as point-like traps, lines and poly lines, and perform operations in-

cluding select, translate, and rotate — all in three dimensions (3D). The front end also allows displays images and synthetic representations of the objects in the 3D workspace, and allows the operator to vary the focal plane of the imaging CCD as required.

This provides an effective user interface, but the system must also scale to handle new and more complex tasks, so it must be part of a larger modular architecture designed to grow to include new capabilities, such as automation, teleoperation, or operation of many systems in parallel. Therefore we have built a modular network-based architecture using message passing for inter-module communication. Modules for an operator interface (GUI), system control, and trap scanning are currently used, with modules for vision, scripting and automation under development. The communications layer is based on the Neutral Messaging Language (NML) developed at NIST so that software modules that reside on one computer during development (such as vision and scanning), can be easily moved to independent processors as the system scales up. These systems can also be combined to support complex fabrication operations in parallel, for example by pipelining or by hierarchical integration of many OT systems.



Figure 1. Graphical user interface for nanoassembly.

To fabricate functional nanodevices with this device we are initially focusing on nanowire-based devices. Nanowires are archetypal components that can function as mechanical elements (rods), conductors (wires), optical elements (waveguides or lasers) and electronic elements (diode junctions or transistors). Yet while we can fabricate a wide variety of nanorods, from carbon nanotubes, to semiconductor nanowires and gold nanorods, little ability exists to assemble predesigned structures from these components.

Light emitting diode junctions can be made by plac-

ing p-type and n-type nanowires in contact. We have assembled prototype crossbar structures with 1 μm alumina microwires as shown in figure 2. Much smaller wires can be used, and the obstacles to efficiently fabricating devices are more technical than fundamental: imaging nanowires undergoing rapid rotational diffusion, controlling adhesion, and drying structures for SEM imaging and testing without damage.

We are also investigating gold nanorod-based structures for plasmonic devices for optical detection and spatial localization of electric fields over ranges much smaller than an optical wavelength. The goal is to use the automation capabilities under development to rapidly move from simple devices to more complex circuits incorporating multiple types of nanowire. These devices also promise very fast operation, but radiation from single conductors with the corollary crosstalk to adjacent wires may limit performance. Using our technique we can also investigate waveguide geometries and structures for impedance matching, although these techniques drawn from RF engineering may be more applicable to plasmonic wavelengths.

Many useful structures can also be made from particles and spheres, but this level of manipulation is already well developed for spheres with diameters on the order of a micrometer. To manipulate smaller particles trap intensity can be increased, but undesirable heating and damage generally results. This is a difficult problem to circumvent physically, but a solution can be engineered using a fast control system to servo out Brownian motion, and maintain particles at the stiffest part of the trap. This allows smaller particles to be trapped and biological systems to be trapped with reduced power, thereby avoiding damage from radiative heating. This has the advantage of making the technique more amenable to nanobiological applications.

Optical trapping has an established history in biological research for manipulating cells and biological particles (e.g. cell sorting, patch clamp, manipulation inside cells), and more recently optical tweezers have been used to measure Raman spectra of cells, and measure biological forces generated by single molecular motors tethered to micron-sized spheres.

To investigate medical applications of this tool we have also begun studying the function of biological nanoparticles (liposomes) used for gene therapy of cancer. When administered, the particles are taken up by cancer cells, releasing DNA that is converted by the cell into a normally occurring protein that terminates the cell. But the process by which the particles enter the cells is not well understood.

Using our system we have trapped the biological nanoparticles (fig. 2), and are beginning to study cell-nanoparticle interactions so that entry of a liposome into a cell can be controlled and measured. The immediate aim of this work is to identify the mechanism of cellular uptake of these nanoparticles, but the long-term goal is development of what might be called single cell metrology -- the accurate measurement of cellular properties and function right down to the molecular level.

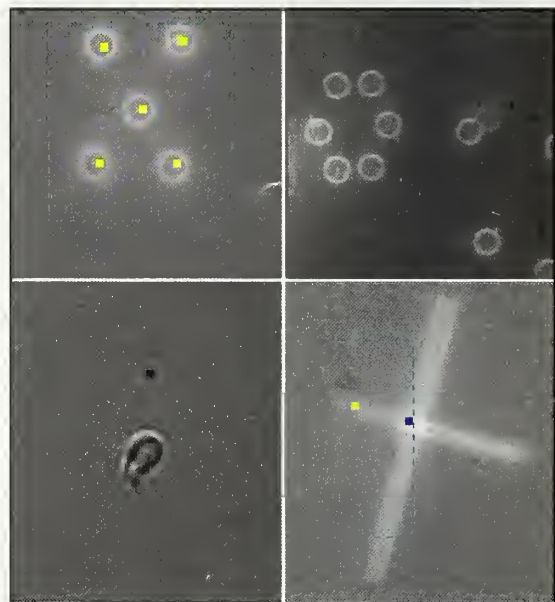


Figure 2. Clockwise from top left: an array of 3 μm spheres automatically selected and positioned, 6 spheres spinning simultaneously, a crossbar structure, a 200 nm liposome and a larger vesicle trapped in tandem.

Development of Nano-tip Electron Guns for the Scanning Electron Microscope

High-resolution scanning electron microscope (SEM) imaging and metrology of nanostructures need new higher resolution electron sources. Experimental nano-tip emitters have shown significant improvements as they offer higher brightness and smaller electron source size, which translate into higher spatial resolution and better signal-to-noise ratio images. Images taken with experimental nano-tips showed a minimum two-fold improvement over the original resolution performance specification of the test SEM. The tip lifetime was found to be many months in light use.

Andras E. Vladar and Michael T. Postek, MEL (821)

Through this work the most important questions and problems associated with nano-tip-based electron guns and their possible applications to SEMs were investigated. These were related to the tip making procedures, the theoretical assessment of the Hitachi S-6000 critical dimension SEM's electron gun and to the preparation of the SEM for insertion of nano-tips, and finally to the experiments with a nano-tip. Figure 1 shows an SEM image of a nano-tip made at NIST that can be used as electron emitter.

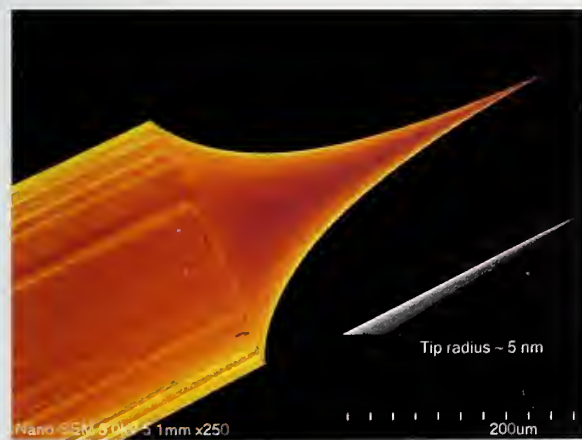


Figure 1. SEM image of a nano-tip.

The S-6000 SEM specifications call for a guaranteed resolution of 15 nm on suitable samples. This includes the decrease due to the non-ideal, practical electron optical column, and unavoidable adverse effects from the environment, such as electric fields and mechanical vibration, etc. In some cases, the resolution performance can be somewhat better than this 15 nm guaranteed specification.

A trial run, designed as a transitional step toward the nano-tip experiments, was carried out with a new, sharp tip. The tip did not go through the usual forming process, after insertion, and as soon as it was turned on, it started to emit at around 3000 V. The tip noise was acceptable, and the tip worked for many hours. The tip worked for several months, even though flashing was never performed. The vacuum in the gun region with occasional bakes was excellent. On this microscope the gun region is pumped with 3 ion-getter pumps. Note the lower extraction voltage for the sharp tip. This indicates that the tip was very sharp, less extraction voltage was needed to be applied to get useful electron beam. The resolution compared to the original tip has improved.

Since nano-tips are susceptible to damage, a tip-making procedure had to be developed to produce tips with predictable properties because characterization methods may render the nano-tips useless. These, while very valuable in the development, were not used for those tips that were put into the microscope. A new, fully computerized, automatic tip making apparatus was designed and developed, see Figure 2. This apparatus makes the tips fully automatically. It uses AC etching to clean the raw tip and DC etching to form well-shaped sharp tips. At the end when the lower part of the wire became separated at the neck that was formed at the region close to the surface, a fast electronic circuitry quickly turned off the etching current. This has prevented the blunting of the newly formed tip. The computer followed and recorded the etching current-to-time and wet cell voltage-to-time curves and based on these curves a decision could have been made about the quality of the tip. This whole process lasted for one hour from tip cleaning to final etch, and it produced nano-tips with good yield.



Figure 2. Fully automatic computerized nano-tip fabrication apparatus.

A tip that had shown good electrical characteristics during its fabrication, and was thought to be a nano-tip was installed in the modified S-6000 CD-SEM. After several long baking procedures when the vacuum of the cathode chamber has reached the low end of the 10^{-8} Pa range, and it stayed stable even after opening the air-lock valve, the gun was turned on. During the preliminary tip tests, when only operating modes with extraction voltages below 600 V were allowed, only noisy but interpretable images appeared on the screen. When extraction voltage was turned on in automatic mode, a stable image was obtained at 761 V. To our pleasant surprise, after a short adjustment of the electron optical column the image showed better resolution than that was ever possible with this microscope.

Figure 3 shows SEM images taken with the original, “sharp” and nano-tips at various locations on the same copper grid sample. The resolution is clearly the best with the nano-tip.

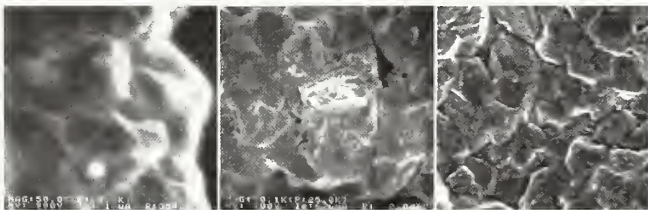


Figure 3. Copper grid sample images taken with the original tip (left), sharp tip (middle) and nano-tip (right). The field-of-view is 3 μm for all images.

The objective lens aperture current, which is related to beam current stayed steady within 11 %. The vacuum measured by the current of IP3 pump degraded by about 30 %, which was normal. The vacuum of the electron gun measured by the current IP1 and IP2 remained essentially unchanged, i.e., the pumps maintained excellent vacuum around the tip. The extraction voltage remained stable at 761 V. The cathode emission current was measured by a LabView-based measuring system, which is believed to be more accurate than the screen emission reading. In approximately 2.5 hours it has changed from close to 2 μA to its half and then stayed relatively stable for the rest of the measurement (the emission current reading on the screen was 4 μA at the beginning and 2 μA at the end). The tip now has been operational for more than many months, without noticeable performance degradation. There were power outages several times, and the gun chamber was not pumped for many hours. Occasional baking procedures restored and kept the good vacuum in the gun chamber. The tip was just lightly used, but it was turned on many times, and it always worked well. Therefore, long-term reliability appears to be high.

Figure 4 shows an image taken on a gold-on-carbon resolution sample. The image obtained with the nano-tip demonstrates a resolution of about 6 nm. It is likely that with further tuning of all circuits and the electron-optical column, it could be improved even further.

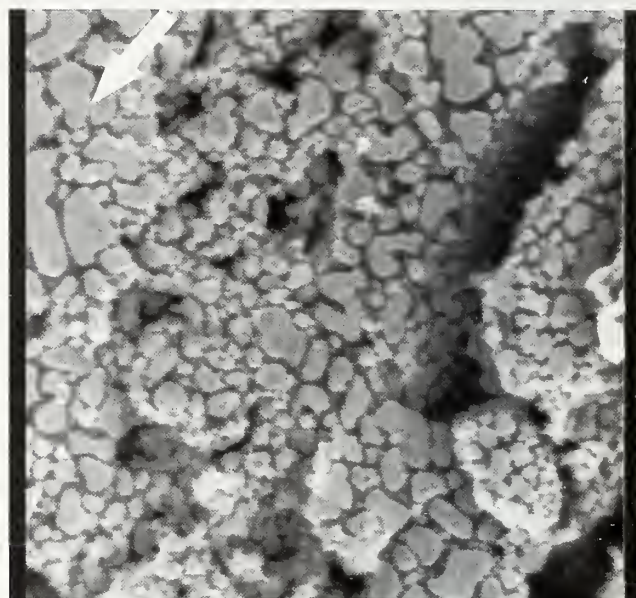


Figure 4. SEM image taken on a gold-on-carbon resolution sample with 900 V accelerating voltage, 2 μA emission current. The gap marked with the arrow is approximately 6 nm wide. The field-of-view is 1.75 μm .

Based on the results of this project, it appears feasible that nano-tip gun technology could replace the standard electron source and thus provide increased instrument performance. The result of this work clearly demonstrated that the improvements predicted by the theoretical calculations can actually be achieved in practice. The lifetime and resolution of the nano-tip gun were surprisingly good, which opens the possibility for the development of a new higher-resolution electron gun technology. The work in this project is continuing and currently long-term emission stability measurements are running.

It is expected that the next major step for the nano-tip electron gun development project a series of tests will be in a more modern cold field emission instrument to determine how far the resolution performance can be pushed.

Measurement Strategy for Line Edge and Linewidth Roughness Metrology

With the sizes of critical integrated circuit features now only a few tens of nanometers, the roughness of device edges is becoming a substantial fraction of their sizes. Some deleterious effects of roughness are already known, and others are feared. This has recently led to specifications for roughness metrology, but the artifacts to which such metrology is subject and appropriate methods to avoid them were largely unknown. This project addressed many of these issues in a collaboration with International SEMATECH.

John S. Villarrubia and András E. Vladár, MEL (821)

Although semiconductor electronics devices are designed with smooth edges, they don't get produced that way. Edges that were meant to be straight end up being rough (Fig. 1). The amount of roughness depends upon a complex interplay between material properties and manufacturing processes. In the semiconductor industry, roughness has typically been measured using a standard deviation metric—3 standard deviations of edge position variation around the average edge for line edge roughness (LER) or 3 standard deviations of linewidth for linewidth roughness (LWR). LWR of 5 nm to 10 nm is not uncommon.

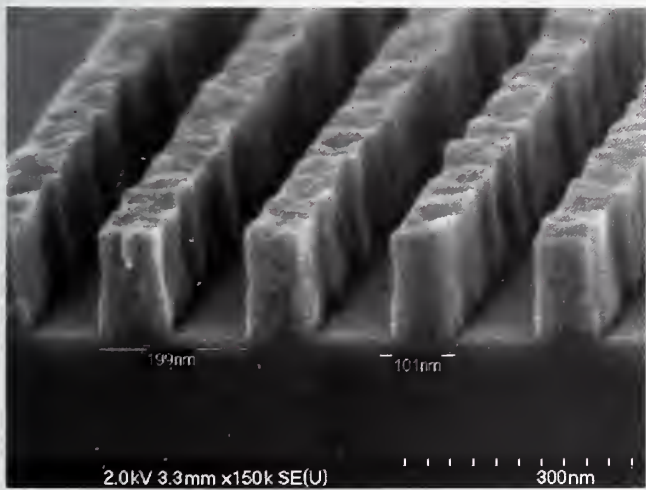


Figure 1. Polycrystalline silicon lines, exhibiting rough edges.

This was not a significant problem when circuit features were larger, but with the physical size of transistor gates now close to 30 nm it is becoming a significant concern. Does the variation of transistor gate length (Fig. 2) degrade transistor performance? Do rough edges reduce interconnect conductivity owing to diffuse scatter-

ing of electrons? Do high electric fields near rough edges of contact holes have deleterious effects? The semiconductor industry concerns about roughness are in an early stage, and there are still more questions than answers—specifications for roughness metrology only first appeared in the International Technology Roadmap for Semiconductors (ITRS) in 2001. However, there are some answers that give concrete reasons to substantiate concerns. For example, simulations and some measurements have associated LWR with high off-state transistor leakage currents and variable threshold voltages (the voltage at which a transistor turns on).

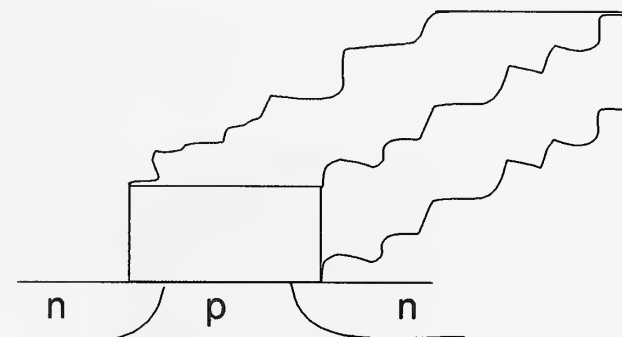


Figure 2. Geometry of a transistor gate, showing a rough-edged gate electrode over doped regions of the silicon substrate. A thin non-conducting dielectric (not shown) separates the gate electrode from the substrate. The (in this case n-type) dopant is implanted after the gate electrode is in place. The gate electrode serves as a mask, preserving the opposite doping of the gate, and incidentally guaranteeing that the dopant concentration edge is initially (before diffusion) as rough as the gate edge.

For the last two years NIST has been engaged in a collaboration with International SEMATECH to study metrology of LER and LWR. The collaboration has identified a number of measurement artifacts in roughness measurement as typically practiced, and has proposed improved measurement methods to deal with them.

As noted, a standard deviation roughness metric is in general use in semiconductor electronics applications. This is determined, for example, by measuring a length L of line at intervals Δ , subtracting the average length, and computing the standard deviation of the resulting set of residuals. Measurement issues identified with this metric include (1) its dependence upon the sampled length of line and the chosen measurement spacing, (2) sampling errors that result from the finite size of line segments used to estimate roughness and (3) random error and measurement bias that result from noise in the scanning electron microscope (SEM) images used to measure roughness.

The first issue is not a measurement artifact per se—

the true value of roughness varies with L and Δ , so it is not an error when measurements with different L and Δ differ—but it may lead to faulty comparisons when it is ignored in practice. Thus, it is not legitimate to conclude that sample A is rougher than sample B if A and B were measured with different L or Δ . The likelihood that such erroneous comparisons will be made is increased by the fact that different measurement tools have different capabilities, so may not customarily be programmed to perform the measurements in the same way. The industry's measurement specification is incomplete; it specifies a maximum allowable LWR and a measurement repeatability, but while it implies a value for L it does not specify Δ .

Sampling error is a consequence of the fact that in practice only a finite length of line can be measured. The chosen segment has a particular configuration of rough edges that will yield a particular value of the roughness. A different randomly chosen sample will have a different roughness. The size of this uncertainty can be reduced by averaging a number of samples for each measurement. The industry specified a repeatability for roughness measurements. This represents a required measurement quality *outcome*, but how many samples must the measurement technician average to assure this outcome? We derived a simple formula showing, among other things, that the number depends upon the roughness power spectral density of the sample.

One of the more significant issues with the industry's current metric is the phenomenon of measurement bias. Bias is a non-random component of error (sometimes called a "systematic" error). A simple measurement of the standard deviation of edge positions or linewidths is subject to bias because noise in the image on average increases this standard deviation. There is a false "noise roughness" variance that adds to the actual roughness variance. This results in an overestimate of the roughness by the standard metric (black curve in Fig. 3). Measured values of noise roughness are comparable to the roughness values specified by the industry for the current generation of devices. In practice, actual product is often far rougher, but if circuits can be made as smooth as the industry's goal, a substantial fraction of the measured roughness would, in fact, be a measurement artifact. We proposed an improved metric that corrects the measurement bias (red curve in Fig. 3).

Finally, in semiconductor electronics applications today, the industry almost exclusively relies upon the standard deviation metric. We pointed out that there are a number of other possible roughness metrics, and under some plausible scenarios, one or more of these others might be more closely related to device performance.

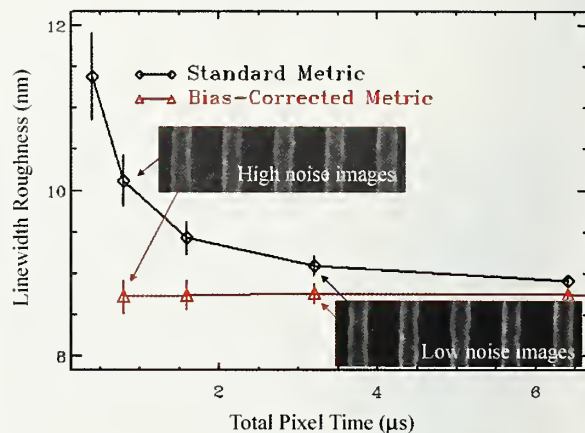


Figure 3. Bias in LWR measurement. The average roughness value as determined by the usual standard deviation metric (black line) increases as the noise level in an image increases. (High noise in this graph corresponds to low total pixel dwell time, to the left of the graph.) All images were taken from the same part of the sample, so the true roughness is unvarying, and the changes in average measured roughness must be a measurement artifact.

Critical dimension SEM suppliers have expressed an interest in modifying their measurement algorithms to make them less susceptible to bias and other measurement artifacts that were brought to light in these studies. Revised language for roughness specifications based upon these results is currently under consideration by ITRS technical working groups.

Selected Publications

1. B. D. Bunday, M. Bishop, D. McCormack, J. S. Villarrubia, A. E. Vladár, T. Vorburger, N. G. Orji, and J. A. Allgair, "Determination of Optimal Parameters for CD-SEM Measurement of Line Edge Roughness," *Proc. SPIE 5375*, 515-533 (2004).
2. J. S. Villarrubia and B. D. Bunday, "Unbiased Estimation of Linewidth Roughness," submitted to *Proc. SPIE 5752* (2005).

Combinatorial Metal Selection for Catalytic Growth of ZnO Semiconductor Nanowires

Semiconductor nanowires (NWs) offer a unique type of nanoscale building block for creating next-generation lasers and chemical/biological sensors. Control of NW dimension and structural and electronic properties is a major barrier to device fabrication. To address these issues, we are developing a strategy for selecting metals for catalytic growth of zinc-oxide (ZnO) nanowires using an approach based on phase diagrams and high-throughput fabrication and analysis.

Albert V. Davydov, MSEL (855)

Semiconductor NWs show significant promise for a wide variety of optoelectronic and electronic devices including nano-lasers, detectors, and chemical and biological sensors. To advance commercialization of such devices, it is necessary to control properties including size, orientation, and structural and electronic defects of the fabricated nanostructures. NWs are often produced using a vapor-liquid-solid (VLS) approach, in which nanometer size islands of catalytic metal act as nucleation and growth sites for semiconductor NW growth. The choice of the metal catalyst can significantly affect the NW properties. We are developing a strategy for selecting appropriate catalytic metals and applying this strategy to VLS growth of ZnO semiconductor. Selection and screening of catalysts is achieved using thermodynamic information from phase diagrams as well as a high-throughput (combinatorial) approach recently demonstrated for metallizations to wide-band-gap semiconductors [1].

We have examined the role of elemental noble metals and their alloys on ZnO NW growth and properties. An experimental library was designed using the ternary silver-gold-copper phase diagram and included elemental, binary and ternary compositions as well as two growth temperatures (900 and 1000 °C). The metal library elements were deposited on a single gallium nitride/sapphire substrate, which was subsequently annealing to form isolated metal droplets upon which the ZnO NWs were grown. The resulting set of metal islands and ZnO NWs was characterized using electron microscopy, x-ray diffraction, and optical spectroscopy. It was found that the ZnO NW growth was significantly influenced by the nature of the catalytic metal droplets formed on the substrate. For example, growth from the Au islands at 900 °C yielded only a thin ZnO nucleation layer with no NWs, while other metal compositions, which melt at lower temperatures than Au, produced a variety of NW

shapes, sizes and orientations at this temperature (Fig. 1). The approach also permitted rapid correlation of the optical properties of the nanowires with the composition of the metal islands from which they were grown. For example, ZnO NWs fabricated from the silver islands at 900 °C produced the sharpest excitonic peak near 3.36 eV on the cathodoluminescence spectrum (comparable to that for bulk ZnO single crystal), indicating superior crystalline structure. In contrast, the spectra were significantly broader for the NWs grown from the gold and copper containing islands. A comprehensive assessment of the correlation of structural and spectroscopic data for the ZnO NW library is still underway. These initial results demonstrate the power of the combined phase diagram/combinatorial approach for controlling semiconductor NW properties.

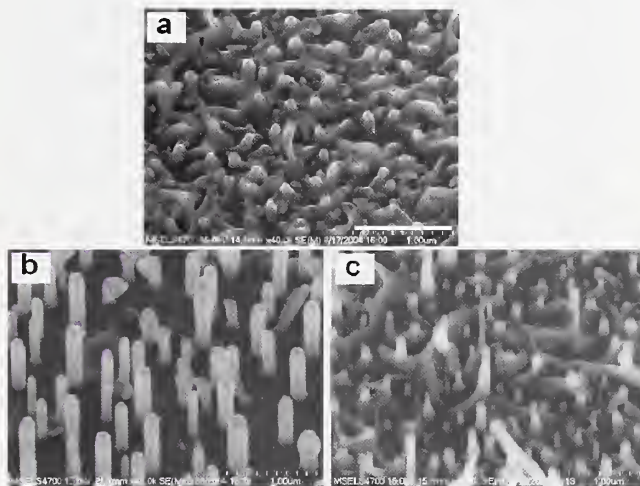


Figure 1. Selected scanning electron microscope images from the combinatorial library: a) ZnO wetting layer grown using gold catalyst (note the absence of NWs); b) ZnO NWs grown using gold-copper alloy catalyst; c) ZnO NWs grown using silver catalyst. Growth temperature is 900 °C. The scale bar on the top image is 1 μm.

Selected Publications

1. A.V. Davydov, A. Motayed, W.J. Boettger, R.S. Gates, Q.Z. Xue, H.C. Lee and Y.K. Yoo., Phys. Stat. Sol.(c), DOI 10.1002/pssc.200461605 (2005).

Electrical Properties of On-Chip Interconnections

Conductors in on-chip metallizations are reaching dimensions where defective seed layers are impacting manufacturing yields and electron scattering on surfaces and grain boundaries is reducing electrical transport. To meet these challenges we have quantified the sources of the resistivity increase of wires made of silver, the most highly conductive of all metals, demonstrated seedless processing routes for copper wires, and improved understanding and modeling of the superfill fabrication process.

Daniel Josell and T. P. Moffat, MSEL (855)

Reduction of transistor size in integrated circuits has been accompanied by shrinkage of the on-chip interconnects that carry electronic signals. This is straining industrial technology for copper seed deposition, a technical challenge noted in the International Technology Roadmap for Semiconductors. Such defects motivated our “seedless” ruthenium barrier process last year and motivate this year’s work on seedless copper superfill using ruthenium or iridium barriers (Fig. 1) deposited by Atomic Layer Deposition.

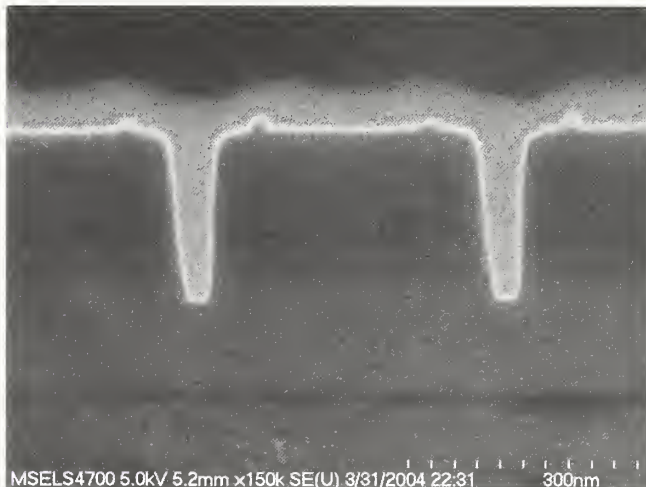


Figure 1. Trenches containing copper that was electrodeposited directly on an ALD iridium barrier (thin bright layer).

Shrinking dimensions are also leading to degraded electrical transport in industrial copper interconnects. Silver wires for electrical studies (Fig. 2) were fabricated using a superfill process developed in the Metallurgy Division. Wire resistivity increased with decreasing wire width (Fig. 3). The Fuchs-Sondheimer analysis for electron scattering was extended to include specular and diffuse scattering and resulting modeling indicated the

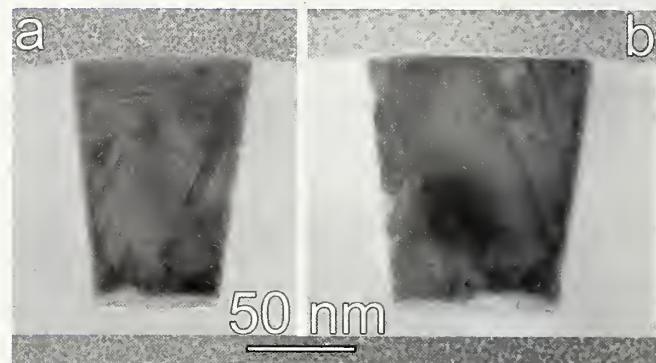


Figure 2. Cross-sections of electrodeposited silver wires after removing metal from the field (transmission electron microscope).

increase arises from grain boundary as well as surface scattering, with significant implications for mitigation.

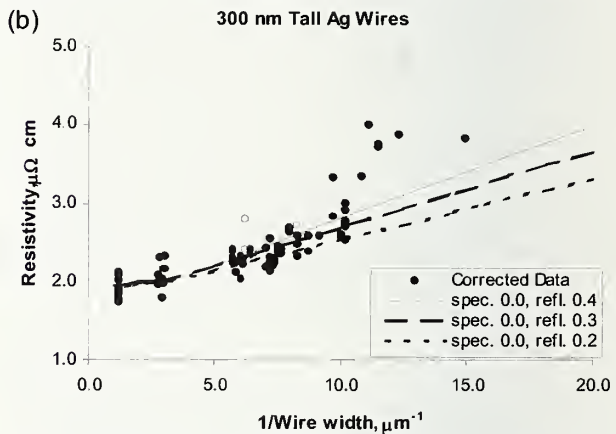


Figure 3. Electrical resistivities of 300 nm tall silver wires with predictions that account for surface scattering with varying amounts of grain boundary scattering. Resistivities for wires less than 100 nm wide are impacted by defects.

We continue to meet the industrial need for feature fill prediction. Experimentally determined deviations from the ideal adsorbate behavior underlying superfill have been added to our CEAC model. This has made our predictions even more accurate.

Industrial outreach continues: code sent by request to Intel, ST Microelectronics, and ATMI and an invited article in the IBM Journal of Research and Development.

Horizontal Growth and In Situ Assembly of Oriented Semiconductor Nanowires

The positioning and directed assembly of semiconductor nanowires (NWs) is of considerable current interest for “bottom-up” approaches to the engineering of intricate structures from nanoscale building blocks. In this regard, we have developed an approach that results in the horizontal growth, *in situ* alignment, and predictable positioning of nanowires. This strategy allows for the large scale production of arrays of nanowires and nanowire based devices.

Babak Nikoobakht and Stephan J. Stranick,
CSTL (837)

The vision of nanotechnology includes the possibility of building powerful, extraordinarily compact devices out of atomic-scale components. Nanowires (NWs), long, thin crystals of metals or semiconductors, are one such component. NWs can be used to not only link nanoelectronic devices, analogous to a conventional wire, but they can also function as unique devices themselves, e.g., photodetectors and/or light-emitting elements.

A crucial barrier to realizing this vision is the inherent difficulty associated with manipulating components so small that only the most sophisticated instruments can track and possibly direct their movement. Even simple manipulation, such as the alignment of NWs, presents an enormous technical challenge. To date, the most successful NW alignment methods have involved multi-step processes that include growth of a large number of the NWs on a suitable substrate, harvesting the NWs by shearing them off of the substrate, mixing the NWs in a solvent, aligning them using an applied field or by flow through microchannels, and finally, critical point drying to remove the solvent. Further, these time consuming procedures do not address the need to place the NW at a predetermined position on a substrate.

In addressing some of these issues, a method was developed in our laboratory by which *in situ* growth of horizontally aligned, crystalline NWs at predetermined (nanoscale) locations on a substrate became possible. We discovered that an Au catalyst droplet 25 nm in size or smaller, at high temperature, in the presence of Zn and O₂ precursors grows horizontally to a ZnO NW with a unique direction on a α -plane sapphire substrate. In this process, Au droplet moves on the surface as NW grows (Figure 1a). Atomic force microscopy also shows the straight growth trajectory of NWs and their smooth, defect-free surface (Figure 1 b). We have found that the

size of the Au catalysts and their spacing are very essential in promoting this type of growth. To pattern a surface with Au droplets that serve as “seed” particles for the horizontal NW growth, soft lithography and electron-beam lithography (EBL) are used. Both techniques can be used to deposit Au on selected areas of a surface. Another advantage of this approach is the ability to control the width of the NWs within a range of 2 to 25 nm. This is achievable by adjusting the lateral dimension of the deposited Au patterns, which results in Au particles 2-20 nm in size.

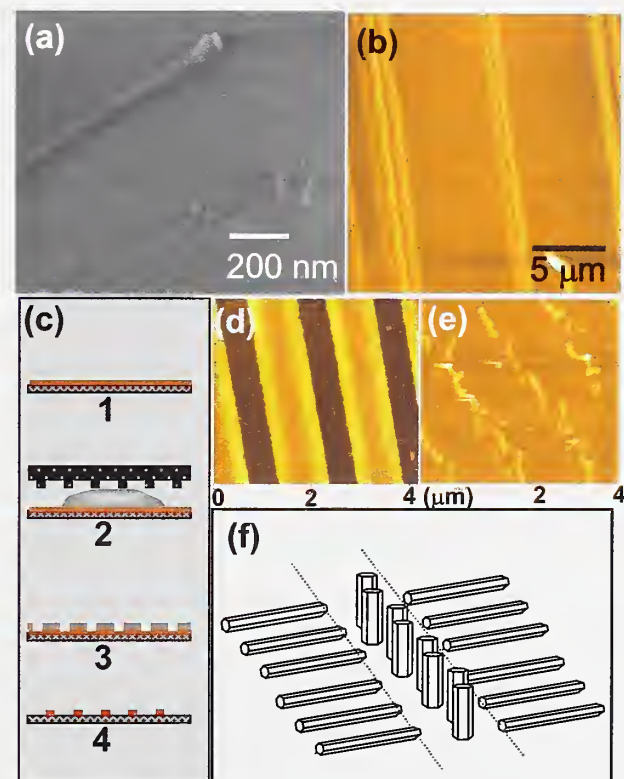


Figure 1. a) SEM image of ZnO NWs grown from Au nanodroplets. The brighter part of the NW is Au. b) AFM image of ZnO NWs shows the smooth surface of NWs and the unique growth direction. c) Steps 1-4 show the preparation of Au lines as catalyst. d) AFM image of polymer lines made in step 3. e) AFM image of Au lines after removing polymer lines in step 3. f) Schematic growth of NWs from an Au line.

Using soft lithography, the developed method begins with patterning a sapphire substrate (1120) with narrow Au lines, oriented perpendicular to the preferred growth direction of the NWs. Au lines are fabricated by depositing 5-6 nm of Au onto the substrate, followed by overcoating it with poly (ethyl methacrylate).

This is immediately followed by placing a micropat-

terned polydimethylsiloxane (PDMS) stamp on the polymer/substrate and removing it once the polymer is solidified at 25° C. The polymer lines are nominally 1.5 μm in width with a 400 nm spacing between them (Fig. 1c, step 3 and Fig. 1d). The patterned substrate is submerged in an Au etchant solution ($\text{KI}/\text{I}_2/\text{H}_2\text{O}$) for 20–40 seconds (depending on the initial Au film thickness) followed by rinsing with deionized water (18 M Ω). The Au film protected by the polymer lines (unetched) results in parallel Au lines, which can be made narrower than 100 nm by increasing the etching time. The last step is to remove the polymer lines by washing with ethanol (Figure 1e). The advantage of using narrow Au lines is that at high temperature, this morphology results in nanodroplets (nanoparticles) with the majority of them forming lines. These are the nanodroplets that catalyze the horizontal growth and result in formation of the organized NWs, which schematically is illustrated in Figure 1f. A SEM image, in Figure 2a, shows the alignment of the NWs and their growth direction. SEM and electron back scattering diffraction were used to determine the growth direction of NWs ($\pm [1\bar{1}00]_{\text{sap}}$) relative to the two known facets of the sapphire wafer.

The width of the NW is a critical parameter in the application of NWs, as this determines the extent of quantum behavior (confinement) in the direction transverse to the long axis of the NW. This effect is often seen in quantum wires with size regimes less than 10 nm, and there are very few examples of fabricating NWs with diameters within this size range. The developed approach enables us to grow quantum wires with very small diameters (Figure 2b). These quantum wires are grown from Au colloidal nanoparticles a few nanometers in diameter.

Precisely positionable and addressable NWs are crucial requirements of nanodevice fabrication; however, despite intense efforts in this direction, there has not been a practical solution to these issues. Our approach takes us one step closer to fulfilling these requirements. As a demonstration, EBL was used to precisely place Au catalyst on a substrate. NWs can be grown at those areas selectively (Figure 2c). These NWs later can be addressed by EBL technique for nanodevice fabrication.

The significant potential impact of this work has been recognized by the scientific community, as the highlights/vignettes have appeared on nearly a dozen nanotechnology focused websites world-wide, ranging from “popular scientific magazines” (e.g., US Tech) to science “foundation” (e.g., The Foresight Institute) venues. The dramatically reduced process time compared with less effective physical alignment procedures mentioned above, together with the inherent control of NW

placement, provide a methods that should facilitate fabrication of nanoscale devices.

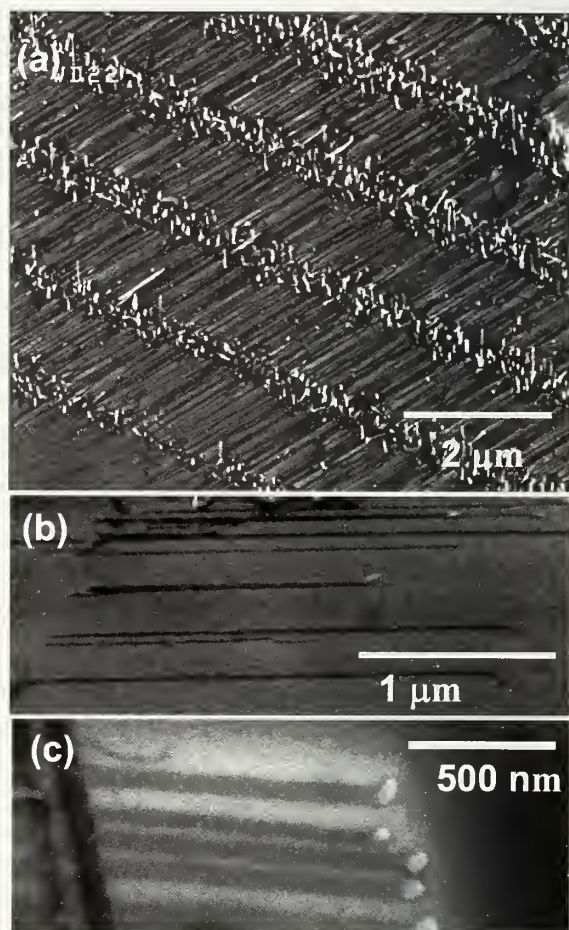


Figure 2. SEM image of arrays of ZnO NWs all oriented in one direction. b) ZnO NWs grown from Au colloidal NPs. Use of colloidal particles also results in growth of quantum wires. c) few NWs originated from an Au line, which was fabricated by e-beam writing.

This work will also serve as a basis for further refinements including, for example, the use of conventional photolithography to form the Au droplet seed pattern, which could allow this approach to be widely used in nanodevice fabrication on an industrial scale.

Selected Publications

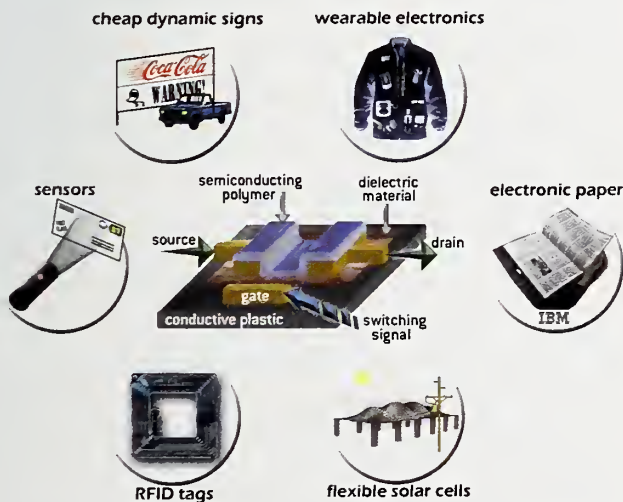
1. B. Nikoobakht, C. A. Michaels, S. J. Stranick and M. D. Vaudin, *Appl. Phys. Lett.* **85**, 3244 (2004).

Organic Electronics

The field of organic electronics has dramatically emerged in recent years as a technology encompassing a wide array of devices and applications including embedded passive devices, flexible displays, organic solar panels, and radio frequency identification tags. Device performance, stability, and function critically depend upon charge transport and material interaction at the interfaces of disparate materials at nanoscale dimensions. We develop and apply nondestructive measurement methods to characterize the electronic and interfacial structure of organic electronics materials with respect to processing methods, processing variables, and materials characteristics.

Eric K. Lin, MSEL (854)

Organic electronic devices are projected to revolutionize integrated circuits through new applications that take advantage of low-cost, high volume manufacturing, nontraditional substrates, and designed functionality. The current state of organic electronics is analogous to the early stages of the silicon electronics industry with the concurrent development of multiple material platforms and processes and a lack of measurement standardization between laboratories. A critical need exists for new diagnostic probes, tools, and methods to address new technological challenges.



Organic electronics present fundamentally different measurement challenges from those identified for inorganic devices. The adoption of this technology will be advanced by the development of an integrated suite of metrologies to correlate device performance with the nanoscale structure, properties, and chemistry of materi-

als and interfaces. We are developing measurement methods to provide the data and insight needed for the rational and directed development of emerging materials and processes.

We have focused on several active organic electronics materials including dielectric measurements of nanocomposites polymer films for embedded passive devices and advanced measurements of the orientation and structure of organic semiconductors for transistor applications.

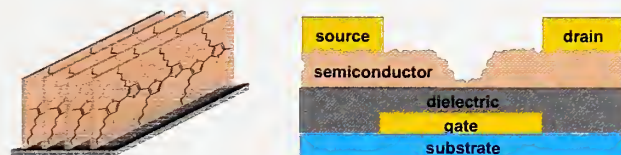


Figure 1. Schematic diagrams of the local structure of poly-3-hexylthiophene, an organic semiconductor near an interface (left) and the architecture for an organic transistor (right).

To meet the metrology needs for embedded passive devices, two new measurement methods were successfully developed and will find widespread use within industry. A NIST-developed Test Method for Dielectric Permittivity and Loss Tangent of Embedded Passive Materials from 100 MHz to 12 GHz was accepted and recommended as a standard test method. In addition, a new test was developed and applied for testing passive materials at high electric fields and voltages.

Finally, near-edge x-ray absorption fine structure (NEXAFS) spectroscopy was applied to several classes of organic electronics materials to investigate the electronic structure, chemistry, and orientation of these molecules near a supporting substrate. NEXAFS provides a powerful and sensitive method to probe the interfacial structure that is critical to the performance of these devices. For example, it was found that several organic semiconductor molecules preferentially align “edge-on” rather than “face-down” on solid substrates.

The NIST Advanced Measurement Laboratory Nanofab

To continue to respond to U.S. science and industry's needs for more sophisticated measurements and standards in the face of heightened global competition, NIST is constructing one of the most technologically advanced facilities in the world—the Advanced Measurement Laboratory, or AML. The NIST AML Nanofab (NF) is one of five buildings in the AML at the Gaithersburg, MD campus. The AML Nanofab will provide researchers at NIST working on a variety of semiconductor and other nanotechnology research the ability to fabricate prototypical nanoscale test structures, measurement instruments, standard reference materials, and electronic devices.

Robert Celotta (CNST) Russ Hajdaj (CNST) and Eric M. Vogel, EEEEL (812)

The AML contains 2 above ground instrument buildings, 2 completely below ground metrology buildings, and 1 class 100 clean room building which will house the NIST AML Nanofabrication Facility. The AML will provide NIST with superior vibration, temperature and humidity control, and air cleanliness.

The NIST AML Nanofab has approximately 10,000 sq. ft. of Class 100, raised floor, bay and chase, clean room space. NIST has invested in a complete suite of new equipment (capable of processing 150 mm wafers) that will be installed over the upcoming year. This includes furnaces (2 banks of 4 tubes each), LPCVD (poly, nitride, LTO), rapid thermal annealer, 3 reactive ion etchers (SF₆/O₂, Metal, Deep), 3 metal deposition tools (thermal, e-beam, sputterer), contact lithography (front- and back-side alignment), e-beam lithography, focused ion beam, and numerous monitoring tools (FESEM, spectroscopic ellipsometer, contact profilometer, 4-point probe, microscope with image capture, etc.).

The NIST AML Nanofab will be operated as shared access user facility. This means that the staff of NIST and its partners, subject to provisions, training, and user fees, will be permitted to independently operate the equipment. The tools will be operated in a manner such that a wide variety of materials can be processed. The facility will be directed by NIST's Semiconductor Electronics Division. Unlike other nanofabs, the NIST AML Nanofab is unique in that it is located next to the most advanced metrology tools in the world, and its focus will be on fabricating nanoscale structures necessary for me

trology and standards in support of the semiconductor industry, nanotechnology, biotechnology, and homeland security.

The NIST Advanced Measurement Laboratory (AML) Nanofabrication Facility (NF) will:

- Enable fabrication of prototypical nanoscale test structures, measurement instruments, standard reference materials, electronic devices, MEMS, and bio-devices critical to NIST's Strategic Focus Areas (Nanotechnology, Homeland Security, Healthcare) and the Nation's Nanotechnology Needs
- Provide access to expensive nanofabrication tools, technologies and expertise in a shared-access, shared-cost environment to NIST and its partners
- Foster internal collaboration in Nanotechnology across NIST's Laboratories
- Foster external collaboration in Nanotechnology with NIST's partners.



Figure 1. The NIST Advanced Measurement Laboratory

Probing Nanoscale Disorder with Neutron Tunneling Spectroscopy

To provide researchers with dynamical probes of atomic and nanoscale disorder using high-resolution neutron tunneling spectroscopic methods.

Robert M. Dimeo and Dan A. Neumann, MSEL
(856)

Structural disorder can have dramatic effects on macroscopic materials properties. Nanoscale disorder is described in terms of distributions of geometrical quantities such as bond lengths and bond angles, which can be determined from diffraction measurements. Alternatively, it can be quantified by the distribution of potential energies experienced by the atomic scale constituents of the system. This distribution is sharp for a highly ordered (crystalline) system, and broad for a disordered system. Rotational tunneling spectroscopy is a powerful tool to characterize the local molecular environment due to its exquisite sensitivity to the local potential. This technique has been used to determine the distribution of rotational potentials felt by methyl iodide molecules adsorbed in a series of nanoporous silica glasses. The degree of confinement-induced disorder in the methyl iodide can be directly related to the pore sizes in the glass.

The silica glasses used in this study have a range of pore size distributions with nominal diameters, $\langle d \rangle$, that vary from 2.5 nm to 14.4 nm. Liquid methyl iodide (CH_3I) was condensed into the porous hosts until 95 % of the open pore volume was filled and then cooled to 5 K. Spectra were collected using the NCNR High-Flux Backscattering Spectrometer with an energy resolution of 0.8 μeV .

The rotational potential felt by methyl (CH_3) groups in methyl iodide (CH_3I) arises solely from interactions with the local environment including the neighboring molecules. The energies of the transitions between rotational states can be found by solving the Schrödinger equation for the model potential by $V_3(1-\cos(3\theta))/2$ in the angular coordinate about the C-I axis, θ . In the limit of an infinitely high barrier, V_3 , the motion of the CH_3 group is that of a torsional oscillator. However, if the barrier is not too large, the wavefunctions will have significant overlap and quantum mechanical tunneling between the potential minima can occur. This results in a splitting of the rotational ground state. The energy of this splitting, which can be directly measured using cold neutron spectroscopy, has a nearly exponential dependence upon the barrier height. This strong dependence on V_3 is the reason why tunneling spectroscopy is so sensi-

tive to the local molecular environment and, in particular, the quenched disorder of adsorbed molecular solids.

The neutron scattering spectra display broad asymmetric lines indicative of a distribution of potential barrier heights. These distributions can be extracted from the neutron scattering data using a simple model in which a sum of Gaussian distributions of potential barriers (which yield an asymmetric tunneling line-shape) is used to fit the spectra. A sum of two potential distributions is sufficient to describe the data. One distribution is quite broad, indicating substantial disorder of the methyl iodide solid, while the other is much narrower suggesting a relatively high degree of order.

The relative weights of the two components show a pronounced dependence on $\langle d \rangle$. Figure 1 shows that the fraction of the total integrated intensity in the disordered component of the tunneling spectrum decreases as $\langle d \rangle$ increases. This behavior can be described with a simple model in which the relatively well-ordered component of the scattering is attributed to CH_3I molecules near the center of the pore while the highly disordered component is associated with a ring of thickness t of disordered molecules near the pore walls. Treating the pores as circular cylinders, the fraction f of disordered molecules is just the ratio of the ring to circular areas:

$$f = 2 \left(\frac{2t}{\langle d \rangle} \right) - \left(\frac{2t}{\langle d \rangle} \right)^2$$

The solid line in Fig. 1 compares this model to the data for $t = 1.41(4)$ nm, which corresponds to ~ 3 molecular layers, and provides an excellent fit to the data.

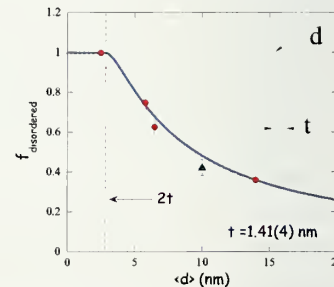


Figure 1. Fraction f versus mean pore diameter. The inset shows a schematic of a single pore.

Probing the Nanostructure of Lipid Membranes with the AND/R (Advanced Neutron Diffractometer/Reflectometer)

To provide researchers with probes of biological nanostructure using neutron reflectometry methods.

M. Mihailescu and David Worcester, MSEL
(856)

Lipids are the major constituents of cell membranes. Arranged as a two-molecule bilayer with a thickness of about 5 nm, they insulate the inside of cells and cell organelles from the outside. Proteins embedded in this bilayer provide the only conduits between the two sides. Intriguingly, the structures of the embedded proteins are shaped by lipid-protein interactions. To understand and describe these interactions quantitatively, the structures of lipid bilayers of varying lipid compositions must be determined. Neutron diffraction is a powerful tool for this purpose. As an illustrative example, we present such a study of bilayer membranes containing cholesterol.

Due to their dual hydrophobic-hydrophilic character, cell membrane lipids organize spontaneously into bilayers, causing the hydrophobic alkyl chains to be hidden in the bilayer center and the polar 'headgroups' to be exposed to water. The deposition of lipids onto a solid substrate (silicon, quartz, or glass) generally results in a stack of bilayers aligned parallel to the substrate surface (Fig. 1). The samples in this study were formed from dimyristoylphosphatidylcholine (DMPC) lipids in mixture with 0.20-mole fraction of cholesterol. Cholesterol, an essential component of mammalian membranes, participates in many physiological processes and plays an important role in organizing other lipids and membrane proteins. There is increasing evidence that it can associate preferentially with saturated lipids to form ordered domains called "rafts". These are believed to play an important role in signaling across cell membranes.

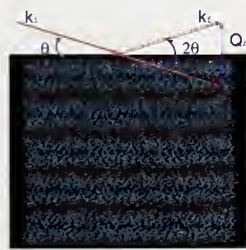


Figure 1. A stack of lipid bilayers at 66 % relative humidity, and $T = 300\text{ K}$ (image courtesy of F. Castro-Roman and R. Benz from UC Irvine).

The usefulness of neutron diffraction for studies of DMPC-cholesterol and other membranes arises because membrane lipids and the surrounding water are rich in

hydrogen atoms that can be selectively replaced with deuterium without changing the structure of the membrane. Deuterium nuclei coherently scatter neutrons much more strongly than protons. Selective deuteration thus allows the deuterated atoms to be readily identified. The structural information sought in our experiments was how the lipid mass (scattering length density) is distributed across the thickness of the membrane. Specular diffraction on oriented lipid multilayers, (i.e. diffraction where the neutron beam incident and emergent angles relative to the sample surface are equal), produces a diffraction peak at Bragg angles related to the d spacing of the bilayers.

The DMPC lipids were deuterium-labeled near the ends of the alkyl chains. 4000 bilayers, deposited on a thin glass slide, were mounted vertically in the beam in a sealed sample chamber at room temperature and a controlled relative humidity of 66 %. Fig. 2 shows two sets of diffraction patterns collected in a specular set-up for two water-contrast conditions: 100 % H_2O and a mixture containing a 0.50 mole fraction of D_2O .

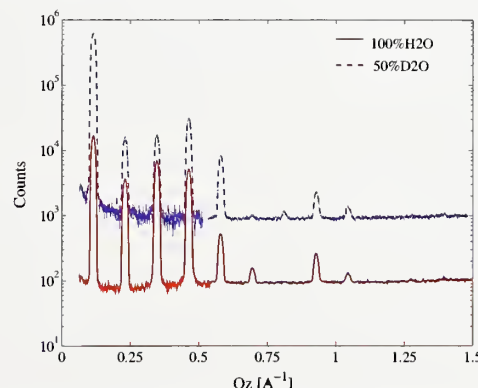


Figure 2. Diffraction intensities for oriented multilayers of DMPC + 0.20 mole fraction of cholesterol at $22\text{ }^\circ\text{C}$.

These data allow the position and extension of the different submolecular groups to be resolved. The bilayer thickness, as determined from the position of the diffraction maxima, is $d = 5.4\text{ nm}$, including the water associated with the lipid. Deuterium labeling at different positions along the lipids would allow a determination of the positions of specifically labeled atoms in the bilayer with a resolution of better than 0.1 nm.

Appendix

Appendix 1 - Cross-Reference to NIST Nanotechnology Focus Areas

Nanometrology (Fundamental science and basic measurement capabilities)

Nanomechanics/ structure

Structure and Dispersion Measurements of Polymeric Building Materials,
Li-Piin Sung (BFRL) 111

Nanomechanical Properties of Polymer Thin Films, Christopher M. Stafford (MSEL)..... 103

Nanomechanical Metrology, Douglas T. Smith and Lyle E. Levine (MSEL) 104

Nanoelectrical

Evanescence Microwave Probing and High-resolution Microwave Power Imaging,
Michael Janezic, James Baker-Jarvis, and Pavel Kabos (EEEL)..... 63

Electrical Properties of On-Chip Interconnections, Daniel Josell and T.P. Moffat (MSEL) 158

Nanochemical/ Nanobiological

Chemical Sensor Microscopy for Nanotechnology, Tinh Nguyen and Xiaohong Gu (BFRL)..... 101

Probing the Nanostructure of Lipid Membranes with the AND/R (Advanced Neutron
Diffractometer/Reflectometer), M. Mihailescu and David Worcester (MSEL)..... 165

Nanoassembly/fabrication

Nanoscale Science, Joseph A. Stroscio and Daniel T. Pierce (PL) 5

Nanotechnology with atom optics, Jabez J. McClelland (PL) 7

Agile Nanoassembly to Prototype, Test, and Manufacture Functional Nanodevices, Thomas W.
LeBrun (MEL) 151

Nanolithography: Next-Generation Polymer Photoresists, Vivek M. Prabhu (MSEL) 16

Combinatorial Metal Selection for Catalytic Growth of ZnO Semiconductor Nanowires, Albert V.
Davydov (MSEL) 157

Dimensional Metrology/ Imaging

Development of High-resolution Variable Pressure Reference Scanning Electron Microscope,
Andras E. Vladar, Michael T. Postek and John S. Villarrubia (MEL) 133

Scanning Probe Microscopy for Nanoscale Measurements, Ronald Dixson, Joseph Fu, George Orji,
and Theodore Vorburger (MEL) 135

Scanning Probe Microscopy for Nanoscale Measurements: Atom-Based Height Standards,
Joseph Fu, Ronald Dixson, George Orji, and Theodore Vorburger (MEL) 137

Appendix

Atom-Based Dimensional Metrology, Rick Silver (MEL)	139
Critical Dimension Metrology using Scanning Electron Microscopy and a Model-Based Library, John S. Villarrubia and András E. Vladár (MEL).....	141
SI traceable force for scanning probe microscopy and instrumented indentation, Jon R. Pratt (MEL).....	143
Phase-sensitive Scatterfield Optical Imaging for sub-10 nm Dimensional Metrology, Rick Silver (MEL).....	145
Improving Image Resolution in Nanotechnology, Alfred Carasso (ITL).....	105
Optical Metrology for Nanolithography, John H. Burnett, Simon G. Kaplan, and Eric L. Shirley (PL)	107
True Three-Dimensional Tomography Utilizing Bayesian Statistical Inference, Donald Malec and Juan Soto (ITL)	109
Advanced Control Systems and Positioning for Nanoscale Measurements and Standards, Nicholas G. Dagalakis (MEL).....	147
Molecular Measuring Machine, John A. Kramar (MEL).....	149
Development of Nano-tip Electron Guns for the Scanning Electron Microscope, Andras E. Vladar and Michael T. Postek (MEL).....	153
Measurement Strategy for Line Edge and Linewidth Roughness Metrology, John S. Villarrubia and András E. Vladár (MEL)	155

Nanocharacterization (Characterization of nanostructured materials)

Nanomechanics/ structure

Creating Visual Models of Nanoworlds, Judith Devaney (ITL)	13
Nanomechanical Characterization of Nanoparticle-filled Polymeric Coatings and Composites, Stephanie Scierka and Peter Votruba-Drzal (BFRL)	11
Mechanical Metrology for Small-Scale Structures, Edwin R. Fuller, Jr. and George D. Quinn (MSEL)	56
Nanotribology and Surface Properties, Stephen Hsu (MSEL).....	116
New Materials to Protect Firefighters from Burn Injuries, Jeffrey Gilman and Kuldeep Prasad (BFRL)	46
Quantitative Nanomechanical Properties, Donna C. Hurley (MSEL).....	119

Appendix

Probing Nanoscale Disorder with Neutron Tunneling Spectroscopy, Robert M. Dimeo and Dan A. Neumann (MSEL)	164
Neutron Reflectometry for Highly Accurate Nanometer Metrology, Joseph A. Dura (MSEL)	117
Nanoelectrical	
Semiconductor Quantum Dot Structure Metrology, Alexana Roshko (EEEL).....	53
Nanochemical/ Nanobiological	
Nanoscale Characterization of Polymeric Materials Degradation, Tinh Nguyen, Xiaohong Gu, and Jon Martin (BFRL).....	9
Polymer Miscibility of Imidazolium Compatibilized Nanotubes, Jeffrey Gilman (BFRL).....	45
Characterization and Photoreactivity of Titanium Dioxide Nanostructures, Stephanie Scierka and Joannie Chin (BFRL)	47
Chemistry and Structure of Nanomaterials, Daniel A. Fischer (MSEL).....	55
Synthetic X-ray Spectrum Images for 3D Chemical Imaging at the Nanoscale, John Henry Scott and Nicholas Ritchie (CSTL).....	113
Gradient Reference Specimens for Advanced Scanned Probe Microscopy, Michael J. Fasolka and Duangrut Julthongpibut (MSEL)	118
Nanoassembly/fabrication	
Brillouin Light Scattering, Ward Johnson, Sudook Kim, Colm Flannery, and Pavel Kabos (MSEL)	15
Highly Charged Ions in EUV Lithography, John D. Gillaspy and Joshua M. Pomeroy (PL).....	120
Highly Charged Ion Modified Materials, Joshua M. Pomeroy and John D. Gillaspy (PL)	57
Carbon Nanotubes/ Nanowires	
Optical Properties of Carbon Nanotubes, John Lehman (EEEL).....	49
Characterization of Single Walled Carbon Nanotubes, Angela R. Hight Walker (PL).....	50
Stability of Nanowires, Geoffrey B. McFadden (ITL).....	51
Chemical Sensing with Nanowires & Nanotubes, Richard E. Cavicchi (CSTL).....	63
III-Nitride Semiconductor Nanowires: Growth and Characterization, Kris Bertness and Norman Sanford (EEEL).....	65
Carbon Nanotube Metrology, Paul Rice and Tammy Oreskovic (MSEL).....	115

Appendix

Nanoelectronics (Nanoscale electronics and optoelectronics)

Nanoelectronics

Organic Electronics, Eric K. Lin (MSEL).....	161
Modeling for Organic Conduction, Carlos A. Gonzalez (CSTL).....	17
Measuring & Understanding Charge Transport in Molecules, Roger van Zee, (CSTL).....	64
Spin Electronics, William H. Rippard and Matthew R. Pufall (EEEL)	19
Nanoscale Metrology of III-Nitride Semiconductor Films and Nanowires, Norman Sanford and John Schlager (EEEL).....	58
Nanoelectronic Device Metrology Project, Curt A. Richter and Eric M. Vogel (EEEL)	70
Horizontal Growth and In Situ Assembly of Oriented Semiconductor Nanowires, Babak Nikoobakht and Stephan J. Stranick (CSTL).....	159
MOS Device Characterization and Reliability Project, John S. Suehle and Eric M. Vogel (EEEL) ..	68
Electrical Test Structure Metrology, Michael Cresswell and Richard Allen (EEEL)	122
The NIST Advanced Measurement Laboratory Nanofab, Robert Celotta (CNST), Russ Hajdaj (CNST) and Eric M. Vogel (EEEL).....	163

Nanomagnetics

Molecular Nanomagnets, Brant Cage and Stephen E. Russek, (EEEL).....	124
Nanomagnetism, John Unguris and Mark Stiles (PL).....	22
Nanomagnetodynamics, Robert D. McMichael (MSEL).....	21
Nanomagnetodynamics: Devices, Stephen E. Russek, (EEEL)	72
Nanomagnetodynamics: Fundamental Properties, Thomas J. Silva, (EEEL)	25
Mathematical Modeling of Nanomagnetism, Michael J. Donahue and Donald G. Porter (ITL)	60
Nanomagnetic Measurements, John Moreland, (EEEL)	126
Synthesis, Characterization, and Manipulation of Magnetic Nanoparticles, Guangjun Cheng and Angela R. Hight Walker (PL)	24
Magnetic Materials For Nanoscale Sensors and Ultra-High Density Data Storage, William F. Egelhoff, Jr. (MSEL).....	62
Nanoscale Engineered Magnetic Sensors, David P. Pappas (EEEL)	74

Appendix

Nanobiotechnology (and Nanochemistry)

Bioelectronics, Michael Gaitan, Darwin Reyes-Hernandez, and Brian Polk, EEEL (812), Laurie Locascio, and Sam Forry CSTL (839).....	27
Single Molecule Nanovials, Michael Gaitan EEEL (812), and Laurie Locascio and Wyatt Vreeland, CSTL (839).....	29
Optical Manipulation of Nanocontainers and Nanotubes, William D. Phillips, Kristian Helmerson (PL)	31
Quantitative single-molecular pair fluorescence resonance, Lori S. Goldner (PL).....	98
Bacteriophage/Quantum-dot nanocomplex to detect biological target in clinical or environmental isolates, Jeeseong Hwang (PL).....	100
Nanoparticle Measurements for Biological Applications, John Moreland, (EEEL)	128
Imaging Methods for Nanoparticle and Cell Systems to Investigate Toxicity, Cynthia J. Zeissler and Peter E. Barker (CSTL).....	130

Quantum Devices, (Computing, and Communications)

Quantum devices

Fundamental Properties of Quantum Dots, Kevin Silverman (EEEL).....	33
Multiscale Modeling of Nanostructures, Vinod Tewary and David Read (MSEL)	35
Precision Metrology for Nanoscale Quantum Technologies, John Lawall and Garnett W. Bryant (PL)	38
Nanoscale Fabrication, James Beall (EEEL)	80
Quantum Sensors, Kent Irwin (EEEL).....	88
Single Electronics for Standards and Metrology, Mark Keller and Neil Zimmerman (EEEL).....	90
Quantum Voltage Metrology, Samuel Benz and Yi-hua Tang (EEEL)	92

Quantum computing

Control of Cold Quantum Gases for Atomic Clocks and Quantum Information Processing, Paul S. Julienne and Eite Tiesinga (PL)	40
Quantum Computing with Trapped Ions, David Wineland and Tom O'Brian (PL)	42
Quantum Computing Using Superconducting Phase Qubits, Ray Simmonds (EEEL).....	86
Neutral Atom Quantum Computation, William D. Phillips, James Porto (PL)	44

Appendix

Synthesis of Quantum Logic Circuits, Stephen S. Bullock (ITL).....	96
Architectures for Fault-tolerant Quantum Computing, Emanuel Knill (EEEL).....	94
Quantum communications	
Designing the Nanoworld: Nanosystems and Nano optics, Garnett W. Bryant (PL).....	36
Single Photon Sources and Detectors, Richard Mirin (EEEL).....	76
Terahertz Technology, Erich Grossman and Robert Schwall (EEEL).....	78
Johnson Noise Thermometry, Wes Tew, Sam Benz, Sae Woo Nam (EEEL).....	82
Quantum Communications, Sae Woo Nam (EEEL).....	84

Appendix

Appendix 2 - Keywords

A

Atom

- (Nano) Manufacturing
- (Nano) Material

B

Biohazard

(Nano) Biological

(Nano) Biotechnology

Bottom up

- (Nano) Materials characterization
- (Nano) Mechanics
- (Nano) Mechanical characterization
- MEMS
- Modeling
- Molecule
- Molecular beam epitaxy

C

Carbon Nanotubes

(Nano) Chemistry

(Nano) Chemical characterization

Combinatorial method/ library

D

Data

Dimensional metrology

- N
- Nanowires
- Neutron characterization

E

(Nano) Electrical characterization

(Nano) Electronics

Environmental

- O
- (Nano) Fabrication
- (Nano) Optical characterization
- (Nano) Optics
- (Nano) Optoelectronics
- Organic

F

(Nano) Fabrication/ Assembly/

Manipulation/ Modification

- P
- (Nano) Particles
- Photons/ Photonics
- Polymers

I

Instrumentation

- Q
- Quantum communications
- Quantum computing
- Quantum devices
- Quantum dots

L

(Nano) Lithography

M

(Nano) Magnetics

Appendix

R

Reference material

S

SI Units

Scanning probe microscopy (electron or optical probe)

Scanning probe microscopy (physical probe)

Scanning Tunneling Microscopy

Semiconductor

Sensors

Societal Dimensions PCA (implications for)

Spectroscopy

Standard Reference Material

Standards

Standards organization

(Nano) Structure/ Structured

T

Traceability

X

X-ray characterization

Appendix





